



HAL
open science

Influence of the metallicity of solid surfaces on the properties of interfacial or confined fluids

Laura Scalfi

► **To cite this version:**

Laura Scalfi. Influence of the metallicity of solid surfaces on the properties of interfacial or confined fluids. Theoretical and/or physical chemistry. Sorbonne Université, 2021. English. NNT : 2021SORUS512 . tel-03718013

HAL Id: tel-03718013

<https://theses.hal.science/tel-03718013>

Submitted on 8 Jul 2022

HAL is a multi-disciplinary open access archive for the deposit and dissemination of scientific research documents, whether they are published or not. The documents may come from teaching and research institutions in France or abroad, or from public or private research centers.

L'archive ouverte pluridisciplinaire **HAL**, est destinée au dépôt et à la diffusion de documents scientifiques de niveau recherche, publiés ou non, émanant des établissements d'enseignement et de recherche français ou étrangers, des laboratoires publics ou privés.



Thèse de doctorat

Pour l'obtention du grade de
Docteur de Sorbonne Université

École doctorale Chimie Physique et Chimie Analytique de Paris Centre (ED 388)

Influence of the metallicity of solid surfaces on the properties of interfacial or confined fluids

présentée par

Laura Claire SCALFI

Directeur de thèse: Benjamin ROTENBERG

Présentée et soutenue publiquement le 1^{er} juillet 2021 devant un jury composé de :

M. Agilio PADUA	Rapporteur
M. Laurent JOLY	Rapporteur
M. Lydéric BOCQUET	Examineur
Mme. Francesca INGROSSO	Examineur
Mme. Marialore SULPIZI	Examineur
M. Benjamin ROTENBERG	Directeur de thèse



À Michele et Élodie

Acknowledgements

This PhD work is the result of three years of research in the laboratory Physicochimie des Électrolytes et Nanosystèmes Interfaciaux (PHENIX) at Sorbonne Université under the supervision of Benjamin Rotenberg. I thank him for his dedication during these years and for the trust and freedom he gave me for my research, while always being present and available for discussions. I learned a lot from him and grew up scientifically throughout this inspiring experience. I am particularly grateful for all the opportunities he encouraged me to take – being able to attend several trainings and conferences – and for the enthusiastic advice for the future.

I would also like to thank Mathieu Salanne, that participated closely to this project, for all the discussions we had, for his trust and for letting me play with MetalWalls and express freely my geek self. Many thanks also to Matthieu Haefele and Abel Marin-Lafèche at Maison de la Simulation that introduced me to high performance computing and helped me learn many new skills.

I also had the chance to work with Benoit Coasne from Laboratoire Interdisciplinaire de Physique at Université Grenoble Alpes, that I thank for his patience and for sharing his experience on confined systems.

I want to thank Agilio Padua and Laurent Joly for reviewing this manuscript and giving their feedback on my work, as well as Lydéric Bocquet, Francesca Ingrosso and Marialore Sulpizi for accepting to be part of the jury for this PhD thesis.

During this PhD I had the opportunity to teach at the university in the chemistry department and to supervise a great master student Mustakim Mustakim. I also participated in the examination of the 51st International Chemistry Olympiads, held in Paris in 2019: I would like to thank Clément Guibert and Élise Duboué-Dijon for this enriching experience and their presence since the time I was myself a student for this competition.

This experience would not have been the same without the scientific and non-scientific environment at PHENIX. I would like to especially thank Laurent Michot and Marie Jardat for their support and good mood, and all the permanents and non-permanents that I had the pleasure to meet in the lab. In particular, thank you to Alessandra and Claire for always being there, Jesse for his everlasting enthusiasm, Thiago, Sam and Seb for all the good memories. Thank you to the former équipe cantine and to Kyle, Thomas, Mitra, Adelchi, Nidhal, Lisbeth, Tadeja, Anastasia, Agathe, Dominika, Mesut, Alexandros, Etienne, Andris, Syvagen, Roxanne, Camille, Jeanne, Tsu-Yao, Loic, Minh-The, Iurii, Giovanni, Pierre, Antony, Jaqui, Arthur, Antonio, Ali... and so many more! Thank you also to the rest of the Italian team, Alessandro and Simone, for all the scientific discussions, pizzas and fondues we had.

Lastly, a thank you to my fellow aikidoka and kenshi that helped me in the good and the bad days, to my former schoolmates, to Valentina that adopted me for a few months of *télétravail* in Milan and a big thank you to all those, friends and family, that supported me (both in the English and the French/Italian meaning of the word) in this adventure and followed my globe-trotting around the world these past years, sometimes since the very beginning. I could not have arrived here without them.

Contents

1	Introduction	11
1.1	Context and inspiration	11
1.1.1	Metallic and electrified interfaces	11
1.1.2	Confinement and phase transitions	13
1.1.3	Interfaces, ionic liquids and metallicity	14
1.2	Metals in molecular simulations	18
1.2.1	The challenge of metallic interfaces	18
1.2.2	Electrodes in classical molecular simulations	18
1.2.3	Influence of electronic polarization: should we take it into account?	21
1.3	Objectives and organization of the thesis	23
2	Molecular simulations of electrochemical systems	24
2.1	Models at the molecular scale	24
2.1.1	Systems investigated	25
2.1.2	The interaction potential	28
2.1.3	Calculation of interactions	33
2.2	Statistical mechanics: from the microscopic to the macroscopic	36
2.2.1	Thermodynamic ensembles and sampling	36
2.2.2	Fluctuations and linear response theory	38
2.2.3	Monte Carlo simulations	39
2.3	Molecular dynamics simulations	40
2.3.1	The ergodic principle	40
2.3.2	Propagating the equations of motion	40
2.4	Extracting molecular properties	43
2.4.1	Structural properties: density profiles and radial distribution functions	44
2.4.2	Electrochemical properties: charge and capacitance	45
2.4.3	Dynamical properties: autocorrelation functions	46
2.4.4	Ensemble averages and statistical errors	47
2.4.5	Phase coexistence	47
2.5	Enhanced sampling methods	50
2.5.1	Heating the system up	51
2.5.2	Biasing the Hamiltonian using Umbrella Sampling	52
2.5.3	Manipulating the Hamiltonian with Thermodynamic Integration methods	53
3	Simulating metals: the constant potential ensemble	56
3.1	Accounting for the electronic polarization	56
3.1.1	Constant potential molecular simulations	57
3.1.2	Statistical mechanics of the constant potential ensemble	59
3.1.3	Sampling the constant potential ensemble	60
3.1.4	Born Oppenheimer sampling	63
3.1.5	The calculation of charge and capacitance	64
3.2	Insulating vs metal: the influence of electronic polarization	70
3.2.1	Electric response to a single ion in vacuum	71

3.2.2	Electric response to ions in solution	73
3.2.3	Impact on surface tension and contact angles	75
4	Accounting for the metallicity: the semiclassical Thomas-Fermi model	78
4.1	Electronic screening and the Thomas-Fermi model	78
4.1.1	The free electron gas and the Local Density Approximation	78
4.1.2	Theory of screening and the Thomas-Fermi model	80
4.1.3	Implementation of the Thomas-Fermi model in constant potential simulations	81
4.2	Impact of metallicity on the electrolyte properties	83
4.2.1	Analytical predictions	83
4.2.2	Calculations for an empty capacitor	84
4.2.3	Electrochemical cells	87
5	Phase transitions under confinement	94
5.1	Crystallization under confinement: thermodynamic origin	94
5.1.1	Interfacial free energies and their consequences	94
5.1.2	Gibbs-Thomson equation from a nucleation point of view	96
5.1.3	Gibbs-Thomson equation from the thermodynamic equilibrium of the phases	96
5.2	Derivation of the Gibbs-Thomson equation	97
5.2.1	A “confined Clapeyron” approach in the $\mu A_W HT$ ensemble	97
5.2.2	Integration along a bulk-to-confined thermodynamic path	98
5.3	Numerical predictions of the Gibbs-Thomson equation	101
5.3.1	Bulk properties	101
5.3.2	Surface tension calculation	103
5.3.3	Melting temperature under confinement	107
5.3.4	Discussion of the Gibbs-Thomson equation	108
6	Effect of metallicity on interfacial free energies	112
6.1	The Thomas-Fermi Thermodynamic Integration	112
6.1.1	Statistical mechanics framework	112
6.1.2	Continuum prediction from a thermodynamic cycle	114
6.1.3	Empty capacitor	115
6.2	Influence of the metallicity on the surface tension: the impact of charge heterogeneity at the surface	117
6.2.1	Thomas-Fermi Thermodynamic Integration for electrochemical cells	117
6.2.2	Influence of voltage	118
6.2.3	Analytical model: charge heterogeneity	119
6.3	Influence of metallicity on the crystallization	125
7	Conclusion and Perspectives	128
A	Publications from this work	131
B	A simulation code: <i>MetalWalls</i>	132
B.1	<i>MetalWalls</i>	132
B.2	Code improvements	133
B.2.1	Input/output	133
B.2.2	Pistons and NP_zT simulations	133
B.2.3	Four-sites water models	133
B.2.4	Python interface to <i>MetalWalls</i>	133
C	Ewald summation	134
C.1	3D Ewald summation for Gaussian and point charges	134
C.1.1	Point charges	134
C.1.2	Gaussian charges	134

C.1.3	Cross interactions	134
C.2	2D Ewald summation for Gaussian and point charges	135
C.2.1	Point charges	135
C.2.2	Gaussian charges	135
C.2.3	Cross interactions	135
D	Implementation of GEMC and GDI simulations	136
D.1	Gibbs-Ensemble Monte Carlo	136
D.2	Widom insertion method	136
D.3	Gibbs-Duhem Integration	137

Chapter 1

Introduction

1.1 Context and inspiration

1.1.1 Metallic and electrified interfaces

The present thesis deals with phenomena occurring at interfaces, or that are influenced by the latter, with a focus on interfaces between a solid wall and a vapor, liquid or solid phase. The competition of interactions between molecules and with the solid wall leads to changes of the properties with respect to the bulk phases, or results in new phenomena. From the thermodynamic point of view, interfaces and confinement between walls bring additional interfacial free energy contributions, which generally shift the phase diagram as discussed in section 1.1.2. From the structural point of view, the finite size of atoms and molecules results in layering, while the presence of an electric charge on the wall leads to the depletion or accumulation of charged species. From the dynamical point of view, the walls not only change the diffusion or hydrodynamics near the fluid, but may also lead *e.g.* to electrokinetic couplings.

More specifically, we focus on metallic surfaces, *i.e.* solid conducting walls (electrodes) which allow the transport of electrons, as opposed to insulating surfaces, where electrons are localized on the atoms. These surfaces are crucial for many electrochemical processes, as energy production and storage¹ (in batteries and capacitors) or electrocatalysis². A schematic view of a capacitor device is shown in figure 1.1a, where two electrodes are separated by a liquid that can transport ionic charges, called an electrolyte. Different sorts of electrolytes can be put in contact with metallic electrodes: aqueous salts, water in salts^{3;4}, polymer electrolytes⁵ or room temperature ionic liquids (see section 1.1.3). The latter are promising electrolytes for battery and capacitor devices, because of their low vapor pressure, high thermal stability and wide electrochemical window.

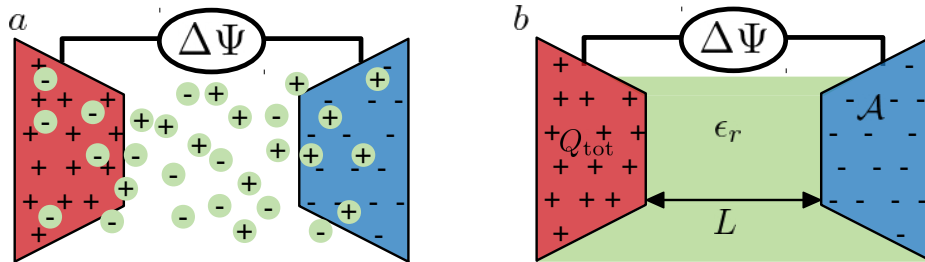


Figure 1.1: Schematic illustration of a capacitor: two electrodes (red and blue) of area \mathcal{A} at a distance L , held at a potential difference $\Delta\psi$ by an external generator are separated by an electrolyte, *i.e.* an ionic solution illustrated as ions embedded in an implicit solvent (a) or by an homogeneous dielectric medium of dielectric constant ϵ_r (b). The total accumulated charge on the positive (red) electrode is Q_{tot} , which then gives the integral capacitance as $C = Q_{\text{tot}}/\Delta\psi$.

Using a generator, one can further impose an electric potential difference, or voltage $\Delta\psi$, between two electrodes. This in turn creates a net accumulation of charge on the electrodes, as schematized in figure 1.1a. The additional coupling between electronic charges on the metallic surface and ionic charges in the interfacial fluid and the finite size of ions yields a characteristic structure of the molecular charges, known as the electric double layer (EDL)⁶. This term refers to a region in the vicinity of the electrode where molecular charges and ions accumulate to screen the electrode's charge, which results in a polarization of the interface. In a battery, the applied potential additionally triggers redox chemical reactions, while in capacitors the energy is stored exclusively in the EDL. The accumulated charge Q_{tot} is of great interest for energy storage applications and depends on the characteristics of the device. The performances are then characterized by the capacitance, *i.e.* the total accumulated charge divided by the applied voltage $C = Q_{\text{tot}}/\Delta\psi$. In the case of a perfect metal, the electric field within the material vanishes. This implies that in the presence of an external perturbation (external charge or finite voltage), a surfacic charge σ is induced at the surface of the material. In the simplest case of an ideal parallel plate capacitor, composed of two planar metallic electrodes of area \mathcal{A} separated by a slab of homogeneous dielectric medium of length L , as shown in figure 1.1b, the capacitance is

$$C = \frac{\epsilon_0 \epsilon_r \mathcal{A}}{L}, \quad (1.1)$$

where ϵ_0 is the vacuum permittivity and ϵ_r the dielectric constant of the medium ($\epsilon_r = 1$ in vacuum). Simple theoretical models (illustrated in figure 1.2) have been since introduced to predict the capacitance of electrochemical cells by solving the mean-field Poisson equation in the direction perpendicular to the electrodes $d^2\psi/dz^2 = -\rho_c(z)/\epsilon_0$, with ψ the Poisson potential and ρ_c the charge density, for the different regions of the capacitor. Each region can then be analyzed in terms of single capacitors and the overall cell corresponds to a circuit of capacitors in series. Helmholtz⁷ first introduced a simple picture of the EDL as a compact layer of ions of opposite charge at the surface, of thickness l , as shown in figure 1.2a, that corresponds to a capacitance $C_H = \epsilon_0 \mathcal{A}/l$ and to a linear potential drop at the interface. Later, Gouy and Chapman^{8;9} considered instead a diffuse layer of both co-ions and counterions, assuming a Boltzmann distribution at the interface, and solved the linearized Poisson-Boltzmann equation (also known as Debye-Hückel theory). In this case, the Poisson potential decreases exponentially towards the bulk potential value, as sketched in figure 1.2b, with a characteristic length $\lambda_D = \sqrt{\epsilon_0 \epsilon_r k_B T / \sum_i z_i^2 c_i^b}$, the Debye length, which depends on the charges of ions z_i and their bulk concentration c_i^b . Finally Stern¹⁰ (see figure 1.2c) combined both models, a Helmholtz layer (also called Stern layer) and a diffuse layer, as two capacitors in series, yielding an overall EDL capacitance $\frac{1}{C_{EDL}} = \frac{1}{C_H} + \frac{1}{C_{GC}}$. The EDL is then composed of the accumulated charges in the metal, an immobile layer of dense ions compensating the metal's charge, where packing and finite ion size effects play a dominant role, and a diffuse layer in which the ions concentration profiles are exponentially decaying, with an excess of co-ions and a depletion of counterions.

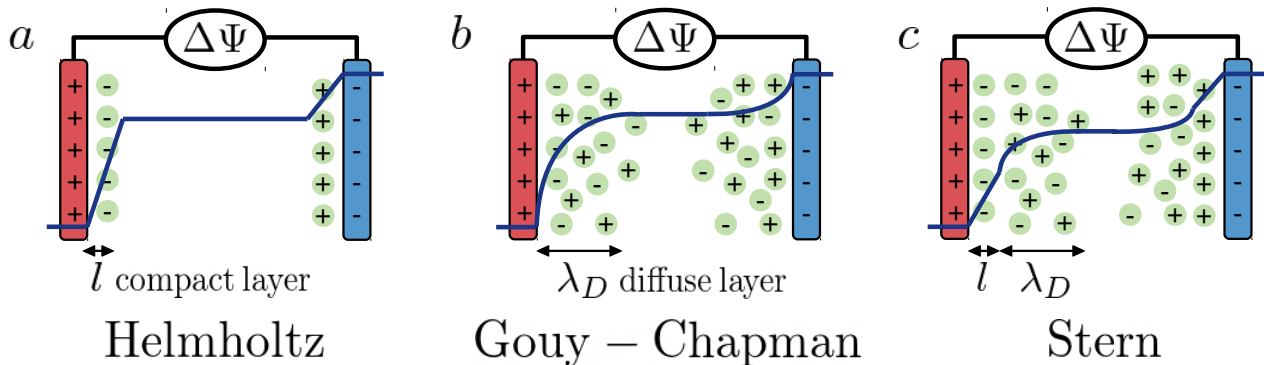


Figure 1.2: Simple models of the electric double layer: the Helmholtz model (a), the Gouy-Chapman model (b) and the Stern model (c). The bold blue lines are sketches of the Poisson potential profile within the electrochemical cell.

These continuum theories however are limited to dilute electrolytes and fail to account for the role

of the solvent, *e.g.* the orientation of water molecules at the interface. Phenomena such as layering at the interface due to the finite size of ions, or the behavior of purely ionic compounds such as ionic liquids or molten salts cannot be predicted. Kornyshev¹¹ proposed a mean-field expression for the EDL capacitance extended to concentrated electrolytes. Although the approximations to obtain an analytical prediction are crude, they predict “bell” and “camel” shapes for the differential capacitances, defined as $C_{\text{diff}} = \partial Q_{\text{tot}} / \partial \Delta\psi$, as a function of the applied voltage depending on the concentration of the electrolyte, which have been observed experimentally. Other extensions of the mean-field Poisson-Boltzmann theory have been proposed that capture the effects of excluded volume or solvent polarization and electrostatic correlations^{12–14} on the structure and capacitance of the EDL in ionic liquids or water-in-salts, as well as on the dynamics of charging^{15;16}. These studies however cannot include all the molecular details of the solvent dynamics and ionic correlations, and this calls for more extensive and systematic studies of concentrated electrolytes in capacitors, such as molten salts, ionic liquids or water-in-salts. As such, molecular simulation is a means to take into account the molecular nature of these interfaces and to extract capacitance values and Poisson potential profiles, which present an oscillatory behavior.

The electronic conduction within the electrode material plays an important role in electrochemical devices. Typical materials for battery electrodes are *e.g.* metals (lead Pb, gold Au, copper Cu, zinc Zn, platinum Pt...). In capacitor devices, other carbon-based electrode materials such as graphite, that are non-ideal conductors, are now being used. In particular, the diversity of different microscopic structures accessible, such as carbon nanotubes, activated carbon, carbide-derived carbons (CDC) or graphene sheets, allows to tune its properties and increase its specific surface area, widening the range of applications¹⁷. Graphite surfaces have for example been investigated for electrowetting applications^{18–20}, electro-tunable friction^{21–28} or as anode materials in batteries. The nanoporous CDC structure further provides specific highly confined environments (nanotubes, nanospheres...) that radically modify the solvation properties of ions thus yielding a very large capacitance^{29;30}. They are employed in supercapacitor devices and recent applications include the extraction of “blue energy” from mixing pure and salty water^{31–33}.

1.1.2 Confinement and phase transitions

A particularly interesting aspect of confinement is its effect on phase transitions. A hint that the presence of the interface modifies the phase behavior of a fluid is for example the formation on certain surfaces of prewetting (liquid-like or solid-like) layers that cover the surface. These layers can come from chemical reactions at the surface, which we do not consider in the following, or specific physical interactions with the fluid molecules. Under very high confinement (smaller than 10 – 20 molecular sizes), the perturbations due to the interface, *e.g.* the modification of the density profiles with a strong layering at the surface, extend over the whole confined volume, giving rise to disjoining pressure effects^{34–39}. These effects result from the fact that the different interfaces “feel” each other and cannot be considered as independent, which becomes even more dramatic for stronger confinement. Interfacial properties then depend on the characteristic length of confinement. In the case of crystallization, the commensurability of the crystal phase and the confining length also yield a rich behavior, *e.g.* the most stable crystal face on a surface, usually determined by the lowest surface energy, can change with the confinement length^{36;37;39} if it allows to better adjust crystal planes in the confined geometry.

Aside from these specific aspects due to very small confining lengths, the interface has an energetic cost, characterized by the interfacial free energy per unit surface or the surface tension γ , which plays a role in the thermodynamics of a confined fluid. In most cases, the interactions of a surface with different phases of a compound (gas G , liquid L , solid S , or other crystalline phases) differ, which results in a stabilization of certain phases with respect to others because of a less unfavorable interaction with the surface wall. This in turn translates into a shift of coexistence properties, such as pressure or temperature of transition⁴⁰. The theoretical aspect of this phenomenon is discussed in chapter 5 and no details are given here.

Phase transitions under confinement were studied extensively both using experiments and simulations^{41;42}. In the case of the vapor-liquid transition, the gas phase condensates in a pore at a pressure lower than the saturation pressure corresponding to the bulk equilibrium. This is known as capillary condensation and described by the Kelvin equation, which predicts an effect inversely proportional to the characteristic confinement length confirmed by experiments⁴³. Capillary condensation impacts for example nanoscale probes such as Atomic Force Microscope (AFM) or Surface Force Apparatus (SFA) measurements, depending on the ambient humidity, by the creation of liquid bridges between the tip of the microscope and the nanoscale-rough considered surface^{44–46}.

In the case of the liquid-solid transition^{47;48}, the melting temperature either increases or decreases in confinement with respect to the bulk. The sign depends on the relative (de)stabilization of the liquid with respect to the solid due to the interface, and is computed from the sign of the difference in surface tension between the liquid and the wall on the one hand, and the solid and the wall on the other hand. The shift is given by the Gibbs-Thomson equation, which we discuss at length in chapter 5, for large enough pores that can be treated by continuum thermodynamics. Understanding the crystallization under confinement is important from a fundamental point of view, and because it allows to probe states of matter that are not accessible otherwise (such as supercooled liquids)⁴⁹. It also has a significant impact on industrial processes, which widely use micro- and meso-porous materials (such as zeolites or activated carbons) for catalysis, extraction and separation of compounds, removal of pollution and contaminants. A majority of rocks are also porous materials, and many geophysical phenomena related to temperature variations and the crystallization of water in rocks, such as freeze-thaw weathering or frost heaving, are not fully understood⁵⁰. This in turn impacts the civil engineering constructions and is particularly important for the preservation of the architectural cultural heritage. Other impacts are in lubrication applications and for flow and diffusion in porous structures at temperatures close to the freezing temperature.

1.1.3 Interfaces, ionic liquids and metallicity

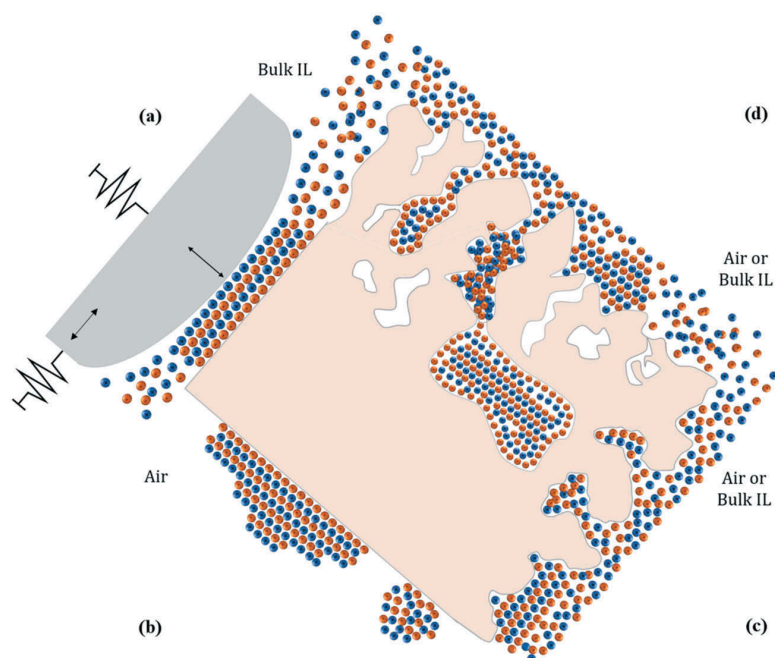


Figure 1.3: Illustration of ionic liquids in various confined geometries at the nanoscale. Red and blue dots represent the ionic liquid's cations and anions. Reproduced from Ref. 51.

In light of the previous sections, combining confinement effects on phase behavior and metallic interfaces promises interesting phenomena. This has been in particular studied for ionic liquids in contact with different interfaces. They have the peculiarity of being solvent-free, *i.e.* they are only

composed of ions. They are separated into molten salts, *i.e.* standard salts such as NaCl that are liquid at very high temperatures (thousands of Kelvin), and room temperature ionic liquids (RTIL), with a melting temperature below 100°C. RTILs are usually composed of large asymmetric organic cations (*e.g.* imidazolium-based cations) and inorganic or organic anions (such as PF_6^- , BF_4^- or bis(perfluoromethyl-sulfonyl)imide $(\text{CF}_3\text{SO}_2)_2\text{N}^-$). Their purely ionic nature sparks interest both fundamentally to understand the liquid state⁵² and in various applications as solvents for synthesis, catalysis or extraction, as electrolyte in capacitors or as lubricants because of their low vapor pressure, high thermal stability, wide electrochemical window and good conductivity⁵³. Additionally, choosing the chemical composition of the anion and cation allows to tune the properties of the RTIL to match a given application.

Although in principle their bulk behavior makes them excellent candidates for industrial applications, some applications such as lubrication or heterogeneous catalysis crucially depend on the behavior of IL at interfaces, illustrated in figure 1.3. These fluids are thus extensively investigated to understand their structure and dynamics in order to improve their properties^{54;55}. There is now strong evidence that supports the existence of a pronounced layering at the interface, that extends for several molecular layers within the electrolyte, and of a specific organization at the surface, as shown *e.g.* by scanning tunneling microscopy (STM)⁵⁶, surface force balance (SFB)^{57;58} or molecular simulations⁵⁹. Using atomic force microscopy (AFM), profiles of force *vs* separation from the surface, such as in figure 1.4b, were measured and showed up to 9 indentations due to squeezed out molecular layers of $\sim 0.5\text{--}0.7\text{ nm}$, consistent with the size of an ion pair^{60–62}. Such behavior was observed for various IL, with different deposition techniques, on a variety of surfaces from mica and amorphous silica to graphite, gold and sapphire. Upon application of voltage, potential-driven structural transitions in the interfacial layer at the interface with metallic electrodes were also observed^{63–66} and addressed with theoretical models^{67;68}. Interfaces and voltage also affect the dynamics of IL^{69;70} at the interfaces or their wetting properties.

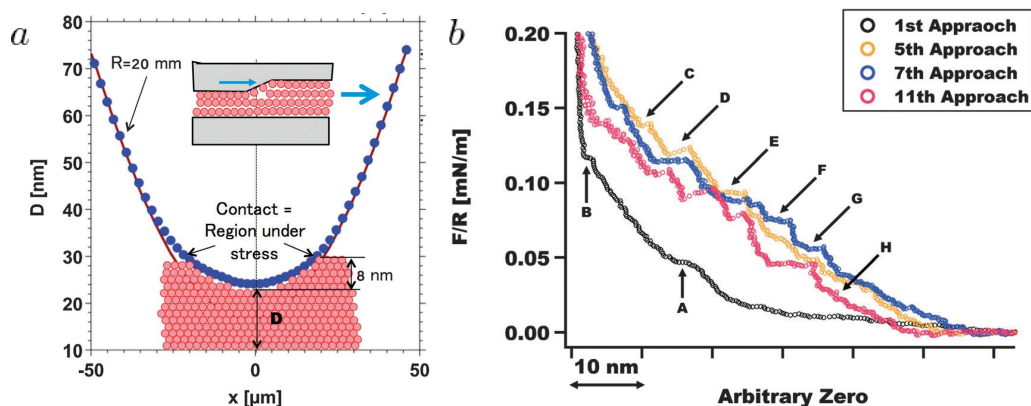


Figure 1.4: Irreversible liquid to solid transition induced by the nanoconfinement, using an extended surface force apparatus (SFA), of an ionic liquid. (a) 2D profile of the contact interface at the largest compression of the ionic liquid film. (b) Force-separation profiles measured by atomic force microscopy (AFM) for dry $[\text{HMIM}][\text{EtSO}_4]$ on mica in dry nitrogen during different approaches. Adapted from Ref. 71 with permission from the PCCP Owner Societies.

A growing number of studies (for a recent review see Ref. 51 and references therein) also evidence the presence of solid-like layers at the surface, on distances of the order of several nanometers up to thousands of nanometers from the surface^{71–76}. An example of such experiments performed by Jurado *et al.* is given in figure 1.4, which measured force-position profiles (setup in figure 1.4a) that show solid-like behavior on several tens of nanometers (see figure 1.4b). These solid-like layers have in general an insulating character and a Young’s modulus measured by AFM indentation of a few GPa^{77;78}. These experiments were all carried out with some driving force, *e.g.* their deposition process by evaporation of a volatile solvent, their introduction in microporous matrices or their confinement under a micrometric tip. In some cases, this nanoconfinement resulted in a shift in the freezing-

melting behavior of the RTIL, either decreasing the melting temperature^{79–82} or increasing it^{71;83–85}. The data and interpretations however do not always agree and it seems that the phase behavior of ILs at interfaces and under confinement remains to be fully characterized.

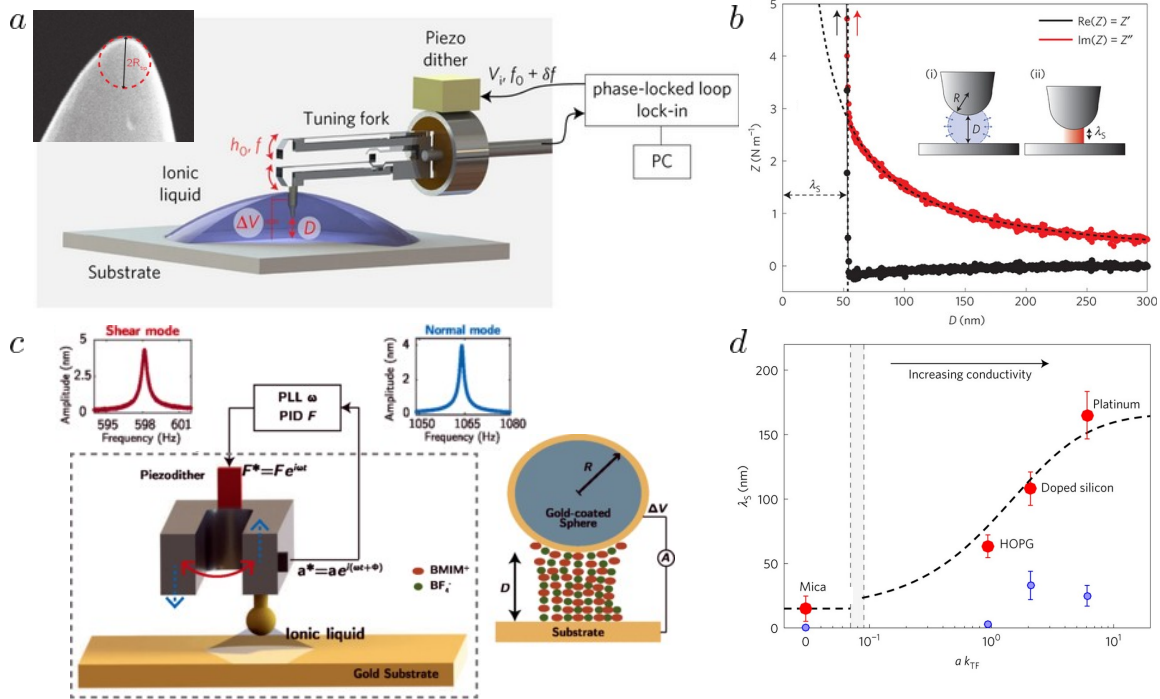


Figure 1.5: (a) Experimental setup of Ref. 84: a tungsten tip of curvature radius R between 50 nm and 2.5 μm glued to a tuning fork is immersed in an ionic liquid drop and excited by a piezo dither in a vacuum chamber. (b) Real (Z' , black) and complex (Z'' , red) parts of the mechanical impedance during a typical approach curve of the tungsten tip on a graphite substrate, as a function of the tip-substrate separation D . (c) Experimental setup of Ref. 86: the prongs of the tuning fork oscillate along a shear (red) and normal (blue) mode simultaneously under the excitation by a piezo dither. A spherical gold probe is glued at the end of one prong and is immersed in a [BMIM][BF₄] drop on a gold substrate. (d) Variation of the average confinement length λ_S at which solidification occurs (red dots) for four different substrates as a function of the normalized Thomas-Fermi wavevector $a k_{TF}$, with a half of the ionic crystal lattice. Blue dots are the height of pre-existing prewetting solid-like layers. Panel c was adapted from Ref 86. Panels a-b-d are adapted from Ref. 84, Copyright ©2017, Nature Publishing Group.

In particular, the group of Prof. Lydéric Bocquet at École Normale Supérieure performed pioneering experiments using an atomic force spectrometer⁸⁴ and later using a dynamic surface force tribometer⁸⁶, to investigate ionic liquids under confinement by the tip of the device. These devices are based on a tuning fork attached to a tip or sphere, of the order of $R \sim 0.5 - 2.5 \mu\text{m}$ for the former (see figure 1.5a) and $R \sim 1.5 \text{ mm}$ for the latter (see figure 1.5c). Although on two different scales, both devices are able to probe the rheological response of the IL by exciting the tuning fork, and the MicroMegascope^{87;88} has the possibility to excite and monitor both the normal and shear modes as shown in figure 1.5c.

As shown in figure 1.5b, these experiments⁸⁴ exhibit a divergence in the measured mechanical impedance under a characteristic distance λ_S , which the authors interpret as nanoscale capillary freezing. Later measurements with the MicroMegascope⁸⁶ revealed rather a glass transition instead of a purely crystalline structure. Using a sharp AFM tungsten tip (of radius $R \sim 10 - 50 \text{ nm}$) to sample directly the surface and to not reproduce a slit-like pore, they confirmed that this effect is not related to prewetting layers, present on the surface (purple dots on figure 1.5d) but on much smaller widths. This interpretation is not universally accepted, and Garcia *et al.* in Ref. 89 using dynamic SFA measurements instead conclude that this is a hydrodynamic effect that probes the solid-like layers at the interface from far away, as depicted in figure 1.6.

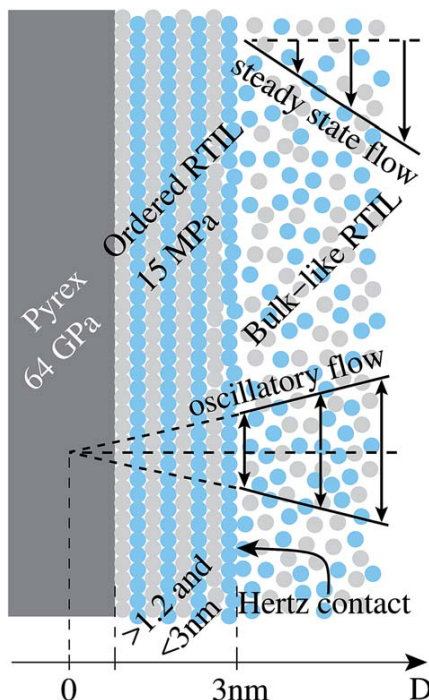


Figure 1.6: Schematical representation of a RTIL (represented by blue and grey dots)-Pyrex interface, with an ordered solid-like layer of about 3 nm from the surface. The steady state velocity vanishes at this interface while the oscillatory flow extends further within the solid-like layer. Reproduced from Ref. 89 with permission from The Royal Society of Chemistry.

Explanations to these various solid-like layers include the varying surface charge of the different surfaces⁹⁰, but Comtet *et al.* in Ref. 84 suggested parametrizing the problem using the metallicity of the material. Indeed, the authors investigated a range of surfaces including mica, graphene, doped silicon and platinum and observed a different response in each case, which is consistent with the dynamic SFA experiments of Garcia *et al.*⁸⁹ on pyrex and platinum. Most interestingly, Comtet *et al.* used the framework of the Thomas-Fermi model, introducing the concept of electronic screening of the material, to explain the effect of the substrate on the confinement-induced freezing of the ionic liquid, shown in figure 1.5d. This effect is not negligible as the confinement length at which solidification appears varies from ~ 10 nm for mica to ~ 180 nm for platinum. The authors also developed a simplified model^{84;91} based on a periodic chain of point charges to model the crystal, obtaining an analytical expression for the dependence of the surface tension with respect to the “metallicity” of the substrate, which agrees remarkably with the data. This metallic character quantifies the ability of the material to conduct electricity, and is computed in this study as the inverse Thomas-Fermi length l_{TF}^{-1} times the typical interplanar distance in the crystal structure of the material. The Thomas-Fermi model is discussed in chapter 4 but in short this length l_{TF} corresponds to the characteristic length over which an external perturbation (a charge or an external field) is screened, thereby resulting in a vanishing electric field in the bulk of the material, far from the perturbation.

The present thesis is inspired from this study and its parametrization as a function of the metallicity of the substrate. All these phenomena occur at length scales of a few tens of nanometers, and are probably governed by the behavior at the interface on these small lengthscales. Therefore they are system perfectly suited to be studied by numerical simulations at the molecular scale: such simulations not only allow to predict macroscopic observables such as the surface tension γ if parametrized correctly, but they have the advantage that they can be very well controlled. In particular, it is possible to separately investigate the effect of a single parameter, in our case the metallicity of the surface, without changing many other variables such as the whole structure of the substrate. It thus offer a unique tool to test hypotheses in a controlled fashion, which is not always possible in real-life (and not computer) experiments.

1.2 Metals in molecular simulations

1.2.1 The challenge of metallic interfaces

Modeling metallic interfaces in contact with electrolytes is a challenge for numerical simulations because it requires both a good description of a large amount of ions and solvent molecules and of the electrons in the solid, on timescales of several nanoseconds to explore diffusion, charge and discharge dynamics or adsorption at the interface. These systems are therefore a place where quantum chemistry meets statistical physics, *i.e.* where we need an accurate description of the electronic distribution and a large sampling of phase space. These concepts are developed in chapter 2, and they impose the use of a classical level of theory to treat the electrolyte, to have a reasonable computational cost.

The modeling of metallic electrodes in classical molecular simulations then brings up the more general question of the electrostatic response of a medium to an electric charge (ion, or partial charges from molecules), which is faced not only in electrochemistry, but in all systems involving interfaces, as in biological macromolecules. In an insulator, the existence of a band gap prevents the conduction of electrons in the material, which are then localized on the nuclei and are modeled using Coulomb interactions between effective charges. Electric conduction in metals however allows the delocalization of electrons in the conduction band over the whole material, which rearrange in response to external perturbations as an electric charge.

In a classical continuum approach, these interfaces are characterized by a contrast in the polarization response of the different media, quantified by their dielectric constant ϵ_r , ranging from 1 for vacuum to ~ 80 for liquid water and ∞ for a perfect metal. This dielectric contrast is usually expressed in terms of “image charges”, and strongly impacts the charge distribution close to the interface. Consider a sharp planar interface between two media 1 (polar solvent) and 2 (solid wall) with dielectric constants ϵ_1 and ϵ_2 , and a set of charges $\mathbf{q}^{\text{ext}} = \{q_1^{\text{ext}}, \dots, q_N^{\text{ext}}\}$ embedded in medium 1. Within this medium, the electrostatic potential created by this set of charges is identical to that created by a fictitious system in which the dielectric constant discontinuity is suppressed, *i.e.* medium 2 is given a dielectric constant ϵ_1 , and a set of image charges are placed symmetrically with respect to the boundary, as in figure 1.8b, with magnitudes

$$\mathbf{q}^{\text{im}} = \frac{\epsilon_1 - \epsilon_2}{\epsilon_1 + \epsilon_2} \mathbf{q}^{\text{ext}}. \quad (1.2)$$

This yields two opposing responses: for an insulating interface, such as water-vacuum ($\epsilon_1 \gg \epsilon_2$), the image charges are close to the source charges $\mathbf{q}_{\text{im}} \approx \mathbf{q}^{\text{ext}}$, while for a perfect metallic interface ($\epsilon_2 \rightarrow \infty$), the images have opposite charges $\mathbf{q}_{\text{im}} = -\mathbf{q}^{\text{ext}}$. This results in radically different electrostatic interactions of the charge distribution with its image, which is attractive for metals and repulsive for insulators.

1.2.2 Electrodes in classical molecular simulations

To capture the effect of image charges in simulations, alternative approaches have been developed to avoid performing quantum calculations to compute the electronic density, which would prevent a correct sampling of phase space needed in our large electrochemical cells. It should be stressed that these models do not aim at providing a truthful description of the metal and its properties, but rather at reproducing the appropriate boundary conditions for the electrolyte. In this context, there are two key features that need to be addressed to describe electrochemical interfaces: the possibility to accumulate a net charge on the interface, *e.g.* in the presence of an applied voltage between two electrodes and the polarization of the metal by the electrolyte.

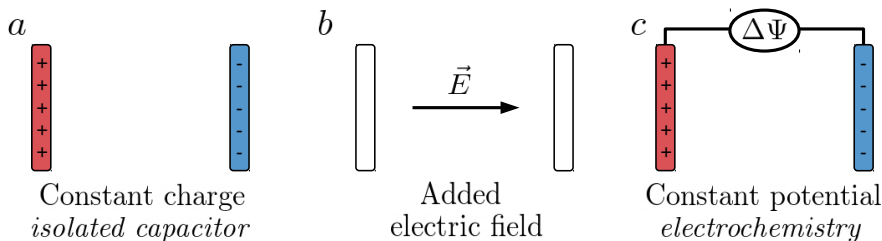


Figure 1.7: Electrodes bearing a net charge can be modeled with opposite constant surface charges (a), by applying an external field on the electrolyte (b) or by maintaining the two electrodes at a constant potential difference (c).

1.2.2.1 Electrodes with a net charge

The accumulation of a net charge on the surface can be achieved by different methods, illustrated in figure 1.7. The simplest method consists in explicitly assigning a constant net charge on the electrode, using a surface charge on a wall^{92–97} or discrete point charges^{98–100} (see figure 1.8a). The electroneutrality of the system can be respected by an excess of ions in the electrolyte or by an opposite charge on a second electrode. This setup corresponds *e.g.* to a charged pore or an isolated charged capacitor, as shown in figure 1.7a.

Two oppositely and homogeneously charged wall induce a uniform electric field between them, so that a second method to describe the effect of charged electrodes on an electrolyte is to apply an external electric field (see figure 1.7b) on the liquid confined in the electrochemical cell^{19;101–107}.

Lastly, to simulate a capacitor connected to a voltage generator that maintains a constant electric potential difference between the electrodes and allows the exchange of charge between them^{94;95;108–114} (see figure 1.7c), specific constant potential simulations have been devised in the literature, which are extensively used in this work and are discussed in chapter 3.

1.2.2.2 Accounting for the electronic polarization of the metal

Whether charged or neutral, due to the mobility of electrons in a conductor, a metallic surface becomes polarized in response to an external perturbation. This important phenomenon is also known as screening. The description of the charge distribution within the electrode is therefore an important but complex aspect to capture. Simplistic charge distributions, in particular used in conjunction with simulations with a net surface charge, display homogeneous surface charges or charged walls with discrete static point charges^{92–100} (see figure 1.8a). In some cases, such as the typical planar slab geometry of capacitors, a number of simplifications are possible, including analytical expressions of the electrostatic energy and forces acting on the charges. For example, a simple description of the electronic charge distribution at a flat interface and its “spilling” outside the electrode, based on a quantum chemical treatment of the interface, is the use of the *Jellium* model. It represents an electronic plasma that smoothly decays a few angströms away from the interface within a sharp homogeneous positively charged background representing the nuclei and core electrons^{96;116}.

However such descriptions lack the lateral charge inhomogeneities due to the local dynamic structure of the electrolyte. To tackle this aspect and take into account the many-body effects due to the coupling with the electrolyte, an efficient strategy is to use the concept of image charges discussed in section 1.2.1. It can only be applied in the case of planar interfaces but this includes a wide range of systems. They can be included explicitly, as in figure 1.8b, or accounted for implicitly in modified Green functions^{106;114;117–122}. For explicit image charges, the implementation is rather straightforward as it simply includes additional charges that mirror the corresponding source charges of the electrolyte and bear a charge given by Eq. 1.2. Computing electrostatic interactions using periodic boundary conditions (see section 2.1.3.1) also requires special care, and efficient algorithms have been

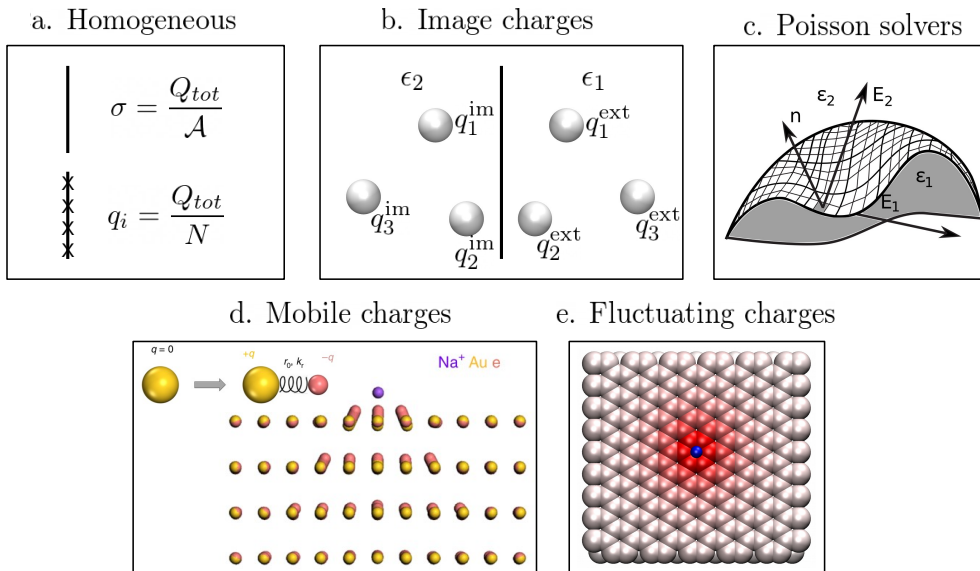


Figure 1.8: Accounting for the polarization of the metal by the electrolyte in molecular simulations: using a homogeneous distribution (a), introducing image charges q^{im} , given by Eq. 1.2, inside the solid with permittivity ϵ_2 , mirroring the electrolyte charges q^{ext} in a medium of permittivity ϵ_1 (b), solving the Poisson equation on a grid to compute the induced charges (c), describing the electronic response with mobile charges, as in the Drude model (d) or with fixed sites with fluctuating charges (e). In panel d, gold atoms are modeled with negative shells (pink) tethered to the positive fixed nuclei (yellow), adapting to the presence of a sodium ion (purple). In panel e), the inhomogeneous distribution of charge in response to the presence of a cation such as Li^+ (blue) on an atomistic graphite electrode is shown (darker red means more negative). Panel b is reproduced from Ref. 115 with the permission of AIP Publishing, panel c is reproduced from Ref. 100 with permission of Springer Nature.

developed that deal with the image charges in simulations^{123;124}. The image charges method is rooted in continuum electrostatic theory – it has also been improved to include a Thomas-Fermi screening term to account for non-ideality of the material¹²⁵ – and thus breaks down close to the interface. Combined with atomistic non-electrostatic interactions, this method also raises the question of the placement of the sharp interface with respect to an atomistic description of matter.

To model more complex systems, *e.g.* including porous structures, methods that solve the Poisson equation have been proposed. The Induced Charge Computation (ICC) treats the charge density as a dynamical variable discretized on a grid, as shown in figure 1.8c and solves the Poisson equation to obtain the induced charge. The dielectric medium is then characterized by a space-dependent dielectric constant $\epsilon(\mathbf{r})$ which can in principle describe arbitrarily shaped interfaces and non-homogeneous media, but are in practice limited to sharp interfaces (no ϵ gradient) and smooth shapes (no atomistic representation). Introduced using a variational procedure by Allen *et al.* for solid-electrolyte interfaces¹²⁶, it was then extended by using a matrix formulation¹²⁷ or an iterative algorithm (ICC*)^{115;128}.

To include the molecular shape and atomistic details of the interface, descriptions based on the electrode atoms have been developed, treating the metal with dedicated force fields. This allows to get rid of the restriction to slab geometries and to deal with disordered porous electrodes. A first attempt consisted in creating a corrugated potential for platinum, in order to avoid the calculation of pair terms while reproducing the local roughness of the substrate¹²⁹. These potentials were fitted on *ab-initio* calculations, both for the intramolecular and the electrostatic part, to include implicitly a mean effect of the polarization of the metal.

Aside from this mean-field technique, one can introduce mobile charges that rearrange in response to the configuration of the electrolyte. This is the case of core-shell models, that introduce a mobile negative charge representing the electrons, attached to a positive nucleus. The effective charges are

constant in time and the motion of the negative charge allows to model the response of the electronic distribution. The Drude oscillator tethers the charge using a spring¹⁰⁰ (see figure 1.8d), but another option is the rod model^{130–132}, where the negative charge can only rotate at a fixed distance around the positive nucleus. These models are easily implemented in standard molecular simulation codes, but they usually require short timesteps and a great care when choosing the mass of the auxiliary charge and the spring strength or rod length to ensure a correct adiabatic separation of the charge dynamics and avoid instabilities and/or energy transfers. A recent study also introduces light mobile charges and models the metal as a “virtual Thomas-Fermi fluid”¹³³ by analogy to the Debye-Hückel equation for electrolytes.

Another class of models considers instead charges that are fixed on atomic sites but that are allowed to fluctuate in magnitude, as illustrated in figure 1.8e. Early models in fact included both fluctuating charges and induced dipoles at the atomic sites as additional degrees of freedom^{134;135}, but this approach has not been explored further. A detailed description of the constant-potential method with fluctuating charges is given in chapter 3 and we only briefly describe here the variety of similar methods that exist in the literature. In these models, the charges \mathbf{q} on the electrode atoms are determined at each time step according to an equation of motion, or by imposing the value of the electric or electrochemical potential of electrode atoms. Fluctuating charge models were first used for molecules, with the charge equilibration (QE) method or the electronegativity equalization method (EEM)^{136–138}, and were then extended to electrochemical systems^{109;111;139–144}. The various implementations differ in the enforced constraint (electronegativity equalization, constant potential difference . . .) and in the expressions of the energy, which come from a purely electrostatic picture or can involve terms such as electronegativities and chemical hardnesses. The split charge equilibration approach additionally includes bond-specific terms in the energy¹⁴⁵.

Pastewka *et al.* went further in the concept of fluctuating charges, by parametrizing the band-structure energy at the tight-binding level¹⁴⁶. They were able to take into account the different band structures, and *e.g.* differentiate between graphene and carbon nanotubes, using a classical description of various carbon electrodes. Similar simplified quantum mechanical treatments of the interface in classical simulations have also been developed such as the “direct dynamics”^{147;148}.

To conclude, a variety of methods have been employed in the literature that mix the way of treating (or not) the polarization of the electrode and how to assign a net charge to it. Many combinations, although not all, are possible and have been implemented in the literature. However, these models mostly treat the material as an ideal metal, including the specificities of the metal only in the non-electrostatic interactions, instead of accounting for the electronic response of electrodes (*e.g.* graphite, carbone nanotubes or platinum) which differ considerably as shown *e.g.* analytically^{149;150} and in density functional theory-based studies^{151;152}. This limits the applications to real systems and the ability of simulations to predict the properties of electrochemical devices.

1.2.2.3 A molecular simulation code for electrochemistry: *MetalWalls*

In the PHENIX laboratory, we develop a molecular dynamics simulation code tailored to electrochemistry, in particular the simulation of capacitors, called *MetalWalls*¹⁵³. This software has been used throughout this PhD to run most of the simulations and has also been expanded significantly during these 3 years. It is based on the model introduced by Siepmann and Sprik¹⁰⁹ and later extended by Reed *et al.*¹¹¹, as detailed in chapter 3. More information on this code can be found in appendix B.

1.2.3 Influence of electronic polarization: should we take it into account?

While being less computationally expensive than *ab initio* simulations, all the methods presented previously add a significant cost with respect to standard classical molecular simulations. Indeed, they require an additional step, *e.g.* a minimization procedure or a matrix multiplication, to determine the new value of the charge density at each timestep. Similarly, polarizable force fields have been

introduced in the literature, that add atomic dipoles self-consistently determined throughout the simulation, in order to improve the accuracy of simulations. However, the larger computational cost hinders the wider use of this class of force fields, despite their increased accuracy compared to non-polarizable force fields.

In the case of metallic electrified interfaces, a large majority of studies disregards this aspect and uses constant surface charges on the electrodes, homogeneously distributed on the surface¹⁵⁴. For example, charging dynamics can be studied by turning on charges on the electrodes and values of the capacitance are obtained by computing the potential difference across the cell from the charge density. Therefore the question arises of the necessity of these refinements in the simulation of metals, and what is the impact of electronic polarization on the results of simulations. Indeed, capturing the leading effect of accumulating a net charge on the electrodes could be sufficient and the impact of charge fluctuations on the properties of the neighbouring electrolyte are not clear yet. Clarifying this issue is one of the objectives of this thesis.

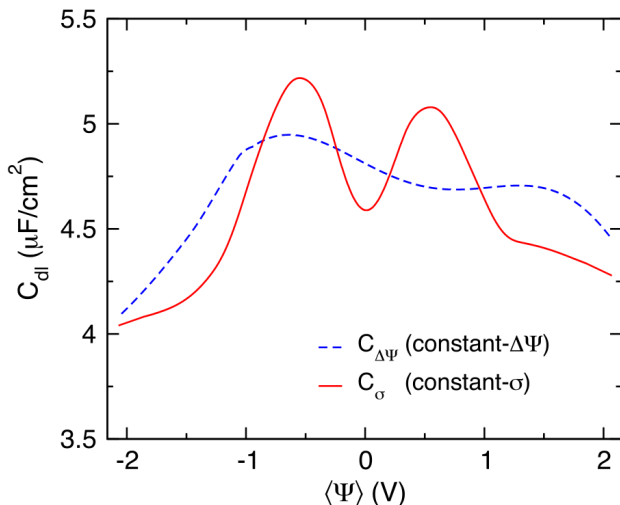


Figure 1.9: Single electrode differential capacitance of a [EMIM][BF₄]/graphite capacitor obtained from constant potential (dashed blue lines) or constant surface charge (solid red line) simulations. Reproduced from Ref. 155 with the permission of AIP Publishing.

With the explanation of a “superionic” state in nanoporous electrodes due to the exponential screening of electrostatic interactions and image charge effects^{156;157}, a few studies have compared the results obtained from constant surface charge simulations with more rigorous constant potential simulations. These studies mostly focus on graphite/ionic liquid capacitors, in which electrostatic effects are more striking. At low voltages, there seems to be no quantitative change in the capacitance curves nor in the structure of the first solvation layer at the surface of the electrode¹²⁸. This result is confirmed by Ref. 158 on a graphite capacitor containing LiClO₄ in acetonitrile. For larger voltages however, $\Delta\psi > 4$ V, a change in structure is observed with the appearance of an “inner-sphere” complex in the constant potential simulations, with Li⁺ ions coming extremely close to the surface, stabilized by image charge effects. Similarly, Merlet *et al.*¹⁵⁹ showed small changes in the ionic density profiles at a planar graphite surface and more strikingly highlighted large difference in the charging kinetics, with unrealistically large temperatures reached in constant charge simulations, while constant potential simulation yielded the temperature raise predicted by the Joule effect. Differences in charging kinetics were also reported by Vatamanu *et al.*¹⁶⁰, which measured relaxation times of a few ps for constant charge simulations versus hundreds of ps for constant potential ones. Finally, Haskins and Lawson¹⁵⁵ carried a detailed comparison of the electrode models and showed in figure 1.9 a similar average value for the single electrode differential capacitance but a shape much more defined in the case of constant charge simulations with respect to a smoother shape for the constant potential model. This was explained by denser ion layers at the surface of constant potential simulations and changes in the ionic liquid orientations.

1.3 Objectives and organization of the thesis

This introduction presented a wide range of phenomena occurring at interfaces or under confinement, that make the nanoscale an intense field of research. The effect of interfaces goes from changing the structure and the dynamics of the system, to modifying its whole phase behavior, by introducing specific interactions with the molecules and ions. When adding charged species between metallic interfaces, the electrostatic couplings present throughout the cell make them difficult to apprehend by analytical theories. However, such interfaces are widely common, in particular in electrochemical devices such as batteries and capacitors, and an understanding of these systems is necessary to improve the properties of such devices. From extensive experiments, it also results that the presence of ionic liquids at interfaces yields a strong layering, and even solid-like layers on the surface, that are still not well understood. The results of Comtet *et al.* on the nanoscale capillary freezing of RTILs as a function of the metallic character of the confining substrate further suggest that the electronic polarization of the substrate plays a determining role in these phenomena.

In this context, molecular simulations are a useful tool to investigate these electrochemical systems and analyze the influence of electronic polarization on the electrolyte. A wide panel of models are available to simulate metallic interfaces, but the impact of accounting for the electronic polarization in simulations has not received a lot of interest yet, and a systematic study of the influence of increasing or reducing this effect has not been carried out. Therefore this PhD thesis has the general objective to investigate the influence of the metallicity of a substrate on the properties of electrolytes at the interface or confined by it. We aim in particular at the effect of metallicity on the freezing transition under confinement, and thus on the interfacial free energies, which has been a guideline for the different developments of this work.

In chapter 2, we first broadly introduce molecular simulations and the specific electrochemical systems studied in this work. We particularly detail the link between microscopic simulations and macroscopic observables and give a theoretical background on statistical mechanics necessary for later developments. We also introduce advanced techniques of enhanced sampling, based on the manipulation of the simulations to drive the system, that have been useful in the course of the PhD.

Chapter 3 is dedicated to the simulation of metals using fluctuating charges subjected to a constant potential constraint. Studying the simulation method in detail and noting recent contradictions in the literature^{155;161}, we write the statistical mechanics of the constant potential ensemble and investigate the impact of the sampling scheme on the final ensemble averages. This allows in particular to correct the calculation of the differential capacitance found in the literature. A first set of comparisons between insulating and metallic models is given.

In chapter 4, we go beyond the state-of-the-art constant potential simulations by introducing the Thomas-Fermi model. We then study the impact of the screening length, characteristic of the metallicity of a material, on the structure and dynamics of different capacitors.

We then set to investigate the interfacial free energies and first take a look back at the Gibbs-Thomson equation. In chapter 5, we propose a detailed derivation using thermodynamics and verify the various assumptions by presenting numerical results on a Lennard-Jones model system. In particular, we devise a thermodynamic integration method that yields the difference in surface tension $\Delta\gamma$ involved in the prediction of the confinement-induced temperature shift.

Because of the computational cost of this method, we then develop another thermodynamic integration technique in chapter 6 that explicitly results in the free energy difference as a function of the Thomas-Fermi length. This allows to obtain a microscopic interpretation of the change in surface tension due to the metallicity of the substrate.

Finally, we give an overview of the work accomplished and open on future perspectives and questions raised by this PhD work.

Chapter 2

Molecular simulations of electrochemical systems

2.1 Models at the molecular scale

Molecular simulations are a set of numerical tools that eventually allow to predict the properties of a system using a computer. They are based on models which contain the characteristics of the system and the laws of Physics or Chemistry used to describe it. This model is fundamental since the computer simulation will only predict reliable data if it is accurate and robust. Different levels of theory can be used, starting from very precise quantum calculations that solve the Schrödinger equation with the least amount of approximations, also called *first principle* or *ab initio* calculations, for a small number of nuclei and electrons. A less expensive level of theory is the Density Functional Theory (DFT), based on the Hohenberg-Kohn theorems¹⁶², that aims at computing the electronic density (instead of the electronic wavefunction): it needs however the definition of the functional dependence of the energy on the electronic density, which is only partially known and has to be approximated. It is then possible to zoom out and use an atomic description of the system: these are the classical models. The electronic degrees of freedom are integrated out and included in an effective potential energy, also called force field, which describes the effective interaction between atoms. The reduction of the degrees of freedom can go further by uniting groups of atoms into beads using a coarse-graining procedure and by computing the effective interactions between these larger beads. Further models can focus on solutes and replace solvent molecules by an effective dielectric constant as in implicit solvent models or by introducing a friction term and random forces as in Brownian or Langevin dynamics. Overall, gathering informations from different levels of theory – from very accurate quantum calculations to mesoscopic or macroscopic models – to parametrize larger simulations and obtain accurate models at each scale of matter is the essence of multiscale modeling.

The choice of the level of theory needed to describe a system is a compromise between accuracy and computational cost – although it should be noted that a well parametrized classical force field can yield better results than a poorly chosen functional in DFT – and will be mainly determined by the system’s size and the length of simulation to observe the studied phenomenon. Because this PhD work focuses on large electrochemical devices presented in section 2.1.1, we will use classical molecular simulations, with different force fields detailed in section 2.1.2, that allow simulations of large systems (several tens of thousands of atoms) for “long” times of several nanoseconds with respect to what can be achieved with DFT. However, because these systems deal with charged electrolytes and metallic interfaces, the electronic description of the interface is adapted to partly reintroduce electronic degrees of freedom. This will be discussed at length in chapter 3.

Given a reliable model, different simulation methods are possible, depending also on the computational resources available. Higher levels of theory will typically only allow for single point energy calculations or geometry optimization while many more energy calculations are possible when using

less expensive models. Two different classes of simulation methods can then be applied: Molecular Dynamics (MD) relies on the propagation of trajectories in time whereas Monte Carlo (MC) simulations aims at producing a representative pool of configurations of a given thermodynamic ensemble. Although it may seem that these simulation methods are disconnected, they are in fact both rooted in statistical mechanics and thermodynamics, making the connection between microscopic simulations and macroscopic observables. These aspects will be discussed in section 2.2. This work will mainly use Classical Molecular Dynamics simulations, discussed in 2.3. Typical properties that are extracted from these simulations are shown in section 2.4. Some Monte Carlo simulations were also employed to investigate liquid-solid coexistence and will therefore be discussed in section 2.2.3.

With the knowledge of the models and simulation methods, as well as their cost and limitations, it is then possible to go beyond the simple observation of phenomena and take advantage of the computers to start meddling with Hamiltonians to drive the system and overcome these limitations. This will be the subject of section 2.5.

2.1.1 Systems investigated

Before going into the details of the models used in section 2.1.2, we introduce the different systems investigated in this work. Most are electrochemical cells, either in a capacitor setup with an electrolyte between two parallel electrodes or in a drop configuration with a single electrode and a nanometric drop of electrolyte on top, for which snapshots and codenames are summarized in table 2.1. Another project on the fundamentals of crystallization (see chapter 5) is based on the study of a model systems of Lennard-Jones particles with no charges involved, described in table 2.2.

2.1.1.1 Electrolytes

Different electrolytes were used in these studies starting from pure water, adding a single ion pair then going to a concentrated aqueous sodium chloride solution at 1 mol/L. Finally we considered two ionic liquids: molten sodium chloride NaCl and 1-butyl-3-methylimidazolium hexafluorophosphate (BMI-PF₆). Lastly, we also investigated a model system involving a Lennard-Jones fluid. The description of the interactions in all these systems will be discussed later in section 2.1.2 and we only define here the different geometries and interaction sites for molecules and molecular ions.

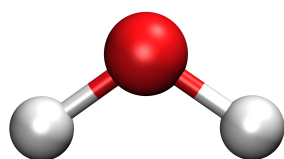


Figure 2.1: SPC/E water molecule geometry¹⁶³ (see also table 2.9).

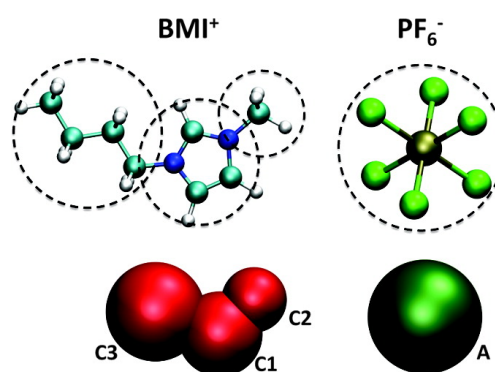


Figure 2.2: BMI⁺ and PF₆⁻ geometries and corresponding coarse grained model⁵⁹ (see also table 2.10). Reprinted with permission from Ref 59. Copyright 2011 American Chemical Society.

Water molecules can be simulated using a variety of models available in the literature, which can be more or less sophisticated, expensive to run and accurate to describe the microscopic structure, dynamics or macroscopic properties of water. We use the Extended Single Point Charge (SPC/E) model introduced in Ref. 163 which is a good compromise – a snapshot is given in figure 2.1. It is a

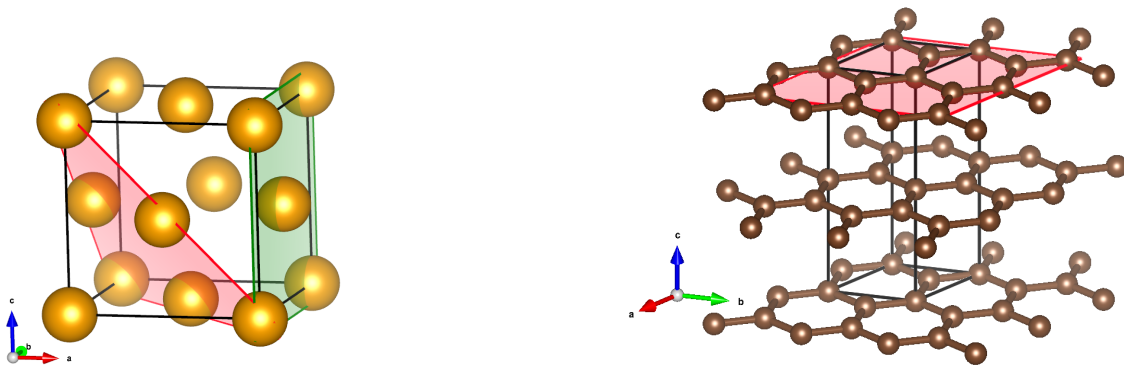
rigid three site model with an oxygen and two hydrogen atoms, with a partial negative charge on the oxygen and partial positive charges on the hydrogens (see table 2.4) and one van der Waals center on the oxygen (see discussion in section 2.1.2.2).

BMI-PF₆ is a commonly used ionic liquid composed of a large cation BMI⁺ and a smaller spherical anion PF₆⁻. Because of the size mismatch of BMI⁺ with respect to PF₆⁻, it is liquid at room temperature, which makes it a good candidate for supercapacitor electrolytes. The model we use for this molecule was developed in Ref. 164. Instead of implementing an atomistic description of the molecule, several atoms are grouped into a larger bead to form a so-called coarse-grained model, as shown in figure 2.2. This coarse-graining allows to reduce the number of degrees of freedom and simulate larger systems for longer times, which is needed for ionic liquids because of their viscosity and long correlation times. The interaction parameters developed to describe the beads (see table 2.5) are designed to reproduce macroscopic quantities such as diffusion coefficients or viscosities.

2.1.1.2 Electrodes and confining surfaces

The electrolytes mentioned in the previous section were first studied in bulk conditions (with no interfaces) or with an interface with vacuum to compute their liquid-vapour surface tension. To study interfacial and confinement effects however, several surfaces were introduced, both structured (*i.e.* atomically resolved) and unstructured (depending only on the distance of the atom to the surface). Unless specified otherwise, we will set the surface perpendicularly to the z -axis. All surfaces were treated as rigid bodies, they were either fixed during the simulation or only allowed to translate along z .

We started chronologically to study a model unstructured surface using the Steele formula and parameters corresponding to a mica surface (see Eq. 2.9 and table 2.8) along with a model Lennard-Jones fluid. This system was studied both in the crystal phase and the liquid phase to investigate the melting/freezing transition under confinement. We then went to more realistic, atomically resolved surfaces of gold and graphite. Graphite was considered because of its use in batteries as an electrode material, while gold was interesting because a variety of studies and a good force field were available and its standard crystal structure made it a good model system. Gold crystallizes in the face centered cubic crystal structure, with a lattice parameter $a = 4.07 \text{ \AA}$. Its cubic unit cell is drawn in figure 2.3a (black lines) where two facets are shown: the (100) plane in green and the (111) plane in red.



(a) Face centered cubic crystal structure.

(b) Hexagonal crystal structure.

Figure 2.3: Crystal structures encountered in this work. The axes **a** (red), **b** (green) and **c** (blue) refer to the orientation of the lattice vectors.

The graphite crystal structure is an hexagonal one, shown in figure 2.3b (black lines show one unit cell), with lattice parameters $a = b = 2.461 \text{ \AA}$ and $c = 6.708 \text{ \AA}$ and the (\vec{a}, \vec{b}) angle equal to $2\pi/3$. It is a layered structure, a single layer being a graphene sheet, and the only investigated surface corresponds to these sheets (red plane).

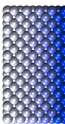
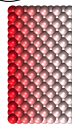
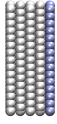
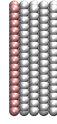
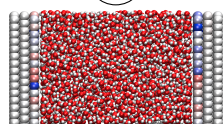
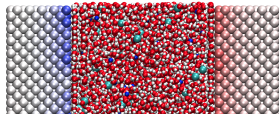
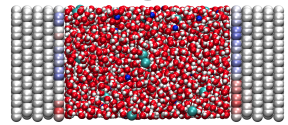
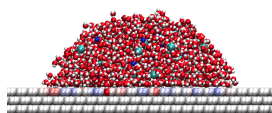
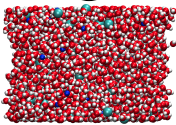
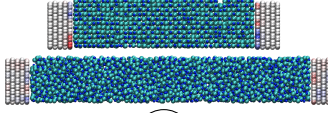
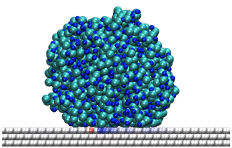
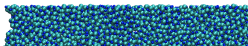
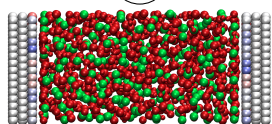
electrode electrolyte	Gold (100) (Au1)  	Graphite (G1)  	Vacuum
SPC/E Water		(G2) 	
SPC/E Water + "Cl ⁺ " + Cl ⁻		(G3) 	
SPC/E Water NaCl (1 mol/L)	(Au4) 	(G4)  (D4) 	(B4) 
Molten NaCl		(G5)  (D5) 	(B5) 
BMI ⁺ -PF ₆ ⁻		(G6) 	

Table 2.1: Snapshots of the main electrochemical systems investigated. Each row corresponds to a different electrolyte while each column is a different boundary condition (electrode surface or vacuum).

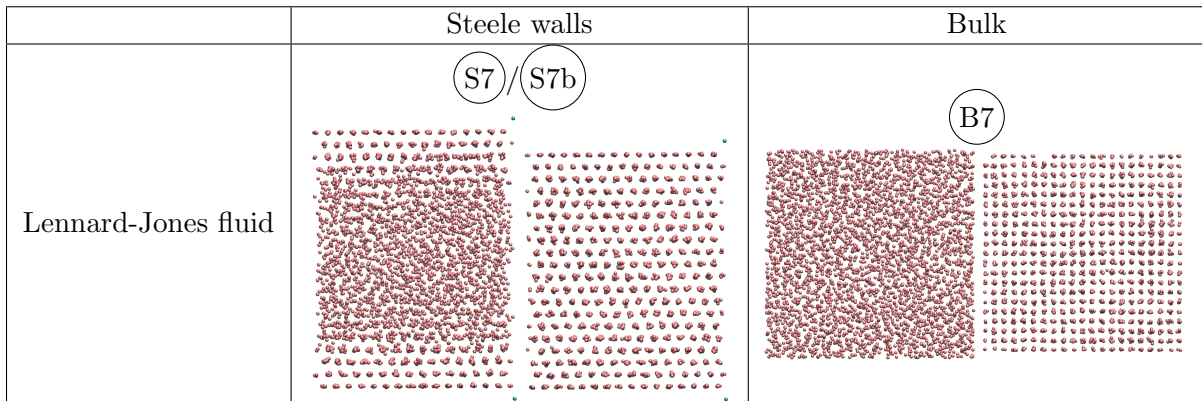


Table 2.2: Snapshots of the Lennard-Jones model systems under confinement or bulk.

From the surface, these materials both appear as atomic planes stacked to each other, characterized by their interplane distance d , with $d_{\text{gold}} = 2.035 \text{ \AA}$ and $d_{\text{graphite}} = 3.354 \text{ \AA}$. This interplane distance will be an important parameter when constructing mean field models (see for example section 4.2.1) because it acts as a characteristic atomic length.

2.1.1.3 Simulation details

Simulation details for the main molecular dynamics simulations studied are given in table 2.3. Some quantities such as the potential difference will be detailed in the following sections.

2.1.2 The interaction potential

An essential ingredient of classical molecular simulations is the force field, which defines the interactions between any species in the system. While one should in principle solve the time-dependent Schrödinger equation for both the nuclei and electrons, it is possible to construct classical force fields where most of the degrees of freedom except the nuclear coordinates have been integrated out and which accurately reproduce the effective potential energy of interaction between atoms.

There exist different ways of constructing such force fields: a first solution is to obtain the potential energy profile from higher level calculations, which depending on the method (DFT, post-Hartree Fock methods¹⁶⁵) can be computationally very expensive. The obtained profile can then be tabulated or fitted using different functions. A significant research effort has also recently been put into using machine learning and neural network techniques^{166;167} to fit force fields which will not be limited by the definition of an energy functional, trained on *ab initio* molecular dynamics. Another way of fitting force fields can be on the contrary from experimental data such as density, thermodynamic quantities or spectroscopy data, using empirical energy functionals of the literature. The latter will be more performant at reproducing macroscopic quantities but the transferability of the parameters will be poorer: *e.g.* using interaction parameters for oxygen-hydrogen fitted on water properties will yield the good water density or structure but will not be so accurate if transferred to different systems with alcohol or aldehyde functions.

In general, any potential energy functional used in classical force fields is somewhat arbitrarily divided into different energy contributions: the electrostatic energy \mathcal{U}_{el} , the intramolecular energy $\mathcal{U}_{\text{intra}}$ and the intermolecular energy $\mathcal{U}_{\text{inter}}$, which contains repulsion and dispersion terms. Each term will be detailed in the following sections.

We consider a system made of M electrode atoms and N electrolyte atoms, which can form molecules defined by N_b bonds and N_a angles. The position of an atom i is \mathbf{r}_i so that the distance between two atoms i and j is $r_{ij} = |\mathbf{r}_j - \mathbf{r}_i|$, and the angle formed by three atoms i , j and k is θ_{ijk} . The total

	T (K)	Δt (fs)	$\Delta\psi$ (V)	$N_{\text{electrolyte}}$	N_{elec}	N_{pl}	$N_{\text{elec/pl}}$	Box lengths	Force field
(Au1)	298		1, 2	0	2	≤ 50	162 Au	$L_x = 36.630\text{\AA}$ $L_y = 36.630\text{\AA}$ $L_z = 10 - 300\text{\AA}$	Tab. 2.6
(Au4)	298	1	0, 1, 2	2160 H ₂ O 39 (Na ⁺ , Cl ⁻)	2	10	162 Au	$L_x = 36.630\text{\AA}$ $L_y = 36.630\text{\AA}$ $L_z = 50.669\text{\AA}$	Tab. 2.4& 2.6
(G1)	298		1, 2	0	2	≤ 50	480 C _{AQ}	$L_x = 34.101\text{\AA}$ $L_y = 36.915\text{\AA}$ $L_z = 10 - 300\text{\AA}$	Tab. 2.6
(G2)	298	1	0, 2	2160 H ₂ O	2	3 to 5	480 C _{AQ}	$L_x = 34.101\text{\AA}$ $L_y = 36.915\text{\AA}$ $L_z = 55.11\text{\AA}$	Tab. 2.4&2.6
(G3)	298	1	0	2071 H ₂ O 1 ("Cl _{GR} ⁺ ", Cl _{GR} ⁻)	2	3	480 C _{GR}	$L_x = 34.101\text{\AA}$ $L_y = 36.915\text{\AA}$ $L_z = 55.11\text{\AA}$	Tab. 2.4&2.6
(G4)	298	1	0, 2	2160 H ₂ O 39 (Na ⁺ , Cl ⁻)	2	3 to 5	480 C _{AQ}	$L_x = 34.101\text{\AA}$ $L_y = 36.915\text{\AA}$ $L_z = 56.2\text{\AA}$	Tab. 2.4&2.6
(D4)	298	1	0	2160 H ₂ O 39 (Na ⁺ , Cl ⁻)	1	3	4320 C _{AQ}	$L_x = 102.302\text{\AA}$ $L_y = 110.745\text{\AA}$	Tab. 2.4&2.6
(G5)	800 900 1200 1300	2	0	2000 (Na ⁺ , Cl ⁻)	2	5	336 C _{AQ}	$L_x = 29.838\text{\AA}$ $L_y = 29.532\text{\AA}$ $L_z = [125.814,$ 127.278, 192.364, 200.117] \AA	Tab. 2.7&2.6
(D5)	1300	2	0	2000 (Na ⁺ , Cl ⁻)	1	3	5376 C _{AQ}	$L_x = 119.352\text{\AA}$ $L_y = 118.128\text{\AA}$	Tab. 2.7&2.6
(G6)	400	2	0, 2	240 (BMI ⁺ , PF ₆ ⁻)	2	3 to 5	480 C _{IL}	$L_x = 34.101\text{\AA}$ $L_y = 36.915\text{\AA}$ $L_z = 74.11\text{\AA}$	Tab. 2.5&2.6
(B4)	298	1		2160 H ₂ O 39 (Na ⁺ , Cl ⁻)	0			$L_x = 34.101\text{\AA}$ $L_y = 36.915\text{\AA}$	Tab. 2.4
(B5)	1300	2		2000 (Na ⁺ , Cl ⁻)	0			$L_x = 29.838\text{\AA}$ $L_y = 29.532\text{\AA}$	Tab. 2.7
(S7)	79	2		4116 LJ	2			$L_x^* = 16.4$ $L_y^* = 14.2$ $H^* = \text{var.}$	Tab. 2.8
(S7b)	var.			var.	2			$L_x^* = 21.1$ $L_y^* = 20.3$ $H^* = [8.7, 11.6,$ 14.5, 17.3, 20.2, 23.1, 26.0, 28.8]	Tab. 2.8
(B7)	var.	2		4000 LJ	0			$L_x = L_y = L_z = \text{var.}$	Tab. 2.8

Table 2.3: Simulation details for each system: temperature T , timestep Δt , potential difference $\Delta\psi$ if any, number of electrolyte atoms or molecules $N_{\text{electrolyte}}$, number of electrodes N_{elec} , number of electrode planes per electrode N_{pl} and number of electrode atoms per plane $N_{\text{elec/pl}}$, box dimensions L_x, L_y and L_z and corresponding force field used. For confined systems, L_z or H is the separation between the first atomic planes or Steele surfaces. Please refer to tables 2.1 and 2.2 for codenames and table 2.6 for a definition of the different carbon atoms C_X.

potential energy is then written as

$$\mathcal{U}_{\text{pot}} = \mathcal{U}_{\text{el}} + \mathcal{U}_{\text{inter}} + \mathcal{U}_{\text{intra}} \quad (2.1)$$

and the total energy of the system is then $\mathcal{U}_{\text{tot}} = \mathcal{U}_{\text{pot}} + \mathcal{K}$ where $\mathcal{K} = \sum_{i=1}^{N+M} \frac{1}{2} m_i \mathbf{v}_i^2$ is the kinetic energy of the system, with m_i the atomic mass and \mathbf{v}_i the velocity of atom i .

2.1.2.1 Electrostatic energy

The electrostatic energy spawns from the distribution of charges of the system. Because the electronic degrees of freedom are integrated out in classical simulations, the charge distribution is constructed to reflect the effective potential created by other atoms. Usual classical descriptions assign effective point charges on atoms $\rho_{\text{pc}}(\mathbf{r}) = q_i^{\text{pc}} \delta(\mathbf{r} - \mathbf{r}_i)$ (with δ the Dirac function) where q_i^{pc} is the charge on atom i .

In the force field used in this work, the electrode atoms are given instead a Gaussian charge distribution centered on each atom, with width η^{-1} , to better account for the electronic cloud and the delocalization of the charge in metals

$$\rho_{\text{gc}}(\mathbf{r}) = q_j \eta_j^3 \pi^{-3/2} \exp[-\eta_j^2 (\mathbf{r} - \mathbf{r}_j)^2] \quad (2.2)$$

where q_j is the magnitude of the distribution on the electrode atom j . The overall electrostatic energy is then given by

$$\mathcal{U}_{\text{el}} = \frac{1}{2} \iint \frac{\rho_{\text{c}}(\mathbf{r}) \rho_{\text{c}}(\mathbf{r}')}{4\pi\epsilon_0 |\mathbf{r} - \mathbf{r}'|} d\mathbf{r} d\mathbf{r}' \quad (2.3)$$

with ϵ_0 the vacuum permittivity and $\rho_{\text{c}}(\mathbf{r}) = \sum_{i=1}^N \rho_{\text{pc}}(\mathbf{r}) + \sum_{j=1}^M \rho_{\text{gc}}(\mathbf{r})$ the total charge distribution.

The total electrostatic energy can be separated into different contributions and written as a matrix multiplication by introducing a vector of electrode charges $\mathbf{q} = (q_1, \dots, q_M)$ and its transposed vector \mathbf{q}^T as follows

$$\mathcal{U}_{\text{el}} = \frac{\mathbf{q}^T \mathbf{A} \mathbf{q}}{2} - \mathbf{q}^T \mathbf{B}(\mathbf{r}^N) + C(\mathbf{r}^N) \quad (2.4)$$

where the symmetric $M \times M$ matrix $\mathbf{A} = \nabla_{\mathbf{q}} \nabla_{\mathbf{q}} \mathcal{U}_{\text{el}}$ depends on the positions of the electrode atoms and the Gaussian width describing the charge distribution on each atom but not on the charge amplitudes \mathbf{q} , while the components of the vector $\mathbf{B}(\mathbf{r}^N)$ are the electrostatic potential due to the electrolyte on each electrode atom. $C(\mathbf{r}^N)$ is the electrolyte-electrolyte contribution. Explicit expressions for \mathbf{A} and $\mathbf{B}(\mathbf{r}^N)$ for the particular case of Gaussian charge distributions, taking into account two-dimensional Ewald summation for electrostatic interactions, are derived in Refs. 111 and 168 and will partly be discussed later in section 2.1.3.3.

The effective charges used in this work are reported in table 2.4 for aqueous solutions and in table 2.5 for ionic liquid electrolytes. For electrode atoms, the Gaussian width was fixed as $\eta^{-1} = 0.56 \text{ \AA}$ as done in the literature¹⁰⁹, and the value of q is either zero or determined using a constant electric potential condition, which will be discussed in detail in chapter 3.

2.1.2.2 Intermolecular energy: dispersion and repulsion

The intermolecular terms reflect the interactions between a pair of non-bonded atoms, also known as van der Waals forces, as a function of the distance between them. A repulsive term, which comes from the repulsion of electrons and the Pauli exclusion principle, prevents atoms from collapsing onto one another, while attractive terms arise from interactions between electronic clouds, which are deformed by the environment and fluctuate accordingly. Different analytical functions exist in the literature and only two were used in this work.

The Lennard-Jones (LJ) potential is widely used throughout the literature – in part because of its practical and efficient form – and is pair-wise additive as

$$\mathcal{U}_{\text{inter}}^{\text{LJ}} = \sum_{i=1}^{N+M} \sum_{j>i} 4\epsilon_{ij} \left[\left(\frac{\sigma_{ij}}{r_{ij}} \right)^{12} - \left(\frac{\sigma_{ij}}{r_{ij}} \right)^6 \right] \quad (2.5)$$

with ϵ_{ij} and σ_{ij} the LJ energy and diameter. To reduce the number of force field parameters, the ϵ_{ij} and σ_{ij} can be obtained for cross-type interactions from the same type ii parameters using combination rules, such as the Lorentz-Berthelot mixing rule

$$\epsilon_{ij} = \sqrt{\epsilon_{ii} \times \epsilon_{jj}} \quad (2.6)$$

$$\sigma_{ij} = \frac{\sigma_{ii} + \sigma_{jj}}{2}. \quad (2.7)$$

The necessary parameters used in this work are reported in table 2.4 for aqueous solutions, in table 2.5 for ionic liquid electrolytes and in table 2.6 for interaction parameters with structured surfaces. Several force fields were used and combined together depending on the different systems simulated.

	O _{SPC/E}	H _{SPC/E}	Na ⁺	Cl ⁻	Cl _{GR} ⁻	“Cl _{GR} ⁺ ”
$m(\text{u})$	15.9994	1.008	22.9898	35.453	35.453	35.453
$q^{\text{PC}}(\text{e})$	-0.8476	+0.4238	+1.0	-1.0	-1.0	+1.0
$\epsilon_{ii}(\text{kJ/mol})$	0.6502	0.0	0.4184	0.4184	0.4186	0.4186
$\sigma_{ii}(\text{\AA})$	3.166		2.587	4.401	4.52	4.52

Table 2.4: Effective point charges, atomic masses and Lennard-Jones parameters for aqueous systems, with water – modeled using the SPC/E water model described in Ref. 163– and ions (Ref. 169 for Na⁺ and Cl⁻ and Ref. 170 for Cl_{GR}⁻ and “Cl_{GR}⁺”).

	BMI ⁺			PF ₆ ⁻
	C ₁	C ₂	C ₃	
$m(\text{u})$	67.07	15.04	57.12	144.96
$q^{\text{PC}}(\text{e})$	+0.4374	+0.1578	+0.1848	-0.78
$\epsilon_{ii}(\text{kJ/mol})$	2.56	0.36	1.83	4.71
$\sigma_{ii}(\text{\AA})$	4.38	3.41	5.04	5.06

Table 2.5: Effective point charges, atomic masses and Lennard-Jones parameters for BMI-PF₆ systems in the coarse grained model of Ref. 164.

	C _{AQ} ¹⁷¹	C _{GR} ^{†172}	C _{IL} ¹⁷³	Au ¹⁷⁴
$m(\text{u})$	12.0	12.0	12.0	196.97
$\epsilon_{ii}(\text{kJ/mol})$	0.236	ϵ_{CO} : 0.42469	0.23	22.13336
$\sigma_{ii}(\text{\AA})$	3.211	σ_{CO} : 3.367	3.37	2.951

Table 2.6: Atomic masses and Lennard-Jones parameters for electrolyte-electrode interactions. The subscripts C_X indicate different force field parameters for the carbon atom.

†The parameters given for the GROMOS force field¹⁷² are ϵ_{CO} and σ_{CO} (instead of ϵ_{CC} and σ_{CC}) because these have not been obtained using Lorentz-Berthelot rules.

The Fumi-Tosi (FT) potential is another potential energy function¹⁷⁵ given by

$$\mathcal{U}_{\text{FT}} = \sum_{i=1}^N \sum_{j>i} \left[A_{ij} e^{B_{ij}(r_{ij}-\sigma_{ij})} - \frac{C_{ij}}{r_{ij}^6} - \frac{D_{ij}}{r_{ij}^8} \right] \quad (2.8)$$

where A_{ij} , B_{ij} , C_{ij} , D_{ij} , σ_{ij} are the FT parameters and the sum runs over all pairs. We used the force field described in Ref. 176 for molten sodium chloride because it describes accurately the melting temperature of this salt. Parameters are given in table 2.7.

	Na ⁺ -Na ⁺	Na ⁺ -Cl ⁻	Cl ⁻ -Cl ⁻
$A(\text{kJ/mol})$	25.4435	20.3548	15.2661
$B(\text{\AA}^{-1})$	3.1546	3.1546	3.1546
$C(\text{\AA}^6.\text{kJ/mol})$	101.1719	674.4793	6985.6786
$D(\text{\AA}^8.\text{kJ/mol})$	48.1771	837.0770	14031.5785
$\sigma(\text{\AA})$	2.340	2.755	3.170

 Table 2.7: Fumi-Tosi parameters for molten sodium chloride¹⁷⁶.

The Steele potential was used in chapter 5 in combination with a Lennard-Jones fluid to construct a model system. In this part of the thesis, most quantities will be given in reduced LJ units, indicated by a * superscript, *i.e.* $r^* = r/\sigma$ for distances, $E^* = E/\epsilon$ for energies, $T^* = k_B T/\epsilon$ for temperatures, $P^* = P\sigma^3/\epsilon$ for pressures and $\gamma^* = \gamma\sigma^2/\epsilon$ for surface tensions.

The Steele potential energy^{177;178} is designed to mimic the interaction of a fluid with a material surface by modeling it as an unstructured wall, *i.e.* which only depends on the distance z_i of an atom i to the surface

$$\mathcal{U}_{\text{Steele}}^* = \sum_{i=1}^N 2\pi\rho_W^* \epsilon_{WF}^* \sigma_{WF}^{*2} \Delta^* \left[\frac{2}{5} \left(\frac{\sigma_{WF}^*}{z_i^*} \right)^{10} - \left(\frac{\sigma_{WF}^*}{z_i^*} \right)^4 - \frac{\sigma_{WF}^{*4}}{3\Delta^* (z_i^* + 0.61\Delta^*)^3} \right] \quad (2.9)$$

where ρ_W^* is the atomic density of the material, $\epsilon_{WF}^* = \sqrt{\epsilon_W^*}$ and $\sigma_{WF}^* = (1 + \sigma_W^*)/2$ are obtained by combining LJ parameters with surface parameters ϵ_W^* and σ_W^* , and Δ^* corresponds to the distance between atomic crystal planes. The parameters of this study are given in table 2.8 where we set the parameters of the LJ fluid to those of argon¹⁷⁹ and the Steele parameters correspond to a mica surface¹⁸⁰.

$\sigma(\text{\AA})$	$\epsilon(\text{K})$	r_{cut}^*	σ_W^*	ϵ_W^*	ρ_W^*	Δ^*
3.405	119.8	2.5	1.28	7.85	1.0	0.84

 Table 2.8: Lennard-Jones and Steele parameters for the model system studied in chapter 5 using typical values for argon¹⁷⁹ and mica surfaces¹⁸⁰. r_{cut}^* is the cutoff value for the force calculations, introduced later in section 2.1.3.

2.1.2.3 Intramolecular energy and constraints in the molecular geometry

The intramolecular energy concerns interactions between atoms within a molecule. It is usually separated into bonds, angles, dihedrals and impropers contributions depending on the complexity of the molecules. Commonly used potentials for bonds and angles are harmonic

$$\mathcal{U}_{\text{intra}} = \sum_{b=1}^{N_b} \mathcal{U}_{\text{bond}}(r_b) + \sum_{a=1}^{N_a} \mathcal{U}_{\text{angle}}(\theta_a) = \sum_{b=1}^{N_b} \kappa_b (r_b - r_0)^2 + \sum_{a=1}^{N_a} \kappa_a (\theta_a - \theta_0)^2, \quad (2.10)$$

where κ_b and κ_a are the spring constants for bonds and angles respectively, r_0 and θ_0 the equilibrium bond length and angle. Note that because the interaction between atoms is taken into account in the intramolecular energy, the intermolecular terms concerning atoms connected by bonds or angles should be excluded. More complex exclusion rules exist for atoms further than 3 bonds.

The molecules encountered in this work, *i.e.* water molecules and BMI-PF₆ molecules, are however treated as rigid bodies. This means that some geometrical degrees of freedom are kept fixed during the simulation. This is typically done for bonds with a large vibration frequency – such as O-H bonds because of the light mass of hydrogen – so that their fast motion can be suppressed and a larger integration timestep can be chosen. The geometrical constraints imposed to SPC/E water molecules

are given in table 2.9 along with a snapshot of a water molecule in figure 2.1 and for BMI-PF₆ ionic liquid in table 2.10 and figure 2.2.

r_{OH}	θ_{HOH}
1.0 Å	109.47°

Table 2.9: Geometrical constraints for the SPC/E water molecule¹⁶³.

	$x(\text{Å})$	$y(\text{Å})$	$z(\text{Å})$
C ₁	0.0	-0.527	1.365
C ₂	0.0	1.641	2.987
C ₃	0.0	0.187	-2.389

Table 2.10: Constrained relative position of coarse-grained beads in the BMI⁺ molecular ion¹⁶⁴.

Different algorithms are known in the literature to impose this geometry along the trajectory: constraining algorithms that modify the forces on the individual atoms to keep the geometry frozen or rigid-body algorithms that compute the total force and torque acting of the molecule. Because the molecules have only 3 components, we used the SHAKE/RATTLE algorithms described later in section 2.3.2.2.

2.1.3 Calculation of interactions

The implementation of the previously detailed models into a computer program suffers mainly from limitations due to finite computational resources and less frequently from memory. To reduce the computational cost, the straightforward way is to reduce the number of interactions to compute per step, *i.e.* the number of atoms. However to avoid boundary effects we need a very large number of atoms (of the order of $\sim 10^{23}$ atoms). The most popular solution is to use periodic boundary conditions, which define a finite size simulation box and replicate it infinitely in space to simulate an infinite material. This then has different consequences in the calculation of interactions.

2.1.3.1 Periodic boundary conditions

Periodic boundary conditions (PBC) may be used to simulate a pseudo-infinite system by replicating a finite size cell in one, two or three directions. In practice, when an atom moves beyond a periodic box boundary, it goes into the neighboring replica and, because the system is periodic, comes back on the other side of the “main” box. The energy calculations, based on distances between atoms, therefore require some caution and the use of the minimum-image convention, *i.e.* taking the distance between closest replicas. This can be written for two atoms i and j in each of the periodic directions as

$$\begin{aligned} x_{ij} &= (x_j - x_i) - L_x \left\lfloor \frac{(x_j - x_i)}{L_x} + 0.5 \right\rfloor \\ y_{ij} &= (y_j - y_i) - L_y \left\lfloor \frac{(y_j - y_i)}{L_y} + 0.5 \right\rfloor \\ z_{ij} &= (z_j - z_i) - L_z \left\lfloor \frac{(z_j - z_i)}{L_z} + 0.5 \right\rfloor \end{aligned} \quad (2.11)$$

where $x_j - x_i$ is the distance in the x direction (and similar for the y and z directions) within the central replica and $\lfloor x \rfloor$ is the floor function.

Usually 3D-PBC allow to simulate bulk materials since no interface is present in the system (see figure 2.4a), but when considering interfaces and confined systems the choice is not straightforward. Indeed this configuration is in principle 2-dimensional and would require 2D-PBC as shown in figure 2.4b. This in turn changes the calculation of the interactions and most implementations of MD softwares prefer using the configuration in figure 2.4c where a finite vacuum buffer is added in the non-periodic dimension z and 3D-PBC are applied. It is then necessary to correct for the interaction

between replicas in the z direction using the slab correction introduced by Yeh and Berkowitz¹⁸¹. In this work however, specific analytical formulas to compute interactions with 2D-PBC are used and we are able to run rigorous simulations of confined systems.

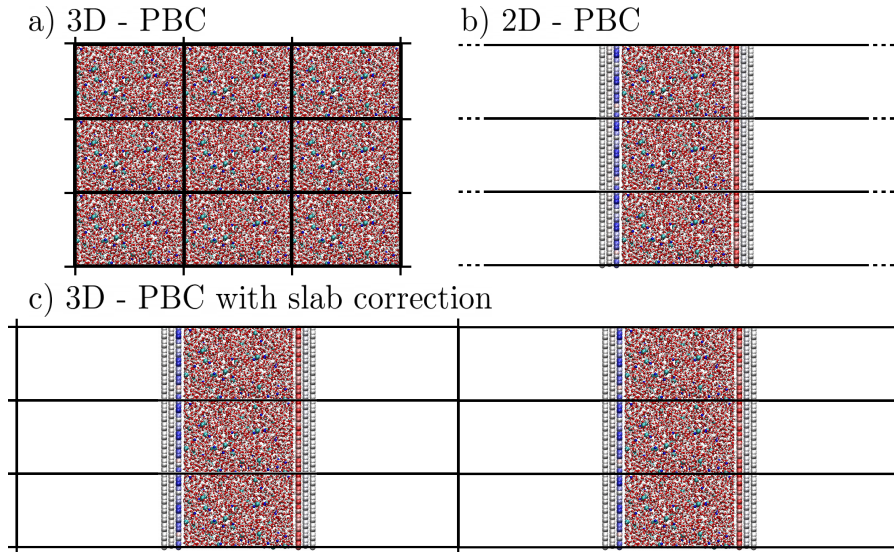


Figure 2.4: Different periodic boundary conditions depending on the modeled system (see text). Black solid lines indicate a periodic boundary. In the case of 3D-PBC (a), the system is replicated in all three dimensions while in 2D-PBC (b) it is replicated only in two dimensions, the system being infinite in the third dimension (indicated by the dashed line). The same system as (b) can be approximated by using 3D-PBC on a simulation box including vacuum slabs in the non-periodic dimension and adding a slab correction (c).

2.1.3.2 Short range interactions: cutoff radius and truncation

With periodic boundary conditions, the calculation of interactions between atoms needs to take into account the different replicas of the box, which are in principle infinite. For interactions that decay rapidly with distance (faster than $\sim r^{-3}$), only the nearest neighbours contribute significantly to the sum and interactions with further atoms are neglected, *i.e.* the potential is truncated at some cutoff value r_{cut} . To minimise the errors arising from the truncation, the cutoff was taken to be half of the smaller box length if not stated otherwise. The main exception is the study of the Lennard-Jones fluid phase diagram which is very sensitive on the truncation of the LJ potential and where we used a cutoff $r_{\text{cut}} = 2.5\sigma$ (see table 2.8).

The truncation is typically how van der Waals interactions are treated (Lennard-Jones or Fumi-Tosi potentials in $\sim r^{-6}$). It can however be treated in different ways giving rise to different flavors of the potential. A large majority of studies perform a truncation of the potential and add a long-range correction by assuming an homogeneous density for distances larger than r_{cut} , which results in additional terms in the energy and the pressure calculations. In this work however, most systems present one or more interfaces and are thus not isotropic. This prevents us from using these long-range corrections. We choose instead truncated shifted potentials, defined for a pair of atoms i and j as

$$u_{ij}^{TS}(r_{ij}) = \begin{cases} u_{ij}(r_{ij}) - u_{ij}(r_{\text{cut}}) & \text{if } r_{ij} < r_{\text{cut}} \\ 0 & \text{otherwise,} \end{cases} \quad (2.12)$$

where u_{ij} is the original potential form (see Eq. 2.5 or Eq. 2.8). The potentials being pairwise additive, we obtain the truncated shifted energy as

$$\mathcal{U}_{\text{inter}}^{TS} = \sum_{i=1}^N \sum_{j>i} u_{ij}^{TS}(r_{ij}). \quad (2.13)$$

2.1.3.3 Long range interactions: Ewald summation

For long-range potentials, especially the Coulomb potential, simply truncating the interactions is not a viable option because the error in the sum over the atoms is not negligible: other methods that explicitly compute the contribution of the periodic replicas need to be used, the most famous being the Ewald summation.

Given the charge distribution ρ_c in Eq. 2.3, the potential energy for a set of N point charges q^{pc} and M Gaussian charges q is

$$\begin{aligned} \mathcal{U}_{\text{el}} = & \frac{1}{2} \sum_{i=1}^N \sum_{j=1}^N \sum_{\mathbf{n}}' \frac{q_i^{\text{pc}} q_j^{\text{pc}}}{4\pi\epsilon_0 |\mathbf{r}_{ij} + \mathbf{n}|} \\ & + \sum_{i=1}^N \sum_{j=1}^M \sum_{\mathbf{n}} \int d\mathbf{r}'' \left(\frac{\eta_j^2}{\pi} \right)^{-3/2} \frac{q_i^{\text{pc}} q_j e^{-\eta_j^2 \mathbf{r}''^2}}{4\pi\epsilon_0 |\mathbf{r}_{ij} + \mathbf{r}'' + \mathbf{n}|} \\ & + \frac{1}{2} \sum_{i=1}^M \sum_{j=1}^M \sum_{\mathbf{n}}' \iint d\mathbf{r}' d\mathbf{r}'' \left(\frac{\eta_i \eta_j}{\pi} \right)^3 \frac{q_i e^{-\eta_i^2 \mathbf{r}'^2} q_j e^{-\eta_j^2 \mathbf{r}''^2}}{4\pi\epsilon_0 |\mathbf{r}_{ij} - \mathbf{r}' + \mathbf{r}'' + \mathbf{n}|} \end{aligned} \quad (2.14)$$

where we separated the point charge-point charge term, the cross term and the gaussian charge-gaussian charge term. The sum $\sum_{\mathbf{n}}$ indicates a sum over all periodic replicas with $\mathbf{n} = n_x \mathbf{a} + n_y \mathbf{b} + n_z \mathbf{c}$ a linear combination of lattice vectors ($\mathbf{a}, \mathbf{b}, \mathbf{c}$), with n_x, n_y, n_z integers. For a 2D-periodic system, we have similarly $\mathbf{n} = n_x \mathbf{a} + n_y \mathbf{b}$. The $\sum_{\mathbf{n}}'$ signifies that the sum should not include the self term $\mathbf{n} = \mathbf{0}$ if $i = j$.

We give here a sense of the method for 2D-PBC point charges only and expressions for terms including gaussians are given in appendix C and can be found in Refs. 111 and 168. The challenge to perform the above sum over all atom pairs including the infinite replicas is its slow convergence. The Ewald summation method splits the sum into two parts by introducing, within the charge density ρ_c , oppositely charged atom-centered gaussian charge distributions

$$\rho_c(\mathbf{r}) = \left[\rho_c(\mathbf{r}) - \sum_{i=1}^N q_i \left(\frac{\alpha}{\pi} \right)^{3/2} e^{-\alpha^2 |\mathbf{r} - \mathbf{r}_i|^2} \right] + \left[\sum_{i=1}^N q_i \left(\frac{\alpha}{\pi} \right)^{3/2} e^{-\alpha^2 |\mathbf{r} - \mathbf{r}_i|^2} \right] \quad (2.15)$$

where α^{-1} is the width of the Ewald gaussian. This manipulation results in a superposition of charge distributions: the electrostatic energy of the first is rapidly decaying in real space, while the second term is easily computed in reciprocal space. Following this, one can show that the potential energy can be written as

$$\begin{aligned} \mathcal{U}_{\text{el}}^{\text{pc-pc}} = & \frac{1}{2} \sum_{i=1}^N \sum_{j=1}^N \frac{q_i^{\text{pc}} q_j^{\text{pc}}}{4\pi\epsilon_0} \sum_{\mathbf{n}}' \frac{\text{erfc}(\alpha |\mathbf{r}_{ij} + \mathbf{n}|)}{|\mathbf{r}_{ij} + \mathbf{n}|} \\ & + \frac{1}{L_x L_y} \sum_{i=1}^N \sum_{j=1}^N \frac{q_i^{\text{pc}} q_j^{\text{pc}}}{4\pi\epsilon_0} \sum_{\mathbf{k} \neq \mathbf{0}} \int_{-\infty}^{+\infty} du \frac{\cos(\mathbf{k} \cdot \boldsymbol{\xi}_{ij} + u z_{ij})}{|\mathbf{k}|^2 + u^2} e^{-\frac{|\mathbf{k}|^2 + u^2}{4\alpha^2}} \\ & - \frac{\sqrt{\pi}}{L_x L_y} \sum_{i=1}^N \sum_{j=1}^N \frac{q_i^{\text{pc}} q_j^{\text{pc}}}{4\pi\epsilon_0} \left(\frac{e^{-z_{ij}^2 \alpha^2}}{\alpha} + \sqrt{\pi} |z_{ij}| \text{erf}(\alpha |z_{ij}|) \right) \\ & - \frac{\alpha}{\sqrt{\pi}} \sum_{i=1}^N \frac{q_i^{\text{pc}2}}{4\pi\epsilon_0} \end{aligned} \quad (2.16)$$

where $\boldsymbol{\xi}_{ij} = (x_j - x_i)\mathbf{e}_x + (y_j - y_i)\mathbf{e}_y$ is the radial in-plane vector and $z_{ij} = z_j - z_i$ (so that $\mathbf{r}_{ij} = \boldsymbol{\xi}_{ij} + z_{ij}\mathbf{e}_z$). This expression is mathematically exact, however the infinite sums over \mathbf{n} and \mathbf{k} need

to be truncated in practice depending on a given tolerance. The first term comes from the short-range charge distribution: it is a sum involving complementary error functions $\text{erfc}(x) = 1 - \text{erf}(x) = (2/\sqrt{\pi}) \int_x^\infty \exp[-t^2] dt$, which decay rapidly and can be safely computed using a truncation method in real space, as explained earlier, with a cutoff value that encompasses the first images only (typically half of the smaller box length). The second and third terms correspond to the Ewald gaussian contribution in Fourier space, where the sums are over the 2D reciprocal vectors $\mathbf{k} = k_x \frac{2\pi}{a} \mathbf{e}_x + k_y \frac{2\pi}{b} \mathbf{e}_y$. In reciprocal space, the sum converges with a reasonable number of \mathbf{k} vectors and allows to reach the desired accuracy. The third term is the case where $\mathbf{k} = \mathbf{0}$, which does not appear with 3D-PBC. Lastly, the fourth term is the self interaction term corresponding to the interaction of a point charge with the associated Ewald gaussian distribution that needs to be subtracted to avoid a double count.

Other formulations using fast Fourier transforms on a grid (PPPM, PME^{182;183}) further improve the speed of this method for computing long-range potentials, but are rarely used for 2D-PBC.

2.2 Statistical mechanics: from the microscopic to the macroscopic

The power of molecular simulations relies on the possibility to not only have a microscopic vision of matter but also to be able to predict macroscopic properties from microscopic measurements. The framework that allows this is called Statistical Mechanics. In this section, we give an overview of this topic but for more informations the reader is referred to Refs 184 and 185.

2.2.1 Thermodynamic ensembles and sampling

Statistical mechanics is based on the idea that a given macroscopic property that can be measured in experiments (as the internal energy E , the pressure P ...) results from an average over many configurations of the same system. These configurations live in the $6N$ -dimensional phase space, made of the coordinates \mathbf{r}^N and momenta \mathbf{p}^N (with $\mathbf{p} = m\mathbf{v}$) of the particles considered in the system, and are characterized by several control variables. All these configurations create a so-called statistical ensemble defined by the chosen control variables: the microcanonical ensemble is an ensemble of configurations with fixed N , V and E . The canonical ensemble groups all configurations with fixed N , V and temperature T ; fixing N , the pressure P and T gives the isobaric-isothermal ensemble and finally having fixed the chemical potential μ , V and T gives the grand-canonical ensemble. To obtain the value of an observable A in a given ensemble, we perform an ensemble average over all configurations

$$\langle A \rangle = \sum_n A_n \mathcal{P}(n) \quad (2.17)$$

where A_n is the value of the observable for configuration n , $\mathcal{P}(n)$ is the probability of observing this configuration n in the ensemble and $\langle A \rangle$ is the macroscopic observable. We will see in section 2.2.3 that Monte Carlo (MC) simulations directly compute this ensemble average.

To compute Eq. 2.17, the knowledge of the probability $\mathcal{P}(n) = \mathcal{P}(\mathbf{r}^N, \mathbf{p}^N)$ of a given configuration in the ensemble is crucial and it depends on the considered ensemble. In the microcanonical NVE ensemble, all configurations have the same probability

$$\mathcal{P}(\mathbf{r}^N, \mathbf{p}^N; N, V, E) = \frac{1}{\Omega(N, V, E)} \quad (2.18)$$

where Ω is the number of degenerate states characterized by N, V and E . This simple relation is the basis for the construction of statistical mechanics. Real experiments rather correspond to the canonical NVT ensemble, or the isobaric-isothermal NPT ensemble. By dividing a large NVE system into the system of interest at NVT and the rest, which acts as a heat bath at constant temperature, one can obtain the canonical probability

$$\mathcal{P}(\mathbf{r}^N, \mathbf{p}^N; N, V, T) = \frac{e^{-\beta \mathcal{H}(\mathbf{r}^N, \mathbf{p}^N)}}{\iint d\mathbf{r}^N d\mathbf{p}^N e^{-\beta \mathcal{H}(\mathbf{r}^N, \mathbf{p}^N)}} \quad (2.19)$$

where $\beta = 1/(k_B T)$ is the inverse thermal energy with k_B the Boltzmann constant, \mathcal{H} is the Hamiltonian of the system and the denominator is a sum over all configurations so that the probability is normalized. The exponential factor $\exp[-\beta\mathcal{H}]$ is called a Boltzmann factor: it gives a measure of the system's energy with respect to the thermal energy $k_B T$. The (classical) ensemble average in the canonical ensemble can therefore be expressed as

$$\langle A \rangle = \frac{\iint d\mathbf{r}^N d\mathbf{p}^N A(\mathbf{r}^N, \mathbf{p}^N) e^{-\beta\mathcal{H}(\mathbf{r}^N, \mathbf{p}^N)}}{\iint d\mathbf{r}^N d\mathbf{p}^N e^{-\beta\mathcal{H}(\mathbf{r}^N, \mathbf{p}^N)}}. \quad (2.20)$$

In classical mechanics, the Hamiltonian is separated in potential and kinetic energy $\mathcal{H}(\mathbf{r}^N, \mathbf{p}^N) = \mathcal{U}(\mathbf{r}^N) + \mathcal{K}(\mathbf{p}^N)$ so that, if computing holonomic observables, *i.e.* that only depend on the coordinates, we can separate the integrals and integrate out the contribution of momenta

$$\langle A \rangle = \frac{\int d\mathbf{r}^N A(\mathbf{r}^N) e^{-\beta\mathcal{U}(\mathbf{r}^N)}}{\int d\mathbf{r}^N e^{-\beta\mathcal{U}(\mathbf{r}^N)}}. \quad (2.21)$$

For structural properties, we can therefore look exclusively at the $3N$ -dimensional configuration space and disregard the momenta. We introduce here the partition function of the canonical ensemble $Q(N, V, T)$, which gives a measure of the size of the ensemble of relevant configurations

$$Q(N, V, T) = \frac{1}{\Lambda^{3N} N!} \int d\mathbf{r}^N e^{-\beta\mathcal{U}(\mathbf{r}^N)} \quad (2.22)$$

where $\Lambda = \sqrt{h^2/(2\pi m k_B T)}$ is the thermal de Broglie wavelength with h Planck's constant. The prefactor comes from the integration of the momenta; we note the configurational part of the partition function $Z(N, V, T) = \int d\mathbf{r}^N \exp[-\beta\mathcal{U}(\mathbf{r}^N)]$, which is the denominator in Eq. 2.21. The partition function is a crucial element of the statistical ensemble, and we can extract most thermodynamic quantities from it. The most important example is the thermodynamic potential: for the canonical NVT ensemble, the free energy F is given by

$$F(N, V, T) = -k_B T \ln[Q(N, V, T)]. \quad (2.23)$$

Similarly one can show that in the isobaric-isothermal ensemble NPT , the partition function is

$$\Delta(N, P, T) = \frac{\beta P}{\Lambda^{3N} N!} \int dV \int d\mathbf{r}^N e^{-\beta(U(\mathbf{r}^N) + PV)}. \quad (2.24)$$

The Gibbs free energy is then given by $G(N, P, T) = -k_B T \ln[\Delta(N, P, T)]$.

Changing ensemble amounts to substituting a control variable by another, say $E \rightarrow T$, $N \rightarrow \mu$ or $V \rightarrow P$. Standard thermodynamics textbooks first introduce the internal energy E as a function of the entropy S , N and V but because the entropy is not practical to control in real experiments, we substitute it by its conjugate variable, the temperature, by introducing the free energy $F(N, V, T) = E(N, V, S) - S \times T$. The change in control variables is clearly seen when looking at the differential expressions for energy

$$dE = TdS - PdV + \mu dN \quad (2.25)$$

$$dF = dE - TdS - SdT = -SdT - PdV + \mu dN. \quad (2.26)$$

Introducing the pressure is then done by defining $G(N, P, T) = F(N, V, T) + V \times P$, which gives

$$dG = dF + PdV + VdP = -SdT + VdP + \mu dN. \quad (2.27)$$

Mathematically, the change from $E(N, V, S)$ to $F(N, V, T)$ or from $F(N, V, T)$ to $G(N, P, T)$ is a Legendre transformation. No information has been lost – we can go backwards and retrieve the internal energy for example without loss – because we simply exchanged conjugate variables: $S \leftrightarrow T$, $V \leftrightarrow P$ or $N \leftrightarrow \mu$.

If we now consider that the system is in contact with a chemical reservoir, *i.e.* which maintains the chemical potential μ , we obtain the grand-canonical μVT ensemble by the Legendre transform $\Omega(\mu, V, T) = F(N, V, T) - \mu \times N$, named the grand potential. The associated grand-canonical partition function is given by

$$\Xi(\mu, V, T) = \sum_{N=0}^{\infty} \frac{1}{\Lambda^{3N} N!} \int d\mathbf{r}^N e^{-\beta(U(\mathbf{r}^N) - \mu N)} \quad (2.28)$$

where again we retrieve the grand potential from the partition function by $\Omega(\mu, V, T) = -k_B T \ln[\Xi(\mu, V, T)]$.

We will show in chapter 3 how to introduce new control variables – the amplitude of electrode charges – and their conjugate variable – the electric potential – and how to compute averages using the associated partition function.

2.2.2 Fluctuations and linear response theory

The statistical mechanics framework allows to extract information by sampling microscopic observables from simulations and performing ensemble averages. These observables can simply be the average value of a microscopic property A but the fluctuations of this property about its average also contain information. These fluctuations are indeed spontaneous and characteristic of a system and of the ensemble. For example, in the NPT ensemble the volume V , which is the conjugate variable of P , fluctuates around its mean value; the amplitude of the fluctuations are related to the isothermal compressibility.

If we consider a perturbation corresponding to the Hamiltonian $\mathcal{H} = \mathcal{H}_0 - fA$, where \mathcal{H}_0 is the unperturbed Hamiltonian and f is the external perturbation that couples with the property A , the average value $\langle A \rangle$ is then modified according to

$$\langle A \rangle_f = \langle A \rangle_0 + \langle \Delta A \rangle_f = \frac{\iint d\mathbf{p}^N d\mathbf{r}^N A e^{-\beta\mathcal{H}_0 + \beta f A}}{\iint d\mathbf{p}^N d\mathbf{r}^N e^{-\beta\mathcal{H}_0 + \beta f A}}. \quad (2.29)$$

By computing explicitly the derivative with respect to the perturbation f , one obtains

$$\frac{\partial \langle A \rangle_f}{\partial f} = \beta \langle \delta A^2 \rangle_f, \quad (2.30)$$

where we introduced the variance of the distribution of A defined as

$$\langle \delta A^2 \rangle_f = \left\langle (A - \langle A \rangle_f)^2 \right\rangle_f = \langle A^2 \rangle_f - \langle A \rangle_f^2. \quad (2.31)$$

The modification of the average value of A due to the perturbation f is thus related to the fluctuations of A , where the average is done in the perturbed ensemble. For $f \rightarrow 0$, we obtain

$$\left. \frac{\partial \langle A \rangle_f}{\partial f} \right|_{f=0} = \beta \langle \delta A^2 \rangle_0, \quad (2.32)$$

where the average is now done in the unperturbed ensemble (with $f = 0$), *i.e.* at equilibrium.

Studying the fluctuations in an ensemble can therefore give information on the response of the system to an external perturbation or to a spontaneous fluctuation in the limit of vanishing perturbation. Eq. 2.32 states that for small perturbations the relaxation towards equilibrium when the perturbation is suppressed can be studied from the fluctuations that spontaneously occur in equilibrium: this is known as Linear Response Theory. It can further be developed for time-dependent perturbations by studying correlation functions, introduced in section 2.4.3.

Typical perturbations can be *e.g.* an electric field (such as in spectroscopy measurements), a magnetic field (as in NMR experiments) or a piston. Similar considerations and mathematical manipulations

will be used in chapter 3 to develop the response of the total charge to the application of an external potential difference.

Finally, let's note that the above equations can also be expressed using the perturbed partition function $Q_f = \iint d\mathbf{p}^N d\mathbf{r}^N e^{-\beta\mathcal{H}_0 + \beta f A}$, in particular the following equations are useful

$$\frac{\partial \ln Q_f}{\partial f} = \beta \langle A \rangle_f \quad (2.33)$$

$$\frac{\partial^2 \ln Q_f}{\partial f^2} = \beta^2 \langle \delta A^2 \rangle_f . \quad (2.34)$$

2.2.3 Monte Carlo simulations

Monte Carlo simulations are simulation methods (not restricted to molecular simulations) that compute ensemble averages using the expression in Eq. 2.21 for the canonical average, or its equivalent for other ensembles. We will show in section 2.3 that another widely used simulation method is Molecular Dynamics, which instead computes time averages.

The problem of Eq. 2.21 however is that calculating the configurational partition function Z by performing the integral over all configurations is intractable for systems of more than a few atoms. To solve this, the Monte Carlo method instead computes directly the ratio of integrals by averaging over a representative subset of configurations. The idea is that, because of the exponential factor $\exp[-\beta\mathcal{U}(\mathbf{r}^N)]$, high energy configurations will have a negligible contribution to the integrals. We thus only need to sample low energy configurations, that have a large probability and weight in the integral, to have a good estimate of the ratio. In Monte Carlo simulations, we therefore generate an ensemble of snapshots according to the probability distribution, $\mathcal{P} = \exp[-\beta\mathcal{U}]/Z$ for the canonical ensemble, by only knowing the relative probability of each configuration, $\exp[-\beta\mathcal{U}]$, instead of the absolute probability. We then perform (unweighed) ensemble averages on this set of representative configurations.

The challenge is to go from a uniform (pseudo-)random number generator, that can be coded in a computer, to a complex probability distribution $\mathcal{P}(\mathbf{r}^N)$. This is done by generating an importance-weighted random walk in configuration space. The Monte Carlo simulation starts from an initial configuration \mathbf{r}^N and proceeds as follows

1. The configuration $\mathbf{i} \equiv \mathbf{r}_i^N$ is known
2. Propose a trial configuration $\mathbf{j} \equiv \mathbf{r}_j^N$ by choosing from pre-defined moves, depending on the ensemble
 - translational move: pick an atom randomly and translate it by a random small displacement $\mathbf{r}_j^N = \mathbf{r}_i^N + \Delta$
 - volume change move (in NPT): expand or contract the cell by a random small factor
 - insertion move (in μVT): add an atom at a randomly chosen position
 - deletion move (in μVT): delete a randomly chosen atom
 - ... other tailored moves can be derived
3. Decide whether to accept or reject the trial configuration
 - if accepted, the new configuration \mathbf{r}_{i+1}^N is \mathbf{r}_j^N
 - if rejected, the new configuration \mathbf{r}_{i+1}^N is \mathbf{r}_i^N
4. Accumulate the ensemble average with A_{i+1} and repeat from step 1 with $i \rightarrow i + 1$

Step 3 is a fundamental step which can be done in several ways, the most famous one being the Metropolis criterion. The idea stems from the fact that once the equilibrium distribution is reached, it should not be destroyed by additional moves. This is achieved by imposing (although it is not required) a detailed balance condition, which states that the average number of accepted moves from a configuration \mathbf{i} to \mathbf{j} is exactly balanced by the average number of reverse moves, *i.e.*

$$\mathcal{P}(\mathbf{i}) \times \pi(\mathbf{i} \rightarrow \mathbf{j}) = \mathcal{P}(\mathbf{j}) \times \pi(\mathbf{j} \rightarrow \mathbf{i}) \quad (2.35)$$

where $\pi(\mathbf{i} \rightarrow \mathbf{j}) = \alpha(\mathbf{i} \rightarrow \mathbf{j}) \times acc(\mathbf{i} \rightarrow \mathbf{j})$ is the transition probability of proposing and accepting the move $\mathbf{i} \rightarrow \mathbf{j}$, α is the probability of attempting such move and acc of accepting it. Because the moves are usually symmetric, the attempt probability is symmetric $\alpha(\mathbf{i} \rightarrow \mathbf{j}) = \alpha(\mathbf{j} \rightarrow \mathbf{i})$, so that

$$\frac{acc(\mathbf{i} \rightarrow \mathbf{j})}{acc(\mathbf{j} \rightarrow \mathbf{i})} = \frac{\mathcal{P}(\mathbf{j})}{\mathcal{P}(\mathbf{i})} \stackrel{NVT}{=} e^{-\beta[\mathcal{U}(\mathbf{j}) - \mathcal{U}(\mathbf{i})]}, \quad (2.36)$$

where the last equation holds for the NVT probability distribution. Finally, different options are available for acc but the Metropolis criterion is

$$acc(\mathbf{i} \rightarrow \mathbf{j}) = \min \left\{ 1, \frac{\mathcal{P}(\mathbf{j})}{\mathcal{P}(\mathbf{i})} \right\} \stackrel{NVT}{=} \min \left\{ 1, e^{-\beta[\mathcal{U}(\mathbf{j}) - \mathcal{U}(\mathbf{i})]} \right\}. \quad (2.37)$$

In the canonical ensemble, this amounts to always accepting moves that decrease the energy of the system and accepting those increasing it with a probability that exponentially decreases with the energy difference.

2.3 Molecular dynamics simulations

2.3.1 The ergodic principle

We showed in section 2.2.3 how ensemble averages could be computed using Monte Carlo (MC) simulations to evaluate the ratio of configurational integrals in Eq. 2.21 by generating a series of relevant configurations describing the statistical ensemble. Molecular Dynamics (MD) also explore phase space and generates a series of configurations, also called trajectory, but does so by propagating in time the initial configuration. The averages computed along this trajectory are then time averages, written \bar{A} here, defined as

$$\bar{A} = \frac{1}{t} \int_0^t A(t') dt' \quad (2.38)$$

where t is the duration of the trajectory. The link with statistical mechanics is granted by the ergodic principle: it states that for sufficiently long trajectories, the time average tends to the ensemble average

$$\lim_{t \rightarrow \infty} \frac{1}{t} \int_0^t A(t') dt' = \langle A \rangle. \quad (2.39)$$

This is equivalent to saying that an MD simulation would sample the entire phase space in an infinite time. Although this is known to be false for a few pathological systems and only an approximation in practice, this is a generally accepted principle which allows to extract meaningful averages from MD simulations and use statistical mechanics tools in MD.

2.3.2 Propagating the equations of motion

In practice, the system is characterized at a given time by the positions \mathbf{r}^N and the velocities \mathbf{v}^N of the atoms. Knowing the interaction potential, which is common for both MD and MC simulations,

the force $\mathbf{F}_i = -\nabla_{\mathbf{r}_i}\mathcal{U}_{\text{pot}}$ acting on each atom i at time t is computed. The following configuration is generated by integrating the equations of motion: time is discretized using a timestep δt small enough to describe atomic displacements, typically 1 femtosecond, and new positions and velocities are computed for time $t + \delta t$. These steps are detailed in next sections. Repeating the force calculation and propagation of equations of motion for a large number of steps (1.000.000 steps of 1 fs to obtain a nanosecond-long simulation) results in a so-called trajectory describing the evolution of the system in time.

2.3.2.1 Time integration and the velocity Verlet algorithm

Hamilton's equations of motion for a system of N interacting atoms are given for each atom i with position \mathbf{r}_i and momentum $\mathbf{p}_i = m_i\mathbf{v}_i$ as

$$\dot{\mathbf{r}}_i = \frac{\partial \mathcal{H}}{\partial \mathbf{p}_i} \quad (2.40)$$

$$\dot{\mathbf{p}}_i = -\frac{\partial \mathcal{H}}{\partial \mathbf{r}_i} \quad (2.41)$$

where $\mathcal{H} = \mathcal{U}_{\text{tot}} = \mathcal{U}_{\text{pot}} + \mathcal{K}$ is the classical Hamiltonian, with \mathcal{U}_{pot} the potential energy and $\mathcal{K} = \sum_{i=1}^N \frac{1}{2}m_i\mathbf{v}_i^2$ is the kinetic energy of the system (values for the atomic masses m_i are given in tables 2.4, 2.5 and 2.6). These equations can be rewritten into Newton's equations of motion

$$\dot{\mathbf{r}}_i = \mathbf{v}_i \quad (2.42)$$

$$m_i\dot{\mathbf{v}}_i = -\frac{\partial \mathcal{U}_{\text{pot}}}{\partial \mathbf{r}_i} = \mathbf{F}_i \quad (2.43)$$

where \mathbf{F}_i is the total force acting on atom i due to all other atoms j derived from the interaction potential \mathcal{U}_{pot} detailed in section 2.1.2. Because, the force depends on the positions \mathbf{r}^N , these are $6N$ coupled differential equations. There are different ways to discretize and integrate these equations, mostly based on the Verlet algorithm¹⁸⁶, and we will use its extension of the Velocity-Verlet algorithm¹⁸⁷. This algorithm works as follows:

0. $\mathbf{r}_i(t)$, $\mathbf{v}_i(t)$ are known at time t and the forces $\mathbf{F}_i(t)$ are calculated

1. The new positions at $t + \delta t$ are computed using

$$\mathbf{r}_i(t + \delta t) = \mathbf{r}_i(t) + \mathbf{v}_i(t)\delta t + \frac{\mathbf{F}_i(t)}{m_i} \frac{\delta t^2}{2} \quad (2.44)$$

2. The new forces $\mathbf{F}_i(t + \delta t)$ at $t + \delta t$ are computed.

3. The new velocities at $t + \delta t$ are given by

$$\mathbf{v}_i(t + \delta t) = \mathbf{v}_i(t) + \left(\frac{\mathbf{F}_i(t) + \mathbf{F}_i(t + \delta t)}{m_i} \right) \frac{\delta t}{2} \quad (2.45)$$

4. $\mathbf{r}_i(t + \delta t)$, $\mathbf{v}_i(t + \delta t)$ and $\mathbf{F}_i(t + \delta t)$ are known. Reiterate from step 1 with $t \rightarrow t + \delta t$.

This algorithm has several advantages: it is fast and easy to implement and requires a single force calculation by step, the error on the positions is small (of the order of δt^4), which makes it a stable algorithm, it is time-reversible and conserves energy rather well. It is therefore one of the best compromises for propagating the equations of motion.

Of course the choice of the timestep δt is crucial and should be done carefully. It should result in similar trajectories (at least for small times) than for a smaller timestep, and have a good conservation of the total energy \mathcal{U}_{tot} . Indeed, Hamilton's equations of motion conserve energy and therefore correspond to a microcanonical ensemble. We will see later in this section how to modify the Velocity Verlet algorithm to impose a constant temperature (canonical ensemble) and pressure (isothermal-isobaric ensemble).

2.3.2.2 Constraining the geometry: SHAKE/RATTLE algorithms

For molecules with high frequency vibrations, such as water molecules, describing accurately the fast motions of these atoms requires a small timestep of about a tenth of the smaller characteristic time. If too large a timestep is chosen, the light atom's movement no longer follows the correct dynamics and energy conservation could be violated. Simulating these degrees of freedom is thus computationally expensive and slows down the calculation, but frequently they are not a crucial feature of the system. In these cases, one can freeze the fast degrees of freedom (*e.g.* the O-H bond length or the H-O-H angle) in order to use a larger timestep.

Several algorithms are available and we will use the RATTLE algorithm¹⁸⁸, which is the equivalent for the Velocity Verlet integrator of the SHAKE algorithm¹⁸⁹ for the Verlet integrator; these are algorithms for enforcing holonomic constraints (*i.e.* that only depend on the positions of atoms, not on velocities). Instead of the Hamiltonian equations of motion, these algorithms are based on the Lagrangian equations of motion, which are equivalent and use the Lagrangian $\mathcal{L} = \mathcal{K} - \mathcal{U}_{\text{pot}}$ in

$$\frac{\partial}{\partial t} \frac{\partial \mathcal{L}}{\partial \dot{\mathbf{r}}} = \frac{\partial \mathcal{L}}{\partial \mathbf{r}}. \quad (2.46)$$

This framework is convenient to impose constraints written in general as $\sigma_k(\mathbf{r}^N) = 0$. For example, to impose a fixed distance r_0 between atoms i and j , we can write

$$\sigma_1(\mathbf{r}_i, \mathbf{r}_j) = r_{ij}^2 - r_0^2 = 0. \quad (2.47)$$

Constrained dynamics then correspond to a new Lagrangian $\mathcal{L}' = \mathcal{L} - \sum_k \lambda_k \sigma_k(\mathbf{r}^N)$ with λ_k a set of to-be-determined Lagrange multipliers. Equation 2.46 for \mathcal{L}' is rewritten as

$$m_i \ddot{\mathbf{r}}_i = -\frac{\partial \mathcal{U}_{\text{pot}}}{\partial \mathbf{r}_i} - \sum_k \lambda_k \frac{\partial \sigma_k}{\partial \mathbf{r}_i} = \mathbf{F}_i + \sum_k \mathbf{G}_i(k) \quad (2.48)$$

where $\mathbf{G}_i(k)$ is the force corresponding to the k -th constraint. In constrained MD, the set of λ_k Lagrange multipliers is determined so that the constraints σ_k are rigorously satisfied at the next timestep. The SHAKE algorithm solves for the λ_k by an iterative procedure over all constraints, one by one, until all constraints have converged to the required tolerance.

2.3.2.3 Fixing the temperature and/or pressure: thermostats and barostats

As mentioned earlier, the equations of motion conserve the Hamiltonian so that the integration scheme samples the microcanonical ensemble, with constant number of particles N , volume V and energy E . The temperature of the system can be computed from the equipartition principle as

$$\frac{N_{\text{dof}} k_B T}{2} = \frac{1}{2} \sum_{i=1}^N m_i \mathbf{v}_i^2 \quad (2.49)$$

where N_{dof} is the number of degrees of freedom in the system, typically $3N$ translational degrees of freedom minus the number of constraints. The initial temperature in the system can be controlled by setting the initial velocities from a Maxwell-Boltzmann distribution

$$\mathcal{P}(\mathbf{v}; T) = \left(\frac{m_i}{2\pi k_B T} \right)^{3/2} \exp \left[-\frac{m_i \mathbf{v}_i^2}{2k_B T} \right]. \quad (2.50)$$

This will however not guarantee a constant temperature all along the simulation. Imposing the temperature requires changing the equations of motion using a thermostat: this can be done in several ways but the algorithm should produce the correct Boltzmann distribution of the temperature.

Nosé-Hoover thermostat and barostat A widely used category of thermostats is the family of Nosé-Hoover thermostats^{190;191}. They are based on an extended-Lagrangian formulation as detailed above in section 2.3.2.2, where an additional coordinate s is introduced such that

$$\mathcal{L} = \sum_{i=1}^N \frac{1}{2} m_i \dot{\mathbf{r}}_i^2 - \mathcal{U}_{\text{pot}}(\mathbf{r}^N) + \frac{Q}{2} \dot{s}^2 - \frac{3N}{\beta} \ln[s] \quad (2.51)$$

with Q an effective mass associated with s . This formulation reproduces the ensemble averages of the canonical (fixed N, V, T) ensemble by expanding the number of degrees of freedom. These equations are deterministic and the dynamics of s are integrated along with the *real* degrees of freedom. In practice, we use Nosé-Hoover chains introduced by Martyna et al.¹⁹², where several thermostats are coupled to one another in chains (we generally set a chain of 5 thermostats).

The same scheme of Nosé-Hoover chains can be extended to simulate a isothermal-isobaric ensemble, with fixed N , pressure P and temperature T , by adding additional variables s_k associated to the thermostats and additional variables ϵ_k corresponding to chained barostats.

The parameter Q characterizes the strength of the thermostat or barostat and it will determine the inertia of the additional variables. We usually set instead an equivalent characteristic time of relaxation of the fluctuations in temperature and/or pressure.

Rigid electrodes and pistons The above-mentioned NPT simulations are useful for equilibrating bulk systems, can be applied in a single dimension or handle non-isotropic and non-orthorhombic boxes. However, in the confined setups used in this work, we consider rigid electrodes that cannot be deformed. This is mainly because the computational cost is considerably reduced and the force fields to account for their flexibility are not yet available for our simulation method. The easiest way of treating these electrodes is to freeze them during the whole simulation. Equilibrating *e.g.* the electrolyte density (see section 2.4) to a known bulk value prior to the simulation then required several iterations by trial and error.

Instead, we introduced within this work the treatment of the electrodes as rigid pistons by adding an external pressure force $\mathbf{F}^P = \pm P \times \mathcal{A} \mathbf{e}_z$, with P the external pressure and $\pm \mathcal{A} \mathbf{e}_z$ the electrode area oriented towards the electrolyte. The total force on each electrode \mathbf{F}_L and \mathbf{F}_R , for the left and right electrode respectively, due to the electrolyte and the other electrode, are computed. Then the electrode is translated in the z direction under the total force $\mathbf{F}_X^{\text{tot}} = \mathbf{F}_X^P + \mathbf{F}_X$ (for $X = L$ or R) according to the Velocity Verlet algorithm (with no thermostating) for the center of mass of the electrode with the total electrode mass. This simple procedure allows to run a NP_zT simulation at constant external pressure.

2.4 Extracting molecular properties

A Molecular Dynamics study starts with the definition of the parameters of the model (force fields, system composition and physical properties), an equilibration phase until some characteristic properties have reached a steady state (*e.g.* temperature, energy, density) and oscillate around a mean value. After this, we can do production runs for the required duration to observe some physical phenomena. A typical computation time for a nanosecond-long simulation and a few thousands of atoms is between a few hours to a few days on a standard super-computer node, depending on the implementation and the type of model used: in our case constant-potential simulations (see chapter 3) are significantly more expensive than constant charges simulations. After the trajectory is run and different configurations have been accumulated, comes the time of the analysis. Aside from more complex calculation which will be described in section 2.5, standard properties to extract are structural and dynamical information on the system. In this work we will also study in detail specific electrochemical properties and the phase coexistence between vapor, liquid or solid phases.

2.4.1 Structural properties: density profiles and radial distribution functions

A trajectory is characterized by the positions \mathbf{r}^N and the velocities \mathbf{v}^N of the atoms at each step, and represents a path in phase space. Because it is a $6N$ -dimensional space too large to be apprehended directly, we analyse the trajectory by computing ensemble averages and extracting collective observables that catch the characteristics of the system. For structural properties, only the coordinates are considered and we work with the probability distribution of finding the system at $\mathbf{r}^N = \{\mathbf{r}_1, \mathbf{r}_2 \dots \mathbf{r}_N\}$.

First, the average density of particles in the system can be computed as $\rho = N/V$. For an NPT or a grand-canonical simulation (see section 2.2), the density and its fluctuations are interesting properties to monitor, at least to check the equilibration or to study its dependence with *e.g.* temperature. In NVT simulations however, the mean density is fixed since N and V are.

When interfaces are present, the density is not uniform across the simulation cell. We thus frequently compute density profiles along z for each atom type

$$\rho(z) = \frac{1}{L_x L_y} \left\langle \sum_{i=1}^N \delta(z_i - z) \right\rangle. \quad (2.52)$$

In practice we accumulate a histogram of the positions z along the trajectory. Typical profiles indicate a layering at the surface with one or more solvation layers and a bulk region far from the interface, as shown in figure 2.5. In these systems, defining the volume of a phase and the boundary between the two phases is not straightforward: one definition for the positioning of the interface is the Gibbs dividing surface (GDS) which is defined as to satisfy

$$\int_{-\infty}^{z_{GDS}} (\rho(z) - \rho_1) dz = \int_{z_{GDS}}^{+\infty} (\rho(z) - \rho_2) dz, \quad (2.53)$$

given two phases 1 and 2 of bulk density ρ_1 and ρ_2 , respectively. The corresponding geometrical construction is shown in figure 2.5.

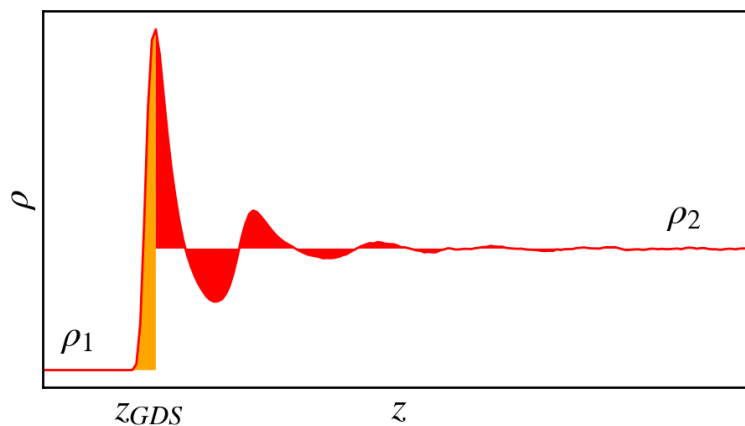


Figure 2.5: Typical density profile as a function of z and schematic representation of the Gibbs dividing surface z_{GDS} . The orange area corresponds to the left hand side of Eq. 2.53 while the red area is the right hand side.

The average density and the density profiles give information on the absolute spatial organization of the system but are quite useless for bulk systems for example, where the density is uniform, although there is a local organization within the system. This is revealed by the so-called pair distribution function, *i.e.* the probability of finding an atom at \mathbf{r}_2 given that there is an atom at \mathbf{r}_1 , normalized by the ideal gas one. For isotropic fluids, this only depends on the distance r_{12} between the two atoms. This radial distribution function gives the spatial correlations between atoms in the system and is

computed as an average over all pairs

$$g(r) = \frac{1}{4\pi r^2 \rho} \left\langle \sum_{i=1}^N \sum_{j>i} \delta(r_{ij} - r) \right\rangle. \quad (2.54)$$

The profile typically shows a first large peak indicating an accumulation of atoms at a given distance, which makes the first coordination shell, and subsequent oscillations that characterize the radial organization of atoms. Upon integration of the first peak, the radial distribution function yields the coordination number $N_C = \int_0^{r_0} 4\pi r^2 g(r) dr$ (where r_0 is an arbitrary cutoff for the coordination shell).

These analysis could also be done in polar coordinates only, in some two-dimensional problems as in a surface plane for example (see section 6.2.3.3). The radial distribution function can be related to experiments by Fourier transformation, which gives the structure factor also obtained by diffraction. These analyses are based on the presence of any atom at given positions but they can be extended to any property (their charge, orientation, coordination number. . .) and restricted to given areas (bulk area, close to the surface. . .).

A telling property to study interfaces with water is the orientation of the water dipole $\boldsymbol{\mu}$. We studied the orientation of the water molecule with respect to the surface by using $\cos \theta = \mathbf{n} \cdot \boldsymbol{\mu} / |\boldsymbol{\mu}|$, where \mathbf{n} is a unit vector normal to the surface, as shown in figure 2.6. In this case the knowledge of the local average $\langle \cos \theta \rangle$ is not sufficient to analyse all different orientations so we computed the probability distribution $\mathcal{P}(\cos \theta)$ in the first water layer – defined as water molecules in the first peak of the water density profile. When $\cos \theta = +1.0$, the water molecule is oriented with its dipole moment pointing away from the surface whereas for $\cos \theta = -1.0$ it is oriented towards it. For $\cos \theta = 0.0$, $\boldsymbol{\mu}$ lays on the x, y plane, and for more information about the O-H bond orientation it is possible to compute probability distributions of the angle using the O-H vector instead of the dipole moment. For examples of distributions, see section 4.2.3.2.

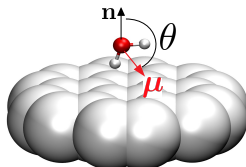


Figure 2.6: Water orientation at an interface is characterized by θ the angle between the normal to the surface (black vector) and the dipole moment $\boldsymbol{\mu}$ (red vector).

2.4.2 Electrochemical properties: charge and capacitance

For our electrochemical systems, additional specific properties are of importance. We are particularly interested in the charge density profile, which is a density profile weighted by the species charge as

$$\rho_c(z) = \left\langle \frac{1}{L_x L_y} \iint dx dy \rho_c(x, y, z) \right\rangle, \quad (2.55)$$

where $\rho_c(x, y, z)$ is the 3D charge density defined in Eq. 2.3 (we used the same notation ρ_c for the 1D and 3D densities for simplicity). If only point charges are present, this results in

$$\rho_c(z) = \frac{1}{L_x L_y} \left\langle \sum_{i=1}^N q_i^{\text{pc}} \delta(z_i - z) \right\rangle. \quad (2.56)$$

From the charge density, the electric potential profile is extracted by integrating twice (from a reference position z_{ref}) the Poisson equation $\partial^2 \psi / \partial z^2 = -\rho_c(z) / \epsilon_0$

$$\psi(z) = -\frac{1}{\epsilon_0} \int_{z_{\text{ref}}}^{z'} dz'' \int_{z_{\text{ref}}}^z dz' \rho_c(z'). \quad (2.57)$$

From these profiles it is then possible to observe the oscillations of the potential at the surface and compute potential drops across the interface.

Using our constant potential simulations, that will be discussed in detail in chapter 3, the charge amplitudes q_i on electrode atoms can fluctuate. This allows in particular to compute the total charge on one electrode, $Q_L = \sum_{i \in L} q_i$ for the left and $Q_R = \sum_{i \in R} q_i$ for the right electrode, in a capacitor setup.

In general we will impose an electroneutrality constraint, which results in $Q_L = -Q_R = Q_{\text{tot}}$. For industrial applications in energy storage, the charge accumulated on the electrodes depending on the applied potential difference $\Delta\psi = \psi_L - \psi_R$ is a crucial characteristic. The first measure is the integral capacitance that can be directly extracted from simulations and is defined as

$$C_{\text{int}}(\Delta\psi) = \frac{\langle Q_{\text{tot}} \rangle}{\Delta\psi} \quad (2.58)$$

where we took the average value of the total charge on the positive electrode. A second measure is the differential capacitance

$$C_{\text{diff}}(\Delta\psi) = \frac{\partial \langle Q_{\text{tot}} \rangle}{\partial \Delta\psi}. \quad (2.59)$$

It can be computed by simulating the system at different applied potentials $\Delta\psi$ but we will show in section 3.1.5 that it can also be extracted from the statistical fluctuations of the total charge Q_{tot} . In the linear regime, the capacitance does not depend on voltage $\Delta\psi$ so that C_{int} is constant and equal to C_{diff} .

More advanced analysis focuses directly on individual charges and their spatial distribution, both as a function of z or by computing the radial distribution function weighted by the charge. Specific analysis will be detailed along the manuscript.

2.4.3 Dynamical properties: autocorrelation functions

Previous analyses perform averages over time (and atoms) of a given quantity, losing the time dependence unique to MD simulations (with respect to MC ones). We can extract information on the dynamics of the system by computing time-dependent quantities and correlating different times in the same way we studied spatial correlations between atoms with pair distribution functions. A typical analysis is to compute the normalized autocorrelation function of an observable $A(t)$ as

$$C_{AA}(t) = \frac{\langle A(\tau) \times A(\tau + t) \rangle}{\langle A \rangle^2} \quad (2.60)$$

where the average is over different initial times τ . In practice, we compute time-autocorrelation functions using the Wiener-Khinchin theorem that uses Fourier transforms to speed up the calculation. This function measures the memory in the system for the given observable: it decreases starting from 1 because different times t and $t + \tau$ start decorrelating. When C_{AA} goes to zero, the system is uncorrelated *i.e.* knowing the observable at some time $A(t)$ we cannot predict its value beyond a characteristic time, named the correlation time t_{corr} . In this time lapse of t_{corr} , the system loses the memory of its previous state. At short times $t \ll t_{\text{corr}}$ on the contrary, fluctuations are small and the memory of the system is retained. We define somewhat arbitrarily the time correlation by

$$\tau_C = \int_0^\infty C_{AA}(t) dt, \quad (2.61)$$

which corresponds to the characteristic time for an exponential decay $\exp[-t/\tau_C]$. This autocorrelation function will in particular be applied to the total charge Q_{tot} to investigate the dynamics of charge and discharge of a capacitor (see section 4.2.3.3).

2.4.4 Ensemble averages and statistical errors

As highlighted in section 2.2, all previous quantities are ensemble averages, *i.e.* averages over configurations belonging to the given ensemble. Several statistical tools are used to characterize the probability distribution of microscopic observables A . In particular, we frequently investigate the mean value $\langle A \rangle$ and the standard deviation $\sigma^2 = \langle \delta A^2 \rangle = \langle (A - \langle A \rangle)^2 \rangle$.

For a statistically independent set of observations (A_1, A_2, \dots, A_n) , the standard error on the mean value of A is given by $\sigma_E = \sigma/\sqrt{n}$, where n is the number of observations. The higher the number of independent observations n , the closer the average over the set of observations is to the correct mean value of the distribution. However, if we add observations that are correlated, the distribution will be smoother but no new information is collected and the standard error is not reduced. For a given set of correlated microscopic observables, the standard error involves the correlation time τ_C in Eq. 2.61 and is given by

$$\sigma_E = \sqrt{\frac{\tau_C}{\tau_S} \langle \delta A^2 \rangle}, \quad (2.62)$$

where τ_S is the total sampling time, so that τ_S/τ_C is the number of statistically independent observations. Similarly, the standard error on the variance of the distribution is given by

$$\sigma_E^{\sigma^2} = \sqrt{\frac{4\tau'_C}{\tau_S} \langle \delta A^2 \rangle} \quad (2.63)$$

where $\tau'_C = \int_0^\infty C_{AA}(t)^2 dt$ is the correlation time extracted from the squared autocorrelation function¹⁹³.

2.4.5 Phase coexistence

In this work, we will be interested in determining the phase coexistence points, *i.e.* the particular values of the pertinent control variables for which two (or more) phases are thermodynamically stable, *i.e.* their thermodynamic potential is equal.

For two bulk phases, the variations in Gibbs free energy are given by Eq. 2.27 so that, for a multi-component system with n components

$$\mu_i = \left. \frac{\partial G}{\partial N_i} \right|_{P,T,N_{j \neq i}}, \quad (2.64)$$

where N_i is the number of particles of the i -th components so that $N = \sum_{i=1}^n N_i$. The chemical potential is thus defined as the partial molar Gibbs free energy. It follows that

$$G = \sum_{i=1}^n \mu_i N_i \quad (2.65)$$

which combined to Eq. 2.27 gives the Gibbs-Duhem relation

$$VdP - SdT = \sum_{i=1}^n N_i d\mu_i \quad \text{or} \quad vdP - sdT = \sum_{i=1}^n \frac{N_i}{N} d\mu_i \quad (2.66)$$

where we introduced the volume per particle $v = V/N$ and entropy per particle $s = S/N$.

Consider now a system with N_1 particles in phase 1 and N_2 particles in phase 2. For given T and P , the system is at coexistence if $dG = 0 = \mu_1 dN_1 + \mu_2 d(N - N_1)$, *i.e.* if $\mu_1 = \mu_2$. Thus for two coexisting phases at fixed T, P , the chemical potentials of the phases are equal.

Additionally, the Clausius-Clapeyron equation is derived from the Gibbs-Duhem relation written for each phase separately and subtracting them

$$(v_1 - v_2)dP - (s_1 - s_2)dT = d\mu_1 - d\mu_2 \quad (2.67)$$

At the coexistence, the equality of the chemical potentials gives $\mu_1 = \mu_2$ and for small deviations along the coexistence line, $\mu_1 + d\mu_1 = \mu_2 + d\mu_2$ so that

$$\frac{dP}{dT} = \frac{s_1 - s_2}{v_1 - v_2} = \frac{\Delta h}{T\Delta v} \quad (2.68)$$

where we introduced the enthalpy per particle $h = H/N = (\mathcal{U} + PV)/N$ and we used that at coexistence $\Delta s = \Delta h/T$. Δh and Δv are respectively the transition enthalpy and transition volume. These steps will be retraced in more detail for a confined phase transition in chapter 5.

2.4.5.1 The Gibbs Ensemble

To find the pressure of coexistence at a given temperature by Monte Carlo simulation, an advanced method has been introduced by Panagiotopoulos *et al.* in Refs. 194 and 195 by running simulations in the Gibbs Ensemble (GE). In a nutshell, it consists in simulating a total system in the NVT ensemble separated into two boxes 1 and 2 with temperatures $T_1 = T_2 = T$, volumes V_1 and $V_2 = V - V_1$ and numbers of particles N_1 and $N_2 = N - N_1$. Each box describes a different phase (*e.g.* liquid and vapor).

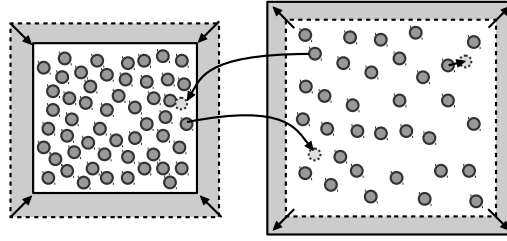


Figure 2.7: Gibbs Ensemble Monte Carlo scheme. Possible moves are shown: the displacement of an atom, the change in volume or the transfer of atoms between boxes.

The different moves allowed, pictured in figure 2.7, and their acceptance probability are

- displacement of a randomly chosen atom

$$acc(\mathbf{i} \rightarrow \mathbf{j}) = \min \left\{ 1, e^{-\beta[\mathcal{U}(\mathbf{j}) - \mathcal{U}(\mathbf{i})]} \right\} \quad (2.69)$$

- change of the volume repartition: $\ln[V_1/V_2] \rightarrow \ln[V_1/V_2] + \Delta$

$$acc(\mathbf{i} \rightarrow \mathbf{j}) = \min \left\{ 1, \left(\frac{V_1(\mathbf{j})}{V_1(\mathbf{i})} \right)^{N_1+1} \left(\frac{V_2(\mathbf{j})}{V_2(\mathbf{i})} \right)^{N_2+1} e^{-\beta[\mathcal{U}(\mathbf{j}) - \mathcal{U}(\mathbf{i})]} \right\} \quad (2.70)$$

- transfer of a randomly chosen atom from one box to the other: $N_1 \rightarrow N_1 - 1$ and $N_2 \rightarrow N_2 + 1$ (or vice versa).

$$acc(\mathbf{i} \rightarrow \mathbf{j}) = \min \left\{ 1, \frac{N_1 V_2}{(N_2 + 1) V_1} e^{-\beta[\mathcal{U}(\mathbf{j}) - \mathcal{U}(\mathbf{i})]} \right\} \quad (2.71)$$

Given a reasonable initial setup, a simulation in the Gibbs Ensemble finds “on its own” the coexistence between both phases, *i.e.* where the pressure and chemical potentials of both boxes are equal. It is then possible to compute the corresponding pressure (using the virial expression for example), the densities ρ_1 and ρ_2 and the chemical potential at coexistence.

2.4.5.2 Widom particle insertion method

To compute the chemical potential, a widely used method is the particle insertion or Widom method. It stems from the definition of $\mu = \partial F / \partial N|_{V,T} = -k_B T (\ln[Q(N+1, V, T)] - \ln[Q(N, V, T)])$ and reads

$$\mu = -k_B T \ln \left[\frac{V}{(N+1)\Lambda^3} \right] - k_B T \ln \left[\int d\mathbf{s}_{N+1} \langle \exp[-\beta(\mathcal{U}(\mathbf{s}^{N+1}) - \mathcal{U}(\mathbf{s}^N))] \rangle_{NVT} \right], \quad (2.72)$$

where the first term is the ideal gas chemical potential, which can be calculated analytically, and in the second we introduced the reduced coordinates $\mathbf{s}^N = \mathbf{r}^N / L$, with L the box size. In practice, the integral is computed by running a canonical MC simulation of N particles and at regular intervals we select a random position \mathbf{s}_{N+1} (as if we were inserting an additional particle) and sample the Boltzmann factor that appears in Eq. 2.72.

2.4.5.3 The Gibbs Duhem Integration method

The Gibbs Ensemble simulation computes the equilibrium pressure for a given temperature on the phase diagram where both phases coexist. However it works well only for liquid-vapor coexistence; for solid-liquid, the transfer of particles or the change of volume moves are hardly accepted because these are condensed phases. To compute the whole phase diagram, it is therefore impractical to only use this method. However, starting from a known point on the coexistence line, one can integrate numerically the Clausius-Clapeyron equation Eq. 2.68 to obtain the whole curve. This is the Gibbs-Duhem Integration (GDI) method, introduced by Kokke *et al.* in Ref. 196. The quantities involved in the Clausius-Clapeyron equation, Δv and Δh , can be readily computed from simulations and are used to evaluate the slope of the phase coexistence line dP/dT . This in turn allows to predict the pressure at coexistence for a different temperature upon integration. It turns out that, for numerical reasons, it is better to recast the Clausius-Clapeyron Eq. 2.68 into

$$\frac{d \ln P}{d\beta} = -\frac{\Delta h}{\beta P \Delta v}. \quad (2.73)$$

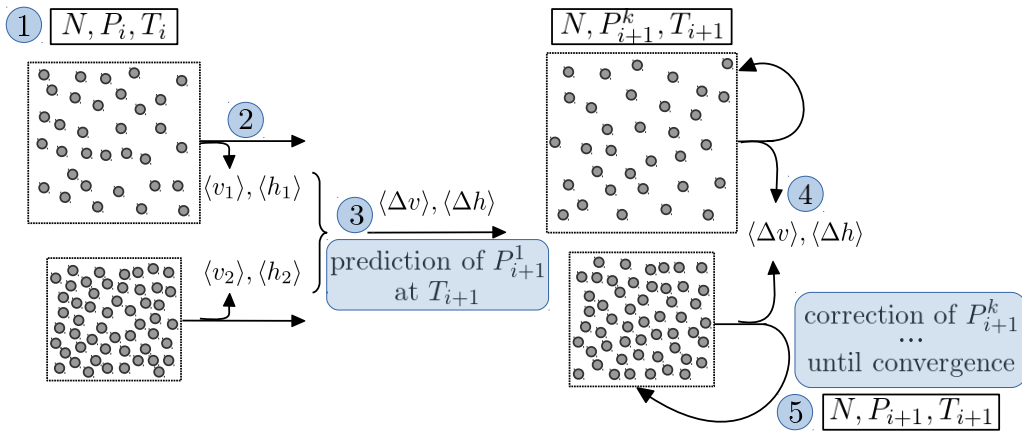


Figure 2.8: The Gibbs Duhem Integration method (see text).

The Gibbs Duhem Integration method is illustrated on figure 2.8: it requires the simulation (using Monte Carlo or Molecular Dynamics simulations) of two independent NPT boxes, each one being a different phase 1 and 2 (liquid and vapor for example). It then proceeds as follows

1. Start from a known (T_i, P_i) point on the coexistence line
2. Run NPT_i simulations for the two phases and collect $\Delta h = h_2 - h_1$ and $\Delta v = v_2 - v_1$
3. Increment the temperature using increments in $\beta = 1/k_B T$: $\beta_{i+1} = \beta_i + \delta\beta$ and predict the new pressure P_{i+1}^1 using Eq. 2.73

4. Run $NP_{i+1}^1 T_{i+1}$ simulations for the two phases and collect Δh and Δv
5. Use a predictor-corrector scheme to correct the pressure $\rightarrow P_{i+1}^2, P_{i+1}^3 \dots P_{i+1}^k$ and repeat 4 until convergence: we obtain the converged pressure P_{i+1} at the coexistence at T_{i+1}
6. Repeat from step 1 with $i \rightarrow i + 1$.

This method has the advantage of giving the whole coexistence line between two phases, given an accurate starting point. It should be noted however that any error on the starting point will be propagated onto the whole line and that the convergence criterion in the predictor-corrector integration scheme can yield numerical errors that could accumulate when moving away from the starting point. The details of the predictor-corrector scheme were taken from Ref. 196 and steps in $\delta\beta$ or $\delta \ln P$ were used depending on the part of the coexistence line studied.

To conclude on these methods to compute phase coexistence, they were a particularly important improvement in the simulation of coexistence because they allow to simulate both phases without explicitly having an interface between them. These aspects will be discussed in more details in chapter 5.

2.4.5.4 Collective variable Q_6

A key feature needed in the simulations of phase coexistence developed in this work is the ability to discriminate between two phases, specifically the solid and liquid phases. This requires to build a collective variable that depends on the coordinates of all atoms in the system and quantifies the degree of order of the system. In this work, we consider a collective variable based on the sixth order Steinhardt parameters, which measures the degree of order in the first coordination shell of a given atom¹⁹⁷⁻²⁰³. The continuous version of the Steinhardt parameters used in this work is a complex vector given for atom i by

$$q_{6m}(i) = \frac{\sum_j \sigma(r_{ij}) Y_{6m}(\mathbf{r}_{ij})}{\sum_j \sigma(r_{ij})}, \quad (2.74)$$

where the sum is on all other atoms j , Y_{6m} is one of the sixth order spherical harmonics, with $m \in \llbracket -6, 6 \rrbracket$ and $\sigma(r_{ij})$ is a switching function that goes smoothly from 1 to 0 for distances r_{ij} between atoms i and j at a given cutoff distance. This cutoff was chosen so as to select only first-shell neighbours of atom i , and in chapter 5 we took the value 1.32σ . The collective variable Q_6 characterizing the whole system is obtained by taking the norm of the average vector $\overline{\mathbf{q}_6}$ over all atoms

$$Q_6(\{\mathbf{r}_i\}) = \sqrt{\sum_{m=-6}^6 |q_{6m}|^2} = \sqrt{\sum_{m=-6}^6 \left| \frac{1}{N} \sum_{i=1}^N q_{6m}(i) \right|^2}. \quad (2.75)$$

A large (resp. low) value of Q_6 corresponds to an ordered (resp. disordered) phase. We used the implementation available in the crystallization module of PLUMED^{204;205}.

2.5 Enhanced sampling methods

What results from the previous section 2.2 is the need for a good sampling of the phase space to ensure the results from ensemble averages are reliable. Achieving this can be particularly challenging with limited time and computer resources, for example in systems with large energy barriers compared to the thermal energy $\beta^{-1} = k_B T$ and slow kinetics such as adsorption/desorption phenomena onto a surface or the exchange of a solvent molecule in the first solvation shell of an ion. Complex energy landscapes with multiple local minima will also be difficult to sample. Another example of rare phenomena that do not occur enough times in a simulation to obtain significant averages are collective transformations such as conformational changes of a protein or phase transitions, which need a concerted motion of atoms.

Several enhanced sampling methods have been introduced in the literature to cope with the sampling of rare events. A first idea is to inject thermal energy for the system to be able to overcome thermodynamic barriers. Different methods based on this idea have been developed and we will present one used in this work, in section 2.5.1. Other techniques directly force the rare event of interest in order to compute the free energy profile along a given reaction coordinate. One approach consists in considering forces, either by adding an external force to drive atoms as in Steering Molecular Dynamics²⁰⁶, often used to investigate folding and unfolding of proteins, or by computing the force to keep a given degree of freedom frozen and do a thermodynamic integration to obtain the potential of mean force (*e.g.* to develop coarse grained models). An alternative approach directly alters the Hamiltonian and thus the energy landscape to direct the simulation towards the regions of interest such as the top of a barrier. Examples of these techniques used in the present work will be discussed in sections 2.5.2 and 2.5.3.

2.5.1 Heating the system up

As mentioned above, an intuitive way to accelerate sampling is to inject energy into the system. Traditionally thermal energy is added but one could in principle use electric fields or other external contributions to add energy. This is known as Simulated Annealing²⁰⁷. The system is heated at a higher temperature, which allows it to cross barriers and explore higher energy configurations, then cooled down to the original temperature slowly. In particular this allows systems that are stuck in a metastable state to find the global minimum of the potential energy landscape.

Alternatively, one can harness information from higher energy configurations by running several replicas of the same system at different temperatures. The different replicas are exchanged during the simulation so as to feed replicas at lower temperatures with configurations at higher temperature, but have otherwise independent trajectories. This method is known as Parallel Tempering or Replica Exchange^{208–210}. It was first developed for Monte Carlo simulations but has later been adapted to Molecular Dynamics and extended to other statistical ensembles, *i.e.* to thermodynamic parameters other than the temperature (number of particles, electric potential...). In practice, we run n different canonical NVT_k Monte Carlo simulations. We then use the usual translational moves plus a swapping move that exchanges the coordinates of two replicas. For this we consider the extended ensemble which combines the n replicas; its partition function is the product of the single partition functions

$$Q_n = \prod_{k=1}^n Q(N, V, T_k) = \prod_{k=1}^n \frac{1}{\Lambda_k^{3N} N!} \int d\mathbf{r}_i^N e^{-\beta_k \mathcal{U}(\mathbf{r}_i^N)} \quad (2.76)$$

Given that each replica (\mathbf{i}, β_a) is defined by its configurations $\mathbf{i} \equiv \mathbf{r}_i^N$, and its reciprocal temperature β_a , the detailed balance related to the swapping move gives

$$\begin{aligned} & \mathcal{P}(\mathbf{i}, \beta_a) \mathcal{P}(\mathbf{j}, \beta_b) \times \alpha[(\mathbf{i}, \beta_a), (\mathbf{j}, \beta_b) \rightarrow (\mathbf{j}, \beta_a), (\mathbf{i}, \beta_b)] \times acc[(\mathbf{i}, \beta_a), (\mathbf{j}, \beta_b) \rightarrow (\mathbf{j}, \beta_a), (\mathbf{i}, \beta_b)] \\ &= \mathcal{P}(\mathbf{j}, \beta_a) \mathcal{P}(\mathbf{i}, \beta_b) \times \alpha[(\mathbf{j}, \beta_a), (\mathbf{i}, \beta_b) \rightarrow (\mathbf{i}, \beta_a), (\mathbf{j}, \beta_b)] \times acc[(\mathbf{j}, \beta_a), (\mathbf{i}, \beta_b) \rightarrow (\mathbf{i}, \beta_a), (\mathbf{j}, \beta_b)] \end{aligned} \quad (2.77)$$

Assuming the attempt probability α is equal for both the forward and backward transformation, we obtain

$$\frac{acc[(\mathbf{i}, \beta_a), (\mathbf{j}, \beta_b) \rightarrow (\mathbf{j}, \beta_a), (\mathbf{i}, \beta_b)]}{acc[(\mathbf{j}, \beta_a), (\mathbf{i}, \beta_b) \rightarrow (\mathbf{i}, \beta_a), (\mathbf{j}, \beta_b)]} = \frac{\mathcal{P}(\mathbf{j}, \beta_a) \mathcal{P}(\mathbf{i}, \beta_b)}{\mathcal{P}(\mathbf{i}, \beta_a) \mathcal{P}(\mathbf{j}, \beta_b)} = e^{(\beta_b - \beta_a)(\mathcal{U}(\mathbf{j}) - \mathcal{U}(\mathbf{i}))} \quad (2.78)$$

and the acceptance probability is taken from the Metropolis criterion as

$$acc[(\mathbf{i}, \beta_a), (\mathbf{j}, \beta_b) \rightarrow (\mathbf{j}, \beta_a), (\mathbf{i}, \beta_b)] = \min\{1, e^{(\beta_b - \beta_a)(\mathcal{U}(\mathbf{j}) - \mathcal{U}(\mathbf{i}))}\} \quad (2.79)$$

In this thesis, we have worked in collaboration with Prof. Benoît Coasne, a researcher in Université Grenoble Alpes, on the problem of crystallization under confinement. To explore this phenomenon, he performed Hyper Parallel Tempering simulations²¹¹ where each replica is no longer a canonical but a

grand canonical $\mu_k VT_k$ simulation with a different $[\mu_k, T_k]$ couple of values for each replica. Figure 2.9 gives a schematic representation of this method. The acceptance probability is then

$$\begin{aligned} acc[(\mathbf{i}, [\mu_a, \beta_a]), (\mathbf{j}, [\mu_b, \beta_b])] &\rightarrow (\mathbf{j}, [\mu_a, \beta_a]), (\mathbf{i}, [\mu_b, \beta_b])] \\ &= \min \left\{ 1, \left(\frac{\Lambda_a}{\Lambda_b} \right)^{3(N_i - N_j)} e^{(\beta_b - \beta_a)(U(\mathbf{j}) - U(\mathbf{i})) + (\beta_a \mu_a - \beta_b \mu_b)(N_j - N_i)} \right\} \end{aligned} \quad (2.80)$$

If the probability distributions of energy and number of atoms overlap, a significant fraction of swapping moves is accepted, thereby improving the sampling by exploiting configurations from neighbouring replicas.

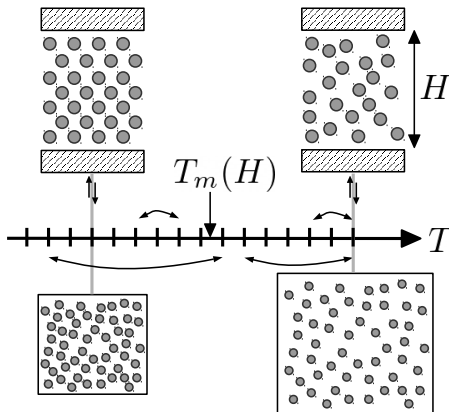


Figure 2.9: Hyper Parallel Tempering Grand Canonical Monte Carlo simulation scheme. The horizontal axis represents all different grand-canonical replicas at $\mu_k VT_k$ and horizontal arrows indicate swapping moves between them. Two replicas are shown (top boxes) at low and high temperature. Each of them is a (confined) system in equilibrium with a different reservoir (lower boxes) that fixes $[\mu_k, T_k]$. After equilibration, the melting temperature T_m can be determined by identifying solid and liquid replicas.

2.5.2 Biasing the Hamiltonian using Umbrella Sampling

While adding energy to the system helps exploring phase space, it does not allow to direct the energy into a desired way. For a wide range of systems, one can identify a relevant collective variable to monitor the various stages of the process of interest. One often refers to such a collective variable as a “reaction coordinate”, even though other collective variables may be necessary to capture the full picture. As an example we study in section 3.2.2 the adsorption of an ion onto a surface and consider the distance from the ion to the surface as a relevant reaction coordinate to investigate.

In these cases, the energy introduced in the system is directed specifically to sample the given reaction coordinate d . To that end, the Hamiltonian is modified by adding a bias on d , $w(d)$. This bias is usually a harmonic bias $w(d) = \frac{k}{2}(d - d_{\text{ref}})^2$, with k the spring constant, centered on the desired value d_{ref} and artificially lowers the relative energy of configurations close to d_{ref} and increases the probability density in this region.

To obtain the free energy profile as a function of the collective variable, and compute activation energies or rates, we use different bias functions to sample a range of d values: this method is called Umbrella Sampling²¹². A complete review of the method is available in Ref. 213 and only an overview is given here. Similarly to the Parallel Tempering technique, different windows i corresponding to different biases w^i are run separately in parallel. The spring constant k is usually kept fixed, whereas the minimum d_{ref} is shifted so that each biased window explores different d values. k^i and d_{ref}^i should be carefully chosen in order to obtain overlapping probability densities $\mathcal{P}_{\text{bias}}^i(d)$ for neighbouring windows.

For each window, the biased probability density $\mathcal{P}_{\text{bias}}^i(d)$ of observing a configuration where the collective variable has the value d is converged, converted into the free energy $\mathcal{F}_{\text{bias}}^i$ and unbiased as

$$F_{\text{unbias}}^i(d) = F_{\text{bias}}^i(d) - w^i(d) = -k_B T \ln[\mathcal{P}_{\text{bias}}^i(d)] - w^i(d) + F^i \quad (2.81)$$

where $F^i = -k_B T \ln[\langle \exp[-\beta w^i] \rangle]$ is a constant to be determined. Each window gives a different estimate of F_{unbias}^i , which is accurate only within the range of sampled d values. The overall unbiased free energy profile can be obtained using the Weighted Histogram Analysis Method (WHAM)^{214;215}, which computes the weight of each window that minimizes the statistical error σ^2 on the probability densities

$$\mathcal{P}_{\text{unbias}}(d) = \sum_i p^i(d) \mathcal{P}_{\text{unbias}}^i(d) \quad \text{with} \quad \frac{\partial \sigma^2(\mathcal{P}_{\text{unbias}})}{\partial p^i} = 0 \quad \text{and} \quad \sum_i p^i = 1, \quad (2.82)$$

where $\mathcal{P}_{\text{unbias}}$ is the unbiased probability density. The corresponding equations on F^i are coupled so that they are solved iteratively until convergence. WHAM results in an unbiased free energy profile $F_{\text{unbias}}(d)$ as a function of the collective variable d .

2.5.3 Manipulating the Hamiltonian with Thermodynamic Integration methods

Using the same idea of directly altering the Hamiltonian to drive the system, another very powerful and versatile technique, broadly called Thermodynamic Integration, allows to compute free energy differences between two (initial and final) states. This method will be used to compute free energy differences in chapter 5 between solid and liquid phases and in sections 6.2 and 6.3 between insulating and metallic systems.

The general framework requires the construction of a new Hamiltonian with a potential energy $\mathcal{U}(\lambda)$ where λ is a control parameter, which allows to drive the system from an initial state with energy $\mathcal{U}_i(\mathbf{r}^N)$ to a final state with energy $\mathcal{U}_f(\mathbf{r}^N)$. A usual choice is a linear combination of the two

$$\mathcal{U}(\mathbf{r}^N; \lambda) = (1 - \lambda)\mathcal{U}_i(\mathbf{r}^N) + \lambda\mathcal{U}_f(\mathbf{r}^N) \quad (2.83)$$

but any function for which $\mathcal{U}(\lambda = 0) = \mathcal{U}_i$ and $\mathcal{U}(\lambda = 1) = \mathcal{U}_f$ is eligible.

Assuming the thermodynamic integration is performed in the canonical NVT ensemble, we aim to compute the free energy difference as

$$\Delta F_{i \rightarrow f} = F_f - F_i = F(\lambda = 1) - F(\lambda = 0) = \int_{\lambda=0}^{\lambda=1} \left. \frac{\partial F}{\partial \lambda} \right|_{NVT; \lambda} d\lambda. \quad (2.84)$$

Given that the free energy is $F(N, V, T; \lambda) = -k_B T \ln[Q(N, V, T; \lambda)]$, we have

$$\frac{\partial F}{\partial \lambda} = -\frac{k_B T}{Q(\lambda)} \frac{\partial Q(\lambda)}{\partial \lambda} = \frac{1}{Q(\lambda)} \int d\mathbf{r}^N \frac{\partial \mathcal{U}}{\partial \lambda} e^{-\beta \mathcal{U}(\mathbf{r}^N; \lambda)} = \left\langle \frac{\partial \mathcal{U}}{\partial \lambda} \right\rangle_{NVT; \lambda}. \quad (2.85)$$

Finally the free energy difference is

$$\Delta F_{i \rightarrow f} = \int_{\lambda=0}^{\lambda=1} \left\langle \frac{\partial \mathcal{U}}{\partial \lambda} \right\rangle_{NVT; \lambda} d\lambda = \int_{\lambda=0}^{\lambda=1} \langle \mathcal{U}_f - \mathcal{U}_i \rangle_{NVT; \lambda} d\lambda, \quad (2.86)$$

where the brackets $\langle \dots \rangle$ is an ensemble average at a given λ value, and the second equality is valid only for the choice of linear combination given in Eq. 2.83. The integration therefore requires running several simulations at different λ values in $[0, 1]$ to converge the energy derivative $\partial \mathcal{U} / \partial \lambda$.

If the ensemble is the isobaric-isothermal NPT ensemble, the appropriate thermodynamic potential is the Gibbs free energy $G(N, P, T; \lambda) = -k_B T \ln \Delta(N, P, T; \lambda)$. The derivative of G with respect to λ is

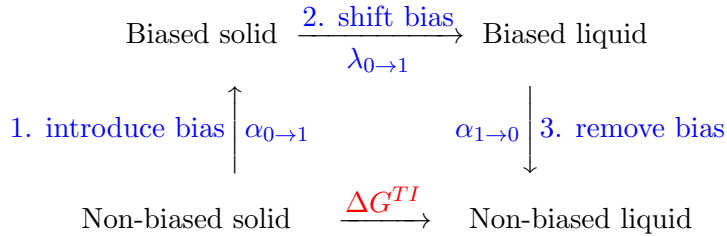
$$\frac{\partial G}{\partial \lambda} = -\frac{k_B T}{\Delta(\lambda)} \frac{\partial \Delta(\lambda)}{\partial \lambda} = \frac{1}{\Delta(\lambda)} \frac{\beta P}{\Lambda^{3N} N!} \int dV \int d\mathbf{r}^N \frac{\partial \mathcal{U}}{\partial \lambda} e^{-\beta(\mathcal{U}(\mathbf{r}^N; \lambda) + PV)} = \left\langle \frac{\partial \mathcal{U}}{\partial \lambda} \right\rangle_{NPT; \lambda}. \quad (2.87)$$

The Gibbs free energy difference is then obtained as

$$\Delta G_{i \rightarrow f} = G(\lambda = 1) - G(\lambda = 0) = \int_{\lambda=0}^{\lambda=1} \left\langle \frac{\partial \mathcal{U}}{\partial \lambda} \right\rangle_{NPT; \lambda} d\lambda = \int_{\lambda=0}^{\lambda=1} \langle \mathcal{U}_f - \mathcal{U}_i \rangle_{NPT; \lambda} d\lambda. \quad (2.88)$$

The strength and great adaptability of this method results from the fact that, contrary to Umbrella Sampling, the path taken to go from the initial to the final state does not have to be physically accurate: all alchemical transformations are possible. For example, Thermodynamic Integration is routinely used to compute hydration free energy differences²¹⁶ between different ions, say K^+ in Cs^+ , by transforming the force field parameters as a function of λ .

In chapter 5, we will use Thermodynamic Integration to introduce a harmonic bias, in the spirit of Umbrella Sampling, and drive a system from the solid state to the liquid state. The details of the bias will be given in that section but, in a nutshell, the method follows a three-step scheme



Using a sensible choice for the driving bias, this allows to build a reversible path from the initial to the final state. Each step of the scheme is a different thermodynamic integration detailed in the following, where \mathcal{U}_0 is the unperturbed Hamiltonian and $\mathcal{U}_{\text{bias}}$ the biasing potential.

1. Introduction of the biasing potential: $\alpha \in [0, 1]$, $\lambda = 0$

$$\mathcal{U}(\alpha) = \mathcal{U}_0 + \alpha \mathcal{U}_{\text{bias}}(\lambda = 0) \quad \text{and} \quad \frac{\partial \mathcal{U}(\alpha)}{\partial \alpha} = \mathcal{U}_{\text{bias}}(\lambda = 0) \quad (2.89)$$

2. Shift of the bias: $\alpha = 1$, $\lambda \in [0, 1]$

$$\mathcal{U}(\lambda) = \mathcal{U}_0 + \mathcal{U}_{\text{bias}}(\lambda) \quad \text{and} \quad \frac{\partial \mathcal{U}(\lambda)}{\partial \lambda} = \frac{\partial \mathcal{U}_{\text{bias}}(\lambda)}{\partial \lambda} \quad (2.90)$$

3. Destruction of the biasing potential: $\alpha \in [1, 0]$, $\lambda = 1$

$$\mathcal{U}(\alpha) = \mathcal{U}_0 + \alpha \mathcal{U}_{\text{bias}}(\lambda = 1) \quad \text{and} \quad \frac{\partial \mathcal{U}(\alpha)}{\partial \alpha} = \mathcal{U}_{\text{bias}}(\lambda = 1) \quad (2.91)$$

The choice for the biasing potential $\mathcal{U}_{\text{bias}}$ and associated collective variable will be given in section 5.3.2 as well as its derivative with respect to λ . The overall Gibbs free energy difference is obtained as

$$\Delta G^{TI} = \int_{\alpha=0}^{\alpha=1} d\alpha \left\langle \frac{\partial \mathcal{U}}{\partial \alpha} \right\rangle_{NPT; \alpha, \lambda=0} + \int_{\lambda=0}^{\lambda=1} d\lambda \left\langle \frac{\partial \mathcal{U}}{\partial \lambda} \right\rangle_{NPT; \alpha=1, \lambda} - \int_{\alpha=0}^{\alpha=1} d\alpha \left\langle \frac{\partial \mathcal{U}}{\partial \alpha} \right\rangle_{NPT; \alpha, \lambda=1}. \quad (2.92)$$

“Forget-me-not”: Molecular simulations of electrochemical systems

- In this work, we study electrochemical cells, made of an electrolyte and one or two solid electrodes, using molecular simulations.
- The link between simulations and macroscopic properties is given by the framework of Statistical Mechanics, through the use of ensemble averages.
- We mainly use Molecular Dynamics simulations to investigate our systems and predict their properties.
- To improve the exploration of phase space or drive the system over barriers, we use and develop enhanced sampling methods.

Chapter 3

Simulating metals: the constant potential ensemble

3.1 Accounting for the electronic polarization

As detailed in chapter 2, the systems studied in this work are mainly electrochemical cells, where an electrolyte is in contact with one or more electrodes made of conducting materials such as gold or graphite. These interfaces are particularly important because this is where the reactivity occurs in batteries and their contribution to the capacitance for capacitors is crucial. Their accurate description is therefore an active subject of research for energy storage applications.

A fundamental feature of these interfaces is that the metallic electrodes can conduct electricity and be polarized by the electrolyte, in the sense that the electronic distribution within the metallic material responds to the external potential created by the electrolyte. Additionally, these electrochemical systems may be included in an electric circuit and submitted to an applied voltage $\Delta\psi$ in order to accumulate charge on the electrodes or drive redox reactions at the interfaces. This specific interaction with the surface results in the creation of an electric double layer (EDL), *i.e.* an accumulation or depletion of ions at the surface. Several analytical theories, discussed in the introduction (see chapter 1) have been developed to account for the effects of the EDL on the properties of the electrochemical systems but they are valid only for low concentrations and do not provide a molecular picture of the EDL, which can only be provided by molecular simulations. As discussed in section 2.1, describing the electronic structure of the metal would in principle require *ab initio* calculations but simulation techniques such as Density Functional Theory based Molecular Dynamics are limited to small system sizes and short time scales. However, as shown in section 2.2, a correct sampling of phase space requires the use of Classical Molecular Dynamics instead. In turn, a dedicated description of the metal and its polarization should be included in the model. Different methods have been proposed in the literature²¹⁷, which are discussed in chapter 1, and we focus here on the method used in this work: the constant potential molecular simulations.

We first describe the setup of these simulations in section 3.1.1 and study the statistical mechanics of the corresponding constant potential ensemble in section 3.1.2. We then describe how the ensemble is sampled by molecular dynamics simulations and the implementation of the method in section 3.1.3. We show in section 3.1.4 that this sampling method has an impact on the statistical mechanical framework²¹⁸ that affects the calculation of quantities such as the differential capacitance, as shown in section 3.1.5. We finally discuss the importance of taking into account the electronic degrees of freedom in this model in section 3.2, where we compute the influence of the simulation method on free energy profiles of ions close to a surface and on the contact angle of a drop of electrolyte on an electrode.

3.1.1 Constant potential molecular simulations

In usual classical MD simulations, as discussed in section 2.1.2, atoms are assigned a fixed effective charge and effective intermolecular interactions such as the Lennard-Jones potential. These come from averaging the interactions of the electronic clouds so that the electronic degrees of freedom do not have to be described explicitly. However, instantaneous fluctuations of the electronic cloud can play a role in the structure and dynamics of the system. With the increase in computational power, new force fields have been developed that partially reintroduce electronic degrees of freedom by refining the charge distribution as an effective charge and an additional fluctuating dipole moment. These are called polarizable force fields and the additional variables are propagated at each step of the trajectory.

In our case, we differentiate electrode and electrolyte atoms and are mainly interested in the charge distribution of metallic electrode atoms. In the same spirit, we add electronic degrees of freedom but because we want to describe the delocalization of the charge among the metallic atoms of the electrode, we treat the charge of each atom as an additional degree of freedom and allow it to fluctuate. The instantaneous charge is then computed at each timestep in order to maintain the electric potential of the electrode atom at a constant value, instead of the charge.

This constant potential simulation method was first proposed by Siepman and Sprik to model the tip of a scanning tunneling microscope near a planar metal surface¹⁰⁹ and later adapted to electrochemical cells by Reed *et al.*¹¹¹. It has a significant impact on the speed of calculations because it needs to propagate equations of motion for additional degrees of freedom or to determine their value at each timestep so as to enforce the constant potential constraint. Compared to other methods that take into account the electronic polarization of the metal and are often applicable only to specific geometries (*e.g.* planar interfaces), it naturally captures the atomic details of the surface and can be applied to any atomic electrode. It can be coupled to any electrolyte and has been used in several studies in the past years with platinum, gold or carbon electrodes and different liquids including molten salts, pure water, aqueous or organic solutions or ionic liquids^{109;160;219–224}.

3.1.1.1 System setup

As in chapter 2, we consider N mobile atoms (ions and molecules) in the electrolyte described by their positions \mathbf{r}^N and momenta \mathbf{p}^N with fixed point charges, and M electrode atoms, with atom-centered charge distributions with fluctuating amplitudes $\mathbf{q} = (q_1, \dots, q_M)$. In practice we use Gaussian charge distributions as given in Eq. 2.2 with fixed width η^{-1} but any distribution centered on the electrode atom with a fluctuating amplitude could be used. In the following, we consider the electrode atoms to be immobile so we can freeze the corresponding degrees of freedom but the following framework can be extended to the case of mobile electrodes.

The Hamiltonian of the system is rewritten as

$$\mathcal{H}(\mathbf{r}^N, \mathbf{p}^N, \mathbf{q}) = \mathcal{K}(\mathbf{p}^N) + \mathcal{U}_{\text{pot}}(\mathbf{r}^N, \mathbf{q}) = \mathcal{K}(\mathbf{p}^N) + \mathcal{U}_0(\mathbf{r}^N) + \mathcal{U}_{\text{fluct}}(\mathbf{r}^N, \mathbf{q}), \quad (3.1)$$

where \mathcal{K} is the kinetic energy of the electrolyte, and we splitted the potential energy \mathcal{U}_{pot} into the electrostatic interaction involving the fluctuating charges $\mathcal{U}_{\text{fluct}}$ and $\mathcal{U}_0(\mathbf{r}^N)$, which contains all other interactions (see section 2.1). From Eq. 2.3, we have that

$$\mathcal{U}_{\text{fluct}}(\mathbf{r}^N, \mathbf{q}) = \frac{\mathbf{q}^T \mathbf{A} \mathbf{q}}{2} - \mathbf{q}^T \mathbf{B}(\mathbf{r}^N), \quad (3.2)$$

so that the electrostatic energy is quadratic in the fluctuating charges. The electrostatic potential on each electrode atom is then equal to the gradient of $\mathcal{U}_{\text{fluct}}$ with respect to \mathbf{q}^T ,

$$\frac{\partial \mathcal{U}_{\text{fluct}}(\mathbf{r}^N, \mathbf{q})}{\partial \mathbf{q}^T} = \mathbf{A} \mathbf{q} - \mathbf{B}(\mathbf{r}^N), \quad (3.3)$$

where \mathbf{A} depends exclusively on the (frozen) positions of the electrode atoms and the charge distribution parameters, and $\mathbf{B}(\mathbf{r}^N)$ also depends on the electrolyte positions.

We split the M electrode atoms into a left (L) and right (R) electrode, with M_L and $M_R = M - M_L$ atoms respectively. For convenience, we take them to be ordered so that

$$\mathbf{q} = \underbrace{(q_1, \dots, q_{M_L})}_{M_L \text{ atoms}}, \underbrace{(q_{M_L+1}, \dots, q_{M_L+M_R})}_{M_R \text{ atoms}}. \quad (3.4)$$

3.1.1.2 Electroneutrality

The aim of the constant potential method is to simulate conducting materials held at a constant potential difference by an external source of energy, *i.e.* a generator, the details of which we do not want to take into account. We therefore study an open system, similarly to the grand-canonical ensemble, where we exchange charge instead of particles with a charge reservoir. It is useful to point out however that to properly separate the electric potential generator from the electrochemical cell, as required in the statistical mechanical derivation, we need to neglect the interactions between them. This implies that both subsystems are electrically neutral to cancel the long-range electrostatic interaction. We will consider the case where no electrochemical reactions occur in the electrolyte system. This leads to the stricter condition that the electrolyte is neutral, and that the total charge of the electrodes vanishes, *i.e.*

$$\sum_{i=1}^M q_i = Q_L + Q_R = 0 \quad \text{or} \quad Q_L = -Q_R, \quad (3.5)$$

where we defined $Q_L = \sum_{i=1}^{M_L} q_i$ and $Q_R = \sum_{i=M_L+1}^{M_L+M_R} q_i$ the total charge of the left and right electrode, respectively. Section 3.1.3.3 will show how the derivation is modified if the electrolyte bears a charge $Q_{\text{electrolyte}}$. While this strict condition of electroneutrality is only true on average for a real system, it needs to be enforced in molecular simulations if the charge reservoir is not included in the description.

3.1.1.3 The constant potential ensemble

We now allow the charge amplitudes \mathbf{q} to fluctuate while fixing the electrostatic potential in the electrodes to a defined value ψ_L and ψ_R for the left and right electrodes respectively, yielding a potential difference or voltage

$$\Delta\psi = \psi_L - \psi_R. \quad (3.6)$$

Each atom is assigned a constant potential ψ_i and we define the vector of constant potentials

$$\Psi^T = \underbrace{(\psi_L, \dots, \psi_L)}_{M_L \text{ atoms}}, \underbrace{(\psi_R, \dots, \psi_R)}_{M_R \text{ atoms}} = \Delta\psi \mathbf{D}^T + \bar{\psi} \mathbf{E}^T, \quad (3.7)$$

where $\bar{\psi}$ is the average potential

$$\bar{\psi} = \frac{M_L \psi_L + M_R \psi_R}{M_L + M_R} \quad (3.8)$$

and we introduced two constant, orthogonal vectors

$$\mathbf{E}^T = \underbrace{(1, \dots, 1)}_{M \text{ atoms}} \quad \text{and} \quad \mathbf{D}^T = \underbrace{(\alpha_L, \dots, \alpha_L)}_{M_L \text{ atoms}}, \underbrace{(\alpha_R, \dots, \alpha_R)}_{M_R \text{ atoms}}, \quad (3.9)$$

with

$$\alpha_L = \frac{M_R}{M_L + M_R} \quad \text{and} \quad \alpha_R = \alpha_L - 1 = -\frac{M_L}{M_L + M_R}. \quad (3.10)$$

For symmetric capacitors, $M_L = M_R$ so that $\alpha_{L/R} = \pm \frac{1}{2}$. Using this notation, the total charge on the electrodes is given by

$$Q_L + Q_R = \mathbf{q}^T \mathbf{E} \quad (3.11)$$

so that the electroneutrality condition of Eq. 3.5 is written

$$\mathbf{q}^T \mathbf{E} = \mathbf{E}^T \mathbf{q} = 0, \quad (3.12)$$

and the charge per electrode is

$$Q_L = -Q_R = \mathbf{q}^T \mathbf{D} = \mathbf{D}^T \mathbf{q}. \quad (3.13)$$

In addition, the work exchanged with the charge reservoir when charging the capacitor from $\mathbf{q} = 0$ to a given charge distribution \mathbf{q} under the constant potentials Ψ is equal to

$$\Psi^T \mathbf{q} = \mathbf{q}^T \Psi = \Delta\psi \mathbf{D}^T \mathbf{q} = Q_L \Delta\psi = -Q_R \Delta\psi. \quad (3.14)$$

3.1.2 Statistical mechanics of the constant potential ensemble

The constant potential ensemble introduces the conjugate variables Ψ to the charge amplitudes \mathbf{q} , thus allowing the charges to fluctuate. This corresponds to a Legendre transform, as introduced in section 2.2.1,

$$F(N, V, T, \Psi) = F(N, V, T, \mathbf{q}) - \mathbf{q}^T \Psi, \quad (3.15)$$

where we used the same notation $F(N, V, T, \Psi)$ to name the thermodynamic potential of the constant potential ensemble. This transformation could be applied to any ensemble seen in section 2.2.1 (NPT , μVT ^{94;95}, Gibbs Ensemble^{225;226}) but is more commonly used with the canonical NVT ensemble^{109;111}, which is the version we develop in the following. Similarly to Eqs. 2.24 and 2.28, the associated partition function has a modified Boltzmann factor that includes the work $\mathbf{q}^T \Psi$ and integrates over all possible configurations $\{\mathbf{r}^N, \mathbf{q}\}$ – we only consider the configurational partition function here. In addition, we select the configurations that satisfy the electroneutrality constraint Eq. 3.12. The (configurational) partition function therefore is given by

$$\begin{aligned} \mathcal{Z} &= \int d\mathbf{r}^N \int d\mathbf{q} e^{-\beta[\mathcal{U}_{\text{pot}}(\mathbf{r}^N, \mathbf{q}) - \mathbf{q}^T \Psi]} \delta(\beta \mathbf{q}^T \mathbf{E}) \\ &= \int d\mathbf{r}^N e^{-\beta \mathcal{U}_0(\mathbf{r}^N)} \int d\mathbf{q} e^{-\beta \left[\frac{\mathbf{q}^T \mathbf{A} \mathbf{q}}{2} - \mathbf{q}^T (\mathbf{B}(\mathbf{r}^N) + \Psi) \right]} \delta(\beta \mathbf{q}^T \mathbf{E}), \end{aligned} \quad (3.16)$$

where $\beta = 1/k_B T$, with k_B Boltzmann's constant, and the Dirac δ function enforces the global electroneutrality constraint. Because the electrostatic energy is quadratic in the charges \mathbf{q} , it is possible to analytically perform the constrained Gaussian integral over \mathbf{q} in Eq. 3.16. We first use the Fourier representation of the Dirac function

$$\delta(\beta \mathbf{q}^T \mathbf{E}) = \frac{1}{2\pi} \int_{-\infty}^{+\infty} dk e^{ik\beta \mathbf{q}^T \mathbf{E}}, \quad (3.17)$$

reverse the order of the integrations over \mathbf{q} and k and use the result for a M -dimensional Gaussian integral with a linear term

$$\int d\mathbf{x} e^{-\frac{1}{2} \mathbf{x}^T \mathbf{M} \mathbf{x} + \mathbf{x}^T \mathbf{N}} = \sqrt{\frac{(2\pi)^M}{\det \mathbf{M}}} e^{\frac{1}{2} \mathbf{N}^T \mathbf{M}^{-1} \mathbf{N}} \quad (3.18)$$

for \mathbf{M} a $M \times M$ symmetric positive-definite matrix. The positive-definitiveness of the matrix \mathbf{A} of electrode-electrode interactions has been discussed in Ref. 227. When it is the case, we can perform the Gaussian integral over \mathbf{q} first

$$\begin{aligned} \mathcal{Z} &= \int d\mathbf{r}^N e^{-\beta\mathcal{U}_0(\mathbf{r}^N)} \frac{1}{2\pi} \int_{-\infty}^{+\infty} dk \int d\mathbf{q} e^{-\beta \left[\frac{\mathbf{q}^T \mathbf{A} \mathbf{q}}{2} - \mathbf{q}^T (\mathbf{B}(\mathbf{r}^N) + \Psi + ik\mathbf{E}) \right]} \\ &= \frac{1}{2\pi} \sqrt{\frac{(2\pi)^M}{\beta^M \det \mathbf{A}}} \int d\mathbf{r}^N e^{-\beta\mathcal{U}_0(\mathbf{r}^N)} e^{+\frac{\beta}{2} [\mathbf{B}(\mathbf{r}^N) + \Psi]^T \mathbf{A}^{-1} [\mathbf{B}(\mathbf{r}^N) + \Psi]} \int_{-\infty}^{+\infty} dk e^{-\frac{\beta}{2} k^2 \mathbf{E}^T \mathbf{A}^{-1} \mathbf{E} + i\beta k \mathbf{E}^T \mathbf{A}^{-1} [\mathbf{B}(\mathbf{r}^N) + \Psi]} . \end{aligned} \quad (3.19)$$

We then perform the Gaussian integral over k as

$$\int_{-\infty}^{+\infty} dk e^{-\alpha k^2 + \gamma k} = \sqrt{\frac{\pi}{\alpha}} \exp \left[\frac{\gamma^2}{4\alpha} \right] \quad (3.20)$$

and finally reorganize the partition function as

$$\mathcal{Z} = \frac{1}{2\pi} \sqrt{\frac{(2\pi)^M}{\beta^M \det \mathbf{A}}} \sqrt{\frac{2\pi}{\beta \mathbf{E}^T \mathbf{A}^{-1} \mathbf{E}}} \int d\mathbf{r}^N e^{-\beta\mathcal{U}_0(\mathbf{r}^N)} e^{+\frac{\beta}{2} [\mathbf{B}(\mathbf{r}^N) + \Psi - \chi(\mathbf{r}^N)\mathbf{E}]^T \mathbf{A}^{-1} [\mathbf{B}(\mathbf{r}^N) + \Psi - \chi(\mathbf{r}^N)\mathbf{E}]} \quad (3.21)$$

where the scalar χ depends on the electrode and electrolyte configurations and the constant potentials as

$$\chi(\mathbf{r}^N) = \frac{1}{\mathbf{E}^T \mathbf{A}^{-1} \mathbf{E}} \mathbf{E}^T \mathbf{A}^{-1} [\mathbf{B}(\mathbf{r}^N) + \Psi] . \quad (3.22)$$

If we had not considered the electroneutrality constraint, *i.e.* if we had not included the $\delta(\beta\mathbf{q}^T \mathbf{E})$ term, the partition function would simply read

$$\mathcal{Z} = \sqrt{\frac{(2\pi)^M}{\beta^M \det \mathbf{A}}} \int d\mathbf{r}^N e^{-\beta\mathcal{U}_0(\mathbf{r}^N)} e^{+\frac{\beta}{2} [\mathbf{B}(\mathbf{r}^N) + \Psi]^T \mathbf{A}^{-1} [\mathbf{B}(\mathbf{r}^N) + \Psi]} . \quad (3.23)$$

Comparing Eqs. 3.21 and 3.23, it appears that $\chi\mathbf{E}$ acts as a potential shift, changing all the potentials Ψ by a constant value to $\Psi - \chi\mathbf{E}$ in order to enforce the electroneutrality constraint. Because it shifts all potential values by the same amount – which however depends on the specific configuration – the voltage, which is really the macroscopic quantity that one can control in experiments, remains unchanged.

3.1.3 Sampling the constant potential ensemble

3.1.3.1 The constant potential constraint

The constant potential ensemble in classical molecular simulations was first introduced by Siepmann and Sprik in Refs. 108 and 109 to study nickel and platinum surfaces in contact with water. They proposed to use Car-Parrinello dynamics, *i.e.* fictitious dynamics of the charge degrees of freedom $\hat{\mathbf{q}}$ that are propagated along the positions and momenta. In this method, coming from *ab initio* molecular dynamics, the electronic degrees of freedom evolve close to the energetic minimum. However, describing the time evolution of the charges requires a careful choice of the effective mass (to ensure energy conservation) and of the timestep, which is usually an order of magnitude smaller than classical MD ones.

Another way of sampling the constant potential ensemble is to use Born-Oppenheimer (BO) dynamics, as done in usual Density Functional Theory MD, and introduced for electrochemical cells with two electrodes by Reed *et al.* in Ref. 111. The BO approximation stems from the very fast electronic

motion with respect to nuclear motion, allowing to consider that the electrons relax instantaneously to the fundamental state. In BO dynamics, the charges \mathbf{q} are thus determined at each timestep using the constant potential constraint

$$\frac{\partial \mathcal{U}_{\text{fluct}}(\mathbf{r}^N, \mathbf{q})}{\partial \mathbf{q}^T} = \Psi . \quad (3.24)$$

Using Eqs. 3.3 and 3.24 without any electroneutrality constraint it follows that the set of charges that satisfy the constant potential constraint is given by

$$\mathbf{A}^{-1} [\mathbf{B}(\mathbf{r}^N) + \Psi] . \quad (3.25)$$

By comparison of Eq. 3.21 with Eq. 3.23, the set of charges \mathbf{q}^* that satisfies both Eq. 3.24 and the global electroneutrality constraint Eq. 3.12 for a given configuration is

$$\mathbf{q}^*(\mathbf{r}^N) = \mathbf{A}^{-1} [\mathbf{B}(\mathbf{r}^N) + \Psi - \chi(\mathbf{r}^N)\mathbf{E}] = \mathbf{S} [\mathbf{B}(\mathbf{r}^N) + \Psi] , \quad (3.26)$$

where we used Eq. 3.22 for the simplification and defined the symmetric matrix

$$\mathbf{S} \equiv \mathbf{A}^{-1} - \frac{\mathbf{A}^{-1}\mathbf{E}\mathbf{E}^T\mathbf{A}^{-1}}{\mathbf{E}^T\mathbf{A}^{-1}\mathbf{E}} . \quad (3.27)$$

We can easily check that the electroneutrality constraint is satisfied by noticing that $\mathbf{S}\mathbf{E} = 0$. This also implies that shifting all the constant potentials by a fixed value ψ_{ref} , *i.e.* changing the reference for the potentials, yields the same set of charges as expected, since $\mathbf{S}[\mathbf{B}(\mathbf{r}^N) + \Psi - \psi_{\text{ref}}\mathbf{E}] = \mathbf{S}[\mathbf{B}(\mathbf{r}^N) + \Psi]$. Using this set of charges in Eq. 3.21, the partition function can be expressed as

$$\begin{aligned} \mathcal{Z} &= \frac{1}{2\pi} \sqrt{\frac{(2\pi)^M}{\beta^M \det \mathbf{A}}} \sqrt{\frac{2\pi}{\beta \mathbf{E}^T \mathbf{A}^{-1} \mathbf{E}}} \int d\mathbf{r}^N e^{-\beta \mathcal{U}_0(\mathbf{r}^N) + \frac{\beta}{2} [\mathbf{B}(\mathbf{r}^N) + \Psi - \chi(\mathbf{r}^N)\mathbf{E}]^T \mathbf{q}^*(\mathbf{r}^N)} \\ &= \frac{1}{2\pi} \sqrt{\frac{(2\pi)^M}{\beta^M \det \mathbf{A}}} \sqrt{\frac{2\pi}{\beta \mathbf{E}^T \mathbf{A}^{-1} \mathbf{E}}} \int d\mathbf{r}^N e^{-\beta \mathcal{U}_0(\mathbf{r}^N) + \frac{\beta}{2} [\mathbf{q}^*(\mathbf{r}^N)]^T \mathbf{A} \mathbf{q}^*(\mathbf{r}^N)} , \end{aligned} \quad (3.28)$$

where we introduced two equivalent expressions of the Boltzmann factor. In the following we use the notation \mathbf{q}^* but one should bear in mind the explicit dependence on the instantaneous electrolyte positions.

The result of Eq. 3.26 can also be seen using the mathematical theory of minimization under constraints and Lagrange multipliers, quickly introduced in section 2.3.2.2 for constrained dynamics. We can revisit the problem of solving Eq. 3.24 by looking for the extremum of the function

$$f(\mathbf{q}) = \mathcal{U}_{\text{fluct}}(\mathbf{r}^N, \mathbf{q}) - \mathbf{q}^T \Psi \quad (3.29)$$

under the constraint of electroneutrality $\mathbf{q}^T \mathbf{E} = 0$. This is done by finding the stationary points of another function

$$\mathcal{L}(\mathbf{q}) = \mathcal{U}_{\text{fluct}}(\mathbf{r}^N, \mathbf{q}) - \mathbf{q}^T \Psi + \chi(\mathbf{r}^N) \mathbf{q}^T \mathbf{E} \quad (3.30)$$

where $\chi(\mathbf{r}^N)$ is the Lagrange multiplier corresponding to the constraint of global electroneutrality. The stationary point of \mathcal{L} is the solution of

$$\frac{\partial \mathcal{L}(\mathbf{q})}{\partial \mathbf{q}} = \mathbf{A} \mathbf{q} - \mathbf{B}(\mathbf{r}^N) - \Psi + \chi(\mathbf{r}^N) \mathbf{E} = 0 , \quad (3.31)$$

and leads to the set of charges \mathbf{q}^* given in Eq. 3.26. In addition, we recognize that the scalar $\chi(\mathbf{r}^N)$ we introduced in Eq. 3.22 is the Lagrange multiplier and we have an explicit expression that depends on the position of the electrode and electrolyte atoms and on the constant potentials applied.

3.1.3.2 Implementation details

The constant potential method has been implemented in various generic simulation packages such as *LAMMPS*^{228–230}, *OpenMM*^{231–233} or *ESPRESSO*^{234;235}. In this work, we used the simulation code *MetalWalls*¹⁵³, developed in the PHENIX Laboratory, which is dedicated to the simulation of electrochemical systems using a constant potential ensemble. It was released publicly during this PhD and is available open-source at <https://gitlab.com/ampere2/metalwalls>. Many new developments were realized in the code during this work and some technical details are given in appendix B.

In practice, there are several ways of implementing the BO dynamics described in the previous section. A first method is to directly perform the matrix inversion \mathbf{A}^{-1} and to compute the set of charges \mathbf{q}^* at each timestep by performing the matrix multiplication in Eq. 3.26. This method can be very efficient if the electrodes are immobile because one can compute the matrix \mathbf{S} once and use linear algebra packages to multiply it by the vector $\mathbf{B}(\mathbf{r}^N) + \Psi$. However if the electrodes are mobile, or at least translate rigidly, the matrix inversion has to be done at each timestep, which is not efficient. Another limitation occurs for very large systems where, depending on the parallelization procedure, storing the $M \times M$ matrix produces memory errors.

Alternatively, one can use constrained conjugate gradient²³⁶ minimization methods to solve the Lagrangian equation Eq. 3.31. This method, because it does not require the matrix inversion, is more efficient for mobile and even flexible electrodes.

Lastly, a new method based on constrained dynamics similar to the SHAKE algorithm (see section 2.3.2.2) was developed recently and introduced in *MetalWalls*²³⁷.

3.1.3.3 Non-neutral electrolytes

In the previous derivation, we used the electroneutrality constraint introduced in section 3.1.1.2. In the case of a neutral electrolyte, this implies that the electrodes are neutral, which corresponds to Eq. 3.12. In order to have electrochemical reactions with the electrodes, we need to be able to exchange charge between the electrodes and the electrolyte. The global electroneutrality condition then reads

$$\mathbf{q}^T \mathbf{E} = -Q_{\text{electrolyte}}, \quad (3.32)$$

where $Q_{\text{electrolyte}}$ is the charge of the electrolyte. The separation between Q_L and Q_R (Eqs. 3.13) is then unknown and we should introduce left and right capacitances of single electrodes. The definition of the partition function Eq. 3.16 is then slightly modified

$$\begin{aligned} \mathcal{Z} &= \int d\mathbf{r}^N e^{-\beta \mathcal{U}_0(\mathbf{r}^N)} \int d\mathbf{q} e^{-\beta \left[\frac{\mathbf{q}^T \mathbf{A} \mathbf{q}}{2} - \mathbf{q}^T (\mathbf{B}(\mathbf{r}^N) + \Psi) \right]} \delta(\beta \mathbf{q}^T \mathbf{E} + \beta Q_{\text{electrolyte}}) \\ &= \frac{1}{2\pi} \sqrt{\frac{(2\pi)^M}{\beta^M \det \mathbf{A}}} \sqrt{\frac{2\pi}{\beta \mathbf{E}^T \mathbf{A}^{-1} \mathbf{E}}} \int d\mathbf{r}^N e^{-\beta \mathcal{U}_0(\mathbf{r}^N)} e^{+\frac{\beta}{2} [\mathbf{B}(\mathbf{r}^N) + \Psi - \chi'(\mathbf{r}^N) \mathbf{E}]^T \mathbf{A}^{-1} [\mathbf{B}(\mathbf{r}^N) + \Psi - \chi'(\mathbf{r}^N) \mathbf{E}]}, \end{aligned} \quad (3.33)$$

which reduces to Eq. 3.21 by defining a modified Lagrange multiplier

$$\chi'(\mathbf{r}^N) = \frac{1}{\mathbf{E}^T \mathbf{A}^{-1} \mathbf{E}} (\mathbf{E}^T \mathbf{A}^{-1} [\mathbf{B}(\mathbf{r}^N) + \Psi] + Q_{\text{electrolyte}}) = \chi(\mathbf{r}^N) + \frac{Q_{\text{electrolyte}}}{\mathbf{E}^T \mathbf{A}^{-1} \mathbf{E}}. \quad (3.34)$$

The set of charges that satisfy the constant potential constraint subjected to the global electroneutrality constraint is now given by

$$\mathbf{q}^*(\mathbf{r}^N) = \mathbf{A}^{-1} [\mathbf{B}(\mathbf{r}^N) + \Psi - \chi'(\mathbf{r}^N) \mathbf{E}] = \mathbf{S} [\mathbf{B}(\mathbf{r}^N) + \Psi] - \frac{\mathbf{A}^{-1} \mathbf{E} Q_{\text{electrolyte}}}{\mathbf{E}^T \mathbf{A}^{-1} \mathbf{E}}, \quad (3.35)$$

where \mathbf{S} was defined in Eq. 3.27. Using these charges we obtain again Eq. 3.28.

3.1.4 Born Oppenheimer sampling

We saw in the previous sections that current implementations of the constant potential ensemble use BO dynamics to sample the ensemble. We show in the following that this sampling does not reproduce exactly the constant potential ensemble probability distribution because it suppresses the thermal fluctuations of the charge around its optimum, so that depending on the observable, a correction may be needed to obtain the correct ensemble average.

First we modify Eq. 3.16 by restricting the integral over the charges \mathbf{q} to the BO charges \mathbf{q}^* . This corresponds to the BO partition function \mathcal{Z}^{BO} defined as

$$\mathcal{Z}^{BO} = \int d\mathbf{r}^N e^{-\beta \left[\mathcal{U}_0(\mathbf{r}^N) + \frac{(\mathbf{q}^*)^T \mathbf{A} \mathbf{q}^*}{2} - (\mathbf{q}^*)^T (\mathbf{B}(\mathbf{r}^N) + \Psi) \right]} = \int d\mathbf{r}^N e^{-\beta \mathcal{U}_0(\mathbf{r}^N) + \frac{\beta}{2} (\mathbf{q}^*)^T \mathbf{A} \mathbf{q}^*}, \quad (3.36)$$

where we simplified the Boltzmann factor using Eq. 3.26 and the electroneutrality $(\mathbf{q}^*)^T \mathbf{E} = 0$. Using Eq. 3.28, the probability of finding a given microscopic configuration $\{\mathbf{r}^N, \mathbf{q}\}$ is then expressed as

$$\mathcal{P}(\mathbf{r}^N, \mathbf{q}) = \frac{e^{-\beta \left[\mathcal{U}_0(\mathbf{r}^N) + \frac{\mathbf{q}^T \mathbf{A} \mathbf{q}}{2} - \mathbf{q}^T (\mathbf{B}(\mathbf{r}^N) + \Psi) \right]} \delta(\beta \mathbf{q}^T \mathbf{E})}{\frac{1}{2\pi} \sqrt{\frac{(2\pi)^M}{\beta^M \det \mathbf{A}}} \sqrt{\frac{2\pi}{\beta \mathbf{E}^T \mathbf{A}^{-1} \mathbf{E}}} \int d\mathbf{r}^N e^{-\beta \mathcal{U}_0(\mathbf{r}^N) + \frac{\beta}{2} (\mathbf{q}^*)^T \mathbf{A} \mathbf{q}^*}} \quad (3.37)$$

$$\mathcal{P}^{BO}(\mathbf{r}^N) = \frac{e^{-\beta \mathcal{U}_0(\mathbf{r}^N) + \frac{\beta}{2} (\mathbf{q}^*)^T \mathbf{A} \mathbf{q}^*}}{\int d\mathbf{r}^N e^{-\beta \mathcal{U}_0(\mathbf{r}^N) + \frac{\beta}{2} (\mathbf{q}^*)^T \mathbf{A} \mathbf{q}^*}} \quad (3.38)$$

for the real and the BO ensembles respectively. We highlight that the probability distribution \mathcal{P}^{BO} only depends on the positions \mathbf{r}^N and not the charges because the electronic degrees of freedom are entirely controlled by the electrolyte configuration. From Eqs. 3.37 and 3.38, the probability distributions in the two ensembles are related through

$$\mathcal{P}(\mathbf{r}^N, \mathbf{q}) = \mathcal{P}^{BO}(\mathbf{r}^N) \times 2\pi \sqrt{\frac{\beta^M \det \mathbf{A}}{(2\pi)^M}} \sqrt{\frac{\beta \mathbf{E}^T \mathbf{A}^{-1} \mathbf{E}}{2\pi}} \delta(\beta \mathbf{q}^T \mathbf{E}) \exp \left[-\frac{\beta}{2} (\mathbf{q} - \mathbf{q}^*)^T \mathbf{A} (\mathbf{q} - \mathbf{q}^*) \right]. \quad (3.39)$$

The full probability distribution is thus different from that in the BO ensemble sampled by standard molecular simulations schemes from the constant potential ensemble. In principle, the ensemble averages computed from these BO simulations may not correspond to the correct ensemble, but we will show this is not so dramatic. To study this in detail, we write the probability distribution of an observable \mathcal{O} given by

$$p(\mathcal{O}) = \int d\mathbf{r}^N \int d\mathbf{q} \mathcal{P}(\mathbf{r}^N, \mathbf{q}) \delta(\mathcal{O}(\mathbf{r}^N, \mathbf{q}) - \mathcal{O}) \quad (3.40)$$

$$p(\mathcal{O}) = 2\pi \sqrt{\frac{\beta^M \det \mathbf{A}}{(2\pi)^M}} \sqrt{\frac{\beta \mathbf{E}^T \mathbf{A}^{-1} \mathbf{E}}{2\pi}} \int d\mathbf{r}^N \mathcal{P}^{BO}(\mathbf{r}^N) \int d\mathbf{q} e^{-\frac{\beta}{2} (\mathbf{q} - \mathbf{q}^*)^T \mathbf{A} (\mathbf{q} - \mathbf{q}^*)} \delta(\beta \mathbf{q}^T \mathbf{E}) \delta(\mathcal{O}(\mathbf{r}^N, \mathbf{q}) - \mathcal{O}). \quad (3.41)$$

In the case of observables that only depend on the positions \mathbf{r}^N and not the charge degrees of freedom, *i.e.* $\mathcal{O}(\mathbf{r}^N, \mathbf{q}) = \mathcal{O}(\mathbf{r}^N)$, the Dirac function $\delta(\mathcal{O}(\mathbf{r}^N) - \mathcal{O})$ can be removed from the integral over \mathbf{q} which can then be treated as in section 3.1.2. This results into

$$\text{for } \mathcal{O}(\mathbf{r}^N, \mathbf{q}) = \mathcal{O}(\mathbf{r}^N) : \quad p(\mathcal{O}) = p^{BO}(\mathcal{O}), \quad (3.42)$$

which means that charge-independent quantities, *i.e.* any structural property, are correctly sampled by the BO dynamics.

For observables that depend on the charges, we can perform a Taylor expansion

$$\mathcal{O}(\mathbf{r}^N, \mathbf{q}) = \mathcal{O}^*(\mathbf{r}^N) + (\mathbf{q} - \mathbf{q}^*)^T \nabla_{\mathbf{q}} \mathcal{O}|_{\mathbf{q}^*}(\mathbf{r}^N) + \frac{1}{2} (\mathbf{q} - \mathbf{q}^*)^T \nabla_{\mathbf{q}}^2 \mathcal{O}|_{\mathbf{q}^*}(\mathbf{r}^N) (\mathbf{q} - \mathbf{q}^*) + \dots \quad (3.43)$$

where $\mathcal{O}^*(\mathbf{r}^N) = \mathcal{O}(\mathbf{r}^N, \mathbf{q}^*)$ is the observable for the values $\mathbf{q} = \mathbf{q}^*$. We consider the case where only the zeroth and first orders are non zero, *i.e.*

$$\mathcal{O}(\mathbf{r}^N, \mathbf{q}) = \mathcal{O}^*(\mathbf{r}^N) + (\mathbf{q} - \mathbf{q}^*)^T \mathbf{G}^*(\mathbf{r}^N), \quad (3.44)$$

where we define $\mathbf{G}^*(\mathbf{r}^N) = \nabla_{\mathbf{q}} \mathcal{O}|_{\mathbf{q}^*}$ the gradient of \mathcal{O} with respect to the charges taken at $\mathbf{q} = \mathbf{q}^*$. This kind of observable corresponds to any linear combination of the charges or can be an approximation to first order of a more complex observable. We then express Eq. 3.41 in this linearly dependent case. We start by introducing the Fourier representations of the Dirac functions (see Eq. 3.17), which is for the second Dirac function

$$\delta(\mathcal{O}(\mathbf{r}^N, \mathbf{q}) - \mathcal{O}) = \frac{1}{2\pi} \int_{-\infty}^{+\infty} dm e^{im(\mathcal{O}^*(\mathbf{r}^N) - \mathcal{O} + (\mathbf{q} - \mathbf{q}^*)^T \mathbf{G}^*(\mathbf{r}^N))}. \quad (3.45)$$

As done in section 3.1.2, we then reverse the integrals over k , m and \mathbf{q} and carry out the Gaussian integrals which eventually results in

$$p(\mathcal{O}) = \int d\mathbf{r}^N \mathcal{P}^{\text{BO}}(\mathbf{r}^N) \sqrt{\frac{\beta}{2\pi[\mathbf{G}^*(\mathbf{r}^N)]^T \mathbf{S} \mathbf{G}^*(\mathbf{r}^N)}} \exp \left[-\frac{\beta}{2} \frac{[\mathcal{O}^*(\mathbf{r}^N) - \mathcal{O}]^2}{[\mathbf{G}^*(\mathbf{r}^N)]^T \mathbf{S} \mathbf{G}^*(\mathbf{r}^N)} \right]. \quad (3.46)$$

By comparing to Eq. 3.40, the Dirac delta function $\delta(\mathcal{O}(\mathbf{r}^N, \mathbf{q}) - \mathcal{O})$ is replaced by a Gaussian distribution centered on $\mathcal{O}^*(\mathbf{r}^N)$ with a variance $\beta^{-1}[\mathbf{G}^*(\mathbf{r}^N)]^T \mathbf{S} \mathbf{G}^*(\mathbf{r}^N)$. By simply averaging in the BO ensemble, *i.e.* using $p^{\text{BO}}(\mathcal{O}) = \int d\mathbf{r}^N \mathcal{P}^{\text{BO}}(\mathbf{r}^N) \delta(\mathcal{O}^*(\mathbf{r}^N) - \mathcal{O})$, we neglect these Gaussian fluctuations around $\mathcal{O}^*(\mathbf{r}^N)$ which correspond to the fluctuations of the charge degrees of freedom suppressed by relaxing them at each timestep. This result not only has consequences in the calculation of electrochemical properties, as we will show in the next section, but should be taken into consideration every time one computes ensemble averages using a sampling procedure that alters the statistical distribution of the given observable.

3.1.5 The calculation of charge and capacitance

3.1.5.1 Average and fluctuations of the total charge

Average charge and integral capacitance An exemple of electrical property that is routinely computed in constant potential simulations is the total charge on the electrodes, which can be written in the form of Eq. 3.44 as

$$Q_L(\mathbf{r}^N) = \mathbf{q}^T \mathbf{D} = Q_L^*(\mathbf{r}^N) + (\mathbf{q} - \mathbf{q}^*)^T \mathbf{D} \quad (3.47)$$

where the gradient $\mathbf{G}^*(\mathbf{r}^N) = \mathbf{D}$ is independent of the electrolyte positions \mathbf{r}^N . The integral capacitance C_{int} , defined in Eq. 2.58, is given by the average of the total charge divided by the applied voltage. Using Eq. 3.46, the average of Q_L in the constant potential ensemble can be computed by directly performing the Gaussian integral as

$$\begin{aligned} \langle Q_L \rangle_{\mathbf{r}^N, \mathbf{q}} &= \int dQ_L p(Q_L) Q_L \\ &= \int d\mathbf{r}^N \mathcal{P}^{\text{BO}}(\mathbf{r}^N) \sqrt{\frac{\beta}{2\pi \mathbf{D}^T \mathbf{S} \mathbf{D}}} \int dQ_L Q_L e^{-\frac{\beta}{2} \frac{(Q_L^* - Q_L)^2}{\mathbf{D}^T \mathbf{S} \mathbf{D}}} \\ &= \int d\mathbf{r}^N \mathcal{P}^{\text{BO}}(\mathbf{r}^N) Q_L^*(\mathbf{r}^N) \\ \langle Q_L \rangle_{\mathbf{r}^N, \mathbf{q}} &= \langle Q_L^* \rangle_{\mathbf{r}^N}^{\text{BO}}. \end{aligned} \quad (3.48)$$

Because the suppressed Gaussian fluctuations are normalized and centered on Q_L^* , the averages in both ensembles coincide so that no correction is needed and correct integral capacitance values are obtained using BO sampling.

Charge fluctuations and differential capacitance We now turn to the differential capacitance, defined in Eq. 2.59, as the derivative of the average total charge with respect to the voltage,

$$C_{\text{diff}} = \frac{\partial \langle Q_L \rangle_{\mathbf{r}^N, \mathbf{q}}}{\partial \Delta\psi}. \quad (3.49)$$

This capacitance can be computed by numerically taking the derivative after computing the average charge at different applied voltages. Alternatively, we use Eqs. 2.33 to evaluate the derivative in Eq. 3.49 using derivatives of the free energy $F = -\beta^{-1} \ln \mathcal{Z}$. Indeed, from the definition of the partition function Eq. 3.16 and with Eq. 3.14 we have

$$\begin{aligned} \frac{\partial F}{\partial \Delta\psi} &= -\frac{1}{\beta} \frac{\partial \ln \mathcal{Z}}{\partial \Delta\psi} = -\frac{1}{\beta \mathcal{Z}} \int d\mathbf{r}^N e^{-\beta \mathcal{U}_0(\mathbf{r}^N)} \int d\mathbf{q} (\beta \mathbf{q}^T \mathbf{D}) e^{-\beta \left[\frac{\mathbf{q}^T \mathbf{A} \mathbf{q}}{2} - \mathbf{q}^T (\mathbf{B}(\mathbf{r}^N) + \Psi) \right]} \delta(\beta \mathbf{q}^T \mathbf{E}) \\ &= -\langle \mathbf{q}^T \mathbf{D} \rangle_{\mathbf{r}^N, \mathbf{q}} = -\langle Q_L \rangle_{\mathbf{r}^N, \mathbf{q}}, \end{aligned} \quad (3.50)$$

where the average is over all microscopic configurations of the constant-potential ensemble. As a side note, we find that the free energy difference due to the charge of the capacitor from zero to a finite voltage $\Delta\psi_{\text{max}}$ is given by

$$\Delta F = -\int_0^{\Delta\psi_{\text{max}}} \langle Q_L \rangle_{\mathbf{r}^N, \mathbf{q}} d\Delta\psi = \int_0^{\Delta\psi_{\text{max}}} \langle Q_R \rangle_{\mathbf{r}^N, \mathbf{q}} d\Delta\psi, \quad (3.51)$$

which is as expected the reversible work exchanged with the charge reservoir.

The differential capacitance is then obtained from the second derivative of the free energy F

$$C_{\text{diff}} = -\frac{\partial^2 F}{\partial \Delta\psi^2} = \frac{\partial \langle Q_L \rangle_{\mathbf{r}^N, \mathbf{q}}}{\partial \Delta\psi} = \beta \langle Q_L^2 \rangle_{\mathbf{r}^N, \mathbf{q}} - \beta \langle Q_L \rangle_{\mathbf{r}^N, \mathbf{q}}^2 = \beta \langle \delta Q_L^2 \rangle_{\mathbf{r}^N, \mathbf{q}}, \quad (3.52)$$

where we used Eq. 2.30 to introduce the charge fluctuations $\langle \delta Q_L^2 \rangle$ with $\delta Q_L = Q_L - \langle Q_L \rangle_{\mathbf{r}^N, \mathbf{q}}$. C_{diff} can thus be computed by sampling the fluctuations of the total charge on the positive electrode in the constant potential ensemble. We have already shown that the average value $\langle Q_L \rangle_{\mathbf{r}^N, \mathbf{q}}$ is correctly sampled by the BO dynamics. Is this also the case for the second moment of the charge distribution $\langle Q_L^2 \rangle_{\mathbf{r}^N, \mathbf{q}}$? Using Eq. 3.46 and the fact that for a Gaussian distribution the average of Q_L^2 is the sum of the squared mean and the variance of the distribution, we obtain

$$\langle Q_L^2 \rangle_{\mathbf{r}^N, \mathbf{q}} = \langle Q_L^{*2} \rangle_{\mathbf{r}^N}^{BO} + \beta^{-1} \langle \mathbf{D}^T \mathbf{S} \mathbf{D} \rangle_{\mathbf{r}^N}^{BO} = \langle Q_L^{*2} \rangle_{\mathbf{r}^N}^{BO} + \beta^{-1} \mathbf{D}^T \mathbf{S} \mathbf{D}, \quad (3.53)$$

where we noticed that $\mathbf{D}^T \mathbf{S} \mathbf{D}$ does not depend on the electrolyte configuration \mathbf{r}^N . This shows that although the average value of Q_L is sampled correctly by BO dynamics, its average squared value, which is related to the fluctuations of Q_L , lacks a term coming from the suppressed charge fluctuations around the set of charges \mathbf{q}^* . The present framework highlights this contribution and gives the tools to compute it analytically. For the differential capacitance, a correction can be derived using Eq. 3.48 and 3.53 as

$$\begin{aligned} C_{\text{diff}} &= \beta \langle Q_L^2 \rangle_{\mathbf{r}^N, \mathbf{q}} - \beta \langle Q_L \rangle_{\mathbf{r}^N, \mathbf{q}}^2 = \beta \langle Q_L^{*2} \rangle_{\mathbf{r}^N}^{BO} + \mathbf{D}^T \mathbf{S} \mathbf{D} - \beta \left(\langle Q_L^* \rangle_{\mathbf{r}^N}^{BO} \right)^2 \\ C_{\text{diff}} &= \beta \langle \delta Q_L^{*2} \rangle_{\mathbf{r}^N}^{BO} + \mathbf{D}^T \mathbf{S} \mathbf{D}. \end{aligned} \quad (3.54)$$

This result is of practical importance since it allows to compute the correct differential capacitance as the sum of the contribution from charge fluctuations in the BO sampling and an extra capacitance term, which arises from the thermal fluctuations that the BO sampling neglects by relaxing the electronic degrees of freedom at each step.

The fluctuation-dissipation relation Eq. 3.52 had already been identified by Nyquist and Johnson^{238;239} and applied to constant-potential Monte Carlo simulations⁹⁴ and constant-potential classical^{65;155;161} and *ab initio*²⁴⁰ molecular dynamics. In the particular case of fluctuating charge simulations, Ref.

161 pioneered the use of histogram reweighting techniques to sample charge fluctuations at different voltages, and of Eq. 3.52 to efficiently sample the differential capacitance using simulations at a single voltage. These studies however did not take into account the impact of the BO sampling and lacked the correction term in Eq. 3.54. The additional contribution was later pointed out by Haskins and Lawson¹⁵⁵ as $\langle \partial Q_L / \partial \Delta \psi \rangle$, and interpreted as “the self-capacitance of the electrodes under the influence of the electrolyte structure”, which they found to be small (though non-negligible) and relatively insensitive to the value of voltage for the considered systems.

With the present derivation, we further have an analytical expression for the additional term, which shows it does not depend on the electrolyte configurations nor on voltage, so that it is no longer an ensemble average and can be computed directly by performing the matrix multiplication $\mathbf{D}^T \mathbf{S} \mathbf{D}$. We thus understood that the BO ensemble samples only the fluctuations of the total charge due to the thermal fluctuations in electrolyte positions \mathbf{r}^N , from which we define an electrolyte contribution to the capacitance

$$C_{\text{diff}}^{\text{electrolyte}} = \beta \left[\langle Q_L^{*2} \rangle_{\mathbf{r}^N}^{BO} - \left(\langle Q_L^* \rangle_{\mathbf{r}^N}^{BO} \right)^2 \right] = \beta \langle \delta Q_L^{*2} \rangle_{\mathbf{r}^N}^{BO}. \quad (3.55)$$

Because in the absence of an electrolyte these fluctuations vanish, the correction term can further be interpreted as the capacitance of the empty capacitor

$$C_{\text{diff}}^{\text{empty}} = \mathbf{D}^T \mathbf{S} \mathbf{D}, \quad (3.56)$$

which combines additively with the electrolyte contribution (this corresponds to an equivalent circuit of capacitors in parallel).

Alternative derivation Eq. 3.54 can also be obtained starting directly from the BO partition function Eq. 3.36

$$C_{\text{diff}} = \frac{\partial \langle Q_L \rangle_{\mathbf{r}^N, \mathbf{q}}}{\partial \Delta \psi} = \frac{\partial \langle Q_L^* \rangle_{\mathbf{r}^N}^{BO}}{\partial \Delta \psi} = \frac{\partial}{\partial \Delta \psi} \left[\frac{1}{\mathcal{Z}^{BO}} \int d\mathbf{r}^N Q_L^* e^{-\beta \mathcal{U}_0(\mathbf{r}^N) + \frac{\beta}{2} (\mathbf{q}^*)^T \mathbf{A} \mathbf{q}^*} \right] \quad (3.57)$$

Using the definitions Eqs. 3.26, 3.7, 3.13 and the electroneutrality constraint 3.12 we have

$$\frac{\partial \mathbf{q}^*}{\partial \Delta \psi} = \mathbf{S} \mathbf{D} \quad (3.58)$$

$$\frac{1}{2} \frac{\partial (\mathbf{q}^*)^T \mathbf{A} \mathbf{q}^*}{\partial \Delta \psi} = (\mathbf{q}^*)^T \mathbf{D} = Q_L^* \quad (3.59)$$

and performing the derivatives we obtain

$$C_{\text{diff}} = \beta \langle \delta Q_L^{*2} \rangle_{\mathbf{r}^N}^{BO} + \left\langle \frac{\partial Q_L^*}{\partial \Delta \psi} \right\rangle_{\mathbf{r}^N}^{BO} \quad (3.60)$$

similarly to Haskins and Lawson in Ref. 155. We recover that the extra capacitance is expressed as

$$\left\langle \frac{\partial Q_L^*}{\partial \Delta \psi} \right\rangle_{\mathbf{r}^N}^{BO} = \left\langle \mathbf{D}^T \frac{\partial \mathbf{q}^*(\mathbf{r}^N)}{\partial \Delta \psi} \right\rangle_{\mathbf{r}^N}^{BO} = \langle \mathbf{D}^T \mathbf{S} \mathbf{D} \rangle_{\mathbf{r}^N}^{BO} = \mathbf{D}^T \mathbf{S} \mathbf{D}, \quad (3.61)$$

and further interpret this correction term as the average response of the electrode to the voltage for each microscopic configuration of the electrolyte.

Block decomposition To further analyze the term $\mathbf{D}^T \mathbf{S} \mathbf{D}$, using Eq. 3.27, we develop it as

$$\mathbf{D}^T \mathbf{S} \mathbf{D} = \mathbf{D}^T \mathbf{A}^{-1} \mathbf{D} - \frac{(\mathbf{E}^T \mathbf{A}^{-1} \mathbf{D})^2}{\mathbf{E}^T \mathbf{A}^{-1} \mathbf{E}}. \quad (3.62)$$

and introduce a block decomposition of the inverse matrix \mathbf{A}^{-1} as

$$\mathbf{A}^{-1} = \left(\begin{array}{c|c} (\mathbf{A}^{-1})_{LL} & (\mathbf{A}^{-1})_{LR} \\ \hline (\mathbf{A}^{-1})_{RL} & (\mathbf{A}^{-1})_{RR} \end{array} \right) \quad (3.63)$$

where the diagonal blocks are of size $M_L \times M_L$ and $M_R \times M_R$ and the off-diagonal blocks of size $M_L \times M_R$ and $M_R \times M_L$. Using $b_{ij} = (\mathbf{A}^{-1})_{ij}$ the components of \mathbf{A}^{-1} and the definitions of \mathbf{E} and \mathbf{D} in Eqs. 3.9, we can express

$$\begin{aligned} \mathbf{D}^T \mathbf{A}^{-1} \mathbf{D} &= \sum_{i=1}^M \sum_{j=1}^M b_{ij} \alpha_i \alpha_j = \alpha_L^2 \sum_{i=1}^{M_L} \sum_{j=1}^{M_L} b_{ij} + \alpha_R^2 \sum_{i=M_L+1}^{M_L+M_R} \sum_{j=M_L+1}^{M_L+M_R} b_{ij} + 2\alpha_L \alpha_R \sum_{i=1}^{M_L} \sum_{j=M_L+1}^{M_L+M_R} b_{ij} \\ &= \alpha_L^2 \Sigma_{LL} + \alpha_R^2 \Sigma_{RR} + 2\alpha_L \alpha_R \Sigma_{LR}, \end{aligned} \quad (3.64)$$

where we defined Σ_{LL} , Σ_{RR} and Σ_{LR} the sums of the elements of the blocks defined in Eq. 3.63. Similarly we have

$$\mathbf{E}^T \mathbf{A}^{-1} \mathbf{D} = \sum_{i=1}^M \sum_{j=1}^M b_{ij} \alpha_j = \alpha_L (\Sigma_{LL} + \Sigma_{LR}) + \alpha_R (\Sigma_{RR} + \Sigma_{LR}), \quad (3.65)$$

and

$$\mathbf{E}^T \mathbf{A}^{-1} \mathbf{E} = \sum_{i=1}^M \sum_{j=1}^M b_{ij} = \Sigma_{LL} + \Sigma_{RR} + 2\Sigma_{LR}. \quad (3.66)$$

Using the definition of α_L and α_R in Eqs. 3.10 and inserting Eqs. 3.64, 3.65 and 3.66 into Eq. 3.62, we find that the extra capacitance corresponding to the empty capacitor is given by

$$C_{\text{diff}}^{\text{empty}} = \mathbf{D}^T \mathbf{S} \mathbf{D} = \frac{\Sigma_{LL} \Sigma_{RR} - \Sigma_{LR}^2}{\Sigma_{LL} + \Sigma_{RR} + 2\Sigma_{LR}}. \quad (3.67)$$

In the case of symmetric electrodes, $\alpha_L = -\alpha_R = 1/2$ and $\Sigma_{LL} = \Sigma_{RR}$, so that we can further simplify the expression as $\mathbf{D}^T \mathbf{S} \mathbf{D} = \mathbf{D}^T \mathbf{A}^{-1} \mathbf{D} = (\Sigma_{LL} - \Sigma_{LR})/2$.

Application to a parallel plate capacitor Computing this matrix multiplication analytically is impossible for a large number of atoms, such as the systems simulated in this work. However, by considering two infinitely thin disk-shaped electrodes for which we have an analytical expression of the electrostatic energy in Ref 241, we can perform the calculation explicitly. Indeed, for two disks of radii R facing each other at a distance L bearing each a charge Q_1 and Q_2 respectively, the electrostatic energy is

$$U_{el} = \frac{1}{2} \left(\frac{4Q_1^2}{3\pi^2 \epsilon_0 R} + \frac{4Q_2^2}{3\pi^2 \epsilon_0 R} + 2 \frac{Q_1 Q_2}{\pi \epsilon_0 R} f\left(\frac{L}{R}\right) \right) \quad (3.68)$$

where we introduced the function $f(x)$ as an integral of the Bessel function J_1

$$f(x) = \int_0^{+\infty} du \left(\frac{J_1(u)}{u} \right)^2 e^{-xu} \underset{x \rightarrow 0}{\approx} \frac{4}{3\pi} - \frac{x}{2}, \quad (3.69)$$

where the second equality is the first order Taylor expansion of f . The matrix of electrode-electrode interactions $\mathbf{A} = \nabla_Q \nabla_Q \mathcal{U}_{el}$ and its inverse can then simply be computed as

$$\mathbf{A} = \begin{pmatrix} \frac{4}{3\pi^2 \epsilon_0 R} & \frac{1}{\pi \epsilon_0 R} f\left(\frac{L}{R}\right) \\ \frac{1}{\pi \epsilon_0 R} f\left(\frac{L}{R}\right) & \frac{4}{3\pi^2 \epsilon_0 R} \end{pmatrix} \quad \text{and} \quad \mathbf{A}^{-1} = \frac{1}{\det \mathbf{A}} \begin{pmatrix} \frac{4}{3\pi^2 \epsilon_0 R} & \frac{-1}{\pi \epsilon_0 R} f\left(\frac{L}{R}\right) \\ \frac{-1}{\pi \epsilon_0 R} f\left(\frac{L}{R}\right) & \frac{4}{3\pi^2 \epsilon_0 R} \end{pmatrix} \quad (3.70)$$

This in turn allows to compute the correction term as

$$C_{\text{diff}}^{\text{empty}} = \mathbf{D}^T \mathbf{S} \mathbf{D} = \frac{\pi R^2 \epsilon_0}{\frac{8R}{3\pi} - 2Rf\left(\frac{L}{R}\right)} \underset{\frac{L}{R} \rightarrow 0}{\approx} \frac{\pi R^2 \epsilon_0}{L}. \quad (3.71)$$

This means that, for $\frac{L}{R} \rightarrow 0$, *i.e.* two disks of infinite radius R , we recover the analytical result for the capacitance per unit surface of a parallel plate capacitor ϵ_0/L . This supports the interpretation of the extra capacitance $\mathbf{D}^T \mathbf{S} \mathbf{D}$ as the capacitance of the corresponding empty capacitor.

3.1.5.2 Numerical results

Comparison with empty capacitors To further confirm the interpretation of the correction term being the differential capacitance for an empty capacitor, *i.e.* without any electrolyte, we computed $C_{\text{diff}}^{\text{empty}}$ using its definition Eq. 3.49 from several simulations of empty capacitors with applied voltages $\Delta\psi$ ranging from 0.0 to 20.0 V. Figure 3.1 shows for graphitic and gold capacitors (systems (G1) and (Au1) in table 2.1) that the total charge per unit surface Q_L/\mathcal{A} is linearly dependent on $\Delta\psi$, as expected. We extract the differential capacitance from the slope, which is independent of the voltage and is equal to the integral capacitance. The prediction for $C_{\text{diff}}^{\text{empty}}$ was also computed from Eq. 3.56 by directly computing the interaction matrix \mathbf{A} from the positions of the electrode atoms and the width of the Gaussian charge distributions and performing the matrix multiplication. It coincides perfectly with the values extracted from the charges as can be seen from the solid lines in figure 3.1.

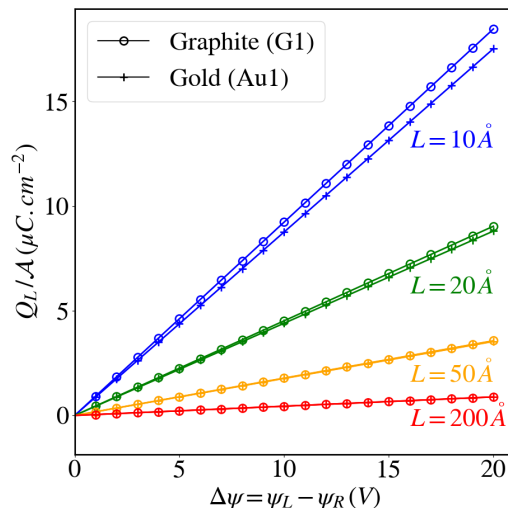


Figure 3.1: Charge of the left electrode Q_L as a function of the applied voltage $\Delta\psi = \psi_L - \psi_R$, for two empty graphite or gold capacitors (systems (G1) and (Au1) in table 2.1). Results are shown for selected distances L between the first atomic planes of the electrodes, ranging from 10.0 to 200.0 Å. The symbols (\circ for graphite, $+$ for gold) are the charge per unit surface determined numerically for various applied voltages between 0.0 and 20.0 V, while the solid lines are the predictions of Eq. 3.56. Adapted from Ref. 218 with permission from the PCCP Owner Societies.

Different capacitors with a variable distance L between electrodes ranging from 10 to 200 Å were studied to compare to the continuum prediction of the capacitance per unit area for a parallel plate capacitor ϵ_0/L . The comparison is shown in figure 3.2a: the numerical results from the slope $Q_L/\Delta\psi$ and from Eq. 3.56 agree within computer precision and are close to the continuum prediction (dashed line $y = x$) down to small distances. The relative error with respect to the continuum prediction is given in figure 3.2b. It is smaller than 1% for most capacitors and decreases with increasing L . For the smallest distance $L = 10$ Å, which is not so large with respect to the interplanar distance (around 2 or 3 Å) and the interatomic distances, the molecular details of the surface come into play, as seen by the deviation between gold and graphite electrodes in figure 3.1. However, the agreement with the continuum formula ϵ_0/L is surprisingly good since the relative error is smaller than 5% even in this

case. To compute ϵ_0/L we used the distance L between first atomic planes but in fact the results are best described using an effective length $L_{\text{eff}} = L - 2d$, with $d = 0.2 \text{ \AA}$ which is comparable to half the Gaussian width $\eta^{-1} = 0.55 \text{ \AA}$, with relative errors (shown in orange circles and cyan crosses in figure 3.2b) smaller than 0.1% for all capacitors. This effective intra-electrode distance can be seen as accounting for the spilling of the electrons within the electrolyte on a characteristic length d . A more detailed comparison will be discussed in section 4.2.2 by introducing the jellium model.

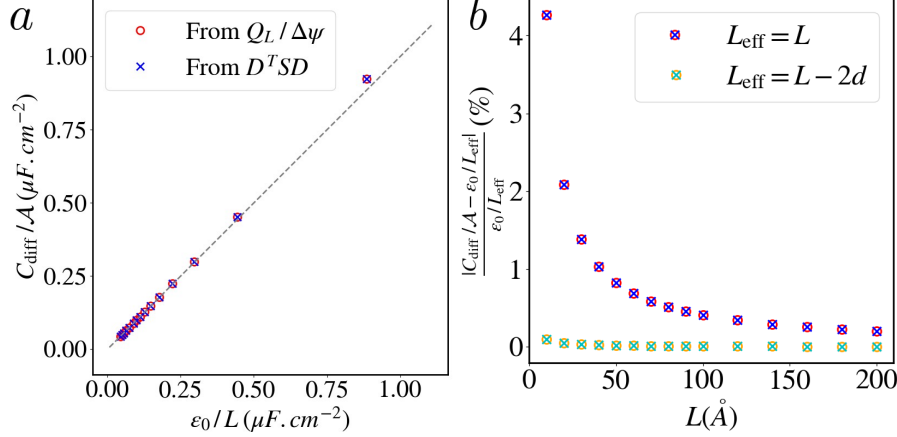


Figure 3.2: (a) Differential capacitance per unit area, $C_{\text{diff}}/\mathcal{A}$ of an empty capacitor with graphite electrodes (system (G1) in table 2.1) as a function of the analytical prediction ϵ_0/L for an empty capacitor with structureless electrodes, with \mathcal{A} the area and L the distance between the electrodes ranging from 10 to 200 \AA . The dashed line corresponds to $y = x$. (b) Relative error in percentage, with respect to the prediction $\epsilon_0/L_{\text{eff}}$, as a function of the capacitor size L . Red circles and blue crosses are computed for an effective length $L_{\text{eff}} = L$ while orange circles and cyan crosses for an effective length $L_{\text{eff}} = L - 2d$, with $d = 0.2 \text{ \AA}$. In both figures, we give values computed from the slope of figure 3.1 (open circles) and from the predictions of Eq. 3.56 (crosses). Panel a) was reproduced from Ref. 218 with permission from the PCCP Owner Societies.

Capacitances for electrochemical cells The theoretical developments detailed in this chapter allow to extract capacitances from molecular simulations of electrochemical cells. We show here the case of graphitic electrodes with different electrolytes: pure water, a concentrated sodium chloride aqueous solution and an ionic liquid, corresponding to systems (G2), (G4) and (G6) of table 2.1, respectively. These systems were simulated for several nanoseconds each (9 ns, 9 ns and 40 ns, respectively) and the total charge per electrode was sampled every 100 steps. Simulations were carried for both $\Delta\psi = 0 \text{ V}$ and 2 V .

An overview of results is given in figure 3.3. Panel a) shows the probability distribution in log-scale of the total charge Q_{tot}^* at $\Delta\psi = 0 \text{ V}$ while panel b) shows the distribution of both Q_L^* and Q_R^* at $\Delta\psi = 2 \text{ V}$. The solid lines correspond to a normalized Gaussian probability distribution with mean and variance extracted from the simulated data. The distributions nicely coincide with the Gaussian functions in this range of charges.

The integral capacitance per unit area $C_{\text{int}}/\mathcal{A}$ is easily extracted for the runs at $\Delta\psi = 2 \text{ V}$ from the average value of the distribution $\langle Q_{\text{tot}}^* \rangle$, with a standard error estimated using Eq. 2.62. The differential capacitance is obtained as a sum of the empty capacitance $C_{\text{diff}}^{\text{empty}}$ from Eq. 3.56 and the contribution from the electrolyte $C_{\text{diff}}^{\text{electrolyte}}$ computed using Eq. 3.54 from the variance of the total charge distribution. The uncertainty is evaluated using the standard error on the variance Eq. 2.63.

The differential capacitances at 0 and 2 V and the integral capacitance are given in figure 3.3c. In all cases the relative contributions in Eq. 3.54 coming from the suppressed thermal contributions $C_{\text{diff}}^{\text{empty}}$ with respect to the contribution from the electrolyte fluctuations $C_{\text{diff}}^{\text{electrolyte}}$ are small, between 5 and 6%. The correction term is also of the same order of magnitude of the statistical uncertainties on the

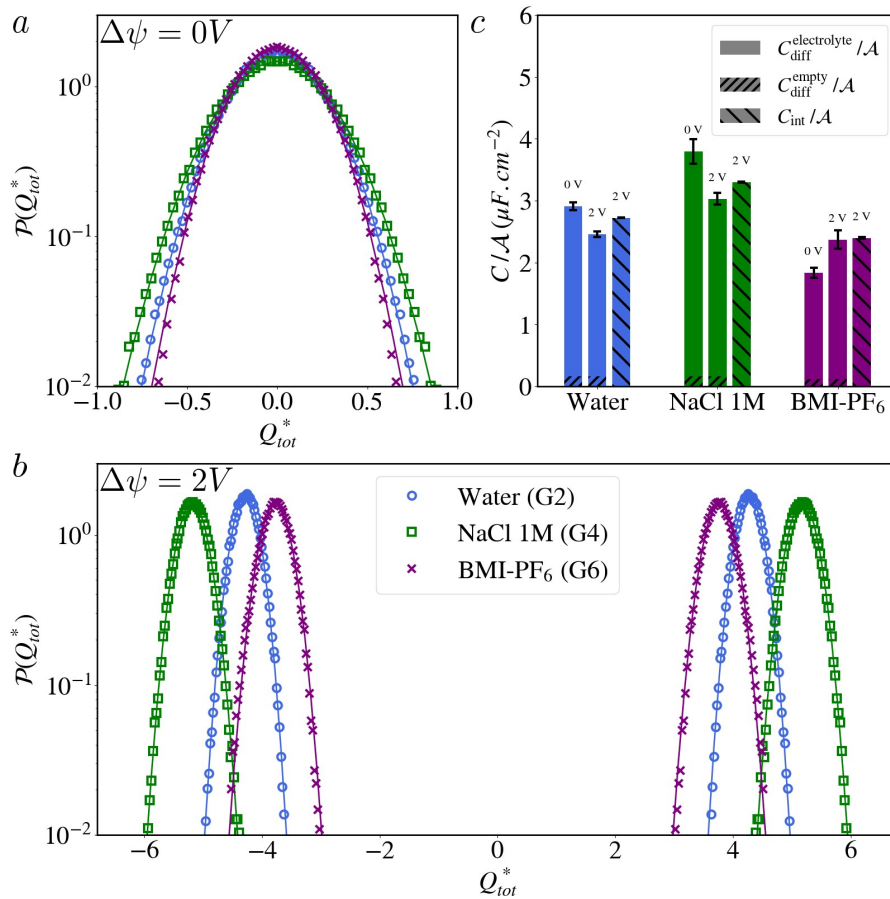


Figure 3.3: Normalized probability distribution of the total charge Q_{tot}^* for three graphitic capacitors with pure water (blue circles), aqueous sodium chloride (green squares) and BMI-PF₆ (purple crosses) (systems (G2), (G4) and (G6) in table 2.1) for a potential difference of 0 V (a) and 2 V (b). Solid lines are Gaussian distributions with corresponding mean value and variance. Panel c) shows the integral capacitance per unit area at 2 V and differential capacitances per unit surface at 0 and 2 V. Contributions to the differential capacitance per unit area $C_{\text{diff}}/\mathcal{A}$ (see Eq. 3.54) are given from the empty capacitor, $C_{\text{diff}}^{\text{empty}} = \mathbf{D}^T \mathbf{S} \mathbf{D}$, and from the charge fluctuations induced by the electrolyte, $C_{\text{diff}}^{\text{electrolyte}} = \beta \langle \delta Q_L^{*2} \rangle_{\mathbf{r}^N}^{BO}$. Error bars correspond to standard errors corrected for data correlations (see section 2.4.4).

evaluation of the variance. There are also differences between C_{diff} at 0 and 2 V and C_{int} which are due to non-linearities of the capacitance and possibly to an insufficient equilibration of the system.

3.2 Insulating vs metal: the influence of electronic polarization

The main focus of this PhD thesis is to investigate the influence of the electronic polarization (related to the so-called metallicity) of the surface on the properties of the system. In order to only extract the influence of the polarization, and not the dominant effect of the net accumulation of charge on the electrodes when a voltage is applied, most of the following results in the rest of this chapter are done by short-circuiting the studied devices, *i.e.* by applying a zero voltage. We first study the energetic profile for an ion of charge q at a distance z from the surface. For a single ion in vacuum, detailed in section 3.2.1, we study the electrostatic energy profile while for an ion in water we compute the free energy profile, discussed in section 3.2.2. We then present in section 3.2.3 the impact of the charge distribution on surface tension, by measuring contact angles of electrolyte drops on a surface.

3.2.1 Electric response to a single ion in vacuum

Let us consider a uniformly charged surface perpendicular to the z -axis at $z = 0$, with surface charge density $\sigma = -q/\mathcal{A}$, where \mathcal{A} is the surface area. The electric field generated along z is $E_z = \frac{\sigma}{2\epsilon_0}$, and the electric potential energy of an ion of charge q at a distance z from the surface is

$$U^Q(z) = -q\frac{\sigma z}{2\epsilon_0} = +\frac{q^2 z}{2\epsilon_0 \mathcal{A}}. \quad (3.72)$$

For a metal, the electrostatic energy due to the charge distribution can be obtained by using the method of image charges and gives²⁴²

$$U^{\Delta\psi}(z) = -\frac{q^2}{16\pi\epsilon_0 z}. \quad (3.73)$$

Aside from the fact that these expressions take as references for the energy the position of the charged plane $z = 0$ and $z = +\infty$, respectively, the energy dependence with distance is drastically different depending on the charge distribution at the interface: linear $U^Q \propto z$ in the insulating case and inversely proportional $U^{\Delta\psi} \propto z^{-1}$ in the metallic case.

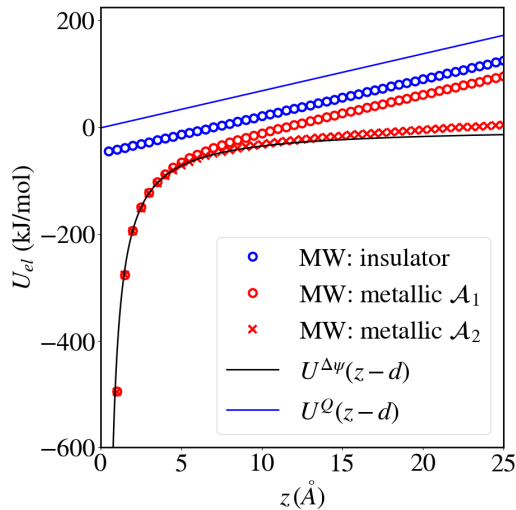


Figure 3.4: Electrostatic energy for an ion at a distance z from an insulator or metallic surface from simulations (symbols) and from Eqs. 3.72 (blue line) and 3.73 (black line). Predictions are shown for an effective distance $z_{\text{eff}} = z - d$ with $d = 0.2 \text{ \AA}$. Simulations were run for a single graphitic electrode taken from system (G1) in table 2.1, with area \mathcal{A}_1 , and an ion of charge $q = 1e$ at a distance z from the first atomic plane, either with constant charges (blue circles) or a constant potential (red circles). A metallic system with a larger surface $\mathcal{A}_2 = 4\mathcal{A}_1$ (red crosses) is also reported.

Using *MetalWalls*¹⁵³ we compute for both cases the energy of an ion of charge $q = 1e$ at a distance z from a single graphitic electrode, taken from system (G1) in table 2.1, with area $\mathcal{A}_1 = 34.101 \times 36.915 \text{ \AA}^2$ and $n = 5$ atomic planes (the distance z is taken from the first atomic plane). The insulator is modelled using constant (Gaussian) charges $q' = -q/M = -e/M$, where M is the number of atoms in the electrode; the metallic case is modelled using the constant potential ensemble described in section 3.1.1 by imposing a zero potential to all atoms, *i.e.* $\Psi = (0, 0, \dots, 0)$. The comparison is shown in figure 3.4, taking an effective distance from the surface $z_{\text{eff}} = z - d$ with $d = 0.2 \text{ \AA}$ as done in section 3.1.5.2 and figure 3.2 for comparison with the ideal capacitance $\epsilon_0/(L - 2d)$. Up to an irrelevant constant, the agreement for the insulating case is perfect. For the metallic case, the electrostatic energy agrees well with Eq. 3.73 for small distances but resembles the insulating case at larger distances. This is due to the finite lateral size of the simulation cell: around 5 \AA from the surface, the contribution from the periodic replicas is not negligible and the charge induced on the surface is perturbed by the neighboring replicas. We thus computed the electrostatic energy for a system with a larger surface area ($\mathcal{A}_2 = 68.202 \times 73.830 \text{ \AA}^2 = 4\mathcal{A}_1$). The agreement is much better

and the linear regime appears later and with a much smaller slope (which is inversely proportional to the surface area). Let us emphasize that the disagreement for our box size \mathcal{A}_1 is not worrying when used in combination with electrolytes because the other species screen the effect of the single charges so that these long range effects are not visible. This is tested in the following section 3.2.2.

Furthermore, from continuum electrostatics, the surface charge induced on a metallic surface at $z = 0$ by a charge q at coordinates $(0, 0, z)$ is given by

$$\sigma_{ind}(x, y) = -\frac{q}{2\pi} \frac{z}{(x^2 + y^2 + z^2)^{3/2}}. \quad (3.74)$$

For the same graphitic systems, we computed charge density maps on a grid by integrating the Gaussian charge distributions of each electrode atom in the first atomic layer in each voxel of the grid. These maps are shown in figure 3.5a-b for an ion of charge $q = -1e$ placed on top of a carbon atom, for two distances z from the surface (2.5 and 10.0 Å). The underlying hexagonal structure of the graphite sheet is evident, and so is the radial decay of the induced charge.

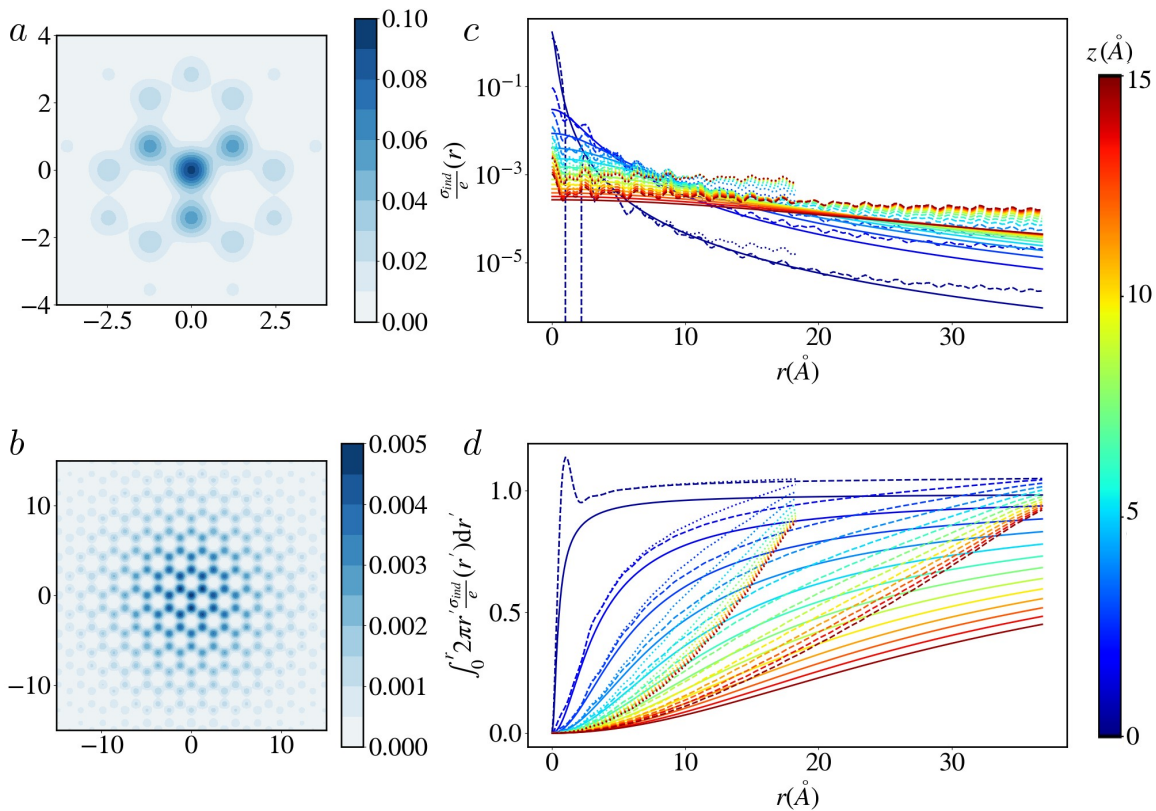


Figure 3.5: 2D-charge density maps for an ion of charge $q = -1e$ at a distance $z = 2.5$ Å (a) and $z = 10.0$ Å (b) from the first atomic plane, on top of a carbon atom, for a single graphitic electrode taken from system (G1) in table 2.1, with area \mathcal{A}_2 . Induced charge profile $\frac{\sigma_{ind}}{e}(r)$ for a range of distances z from the surface (c) and its integral $\int_0^r 2\pi r' \frac{\sigma_{ind}}{e}(r') dr'$ (d) as a function of the radial distance r . Results are shown for a small surface area \mathcal{A}_1 (dotted lines) and a larger surface area $\mathcal{A}_2 = 4\mathcal{A}_1$ (dashed lines) and are compared to continuum predictions Eq. 3.74 (solid lines). Predictions are given for an effective distance $z_{eff} = z - d$ with $d = 0.2$ Å.

The radial charge density $\sigma_{ind}(r)$ is computed as the average of $\sigma_{ind}(x, y)$ on a ring of radius r . Results are given in figure 3.5c for a range of positions of the ion from the surface, for the smaller surface \mathcal{A}_1 (dotted lines) and for the larger surface \mathcal{A}_2 (dashed lines) compared to the predictions of Eq. 3.74, taking an effective distance from the surface $z_{eff} = z - d$ with $d = 0.2$ Å. For small heights z with respect to the box size, the agreement is good, although deviations are observed due to the atomic nature of the surface. At the extreme position with $z = 0.5$ Å, a negative charge is even induced on the neighboring atoms to balance the large positive charge on the underlying carbon atom. Differences between the smaller and larger surface areas at large distance r are observed that are more significant

for larger heights z , and coincide with larger deviations from the continuum prediction. We interpret these deviations by observing in figure 3.5d the integrated charge density, which increases to $\sim 1e$, *i.e.* the total charge of the electrode $-q$ within the box area. Note that curves that do not always rise to $-q$ because the integration is only on a disk of radius $\min(L_x, L_y)/2$ and not the whole electrode, and because the charge on the first plane is not strictly $-q$ due to the presence of other planes. The total charge of the electrode is enforced by the electroneutrality constraint (see section 3.1.1.2), which explains the steeper rise for a small surface area than for the larger one and with respect to the even slower behavior of the continuum predictions. On the induced charge profiles of figure 3.5c we thus understand the appearance of a constant background of homogeneous, non zero charges that enforce the electroneutrality constraint within the simulation box and deviate from the predictions of Eq. 3.74. For larger boxes, this upward deviation appears at larger distances and has a smaller value. Therefore, the local electronic response for an ion close to the surface is well reproduced but deviations arise due to atomic details when approaching the surface too close or due to finite size effects and the constraint of electroneutrality. The same conclusions can be drawn for the case of an ion on top of a carbon ring instead of a carbon atom (not shown).

3.2.2 Electric response to ions in solution

The different behavior for a uniformly charged surface results from the long-range electric field, which is uniform on either side of the surface and does not decay at large distances. However, if instead of vacuum the ion is placed in a solvent or is part of an electrolyte, the electric field created by the surface is screened within a few atomic layers from it, thereby decreasing importantly this effect. This explains why the influence of electronic polarization is often neglected in earlier and present works, by using a uniform charge distribution on the metallic material, *i.e.* treating it as insulating. Several studies have however highlighted the importance of polarization on the interfacial properties^{55;128;155;243;244}, as discussed in the introduction.

In this section, following the publication of Ref. 245 presenting the free energy profile for a chloride ion approaching an insulating graphite surface, we studied the effect of the polarization of the surface on this free energy profile, in collaboration with the authors Prof. Roland Netz and Philip Loche at Freie Universität Berlin. We chose a similar graphitic capacitor from the original publication, corresponding to system (G3) in table 2.1, made of three graphene layers per “electrode” separated by water molecules. To focus on a single surface, only the left electrode was modified to be either insulating or metallic, while the right electrode atoms were given a zero charge. The insulating simulation was made by assigning a zero charge to each atom of the left electrode, while the metallic simulation was run by keeping all atoms of the left electrode at the same electric potential and imposing the electroneutrality of the electrode. In order to enforce the electroneutrality of the system, we adopted the setup of Ref. 245 where a counterion “Cl⁺” is introduced along with the Cl⁻ ion (with the same force field parameters but an opposite charge). The counterion is fixed at a position equidistant from both surfaces.

Contrary to the original publication, which used a thermodynamic integration technique to first introduce the ion (by switching on the Lennard-Jones parameters) and then its charge (thus yielding both the non-electrostatic and electrostatic contributions), we used Umbrella Sampling as described in section 2.5.2 to obtain the free energy profile. The reaction coordinate was taken as the distance z between the chloride ion and the first atomic plane and we imposed harmonic biases $w(z) = \frac{k}{2}(z - z_{\text{ref}})^2$ using the PLUMED library^{204;205} interfaced with the molecular simulation code *MetalWalls*. The different biasing windows are specified in table 3.1. Each window corresponds to a trajectory of 10 ns and several windows with increasing bias were used for $z_{\text{ref}} = 0.2$ nm in order to force the ion to approach the surface, where we expect the difference of free energy to be larger.

The unbiased free energy profiles are obtained using the WHAM method²⁴⁶, as detailed in section 2.5.2 and error bars are extracted by Monte Carlo bootstrapping error analysis²⁴⁷. Figure 3.6a-b compare the free energy profiles for the conducting (ΔF^Ψ) and insulating (ΔF^Q) systems, while figure 3.6c

z_{ref} (nm)	k (kJ/mol/nm ²)
0.2	500
0.2	5,000
0.2	20,000
0.2	50,000
0.2	100,000
0.2	200,000
0.4	250
0.6	250
0.8	250
1.0	250
1.2	250
1.4	250
1.6	250

Table 3.1: Reference position z_{ref} and spring constant k for the various windows used for Umbrella Sampling.

shows the difference $\Delta F^\Psi - \Delta F^Q$. The profiles are indistinguishable within the error bars for usual distances (panel b), *i.e.* where the free energy difference with respect to the bulk is smaller than a few $k_B T$. Using very strong biasing potentials, we managed to explore the region of space very close to the surface ($z \approx 2.5 - 3.5$ Å- panel a) and could measure a deviation between the profiles. The difference between insulating and metallic $\Delta F^\Psi - \Delta F^Q$ is small with respect to the value of ΔF , of the order of $10 k_B T$, but significant.

We can explain the difference in free energy in the metallic case with respect to the insulating one by considering that it is due to the additional electrostatic interaction between the ion at the surface and its image charge. In the presence of a dielectric medium, this electrostatic interaction is given by

$$\Delta F^\Psi - \Delta F^Q \approx \mathcal{U}_{\text{el}}^{\Delta\psi} = -\frac{q^2}{16\pi\epsilon_0\epsilon_L z}, \quad (3.75)$$

with ϵ_L the dielectric constant of the medium and we have $\epsilon_L = 70.7$ for SPC/E water²⁴⁸. Figure 3.6c shows this expression gives a poor result if using a constant ϵ_L value (green line). One explanation could be that at the interface a continuum view of electrostatics does not hold and the inhomogeneity of water at the surface, as shown by the density profile in figure 3.6d, induces an inhomogeneous dielectric response. The electrostatic interaction would then be given by solving the Poisson equation with a z -dependent dielectric constant^{245;249;250}. This is outside of the primary scope of this work but we can instead use an ansatz by assuming a z -dependence of the dielectric constant as

$$\epsilon_L(z) = \frac{\epsilon_L}{2} \left(\tanh\left(\frac{z - z_O}{w}\right) + 1 \right), \quad (3.76)$$

where z_O is the position of the first peak in the oxygen density profile, as shown in figure 3.6d, and w corresponds to its width, taken as $w = 1$ Å, and replacing ϵ_L directly in Eq. 3.75. With this ansatz, we obtain a satisfactory prediction for the free energy difference, as seen in figure 3.6c.

These Umbrella Sampling simulations confirm that there is an impact of the charge distribution on the free energy profile of an ion approaching a surface but it is non negligible only for very short distances, that are very rarely sampled by the ion. This explains why simulations often do not take the polarization of the metal into account and why the structure of the electrolyte at the interface is not greatly influenced by the charge distribution on the surface, as we will see later in section 4.2.3.2. We can however imagine that in some cases, for small atoms such as Na^+ , depending on the accumulation of charge at the interface, inner-sphere adsorption could become favorable, *i.e.* an equilibrium position close to the surface, which would exist only in the metallic case, and more clearly modify the free energy profile at the interface.

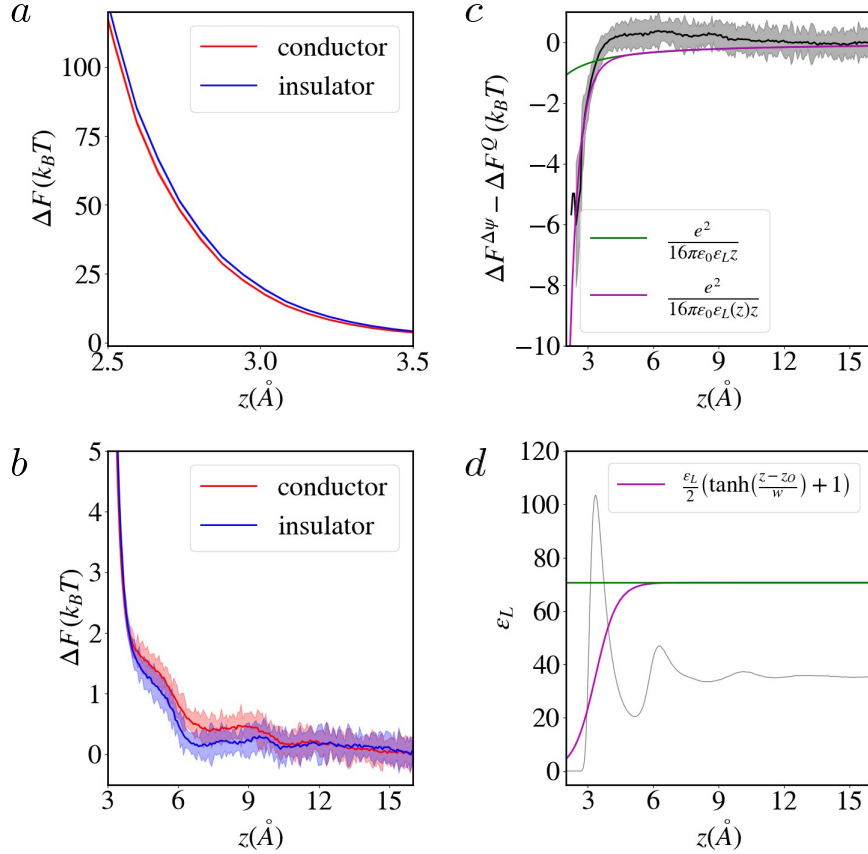


Figure 3.6: Free energy profile for a chloride ion in a graphite-water capacitor (system (G3) in table 2.1), as a function of the distance z to the surface, in the insulator (blue line) and metallic case (red line), for short distances (a) and longer distances (b). Error bars are estimated using Monte Carlo bootstrapping error analysis and are shown using shaded areas. Difference in free energy $\Delta F^{\Delta\psi} - \Delta F^Q$ (c) from simulations (solid black line and shaded grey area). Continuum predictions Eq. 3.75 are shown for a constant $\epsilon_L = 70.7$ (green line) or an ansatz where ϵ_L depends on the distance z as given by Eq. 3.76 (purple line). Corresponding dependence of ϵ_L with respect to distance z (d) superimposed to the water density profile (grey line).

3.2.3 Impact on surface tension and contact angles

We now indirectly investigate the influence of electronic polarization of the electrode on the surface tension γ by computing contact angles of drops of sodium chloride aqueous electrolyte on a graphite surface treated as insulating or metallic. The setup corresponds to the system (D4) in table 2.1 and contains only one electrode, at constant zero potential or at constant zero charges, and a drop of electrolyte that spontaneously takes a spherical shape. Each simulation was performed for 3 ns and the equilibration of the drop was checked by monitoring the height of its center of mass and by comparing the results from 5 different portions of simulation. Typical snapshots of the system are shown in figure 3.7 for a metallic surface seen from the side (a) and from top (b), where only a quarter of the drop is shown so to see the individual charge fluctuations on the surface. The 2-dimensional density $\rho(z, r)$, where z is the height with respect to the first atomic plane and r the radial distance to the center of mass of the drop, is extracted from the simulations and shown in figure 3.7c for the metallic case. To better compare the drop shape in the metallic and insulating cases, we plot the one-dimensional densities $\rho(z) = \int \rho(z, r) 2\pi r dr$ shown in figure 3.7d and $\rho(r) = \int \rho(z, r) dz$ shown in figure 3.7e. We observe a small but quantitative difference between insulating and metallic surfaces, which is exclusively due to the electronic polarization of the surface. Because the contact angle θ results from the balance between liquid-vapor (LG), liquid-surface (SL) and vapor-surface (SG)

surface tensions γ , as given by the Young equation

$$\gamma_{SG} - \gamma_{SL} - \gamma_{LG} \cos \theta = 0, \quad (3.77)$$

this difference in contact angle measures the evolution of surface tensions due to the metallic character of the surface.

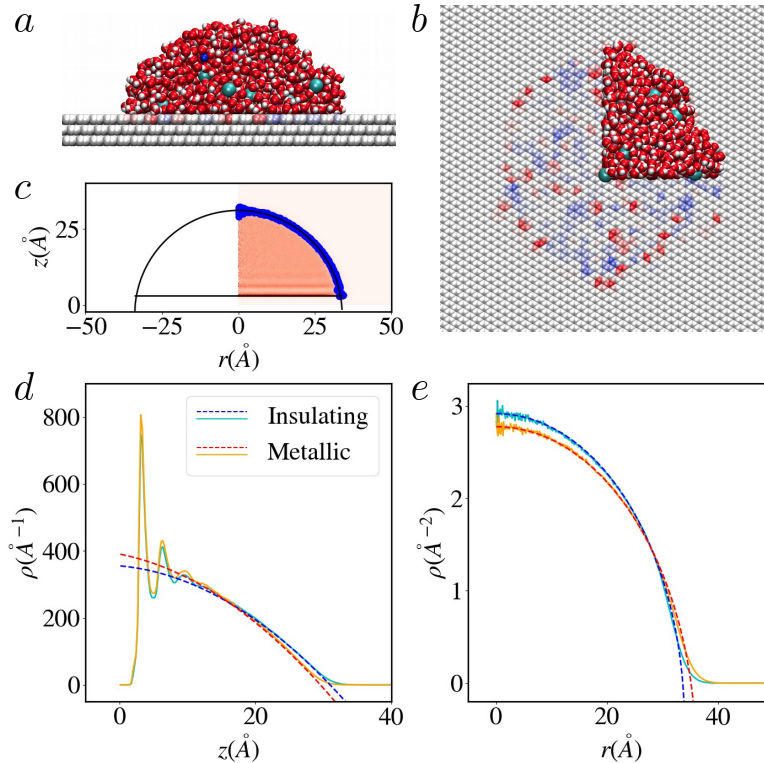


Figure 3.7: Contact angles for a 1M NaCl electrolyte drop on graphite (system (D4) in table 2.1). Typical snapshots from the side (a) and top (b) of the metallic system. Only a quarter of atoms are shown in panel (b) to show the charge fluctuations on the surface underneath. Two-dimensional density maps (c) in the (r, z) plane, with z the height with respect to the first atomic graphite layer and r the radial distance to the center of mass of the drop. The blue points correspond to the liquid-vapor interface (see text) and are fitted to a circle (solid black line). One-dimensional density profiles as a function of z (d) and r (e) for the metallic case (solid orange line) and insulating case (solid cyan line), and their corresponding predictions Eqs. 3.80 and 3.81 (dashed red and blue lines).

Values of the contact angle are extracted from density maps in the (r, z) plane, as the one shown in figure 3.7c. The shape is determined by the points (in blue) where the local density is equal to half of the bulk density ρ_0 at the center of the drop, and is fitted using a circle of radius R_C and centered in $(r = 0, z = z_C)$. The value of θ is then deduced by the intersection of the spherical fit and the interface plane. Once again, the choice of the position of the interface is not trivial in an atomistic system and has a small influence on the final result but does not modify the conclusions of the study. Using the first atomic plane of the electrodes, we find

$$\begin{aligned} \theta^Q &= 85.0 \pm 0.3^\circ \\ \theta^{\Delta\psi} &= 79.7 \pm 0.4^\circ, \end{aligned} \quad (3.78)$$

while using the plane corresponding to the first water layer $z = 3.12 \text{ \AA}$, we have

$$\begin{aligned} \theta^Q &= 79.6 \pm 0.3^\circ \\ \theta^{\Delta\psi} &= 74.6 \pm 0.4^\circ. \end{aligned} \quad (3.79)$$

In both cases, the difference in contact angle is about $\Delta\theta = \theta^Q - \theta^{\Delta\psi} \approx 5^\circ$, and the metallic surface is more hydrophilic than the insulating one. To verify these values, we consider the case of a homogeneous

sphere of density ρ_0 , radius R_C and centered in $(r = 0, z = z_C)$, cut by a plane in $z = z_0$. The corresponding one-dimensional densities are

$$\rho(z) = \rho_0 \pi (R_C^2 - (z - z_C)^2) \quad (3.80)$$

$$\rho(r) = \rho_0 \left(z_C - z_0 + \sqrt{R_C^2 - r^2} \right) \quad (3.81)$$

and, taking empirically $z_0 = 3.12 \text{ \AA}$ as the first water layer, we obtain a good agreement with the measured densities, as shown in figures 3.7d-e, except for the deviations due to the layering of water molecules at the surface ($z \leq 10 \text{ \AA}$).

Note that for a single surface in vacuum at $\Delta\psi = 0 \text{ V}$ the induced charge on each atom is equal to zero and the difference $\Delta\gamma_{SG} = \gamma_{SG}^Q - \gamma_{SG}^{\Delta\psi}$ vanishes. Therefore, using Eq. 3.77 and the values of Eq. 3.79, we obtain the difference in surface tension as

$$\Delta\gamma_{SL} = \gamma_{SL}^Q - \gamma_{SL}^{\Delta\psi} = -\gamma_{LV}(\cos\theta^Q - \cos\theta^{\Delta\psi}) = 5.4 \pm 0.6 \text{ mN.m}^{-1}, \quad (3.82)$$

where $\Delta\gamma_{SL}$ is the difference in liquid-surface surface tension of the insulating surface with respect to the metallic one. Using the values of Eq. 3.78, we obtain $\Delta\gamma_{SL} = 5.7 \pm 0.6 \text{ mN.m}^{-1}$. The liquid-vapor surface tension is obtained from the normal and tangential components of the pressure tensor, p_N and p_T , computed in a 10 ns simulation of a slab of electrolyte in vacuum (system (B4) in table 2.1 – simulated using LAMMPS^{228;229}) with a box length L_z in the direction perpendicular to the interfaces, as $\gamma_{LG} = \frac{L_z}{2}(p_N - p_T) = 62.7 \pm 0.6 \text{ mN m}^{-1}$.

Although the charge distribution has only a small effect on the free energy profile of an ion in solution, which is significant only in a region of phase space barely explored by the ion, as computed in section 3.2.2, the change in contact angle shows that electronic polarization has a measurable impact on surface tension. A more detailed and systematic study of interfacial free energies as a function of metallicity are presented in chapter 6.

“Forget-me-not”: Simulating metals with the constant potential ensemble

- To model large electrochemical cells, we account for the polarization of the metallic electrodes using simulations sampling the Constant Potential ensemble where we impose a constant voltage to electrode atoms.
- In these simulations, charges on electrode atoms are Gaussian and their magnitudes fluctuate to satisfy both an electroneutrality and a constant electric potential constraint.
- In practice, these simulations implement a Born-Oppenheimer sampling of the Constant Potential ensemble.
- This sampling method has an influence on some ensemble averages, in particular for the calculation of the charge fluctuations, which are related to the differential capacitance.
- Including the polarization of the electrodes has a strong impact on the energy of a single charge with an electrode, but is almost negligible for the free energy of an ion and an electrode in the presence of a solvent.
- Due to the charge distribution at the interface, a metallic surface is more hydrophilic than an insulating one, as shown by contact angle measurements.

Chapter 4

Accounting for the metallicity: the semiclassical Thomas-Fermi model

4.1 Electronic screening and the Thomas-Fermi model

In chapter 3, we treated the electronic polarization in a classical framework by considering a fluctuating charge distribution under a macroscopic constant voltage constraint. This allowed to simulate two extreme cases: metallic materials, where the valence (or conduction) electrons are free to move in the potential energy landscape of positive ions (made of the nuclei and core electrons) and respond to external electric fields, and insulator materials, where electrons are localized and bound to the nuclei so that the charge per atom remains constant. One of the objectives of this work was to go further in the description of the electrode material, by introducing a simple quantum mechanical theory in the treatment of the electronic degrees of freedom, that is by adding the kinetic energy of the free electron gas to the classical electrostatic energy. We first introduce in section 4.1.1 standard solid state concepts related to the free electron gas and the Local Density Approximation^{251–253}. We then present the theory of screening and in particular the Thomas-Fermi theory in section 4.1.2. Section 4.1.3 describes the implementation of the theory into constant potential simulations and we briefly discuss other extensions of the constant potential simulations present in the literature. We then study the impact of the metallicity on different properties for an empty capacitor and for electrochemical cells in section 4.2.

4.1.1 The free electron gas and the Local Density Approximation

The free electron gas model is the simplest model of energy conduction in metals: it spawns from the observation that in metals for each atom, with Z_a protons, only a fraction of its Z_a electrons are bound to the nucleus and that Z valence or conducting electrons are “detached” from their nucleus and can move in the whole material. The free electron gas model thus describes a gas of N_e free and non-interacting electrons in a volume V , of density $\rho_e = N_e/V$. No specific interaction with the nuclei lattice is taken into account, except for the restriction of the volume in which the electron gas evolves, which is taken for simplicity to be a parallelepiped $V = L_x L_y L_z$, using periodic boundary conditions²⁵¹. Because the electrons do not interact with each other, nor with the nuclei, they satisfy the time-independent Schrödinger equation

$$-\frac{\hbar^2}{2m_e} \nabla^2 \Psi(\mathbf{r}) = E \Psi(\mathbf{r}) \quad (4.1)$$

where Ψ is the single electron wavefunction, E its energy, m_e is the electron mass and $\hbar = h/2\pi$ the reduced Planck constant. The (plane waves) solutions and corresponding energies are

$$\Psi_{\mathbf{k}}(\mathbf{r}) = \frac{1}{\sqrt{V}} \exp[i\mathbf{k} \cdot \mathbf{r}] \quad \text{and} \quad E_{\mathbf{k}} = \frac{\hbar^2 |\mathbf{k}|^2}{2m_e}, \quad (4.2)$$

where $\mathbf{k} = (k_x, k_y, k_z)$ is a vector to be determined. Note that the energy can be cast in the usual kinetic form $E = \frac{p^2}{2m}$ with momenta $\mathbf{p} = \hbar\mathbf{k}$. The boundary conditions introduce a constraint on the \mathbf{k} vectors, which must be of the form $k_x = \frac{2\pi n_x}{L_x}$, $k_y = \frac{2\pi n_y}{L_y}$, $k_z = \frac{2\pi n_z}{L_z}$ with n_x, n_y, n_z integers (positive, zero and negative).

To determine the ground state of an N_e electron system, each electronic level is filled by two electrons (one spin up and one spin down because of the Pauli exclusion principle) starting from the lowest energy level corresponding to $\mathbf{k} = \mathbf{0}$. Because the energy of each level is proportional to $|\mathbf{k}|^2$, the ground state in k-space resembles a sphere of radius k_F , called the Fermi wavevector. The energy of the highest occupied level is known as the Fermi energy and given by

$$E_F = \frac{\hbar^2 k_F^2}{2m_e}. \quad (4.3)$$

It separates the occupied from the unoccupied levels and thus corresponds to the chemical potential of electrons, *i.e.* the energy required to add or remove an electron from the system²⁵². Knowing that the number of allowed k-values per unit volume of k-space is $\frac{V}{8\pi^3}$, the density of electrons is also related to the Fermi wavevector $\rho_e = N_e/V = \frac{2}{V} \frac{4\pi k_F^3}{3} \frac{V}{8\pi^3}$ so that

$$\rho_e = \frac{k_F^3}{3\pi^2}. \quad (4.4)$$

This relationship is of practical use to compute the value of the Fermi wavevector knowing the density of charge carriers from experiments. The total energy of a free electron gas of density ρ_e is simply the sum of the occupied energy levels. Performing the integral in spherical coordinates yields

$$E = \sum_{|\mathbf{k}| < k_F} E_{\mathbf{k}} = \int_{|\mathbf{k}| < k_F} 2 \frac{V}{8\pi^3} \frac{\hbar^2 |\mathbf{k}|^2}{2m_e} d\mathbf{k} = \int_{k=0}^{k_F} \frac{2V}{8\pi^3} \frac{\hbar^2 k^2}{2m_e} 4\pi k^2 dk, \quad (4.5)$$

where we used Eq. 4.3 and Eq. 4.4, and an energy density

$$\frac{E}{V} = \frac{\hbar^2 k_F^5}{10\pi^2 m_e} = \frac{3\hbar^2}{10m_e} (3\pi^2)^{2/3} \rho_e^{5/3} = \frac{3}{5} E_F \rho_e. \quad (4.6)$$

The energy per electron is then given by

$$\frac{E}{N_e} = \frac{3\hbar^2 k_F^2}{10m_e} = \frac{3\hbar^2}{10m_e} (3\pi^2)^{2/3} \rho_e^{2/3} = \frac{3}{5} E_F. \quad (4.7)$$

The free electron gas is not a good approximation for metals because the electronic density is not homogeneous throughout the material. However, Thomas²⁵⁴ and Fermi²⁵⁵ made the bold approximation that the properties of matter could be deduced by applying locally the properties of the free electron gas. This is also known as Local Density Approximation and requires a spatially slowly varying electronic density. Within this approximation, the kinetic energy is written from Eq. 4.6 as

$$\mathcal{T}[\rho_e] = \int \frac{3\hbar^2}{10m_e} (3\pi^2)^{2/3} \rho_e(\mathbf{r})^{5/3} d\mathbf{r}, \quad (4.8)$$

for a spatially-dependent electron density $\rho_e(\mathbf{r})$. The Thomas-Fermi energy functional for an atom can be defined by neglecting exchange-correlation terms as²⁵²

$$E_{\text{TF}}[\rho_e(\mathbf{r})] = \mathcal{T}[\rho_e(\mathbf{r})] - Z \int \frac{\rho_c(\mathbf{r})}{4\pi\epsilon_0|\mathbf{r}|} d\mathbf{r} + \frac{1}{2} \iint \frac{\rho_c(\mathbf{r}_1)\rho_c(\mathbf{r}_2)}{4\pi\epsilon_0|\mathbf{r}_1 - \mathbf{r}_2|} d\mathbf{r}_1 d\mathbf{r}_2, \quad (4.9)$$

where $\rho_c(\mathbf{r}) = -e\rho_e(\mathbf{r})$ is the charge density, *i.e.* the electronic density times the elementary charge of an electron $-e$. The two last terms are the Coulomb interactions with the ion of charge Z (nucleus plus core electrons) and with all other electrons. In classical simulations, these terms are computed using known charge distributions ρ_c as detailed in section 2.1.2.1. Therefore we only need to introduce the kinetic energy term in the classical model.

4.1.2 Theory of screening and the Thomas-Fermi model

Before going into the details of the implementation of this semi-classical theory in constant potential simulations, we briefly present the phenomenon of screening^{251;253}, an important consequence of electron-electron interactions. Consider introducing an external charge ρ_{ext} , which creates an electric field, in a free electron gas. Because they are free to move, the electrons rearrange to exactly cancel the electric field far from the source so that on average we measure an excess charge around the external perturbation. The induced charge is expressed as the difference between the charge density and the free electron gas one, $\rho_{\text{ind}}(\mathbf{r}) = -e(\rho_e(\mathbf{r}) - \rho_e)$. Within the Thomas-Fermi local approximation, in the presence of the perturbation, the effective Fermi energy is equal to $E_F(\mathbf{r}) = E_F - e\psi(\mathbf{r})$, *i.e.* it is raised or lowered, with respect to the homogeneous electron gas, by the local electric potential. Using Eq. 4.4, these equations give $\rho_{\text{ind}}(\mathbf{r}) = -e(\rho_e[1 - e\psi(\mathbf{r})/E_F]^{3/2} - \rho_e)$. Linearizing this expression, writing the Poisson equation for the total charge distribution and using Eqs. 4.3 and 4.4 gives

$$\nabla^2\psi = \frac{\rho_{\text{ext}}(\mathbf{r})}{\epsilon_0} + \kappa_{TF}^2\psi(\mathbf{r}), \quad (4.10)$$

where we defined the Thomas-Fermi screening wavevector κ_{TF} as

$$\kappa_{TF} = \sqrt{\frac{m_e e^2 k_F}{\epsilon_0 \pi^2 \hbar^2}}, \quad (4.11)$$

or equivalently the Thomas-Fermi screening length l_{TF} as

$$l_{TF} = \sqrt{\frac{\epsilon_0 \pi^2 \hbar^2}{m_e e^2 k_F}}. \quad (4.12)$$

In the limit of vanishing perturbation, the Poisson equation reads

$$\nabla^2\psi = \kappa_{TF}^2\psi(\mathbf{r}), \quad (4.13)$$

which is similar to the Debye-Hückel theory for screening in solutions. For a point charge $\rho_{\text{ext}}(\mathbf{r}) = q_{\text{ext}}\delta(\mathbf{r})$, the electric potential decays exponentially as²⁵³

$$\psi(\mathbf{r}) = \frac{q_{\text{ext}}}{4\pi\epsilon_0|\mathbf{r}|} e^{-\kappa_{TF}|\mathbf{r}|}. \quad (4.14)$$

The effect of the surrounding electron gas is thus to “screen” the electric potential of the external charge and this screening occurs on a characteristic length equal to the Thomas-Fermi length l_{TF} .

4.1.2.1 Orders of magnitude

From the definition of l_{TF} in Eq. 4.12 and the relationship between the Fermi wavevector and the electron density Eq. 4.4, we obtain

$$l_{TF} = \left(\frac{\pi}{192} \frac{a_0^3}{\rho_e}\right)^{1/6} \approx 0.5 \left(\frac{a_0^3}{\rho_e}\right)^{1/6}, \quad (4.15)$$

where we introduced the Bohr radius $a_0 = \frac{4\pi\epsilon_0\hbar^2}{m_e e^2}$. The Thomas-Fermi length can then be estimated from experimental values of the charge carrier density. Typical values for l_{TF} can be found in the Supplementary Information of Ref. 84 and are reproduced in table 4.1. Good metals such as platinum or gold have a small screening length of ~ 0.5 Å while for non-ideal metals it is of the order of a few angströms. For insulating materials, $\rho_e \rightarrow 0$ so that $l_{TF} \rightarrow \infty$.

Material	l_{TF}
Mica	∞
Highly oriented pyrolytic graphite (HOPG)	3.6 Å
Doped (100) Silicon	1.5 Å
Platinum	0.5 Å

Table 4.1: Thomas-Fermi length for different materials, taken from Supplementary Information of Ref. 84.

4.1.3 Implementation of the Thomas-Fermi model in constant potential simulations

The constant potential simulations discussed in chapter 3 only account for the potential energy of the electrons, through the calculation of electrostatic interactions. Adding the kinetic energy contribution of electrons would allow to improve the description of the metallic material by tuning the screening through the introduction of varying Thomas-Fermi screening lengths. The following section is dedicated to the implementation of the Thomas-Fermi model in classical constant potential simulations, developed in collaboration with Dr. Thomas Dufils and Prof. Mathieu Salanne²⁵⁶.

4.1.3.1 Homogeneous voxel approximation

We consider a system of M identical electrode atoms in a volume V . In the constant potential simulations introduced in chapter 3, the local electronic density is given by

$$\rho_e(\mathbf{r}) = \rho Z + \frac{\rho_{gc}(\mathbf{r})}{-e} = \rho Z + \sum_{i=1}^M \frac{q_i}{-e} \frac{\eta_i^3}{\pi^{3/2}} e^{-\eta_i^2 |\mathbf{r}-\mathbf{r}_i|^2}, \quad (4.16)$$

where ρ_{gc} was defined in Eq. 2.2. The kinetic energy then reads

$$\mathcal{T} = \frac{3\hbar^2}{10m_e} (3\pi^2)^{2/3} \int \left[\rho Z + \sum_{i=1}^M \frac{q_i}{-e} \frac{\eta_i^3}{\pi^{3/2}} e^{-\eta_i^2 |\mathbf{r}-\mathbf{r}_i|^2} \right]^{5/3} d\mathbf{r}. \quad (4.17)$$

However, because of the correlations between each atomic Gaussian charge distribution, this calculation is impractical. Instead, we make approximation that the charge $-Ze + q_i$ of each atom i is homogeneously distributed in a voxel $d\mathbf{V}_i$ of volume V/M centered on each atom, and we write the electronic density as

$$\rho_e(\mathbf{r}) = \sum_{i=1}^M \left(Z + \frac{q_i}{-e} \right) \rho H_i(\mathbf{r}) = \sum_{i=1}^M \left(1 + \frac{q_i}{-eZ} \right) \rho Z H_i(\mathbf{r}), \quad (4.18)$$

where $\rho = M/V$ is the atomic density and we introduced the functions

$$H_i(\mathbf{r}) = \begin{cases} 1 & \text{if } \mathbf{r} \in d\mathbf{V}_i \\ 0 & \text{otherwise} \end{cases} \quad (4.19)$$

so that $\int H_i(\mathbf{r}) d\mathbf{r} = V/M = 1/\rho$. The homogeneous electron gas is recovered if there are no charge fluctuations ($\mathbf{q} = \mathbf{0}$) and is then equal to $\rho_e = N_e/V = MZ/V = \rho Z$. Using Eq. 4.8, the kinetic energy reads

$$\mathcal{T} = \frac{3\hbar^2}{10m_e} (3\pi^2)^{2/3} \int \left[\sum_{i=1}^M \left(1 + \frac{q_i}{-eZ} \right) \rho_e H_i(\mathbf{r}) \right]^{5/3} d\mathbf{r}. \quad (4.20)$$

Because the different terms are independent and do not overlap, we can take out the sum over the electrode atoms and the spatial dependence $H_i(\mathbf{r})$ from the power $5/3$. Using the definitions Eqs. 4.3 and 4.4, we then write

$$\mathcal{T} = \frac{3\hbar^2}{10m_e} (3\pi^2)^{2/3} \rho_e^{5/3} \sum_{i=1}^M \int \left(1 + \frac{q_i}{-eZ}\right)^{5/3} H_i(\mathbf{r}) d\mathbf{r} = \frac{3}{5} E_F \rho_e \frac{1}{\rho} \sum_{i=1}^M \left(1 + \frac{q_i}{-eZ}\right)^{5/3} \quad (4.21)$$

$$= \frac{3}{5} E_F Z \sum_{i=1}^M \left(1 + \frac{q_i}{-eZ}\right)^{5/3}. \quad (4.22)$$

Because q_i is the magnitude of the charge fluctuations, it is safe to assume that $\frac{q_i}{-e} \ll Z$ so that we can use the Taylor expansion $(1+x)^\alpha \approx 1 + \alpha x + \frac{\alpha(\alpha-1)}{2} x^2$

$$\mathcal{T} \approx \frac{3}{5} E_F Z \sum_{i=1}^M \left(1 + \frac{5}{3} \frac{q_i}{-eZ} + \frac{5}{9} \frac{q_i^2}{e^2 Z^2}\right) = \frac{3}{5} M Z E_F + \frac{E_F}{-e} \sum_{i=1}^M q_i + \frac{E_F}{3e^2 Z} \sum_{i=1}^M q_i^2. \quad (4.23)$$

The zeroth order term corresponds as expected to the energy of the homogeneous free electron gas with $N_e = MZ$ electrons. The first order term is the chemical potential of the excess/depleted electrons, *i.e.* the energy necessary to add or remove an electron from the system, depending on the sign of the charge fluctuation q_i . The second order term can be expressed using the Thomas-Fermi screening length Eq. 4.12 as

$$\mathcal{T}^{(2)} = \frac{E_F}{3e^2 Z} \sum_{i=1}^M q_i^2 = \frac{\pi^2 \hbar^2 \rho}{2e^2 m_e k_F} \sum_{i=1}^M q_i^2 = \frac{l_{TF}^2 \rho}{2\epsilon_0} \sum_{i=1}^M q_i^2. \quad (4.24)$$

It thus corresponds to an energy cost related to the localization of charges, which is always positive and has its minimum when no charges are induced on the electrodes. This energy is quadratic in the screening length l_{TF} so that it is more costly to localize electrons to screen external perturbations for larger l_{TF} .

4.1.3.2 Constant potential framework

Using the expressions for the kinetic energy of electrons Eq. 4.23, the Hamiltonian reads

$$\mathcal{H}(\mathbf{r}^N, \mathbf{p}^N, \mathbf{q}) = \mathcal{K}(\mathbf{p}^N) + \mathcal{U}_{\text{pot}}(\mathbf{r}^N, \mathbf{q}) + \mathcal{T}(\mathbf{q}) = \mathcal{K}(\mathbf{p}^N) + \mathcal{U}'_0(\mathbf{r}^N) + \mathcal{U}'_{\text{fluct}}(\mathbf{r}^N, \mathbf{q}), \quad (4.25)$$

where $\mathcal{U}'_0(\mathbf{r}^N) = \mathcal{U}_0(\mathbf{r}^N) + \frac{3}{5} M Z E_F$ and the interactions involving fluctuating charges Eq. 3.2 include additional terms

$$\mathcal{U}'_{\text{fluct}}(\mathbf{r}^N, \mathbf{q}) = \frac{\mathbf{q}^T \mathbf{A} \mathbf{q}}{2} - \mathbf{q}^T \left(\mathbf{B}(\mathbf{r}^N) + \frac{E_F}{e} \mathbf{E} \right) + \frac{l_{TF}^2 \rho}{2\epsilon_0} \mathbf{q}^T \mathbf{q} \quad (4.26)$$

$$= \frac{\mathbf{q}^T \mathbf{A}_{\text{TF}} \mathbf{q}}{2} - \mathbf{q}^T \left(\mathbf{B}(\mathbf{r}^N) + \frac{E_F}{e} \mathbf{E} \right), \quad (4.27)$$

with \mathbf{E} defined in Eq. 3.7, and where we assumed that the Fermi energy E_F and the Thomas-Fermi length l_{TF} are the same for each atom and each electrode, and introduced a modified symmetric matrix \mathbf{A}_{TF}

$$\mathbf{A}_{\text{TF}} = \mathbf{A} + \frac{l_{TF}^2 \rho}{\epsilon_0} \mathbf{I}, \quad (4.28)$$

with \mathbf{I} the $M \times M$ identity matrix.

The first order term, linear in the charges, appears as a constant potential shift of the electric potential vector \mathbf{B} but doesn't affect the calculation of charges as discussed in section 3.1.3 after Eq. 3.27. Additionally, if the electrolyte is neutral and the electroneutrality constraint Eq. 3.12 is applied, this term cancels and simply gives

$$\mathcal{U}'_{\text{fluct}}(\mathbf{r}^N, \mathbf{q}) = \frac{\mathbf{q}^T \mathbf{A}_{\text{TF}} \mathbf{q}}{2} - \mathbf{q}^T \mathbf{B}(\mathbf{r}^N). \quad (4.29)$$

Thus the only significant modification is in the matrix \mathbf{A}_{TF} with an additional diagonal term $l_{TF}^2 \rho / \epsilon_0$. The constant potential simulation procedure detailed in section 3.1.3 does not need any further changes and only requires one additional parameter: the Thomas-Fermi length l_{TF} that characterizes the screening within the electrode material.

4.2 Impact of metallicity on the electrolyte properties

After implementing the Thomas-Fermi model in section 4.1.3, we now investigate its impact on the properties of the system. The link between this framework and the insulating/metallic distinction made in section 3.2 is the ability of a material to screen an external charge, also known as the “metallicity”, or metallic character, of a material. For an ideal metal, in continuum theories, the electric field within the material vanishes so that any external perturbation (outside the material volume) is compensated solely by a surface charge distribution (as opposed to charge being distributed within the bulk volume of the material). The ideal metal thus corresponds to a perfect screening of the charge, *i.e.* $l_{TF} = 0$. The energy cost to localize electrons $\mathcal{T}^{(2)}$ then vanishes and electrons accumulate on the surface. For real materials however, the external perturbations are screened with a characteristic length l_{TF} as shown in Eq. 4.14. The limit of insulating materials is recovered for $l_{TF} \rightarrow \infty$, where the cost to induce charge fluctuations $\mathcal{T}^{(2)}$ is infinite, *i.e.* there is no delocalization of electrons throughout the material.

In this section, we first derive analytical expressions for a simple system in section 4.2.1 then compare them to simulations of empty capacitors in section 4.2.2 and of electrochemical cells in section 4.2.3. In each case, we study a range of Thomas-Fermi lengths to systematically test the impact of the metallicity on different properties: the spatial charge distribution in the electrode, the total charge accumulated and the structure and dynamics of the electrolyte.

4.2.1 Analytical predictions

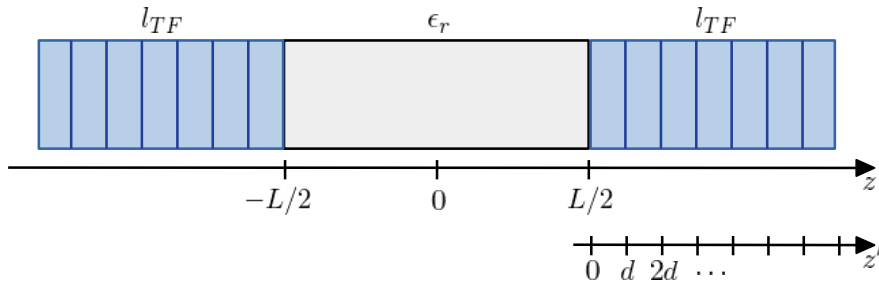


Figure 4.1: Continuum description of a homogeneous dielectric medium of dielectric constant ϵ_r in contact with two homogeneous Thomas-Fermi electrodes with screening length l_{TF} occupying the two semi-infinite spaces at $z < -L/2$ and $z > L/2$. Real electrodes are instead composed of several atomic planes, separated by an interplanar distance d , showed by the alternative coordinate $z' = z - L/2$.

Consider the continuum system pictured in figure 4.1 composed of two homogeneous electrodes characterized by their Thomas-Fermi length $l_{TF} = \kappa_{TF}^{-1}$ and separated by a uniform medium with no embedded charges of dielectric constant ϵ_r . The central region is described by the Poisson equation $\nabla^2 \psi = 0$, while within the electrodes we use Eq. 4.13

$$\begin{cases} \nabla^2 \psi = \kappa_{TF}^2 \psi & \text{for } z < -L/2 \\ \nabla^2 \psi = 0 & \text{for } -L/2 < z < L/2 \\ \nabla^2 \psi = \kappa_{TF}^2 \psi & \text{for } z > L/2 \end{cases} \quad (4.30)$$

Using the translational invariance in the x and y directions, the boundary conditions $\psi(-\infty) = \psi_1$ and $\psi(+\infty) = \psi_2$, the continuity of the electrical potential ψ and that of the normal component of the electrical flux density $\mathbf{D} = \epsilon\mathbf{E}$, we obtain

$$\begin{cases} \psi(z) = \psi_1 + \frac{\Delta\psi}{\lambda+2}e^{\kappa_{TF}(z+L/2)} & \text{for } z < -L/2 \\ \psi(z) = \bar{\psi} + \Delta\psi\frac{\lambda}{\lambda+2}\frac{z}{L} & \text{for } -L/2 < z < L/2 \\ \psi(z) = \psi_2 - \frac{\Delta\psi}{\lambda+2}e^{-\kappa_{TF}(z-L/2)} & \text{for } z > L/2 \end{cases} \quad (4.31)$$

where we denoted $\lambda = L\kappa_{TF}/\epsilon_r$ and we take $\bar{\psi} = \frac{\psi_1+\psi_2}{2}$ and $\Delta\psi = \psi_2 - \psi_1$.

We can express the charge distribution within the right electrode as a function of a shifted position $z' = z - L/2$ as

$$\rho_c(z') = -\epsilon_0 \frac{d^2\psi}{dz'^2} = \frac{\epsilon_0\Delta\psi\kappa_{TF}^2}{\lambda+2}e^{-\kappa_{TF}z'}. \quad (4.32)$$

In the systems studied in this work, described in section 2.1.1, the electrodes are made of atomic planes separated by an interplanar distance d , so it is natural to study the total charge per atomic plane. We thus compute the total charge in a slab of thickness d and area \mathcal{A} at position z' as

$$\frac{Q(z')}{\mathcal{A}} = \int_{z'}^{z'+d} \rho_c(z')dz' = \frac{\epsilon_0\Delta\psi\kappa_{TF}}{\lambda+2}e^{-\kappa_{TF}z'}(1 - e^{-\kappa_{TF}d}). \quad (4.33)$$

The total charge accumulated on the electrode per unit area is also $\frac{Q_{\text{tot}}}{\mathcal{A}} = \int_0^\infty \rho_c(z')dz' = \frac{\epsilon_0\Delta\psi\kappa_{TF}}{\lambda+2}$ and we find that

$$\frac{Q_k}{Q_{\text{tot}}} = e^{-\kappa_{TF}(k-1)d}(1 - e^{-\kappa_{TF}d}), \quad (4.34)$$

where we introduced the slab index k so that $z' = (k-1)d$ as shown on the top right of figure 4.1 and we note $Q_k = Q((k-1)d)$. The charge distribution induced by a potential difference thus decreases exponentially within the electrode.

The expression of Q_{tot} shows that it is proportional to $\Delta\psi$, so that the integral and differential capacitances per unit area are equal and we have

$$\frac{1}{C} = \frac{\Delta\psi\mathcal{A}}{Q_{\text{tot}}} = \frac{L}{\epsilon_0\epsilon_r} + \frac{2l_{TF}}{\epsilon_0}. \quad (4.35)$$

We recognize in this expression the capacitance per unit area of an ideal parallel plate capacitor $C_0 = \epsilon_0\epsilon_r/L$ and a correction coming from the Thomas-Fermi screening, which involves a Thomas-Fermi capacitance, equal to $C_{TF} = \epsilon_0/l_{TF}$. The overall capacitance corresponds to three parallel plate capacitors in series: two Thomas-Fermi capacitors with characteristic length l_{TF} and an ideal capacitor ($l_{TF} = 0$) of length L

$$\frac{1}{C} = \frac{1}{C_{TF}} + \frac{1}{C_0} + \frac{1}{C_{TF}}. \quad (4.36)$$

This concept was used in the literature as a “quantum capacitance” to interpret experimental data^{152;257;258}. The energy cost of localizing charges in Thomas-Fermi metals thus reduces the “ability” of accumulating charge on the electrodes and the overall capacitance. Two effects have been highlighted and are studied in this work: the decrease of the total electrode charge for increasing screening lengths and the spatial distribution of the individual charges.

4.2.2 Calculations for an empty capacitor

We now compare the analytical predictions obtained in section 4.2.1 with simulation results for empty capacitors (systems (G1) and (Au1) in table 2.1 with $n = 50$ planes and varying distances $L_z \in [10, 300]$ Å between first atomic planes). Only the gold capacitors are shown here but very similar data and identical conclusions are obtained from the graphite case. As indicated in section 2.1.1, the interplanar distance for gold is $d_{\text{gold}} = 2.035$ Å.

4.2.2.1 Spatial charge distribution

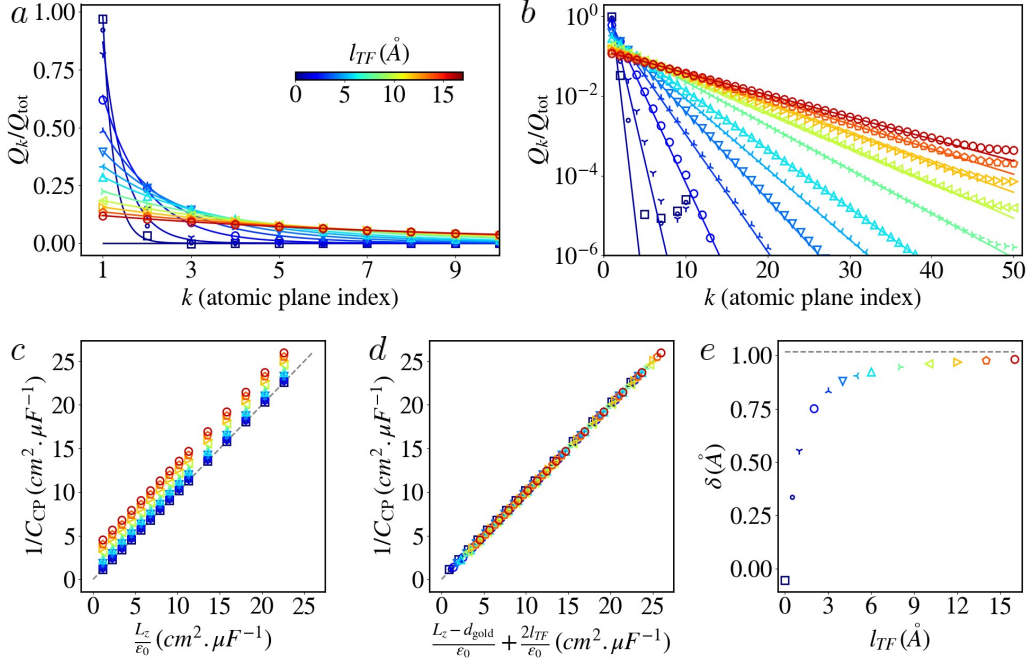


Figure 4.2: Empty Thomas–Fermi capacitor (system (Au1) in table 2.1 with $n = 50$ atomic planes and $L_z = 300 \text{ \AA}$ between the electrodes where not stated otherwise, and a potential difference $\Delta\psi = 1\text{V}$). Charges were computed for a range of Thomas–Fermi lengths $l_{TF} \in [0, 16] \text{ \AA}$. Total charge per plane normalized by the total electrode charge Q_k/Q_{tot} as a function of the atomic plane index k , in linear scale (a) and logarithmic scale (b). The symbols are simulated values for different l_{TF} , while the lines are the prediction of Eq. 4.34. Measured inverse capacitance plotted against the analytical prediction L_z/ϵ_0 for ideal capacitors (c) and for Thomas-Fermi metals using Eq. 4.38 (d), for a range of electrode spacings $L_z \in [10, 200] \text{ \AA}$. Effective distance δ , defined in Eq.4.37, as a function of l_{TF} (e). The dashed line corresponds to $d_{\text{gold}}/2$. Adapted from Ref. 256 with the permission of AIP Publishing.

The total charge per atomic plane Q_k normalized by the total electrode charge Q_{tot} was computed by imposing a potential difference of $\Delta\psi = 1 \text{ V}$ between the left and right electrodes. It is plotted against the plane index $k \in [1, 50]$ in figure 4.2a-b for a wide range of screening lengths $l_{TF} \in [0, 16] \text{ \AA}$, in linear scale for panel a and in log scale for panel b. The predicted exponential decay within the electrode of Eq. 4.34 is also shown in solid lines and agrees very well with the data. Fitting the results to an exponential function confirms that the decay length is equal to l_{TF} within 1 % for values of $l_{TF} \gtrsim d_{\text{gold}}$. Small deviations from the exponential decay arise at large z because of the finite number of atomic planes and for small l_{TF} , comparable to the characteristic atomic distances, where continuum theories are not expected to hold. Figure 4.2a indeed shows that for $l_{TF} \lesssim d_{\text{gold}}$ the predicted decay occurs on a length scale corresponding to only one to two atomic planes.

4.2.2.2 Total charge and capacitance

The total charge induced on the electrodes, measured by the capacitance, is compared to the analytical results of Eq. 4.36 in figure 4.2c-e. Panel c compares the capacitance per unit area from constant potential simulations C_{CP} to the ideal capacitor case $C_0 = \epsilon_0/L_z$, with L_z the distance between the first atomic planes, and confirms the linear relation between them with an offset that depends on l_{TF} . However, the computed values C_{CP} only coincide with the analytical prediction when introducing an effective length $L_{\text{eff}} = L_z - 2\delta$ as

$$\frac{1}{C_{\text{CP}}} = \frac{L_z - 2\delta}{\epsilon_0} + \frac{2l_{TF}}{\epsilon_0}. \quad (4.37)$$

This comes from the somewhat arbitrary choice of where to place the interface in a discrete atomistic model. A compelling choice corresponds to the so-called ‘‘Jellium edge’’²⁵⁹, which takes into account the spilling of electrons around atomic sites and towards the vacuum region²⁶⁰ and places the interface half of the interplane distance d_{gold} away from the electrode, so that $\delta = d_{\text{gold}}/2$. This definition results in the following equivalent circuit capacitance per unit area

$$\frac{1}{C} = \frac{L_z - d_{\text{gold}}}{\epsilon_0} + \frac{2l_{TF}}{\epsilon_0}, \quad (4.38)$$

which agrees well with the simulation data as shown in figure 4.2d. The error with respect to this model is quantified by extracting the value of δ from the simulation data C_{CP} . The comparison between δ and $d_{\text{gold}}/2$ is given as a function of l_{TF} in figure 4.2e. The correction δ indeed approaches half the interplanar distance for large l_{TF} values but deviates for screening lengths close to d_{gold} towards smaller distances, close to the Gaussian width of the charge distribution, as suggested in sections 3.1.5.2 and 3.2.1 for the energy profiles of an ion at a surface for $l_{TF} = 0$.

4.2.2.3 Energy profile

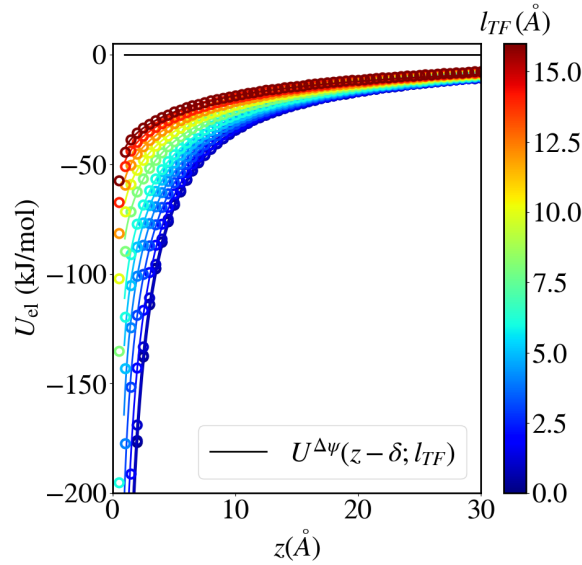


Figure 4.3: Electrostatic energy as a function of the distance z from simulations (symbols) and from Eq. 4.39 (solid lines) for a range of l_{TF} . Predictions are shown for an effective distance $z_{\text{eff}} = z - \delta$, where δ depends on l_{TF} and is taken from the values of Eq. 4.37 and figure 4.2e. Simulations were run for a gold capacitor (system (Au1) in table 2.1 modified with $n = 20$ planes and a surface area $\mathcal{A} = 219.8 \times 219.8 \text{ \AA}^2$) with a single ion of charge $q = 1e$ at a distance z from the first atomic plane.

Finally, Kaiser *et al.*⁹¹ computed the electrostatic response of a Thomas-Fermi metal to an external charge at a distance z from the surface (the generalization of Eq. 3.73 for ideal metals) and gave the following approximate expression of the electrostatic energy

$$U^{\Delta\psi}(z; l_{TF}) = -\frac{q^2}{16\pi\epsilon_0 z} \left[1 - \frac{13.8879(\kappa_{TF}z)^3 + 37.4625(\kappa_{TF}z)^2 + 18.6940(\kappa_{TF}z) + 1}{27.8648(\kappa_{TF}z)^4 + 73.0987(\kappa_{TF}z)^3 + 70.3460(\kappa_{TF}z)^2 + 20.6754(\kappa_{TF}z) + 1} \right], \quad (4.39)$$

which reduces to the result of Eq. 3.73 for $l_{TF} = 0$. The comparison with simulations is done for a gold capacitor with only $n = 20$ planes but a large surface area $\mathcal{A} = 219.8 \times 219.8 \text{ \AA}^2$ (to reduce the linear regime observed on figure 3.4) and a single ion of charge $q = 1e$ at a distance z from the first atomic plane. Results are shown as a function of the distance in figure 4.3. Using the effective interface position given by δ (defined in Eq. 4.37), we obtain a good agreement between simulations and Eq. 4.39, which further supports our interpretation.

4.2.3 Electrochemical cells

Empty capacitor simulations validate the implementation of the Thomas-Fermi model in constant potential simulations and allow to pinpoint the limits of the continuum predictions applied to an atomistic system. For real electrochemical systems with atomistic electrolytes, no analytical prediction can be derived and we use molecular dynamics simulations to investigate the influence of metallicity. In the following, results for a gold capacitor with an aqueous sodium chloride electrolyte (system (Au4) in table 2.1) are presented, where we treated the electrodes as a model material and explored a range of Thomas-Fermi screening lengths $l_{TF} \in [0, 5]$ Å. The simulation cell was first equilibrated for $l_{TF} = 0$ and $\Delta\psi = 0$ V, using a 500 ps NP_zT trajectory where the electrodes were allowed to translate along the z axis under a pressure of 1 atm. The electrode separation was then fixed to the average value (see table 2.3) and trajectories were subsequently accumulated at different voltages $\Delta\psi = 0, 1$ and 2 V for several nanoseconds each. We also prepared in a similar way other systems using graphite electrodes and three different electrolytes: pure water, 1 mol/L sodium chloride aqueous solution and a BMI-PF₆ ionic liquid (systems (G2), (G4) and (G6) in table 2.1). These systems were investigated for a range of screening lengths $l_{TF} \in [0, 4.5]$ Å for the aqueous systems and only two l_{TF} values equal to $l_{TF} = 0$ and 3.423 Å for the ionic liquid capacitor.

4.2.3.1 Charge

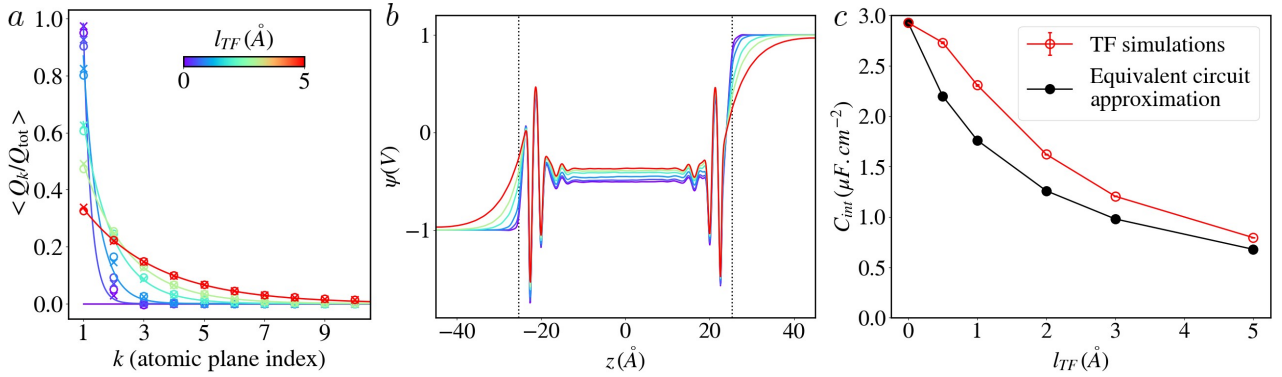


Figure 4.4: Influence of the Thomas-Fermi length on charge storage in an electrochemical cell (system (Au4) in table 2.1) at a potential difference $\Delta\psi = 2$ V. Average of the total charge per plane normalized by the total electrode charge $\langle Q_k/Q_{tot} \rangle$ as a function of the atomic plane index k (a). The symbols are simulated values for different l_{TF} for both electrodes (circles and crosses) while the lines are the prediction of Eq. 4.34. Poisson potential profile ψ as a function of the position z for different l_{TF} (b). The vertical dotted lines indicate the positions of the first atomic planes of each electrode. Computed integral capacitances as a function of the screening length l_{TF} (red open circles) compared to the equivalent circuit approximation of Eq. 4.40 (c). Panels (b-c) are adapted from Ref. 256 with the permission of AIP Publishing.

Spatial charge distribution As for the empty capacitor in section 4.2.2, we first study the charge distribution within the electrodes at fixed potential difference (here we show results for $\Delta\psi = 2$ V) in the presence of an electrolyte. Figure 4.4a shows the average ratio between the total charge per plane and the total electrode charge $\langle Q_k/Q_{tot} \rangle$ as a function of the plane index k . Note that the range of accessible l_{TF} is reduced with respect to the empty capacitor simulations because the electrode dimensions are smaller (only $n = 10$ planes could be used), but corresponds to usual l_{TF} values for conducting materials (see table 4.1). The charge distribution decays exponentially and, importantly, it follows the same analytical prediction of Eq. 4.34 for empty capacitors (solid lines), although the total charge Q_{tot} fluctuates in the presence of an electrolyte.

This feature is also visible in the Poisson potential profile shown in figure 4.4b, computed by Eq. 2.57

using the average charge density profile Eq. 2.55. Inside the electrodes, it exhibits an exponential decay, with a decay length equal to the screening length l_{TF} (see Eq. 4.31). At the interface, we observe a potential drop and oscillations characteristic of the density oscillations of the electrolyte (see section 4.2.3.2), while in the center of the cell the electric potential is constant. This results from another screening effect, due to the presence of ions (*i.e.* mobile charges) in the solution that rearrange to screen the charge accumulated on the electrodes. In the case of pure water, the electric potential profile presents oscillations at the surface but a constant slope in the bulk part because the potential is not screened.

Capacitance The integral capacitance per unit area, computed from Eq. 2.58, is shown in figure 4.4c as a function of l_{TF} . It decreases significantly on this range of screening lengths, with a non negligible variation for $l_{TF} = 0.5 \text{ \AA}$ where the capacitance is already 7 % smaller than the ideal metal case. The concept of Thomas-Fermi or quantum capacitance has been put forward in the literature^{152;257;258} and used to extrapolate the analytical prediction of Eq. 4.36 to electrochemical cells as

$$\frac{1}{C(l_{TF})} = \frac{1}{C_{TF}} + \frac{1}{C(l_{TF} = 0)} + \frac{1}{C_{TF}}, \quad (4.40)$$

where the capacitance $C(l_{TF} = 0)$ measured for an ideal metal is used to predict the value for an arbitrary l_{TF} value. This corresponds to an equivalent circuit where the ideal capacitor is placed in series with two Thomas-Fermi capacitors. This approximation is shown on figure 4.4c (black filled circles) and provides a reasonable qualitative prediction but underestimates the capacitance by 20-30 % for small l_{TF} values. The difference comes from the interplay between the charge distribution in the electrode and the structure in the electrolyte, which highlights the relevance of molecular dynamics simulations.

4.2.3.2 Electrolyte structure

We discussed in section 3.2.2 the free energy profile of an ion approaching a surface, which is simply related to the density profile using $\rho(z) = -k_B T \ln(F(z))$, and concluded that the impact of the metallicity is small at zero voltage. This is also the case for the present system with a 1 mol/L sodium chloride solution. The density profiles, defined in Eq. 2.52, are identical at $\Delta\psi = 0 \text{ V}$ for the range of l_{TF} studied for oxygen and hydrogen atoms and the small deviations observed for sodium and chloride ions are only due to statistical noise. These density profiles, shown in figure 4.5a-b for $l_{TF} = 0 \text{ \AA}$, show two main adsorption layers for water, as expected for an aqueous interface, and a more complex structuration of the ionic density profiles. The smaller Na^+ ion has a large density peak corresponding to the first water hydration layer and a second peak located after the second hydration layer. The larger Cl^- ion has a broad peak corresponding to the second hydration layer, with secondary peaks including a small peak between the first and second hydration layers. Their density fluctuations also extend farther from the electrode than the water profile.

When a finite potential difference is applied and the electrodes bear a net average total charge, the electrolyte responds differently depending on the Thomas-Fermi length l_{TF} . The overall density profile for water is not significantly impacted, and only the orientation of water molecules is. We measure this phenomenon using the distribution of angles θ defined in section 2.4.1 and shown in figure 4.5c-d for the positive and negative electrodes. At zero voltage (black dashed lines), the water molecules mostly lie in a plane parallel to the surface ($\cos\theta = 0$) or with a H-bond pointing towards the surface. At finite voltage, the water dipole moment μ reorients under the electric field created by the electrodes and has a stronger orientation towards/away from the electrodes depending on their charge (negative/positive). This manifests itself at the negative electrode by an increase in probability of $\cos\theta$ values close to -1, *i.e.* a larger portion of molecules pointing towards the surface, decreasing the peak at $\cos\theta \sim 0.5$ corresponding to water molecules with a hydrogen bond lying within the plane and the second pointing towards the bulk. At the positive electrode on the contrary, the population pointing away from the surface increases. As a direct consequence of the larger accumulated charge for

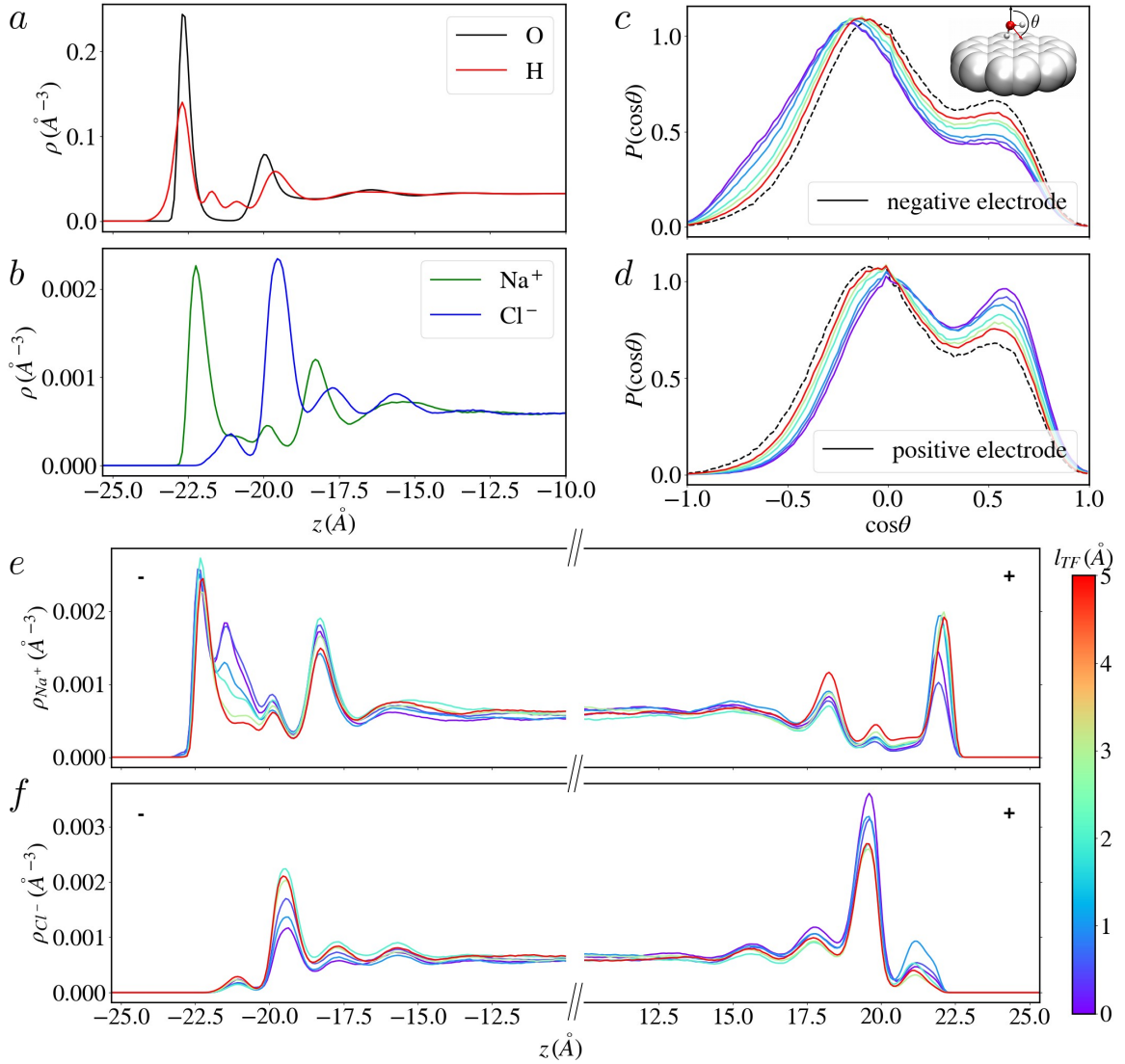


Figure 4.5: Influence of the Thomas-Fermi length on the interfacial structure in an electrochemical cell (system (Au4) in table 2.1). Density profiles for the O and H atoms (a) and for the Na^+ and Cl^- ions (b) near the electrode at zero voltage for $l_{TF} = 0$ Å. For H atoms, the profile is divided by 2 for a better comparison with the O profile. Distribution of the orientation, $\mathcal{P}(\cos\theta)$ defined in section 2.4.1, of water molecules in the first liquid layer adsorbed on the electrodes, under an applied potential of $\Delta\psi = 2$ V for different l_{TF} for the negative (c) and positive (d) electrodes; the distribution for $\Delta\psi = 0$ V and $l_{TF} = 0$ Å is shown (black dashed lines) as a reference. Density profiles for the Na^+ (e) and Cl^- (f) ions under a potential difference $\Delta\psi = 2$ V for different l_{TF} values. The negative/positive electrode is located at negative/positive z . Reproduced from Ref. 256 with the permission of AIP Publishing.

smaller l_{TF} , the orientation of water molecules is the most modified for the ideal metal case relatively to larger l_{TF} values.

Under the applied voltage, the ionic density profiles, shown in figure 4.5e-f, become asymmetric. Although there is statistical noise due to the small number of ion pairs in the simulation cell, a general trend of an increased density of Na^+/Cl^- at the negative/positive electrode is evident. As previously, the magnitude of this effect depends on l_{TF} and is rationalized by the smaller net charge accumulated for larger screening lengths. For the Cl^- ions, the main peak decreases at the negative electrode, while it increases at the positive one. It is also interesting to see similar variations in the smaller peak in between the first and second solvation layers. For the Na^+ ions, the main peak corresponding to the first hydration layer decreases at the positive electrode but only slightly increases at the negative one,

as if no more ions could be accommodated. Instead, we observe the appearance of another peak of Na^+ ions, adjacent to the first one, located between the first and second water layers, with an intensity largely dependent on l_{TF} . This second peak is quasi non-existent for the larger Thomas-Fermi lengths but increases drastically for the smaller values.

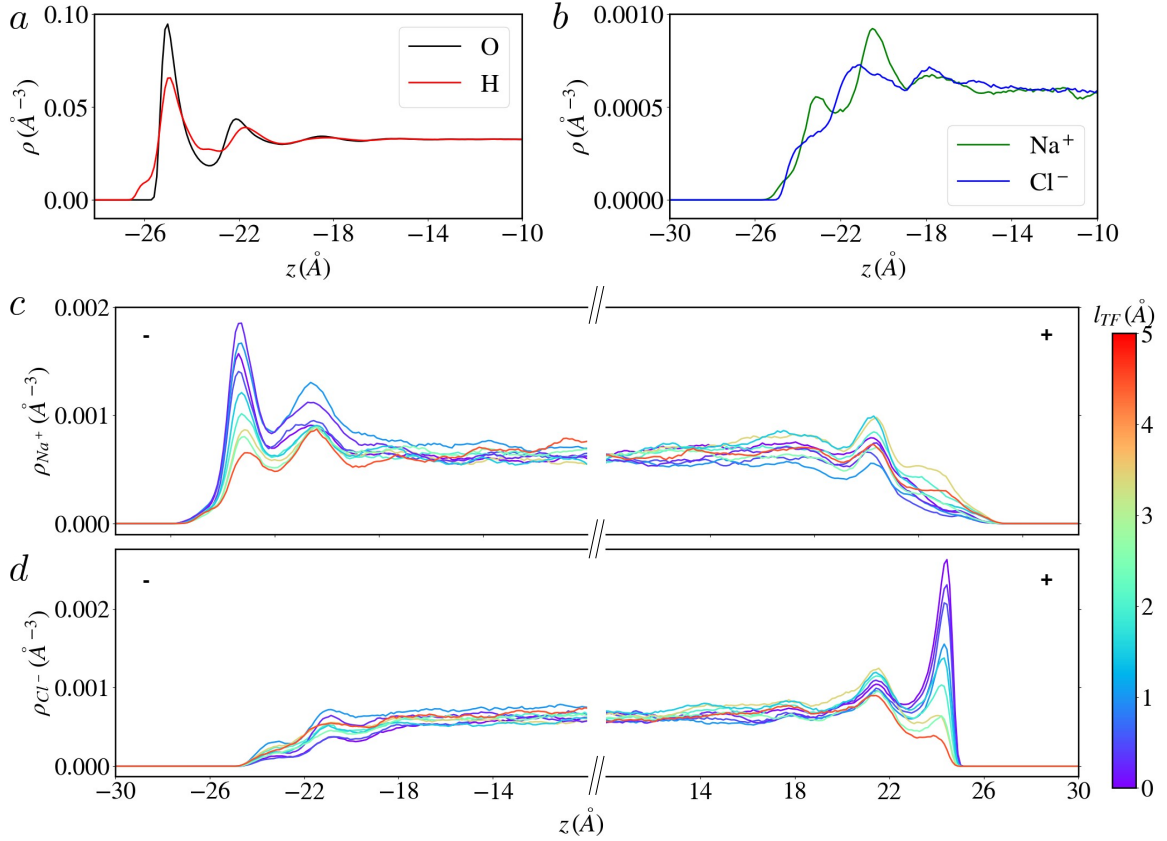


Figure 4.6: Influence of the Thomas-Fermi length on the interfacial structure in an electrochemical cell (system (G4) in table 2.1). Density profiles for the O and H atoms (a) and for the Na^+ and Cl^- ions (b) near the electrode at zero voltage for $l_{TF} = 0$ \AA . For H atoms, the profile is divided by 2 for a better comparison with the O profile. Density profiles for the Na^+ (c) and Cl^- (d) ions under a potential difference $\Delta\psi = 2$ V for different l_{TF} values. The negative/positive electrode is located at negative/positive z .

Similar tendencies are observed for the graphite capacitors, as shown in figure 4.6. The water density profile in figure 4.6a also displays two hydration layers, although the first layer is less strongly bound to the surface than on gold, where the density goes to zero between the layers. There is however a stronger orientation of the hydrogen bonds, with the presence of a “shoulder” in the hydrogen density profile close to the surface, corresponding to hydrogen bonding with the graphite surface. The ionic density profiles shown in figure 4.6b do not exhibit significant layering, as expected from the free energy profiles computed on graphite in section 3.2.2. The Na^+ density profile has two peaks in the first and second hydration layers. At zero voltage, the one further away from the surface is predominant. Upon the application of a voltage of $\Delta\psi = 2$ V, at the negative electrode little difference is observed for large Thomas-Fermi lengths but for small l_{TF} values the peak closer to the surface becomes the main one. The same mechanism occurs at the positive electrode for the Cl^- ions, with a large structural change and a shift of the major density peak from a position far from the surface for large l_{TF} values to the location of the first hydration layer.

Finally, a graphite capacitor with the BMI-PF₆ ionic liquid is investigated at $\Delta\psi = 2$ V, for a finite Thomas-Fermi length $l_{TF} = 3.423$ \AA and considering the graphite as an ideal metal, *i.e.* $l_{TF} = 0$ \AA . Density profiles for the molecular ions are given in figure 4.7a-b, as well as the electric potential profile in figure 4.7c. As observed in experiments, we find a strong oscillatory behavior of the electric potential

that extends over several nanometers from the surface. The impact on the ionic density profiles is more complex than for sodium and chloride ions, with an increase and decrease of density peaks, as well as broadening and the shift of some peaks.

Overall, significant changes to the structure of the electrolytes are observed on a variety of capacitors and with different surfaces, that can ultimately be related to the difference in accumulated charge on the electrode.

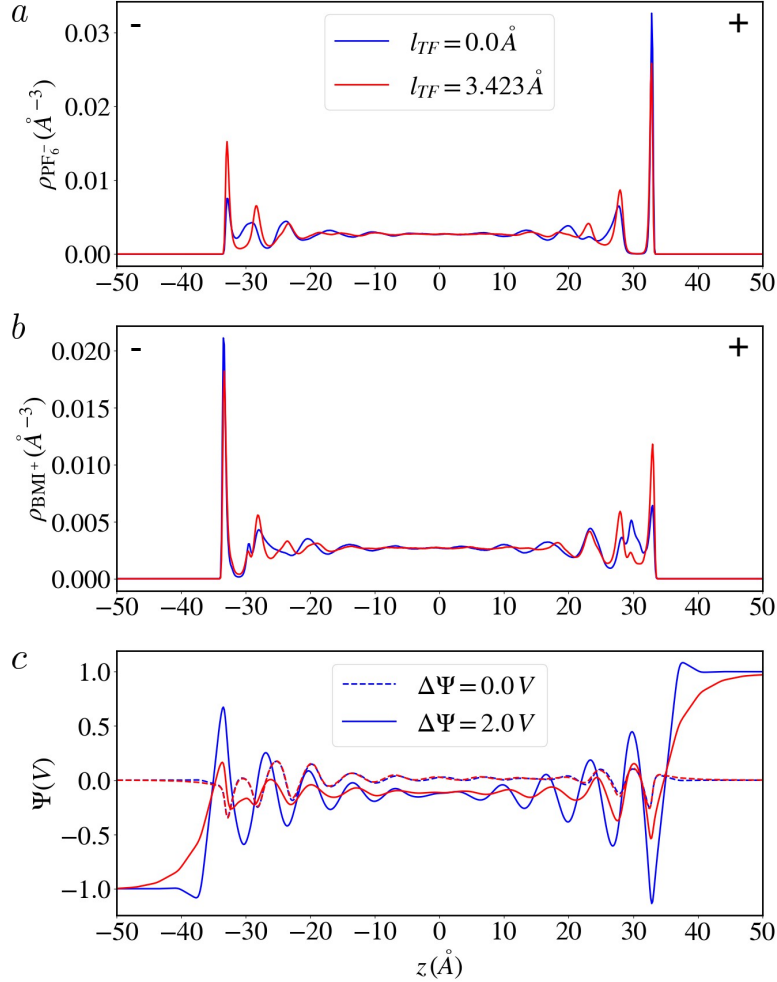


Figure 4.7: Influence of the Thomas-Fermi length on the interfacial structure for a graphite-BMI-PF₆ capacitor (system (G6) in table 2.1), for a potential difference of $\Delta\psi = 0$ V (dashed lines) and $\Delta\psi = 2$ V (solid lines), for two values of screening length: $l_{TF} = 0.0$ (blue lines) and $l_{TF} = 3.423$ Å (red lines). Density profiles at $\Delta\psi = 2$ V for the PF₆⁻ anions (a) and the C1 grain (see table 2.5) of BMI⁺ cations (b). Poisson potential profile ψ as a function of the position z (c). The negative/positive electrode is located at negative/positive z .

4.2.3.3 Charge dynamics

The previous observations on the structure of the electrolyte can be easily rationalized by considering the decrease in capacitance, *i.e.* in the accumulated charge on the electrodes, due to the energy penalty for localizing electrons proportional to l_{TF}^2 . These results however are not equivalent to previous studies^{158;159} that compared constant potential and constant charge simulations with an identical average total charge on the electrodes. Nevertheless, at zero voltage, there is no net charge on the electrodes so that this main effect is not present and the influence of electrode polarization alone can be investigated. As shown in figure 4.4a-b, the structure is not influenced by the metallicity of the surface.

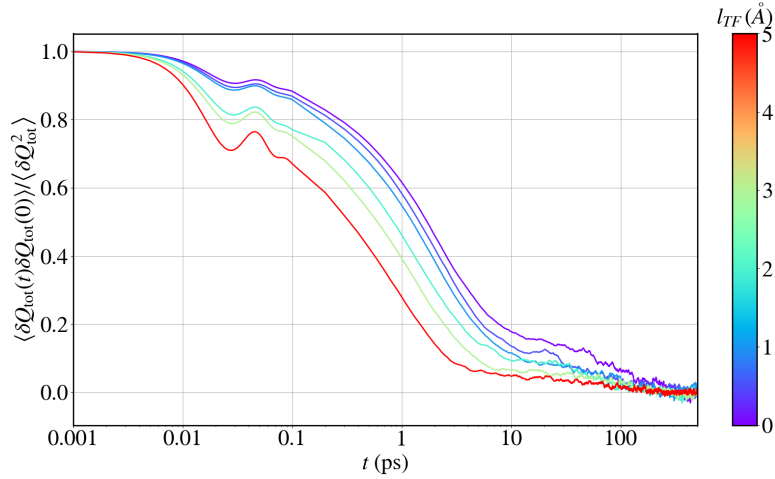


Figure 4.8: Normalized autocorrelation function of the total charge $C_{QQ}(t) = \langle \delta Q_{\text{tot}}(t) \delta Q_{\text{tot}}(0) \rangle / \langle \delta Q_{\text{tot}}^2 \rangle$ at zero voltage for an electrochemical system (system (Au4) in table 2.1) as a function of time t (in logarithmic scale) for a range of $l_{TF} \in [0, 5]$ Å. Adapted from Ref. 256 with the permission of AIP Publishing.

We thus follow Refs. 158 and 159, which found the largest impact of polarization on the dynamics of charge and discharge of a capacitor. However, to better study the influence of metallicity, instead of switching on a given potential difference $\Delta\psi$ and measure the evolution of the total charge with time, we make use of the linear response theory and directly investigate the dynamics of Q_{tot} at $\Delta\psi = 0$ V. Indeed, although there is no net charge on the electrodes, the instantaneous total charge fluctuates around zero according to the differential capacitance, as shown in figure 3.3b. The decrease of the differential capacitance with increasing l_{TF} should thus be reflected in the dynamics of the total charge at $\Delta\psi = 0$ V, measured by the normalized autocorrelation function of Q_{tot} , C_{QQ} , defined in Eq. 2.60 and shown in figure 4.8 for a range of screening lengths. The decay of C_{QQ} with time characterizes the relaxation of a spontaneous charge fluctuation and is therefore related to the charging or discharging time of the capacitor, an important property that quantifies the power delivered by the device. Note that similar decays and l_{TF} dependence is observed for the graphite capacitors with pure water, 1M NaCl solution and BMI-PF₆ ionic liquid.

On figure 4.8, we observe for the gold capacitors that the dynamics are slower for larger l_{TF} values, with an impact on a wide range of timescales. A rough bi-exponential fit allows to extract a first decay at very short times, with a characteristic time between $\tau_1 \approx 15$ fs for small l_{TF} values and $\tau_1 \approx 13$ fs for $l_{TF} = 5$ Å. This fast decay is probably due to the fast reorientation of water molecules at the surface. The difference with metallicity can be explained by weaker interactions of the solvent with the surface in the case of non-ideal metals, also shown with the orientation of water at $\Delta\psi = 2$ V in figure 4.5c-d, leading to faster dynamics. The second decay has a characteristic time of $\tau_2 \approx 1 - 3$ ps, while a noisy third long time decay (of the order of hundreds of ps) contributes to a long tail in the autocorrelation function. These longer timescales can be attributed to ionic diffusion within the hydration layers or to the exchange of ions with the bulk. This is supported by the lack of such very long decays for pure water capacitors. Lastly, the influence of l_{TF} on these time decays is more difficult to assess but further interpretation could spawn from the link with equivalent circuits of capacitors in series.

These results show that, contrary to what seemed from previous studies¹²⁸, and although no impact on the structure is measured at $\Delta\psi = 0$ V, there is an influence of the electrode polarization on the dynamics of the total charge, not only at high voltages.

“Forget-me-not”: Accounting for the metallicity: the Thomas-Fermi semiclassical model

- We improve the description of electronic effects inside the electrodes by including the contribution from the kinetic energy of electrons. This contribution is given by the Local Density Approximation or Thomas-Fermi model and is adapted to Constant Potential simulations. It includes a quadratic term in the charges, which penalizes the localization of charge.
- The Thomas-Fermi model can describe the screening of an external perturbation (charge, applied potential) by a free electron gas and introduces a screening length l_{TF} . Analytical predictions are derived and compared to empty capacitor simulations. Electrochemical cells are systematically studied as a function of l_{TF} .
- The charge distribution within the electrodes decays exponentially with the characteristic length l_{TF} . The capacitance decreases with l_{TF} and can be approximated using equivalent electrical circuits. The structure of the electrolyte depends on l_{TF} for finite voltages due to the different accumulated charges on the electrodes. The dynamics of charging/discharging is slowed down for increasing l_{TF} .

Chapter 5

Phase transitions under confinement

5.1 Crystallization under confinement: thermodynamic origin

As discussed in the introduction, most fluids under confinement exhibit new and unexpected characteristics, due to the interaction with the confining medium. Indeed, when the ratio of interfacial atoms, that are perturbed by the presence of the interface, over bulk atoms cannot be neglected, interesting phenomena emerge from the competition between surface and bulk contributions to the (free) energy. In particular, this work focuses on the phase transitions under confinement depending on the metallicity of the confining surface, building on recent experiments of nanoscale capillary freezing of ionic liquids described in Refs. 84 and 86, and discussed in section 1.1.3. The first aspect highlighted by these experiments is the shift of the transition temperature (here freezing temperature) as a function of the characteristic confining length, known as the Gibbs-Thomson (GT) equation, which links the change in transition temperature to bulk quantities and the difference of surface tension between each phase and the confining medium. The second aspect, *i.e.* the dependence of such phenomenon on metallicity, is discussed in chapter 6.

Here, we first review the thermodynamic origin of changes in phase diagrams due to interfaces in section 5.1 and give a derivation of the GT equation for the crystallization under confinement in section 5.2, discussing the necessary approximations. These are then tested on a model system in section 5.3 by computing the different terms of the GT equation and comparing the predicted value to melting temperatures determined by hyper-parallel tempering Monte Carlo simulations in section 5.3.3.

5.1.1 Interfacial free energies and their consequences

The phase equilibrium is determined by an equality of thermodynamic potentials as demonstrated in section 2.4.5 so that, taking the bulk phase equilibrium as a reference, the additional interactions with the confining surfaces must provoke a change in the phase coexistence point. Taking the example of crystallization, without loss of generality, if the interaction of the surface with both phases is identical, no discrimination between them is introduced and there is no shift in the coexistence curve. But if the interaction of the surface with the liquid phase is favorable with respect to the solid phase, the energy needed to melt the solid will be lower and so will be the melting temperature. In a model system of a liquid (L) confined in a slit pore between two parallel walls (W) at a distance H (see *e.g.* slit pore in figure 5.2b), the shift in melting temperature T_m is given by the GT equation

$$\frac{T_m - T_m^b}{T_m^b} = \frac{2(\gamma_{LW} - \gamma_{SW})}{H\rho\Delta_m h}, \quad (5.1)$$

where T_m^b is the bulk melting temperature, γ_{LW} and γ_{SW} are respectively the liquid-wall and solid-wall surface tensions, $\rho = N/V$ the density and $\Delta_m h = h_L - h_S$ the latent heat of melting per particle. Since $\Delta_m h$ is usually positive, the sign of the temperature shift is determined by the difference in interfacial

free energy between the solid or the liquid phase and the confining wall, *i.e.* by the difference in surface tension $\Delta\gamma = \gamma_{LW} - \gamma_{SW}$, as expected from the previous arguments. Several derivations can be found in the literature^{39–41;261–269} that however differ in the final form, *e.g.* in the use of the solid or liquid density in the denominator, in the use of the solid-liquid surface tension and a contact angle or in the various geometries used for the derivation (slit or cylindrical pores – see figure 5.2). Moreover, several of these derivations do not explicitly state the ensemble and the underlying assumptions, making it difficult to test them.

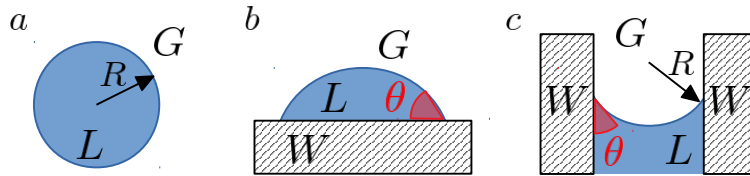


Figure 5.1: Various geometries of curved liquid (L)-gas (G) interfaces: a liquid drop in bulk vapor (a), a liquid drop in vapor on a surface wall (W) (b) and a liquid in a thin capillary (c). In panels (a) and (c) R is the curvature radius while θ is the contact angle in panels (b-c).

An equivalent phenomenon occurs for the liquid-vapor transition, *i.e.* capillary condensation, where vapor condensates in small pores at a temperature above the liquefaction temperature. This situation usually results in the creation of a meniscus at the liquid-vapor interface inside the capillary (see figure 5.1c) because of the balance of surface tensions between the liquid and vapor phases and the walls, related to the contact angle θ by the Young equation

$$\gamma_{GW} - \gamma_{LW} - \gamma_{LG} \cos \theta = 0, \quad (5.2)$$

where γ_{GW} is the vapor-wall surface tension and γ_{LG} is the liquid-vapor surface tension. The curved interface testifies to a difference in pressure ΔP between the two phases, called the Laplace pressure, which is given by the Young-Laplace equation²⁷⁰

$$\Delta P = P_G - P_L = -\frac{2\gamma_{LG}}{R} \quad (5.3)$$

where R is the curvature radius of the liquid-vapor interface. This pressure difference across the interface is responsible *e.g.* for the rise of liquids in a thin capillary (or capillary action). This in turn is related to the nucleation of a small drop of liquid in a bulk vapor phase, which is hindered by the energetic penalty of the interface. Such phenomenon results in the Kelvin equation²⁷⁰

$$\ln \left[\frac{P_G}{P_{\text{sat}}} \right] = \frac{2\gamma_{LG}}{R\rho_L k_B T}, \quad (5.4)$$

where P_{sat} is the bulk saturated vapor pressure at temperature T while P_G is the vapor pressure in the presence of a spherical nucleus of radius R . This equation is similar to the GT equation as it includes a shift in pressure (a similar equation can be derived at constant pressure for a shift in temperature) inversely proportional to a characteristic size of the liquid phase and due to the energetic cost of an interface. However, it is important to consider the differences between the two situations, which are often mixed because of their similarities and the fact that they yield similar expressions. When considering the growth of a nucleus in a bulk phase (*e.g.* solid in liquid, liquid in vapor or inversely vapor in liquid), one quantifies the energy barrier due to the creation of the interface between the two phases and this results, even for thermodynamic conditions where the nucleated phase is more stable than the bulk one, in a critical nucleus size above which the liquid phase can grow²⁷¹. Similarly for the solid-liquid transition, one can express the critical size of a crystal nucleus in a bulk liquid phase, which is very similar to Eq. 5.1. These relations explain why one can obtain supercooled liquid without observing crystallization, or overheated liquid where the vaporization is inhibited until enough energy to create a bubble is given to the system. This problem therefore pertains to a kinetic barrier and does not correspond to a global equilibrium²⁷². These equations are however routinely used to

interpret the modification of phase coexistence properties under confinement and the ambiguity is worsened by the use of the name ‘Gibbs-Thomson equation’ for both the crystal nucleation and the crystallization under confinement, without distinction, in the literature^{272;273}. This results in several derivations of the confined GT equation based on the growth of a nucleus in a confined pore, which are rapidly discussed in the following. Aside from the conceptual difference, note that the assumption of a spherical crystal nucleus, currently used for drops and bubbles, is questionable for faceted solid nuclei¹⁷⁶.

5.1.2 Gibbs-Thomson equation from a nucleation point of view

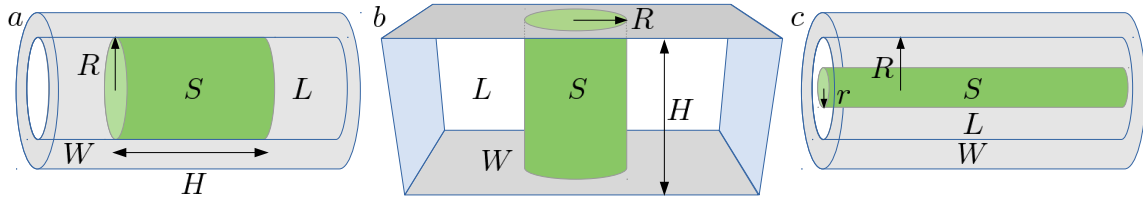


Figure 5.2: Various confined geometries considered for the nucleation of a solid (S) phase in a liquid (L) phase under confinement by planar or cylindrical walls (W). r , R and H are geometrical parameters that characterize the different geometries.

In their derivation, Warnock *et al.*^{261;262} consider a plug of crystal inside a cylindrical pore or a slit pore, as depicted in figure 5.2a-b. The authors write the change in free energy ΔF between the system with the liquid phase and that with a solid plug with a volumetric, a liquid-solid and a wall interfacial contribution

$$\Delta F_{\text{cyl}} = -\pi R^2 H \rho_S \Delta_m s (T_m^b - T) + 2\pi R H (\gamma_{SW} - \gamma_{LW}) + 2\pi R^2 \gamma_{LS} \quad (5.5)$$

$$\Delta F_{\text{slit}} = -\pi R^2 H \rho_S \Delta_m s (T_m^b - T) + 2\pi R^2 (\gamma_{SW} - \gamma_{LW}) + 2\pi R H \gamma_{LS} \quad , \quad (5.6)$$

where $\Delta_m s$ is the entropy of melting per particle and R and H are geometrical parameters defined in figure 5.2a-b. The free energy difference is thus depends on the plug size (H or R) so that the crystal nucleus can either expand infinitely or disappear, depending on the temperature. The melting point is determined by finding the thermodynamic conditions for which $\partial\Delta F/\partial H = 0$ (or $\partial\Delta F/\partial R = 0$), which ultimately gives the GT equations

$$T_{\text{cyl}} = T_m^b + 2 \frac{\gamma_{LW} - \gamma_{SW}}{R \rho_S \Delta_m s} \quad (5.7)$$

$$T_{\text{slit}} = T_m^b + 2 \frac{\gamma_{LW} - \gamma_{SW}}{H \rho_S \Delta_m s} - \frac{\gamma_{LS}}{H \rho_S \Delta_m s R} \xrightarrow{R \rightarrow \infty} T_m^b + 2 \frac{\gamma_{LW} - \gamma_{SW}}{H \rho_S \Delta_m s} \quad , \quad (5.8)$$

where we took $R \rightarrow \infty$ for the slit pore. However when considering a similar concept with the setup of figure 5.2c with an axial cylindrical solid nucleus, one finds instead

$$T_{\text{cyl}} = T_m^b - \frac{\gamma_{LS}}{r \rho_S \Delta_m s} \quad , \quad (5.9)$$

which differs from Eq. 5.7, even for $r \rightarrow R$. Moreover, the choice of the ensemble and of the free energy as thermodynamic potential is not clear.

5.1.3 Gibbs-Thomson equation from the thermodynamic equilibrium of the phases

The argument of the growth of a crystal nucleus results in the appearance of the solid-liquid surface tension γ_{LS} related to the solid-liquid interface. However, the shift of phase coexistence under confinement needs only to be related to the presence of interfaces with the walls, which modify the free energy of the system because of the change in interfacial free energy, without any reference to an

interface between the solid and liquid phases. We are thus interested in the equilibrium coexistence of two confined phases, *i.e.* the points of the phase diagram where both phases are equally stable (as is done for the solid-liquid bulk coexistence).

The developments by Evans *et al.*^{41:274-277} correspond to this goal. Their considered setup is a slit pore formed by two confining walls of area A_W separated by a distance H and immersed in an explicit reservoir at fixed chemical potential μ , volume V and temperature T . The two additional variables A_W and H are two new thermodynamic fields with their conjugate fields γ the surface tension and $A_W f$ the force between the walls. The authors thus study the grand potential $\Omega = U - TS - \mu N$ (see section 2.2.1) and write its variations as

$$d\Omega = -SdT - PdV - Nd\mu + 2\gamma dA_W - (A_W f)dH \quad (5.10)$$

with P the pressure in the reservoir, N the number of particles and S the entropy. The derivation²⁷⁴ considers excess quantities with respect to the bulk reservoir without the plates and shows that $\Omega = -PV + 2\gamma A$. It demonstrates several Maxwell relations and analyses stability and phase equilibria. These thermodynamic equations are then applied to the capillary condensation. In a nutshell, the difference in chemical potential with respect to the bulk $\Delta\mu \equiv \mu_{sat} - \mu$ is expressed as

$$\Delta\mu = \frac{\Delta P}{\rho_G} = \frac{\Delta T}{\rho_G} \frac{\partial P_{sat}}{\partial T} = \frac{\Delta T}{\rho_G} \frac{\Delta_{vap} s}{(1/\rho_G - 1/\rho_L)}, \quad (5.11)$$

where ΔT and ΔP are the shifts in temperature and pressure due to confinement and the last equality is from the Clapeyron equation Eq. 2.68. Using a version of the Kelvin equation, they obtain

$$\Delta T = \Delta\mu \frac{1 - \rho_G/\rho_L}{\Delta_{vap} s} = 2\Delta\gamma \frac{1 - \rho_G/\rho_L}{H(\rho_L - \rho_G)\Delta_{vap} s} = \frac{2\Delta\gamma}{H\rho_L\Delta_{vap} s}. \quad (5.12)$$

Our derivation is largely inspired from this thermodynamic treatment, applying it to the crystallization transition and using a simpler setup.

5.2 Derivation of the Gibbs-Thomson equation

5.2.1 A “confined Clapeyron” approach in the $\mu A_W HT$ ensemble

As underlined in the previous section, the focus of this derivation of the GT equation is the determination of the thermodynamic conditions for which two phases, in this particular case the solid and liquid phases, are both stable under confinement. The system and ensemble chosen in this work are inspired from the experimental setup of Refs. 84 and 86, discussed in section 1.1.3 and schematized in figure 5.3. Because of the large radius of the confining tip ($\sim 1.5 - 5\mu\text{m}$ and $\sim \text{mm}$), we consider the confined geometry as a model slit pore (see inset of figure 5.3), with two parallel walls at a distance H separated by either the solid or the liquid phase. Note that these phases are never considered in contact with one another but entirely fill the pore volume. The walls, that we assume identical, have a surface area A_W so that the confined volume is $V = A_W H$. In addition, we take this to be an open system that exchanges particles with the external reservoir, in the case of figure 5.3 the non-confined liquid drop on the surface, which fixes the chemical potential μ in the confined phase. Lastly, the system is kept at fixed temperature T , so that the thermodynamic ensemble corresponding to this experiment is the $\mu A_W HT$ ensemble. This system is thus simpler than the one considered by Evans *et al* in their derivation^{41:274-277}.

Similarly to the grand canonical ensemble discussed in section 2.2.1, the thermodynamic potential in the $\mu A_W HT$ ensemble is the grand potential

$$\Omega = U - TS - \mu N = -PA_W H + 2\gamma A_W, \quad (5.13)$$

with the exception that we added a surface contribution $2\gamma A_W$ where the factor 2 is because of the two interfaces and γ is taken as a free energy per unit area. Borrowing from the traditional considerations

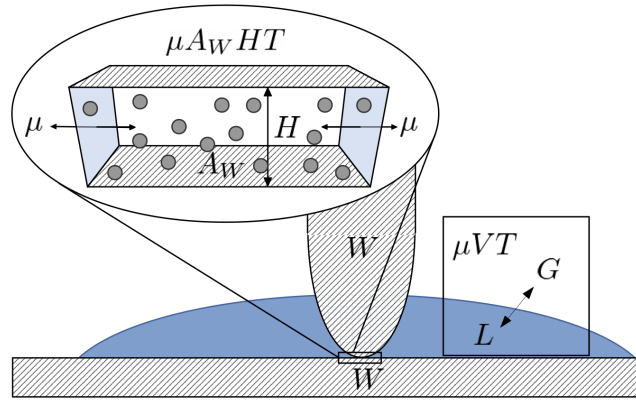


Figure 5.3: Representation of the experimental setup of Refs. 84 and 86 where a drop of ionic liquid is confined between a surface and a tip of an Atomic Force Microscope or of a dynamical surface force tribometer. The macroscopic liquid drop is in a liquid-vapor equilibrium, while the inset shows the model system chosen to represent the confined fluid in the $\mu A_W H T$ ensemble. Reproduced from Ref. 278 with the permission of AIP Publishing.

of phase coexistence given in section 2.4.5.1, at the confined coexistence, the thermodynamic potentials of the liquid and solid phases are equal, *i.e.* $\Omega_L = \Omega_S$. From Eq. 5.13, it follows that the pressures P_L and P_S for a pore filled with liquid or with solid are related by

$$P_L - P_S = \frac{2(\gamma_{LW} - \gamma_{SW})}{H}. \quad (5.14)$$

Following the derivation of the Clausius-Clapeyron equation Eq. 2.68, we consider the changes in the grand potential associated with a change in the relevant thermodynamic variables $d\mu$, dA_W , dH , dT along the phase coexistence, so that $\Omega_S + d\Omega_S = \Omega_L + d\Omega_L$ thus $d\Omega_S = d\Omega_L$. The thermodynamic identities Eqs. 2.25 are modified as

$$d\Omega = -SdT - PA_W dH + (2\gamma - PH)dA_W - Nd\mu. \quad (5.15)$$

Using Eq. 5.14 to simplify the term in dA_W , we obtain

$$(S_L - S_S)dT + \frac{2A_W(\gamma_{LW} - \gamma_{SW})}{H}dH + (N_L - N_S)d\mu = 0, \quad (5.16)$$

which relates the variations of the control variables T , H and μ along the solid-liquid coexistence, as does the Clapeyron equation Eq. 2.68 for the variations of T and P along the bulk coexistence in the NPT ensemble. As expected, the variations of the surface area have no effect on Eq. 5.16.

5.2.2 Integration along a bulk-to-confined thermodynamic path

Integration of Eq. 5.16, from an unconfined bulk system ($H \rightarrow \infty$ at T_m^b) down to a confined system at finite H and corresponding melting temperature T_m , yields the relationship between the changes in control variables, *i.e.* the GT equation. The next step requires the specification of additional information on the external reservoir that relates the variation of the chemical potential to the variations of temperature $d\mu/dT$ along the bulk-to-confined integration path. We isolate this dependence by rearranging Eq. 5.16 as

$$\frac{dH}{H^2} = -\frac{dT}{2(\gamma_{LW} - \gamma_{SW})} \left[\rho_L s_L - \rho_S s_S + (\rho_L - \rho_S) \frac{d\mu}{dT} \right], \quad (5.17)$$

where we used the densities $\rho = N/V$ and entropies per particle $s = S/N$.

5.2.2.1 Determination of $d\mu/dT$

In the simpler case of an external isobaric liquid, the chemical potential dependence on temperature is easily given by

$$\left(\frac{d\mu}{dT}\right)_{N,P} = \left(\frac{\partial^2 G_L}{\partial T \partial N}\right)_{N,P} = \left(\frac{\partial^2 G_L}{\partial N \partial T}\right)_{N,P} = -\left(\frac{\partial S_L}{\partial N}\right)_{N,P} = -s_L. \quad (5.18)$$

In the setup described in figure 5.3, the liquid drop is in equilibrium with its vapor, as illustrated in the right part of the figure. The chemical potential imposed by the reservoir is thus set by the bulk liquid-vapor coexistence, *i.e.* $\mu(T) = \mu_L(T) = \mu_G(T)$. Following the same procedure as in the previous section, the equality of the grand potential and of its variations along the coexistence line results in the equality of pressures $P_G = P_L$ and

$$-S_G dT - P_G dV - N_G d\mu = -S_L dT - P_L dV - N_L d\mu, \quad (5.19)$$

which ultimately yields

$$\frac{d\mu}{dT} = -\frac{\rho_L s_L - \rho_G s_G}{\rho_L - \rho_G}. \quad (5.20)$$

In general, the liquid phase is denser than the vapor one ($\rho_L \gg \rho_G$) and the entropy per particle for the gas is larger than for the liquid ($s_G \gg s_L$). To simplify Eq. 5.20, we explicitly compute this quantity for the van der Waals fluid because it is a good approximation for both the liquid and vapor phases. It includes an excluded volume term b and an attractive term a . The entropy per particle of the van der Waals fluid of density ρ is known²⁷⁹ and equal to

$$\frac{s}{k_B} = \ln\left(\frac{1 - b\rho}{\rho\lambda^3}\right) + \frac{5}{2}, \quad (5.21)$$

where λ^3 is the quantum volume with λ the De Broglie wavelength. Introducing $\epsilon_\rho = \rho_G/\rho_L$ we obtain

$$\frac{\rho_G s_G}{\rho_L s_L} = \frac{\epsilon_\rho [\ln(1 - b\rho_G) - \ln(\rho_L \lambda^3) + 5/2] - \epsilon_\rho \ln \epsilon_\rho}{\ln(1 - b\rho_L) - \ln(\rho_L \lambda^3) + 5/2}. \quad (5.22)$$

Noting that $\epsilon_\rho \ll 1$ and $b\rho_G \ll 1$, we have $\rho_G s_G \ll \rho_L s_L$, so that we can approximate Eq. 5.20 by

$$\frac{d\mu}{dT} \approx -s_L. \quad (5.23)$$

We tested numerically this approximation for a van der Waals fluid using the coexistence curve derived in Ref. 279 for $b = \sqrt{2}\sigma^3$ and $a/b = 5\pi\epsilon/9$. Results are shown in figure 5.4, expressed in reduced units with respect to the critical temperature $T_c = 8a/(27b)$, pressure $p_c = a/(27b^2)$ and volume $v_c = 3b$. The relative error due to Eq. 5.23 is smaller than 10 % on a large temperature range and much smaller for temperatures far from the critical point.

We thus write the derivative of the chemical potential with respect to temperature as

$$\frac{d\mu}{dT} = -\frac{\rho_L^b s_L^b - \rho_G^b s_G^b}{\rho_L^b - \rho_G^b} \approx -s_L^b, \quad (5.24)$$

where we used the superscript b to refer to the bulk external liquid and vapor phases. From Eq. 5.24 and Eq. 5.17, we write

$$\frac{dH}{H^2} = -\frac{(\rho_L - \rho_S)(s_L - s_L^b) + \rho_S(s_L - s_S)}{2(\gamma_{LW} - \gamma_{SW})} dT, \quad (5.25)$$

where we carefully distinguished the bulk and confined properties. For sufficiently large confining distances, the effect of confinement on these properties is expected to become negligible and we approximate the densities and entropies per particle of the confined phases by the bulk ones, which results in

$$\frac{dH}{H^2} = -\frac{\rho_S^b \Delta_m s^b}{2(\gamma_{LW} - \gamma_{SW})} dT, \quad (5.26)$$

where $\Delta_m s^b = s_L^b - s_S^b$ is the bulk entropy of melting per particle.

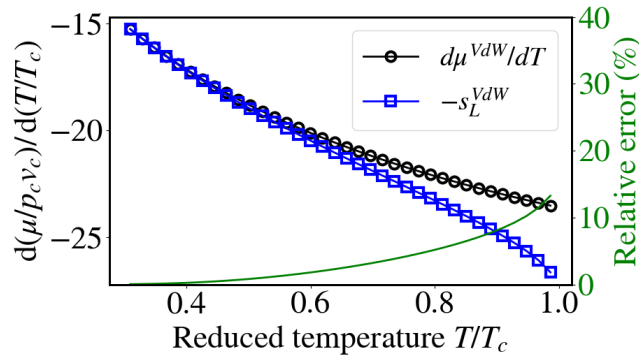


Figure 5.4: Comparison between $d\mu/dT$ estimated by Eq. 5.20 (black circles) and $-s_L$ computed by Eq. 5.21 (blue squares) as a function of temperature in reduced units for a van der Waals fluid ($\mu_{red} = \mu/p_c v_c$ et $T_{red} = T/T_c$, where the c subscript refers to the critical point). Associated relative error (green line) corresponding to the approximation Eq. 5.23, with values indicated on the right y-axis. Reproduced from Ref. 278 with the permission of AIP Publishing.

5.2.2.2 Integration along the thermodynamic path

Eq. 5.26 relates the variations of confinement height H with those of the temperature T along the coexistence. We now take a thermodynamic path between the unconfined bulk system with $H \rightarrow \infty$ at temperature T_m^b and a confined system with a finite H and corresponding melting temperature T_m , and integrate the joint variations of H and T along the coexistence. Assuming that the ratio $\frac{\rho_S^b \Delta_m s^b}{2(\gamma_{LW} - \gamma_{SW})}$ is independent of T and H along the integration path, which should be accurate in the limit of large pore sizes and small temperature shifts, we have

$$\int_H^{+\infty} \frac{dH}{H^2} = -\frac{\rho_S^b \Delta_m s^b}{2(\gamma_{LW} - \gamma_{SW})} \int_{T_m}^{T_m^b} dT. \quad (5.27)$$

In the setup of figure 5.3, because the external reservoir is a liquid-vapor equilibrium, the melting temperature T_m^b is actually the bulk triple point T_T^b , so that the GT equation in this particular case reads

$$T_m(H) = T_T^b + \frac{2(\gamma_{LW} - \gamma_{SW})}{H \rho_S^b \Delta_m s^b}. \quad (5.28)$$

Another way of writing the GT equation which is more readily applicable to the experiments is

$$H_m(T) = \frac{2(\gamma_{LW} - \gamma_{SW})}{(T - T_T^b) \rho_S^b \Delta_m s^b}, \quad (5.29)$$

which gives the height $H_m(T)$ at which the system is at coexistence point for a given temperature T .

5.2.2.3 Other external conditions and geometries

In the case of an isobaric liquid, the melting temperature at a given pressure P should be used instead

$$T_m(H) = T_m^b(P) + \frac{2(\gamma_{LW} - \gamma_{SW})}{H \rho_S^b \Delta_m s^b}. \quad (5.30)$$

Because no assumption on the densities (such as $\rho_L = \rho_S$) was made, the present derivation can be directly applied to other situations, *e.g.* to the capillary condensation studied by Evans *et al.*²⁷⁴. For a liquid-vapor equilibrium under confinement with a vapor reservoir at P_{ext} , we easily obtain

$$T_{vap}(H) = T_{vap}^b(P_{ext}) + \frac{2(\gamma_{GW} - \gamma_{LW})}{H \rho_L^b \Delta_{vap} s^b}. \quad (5.31)$$

It can also be extended to other geometries such as a cylindrical pore as in figure 5.2a by modifying the volume $V = \pi R^2 H_c$ and area $A_W = 2\pi R H_c$ expressions, where R is the radius and plays the role of the confinement length H while H_c is the cylinder length. We then obtain

$$T_m(H) = T_m^b(P) + \frac{2(\gamma_{LW} - \gamma_{SW})}{R\rho_S^b\Delta_m s^b}. \quad (5.32)$$

5.3 Numerical predictions of the Gibbs-Thomson equation

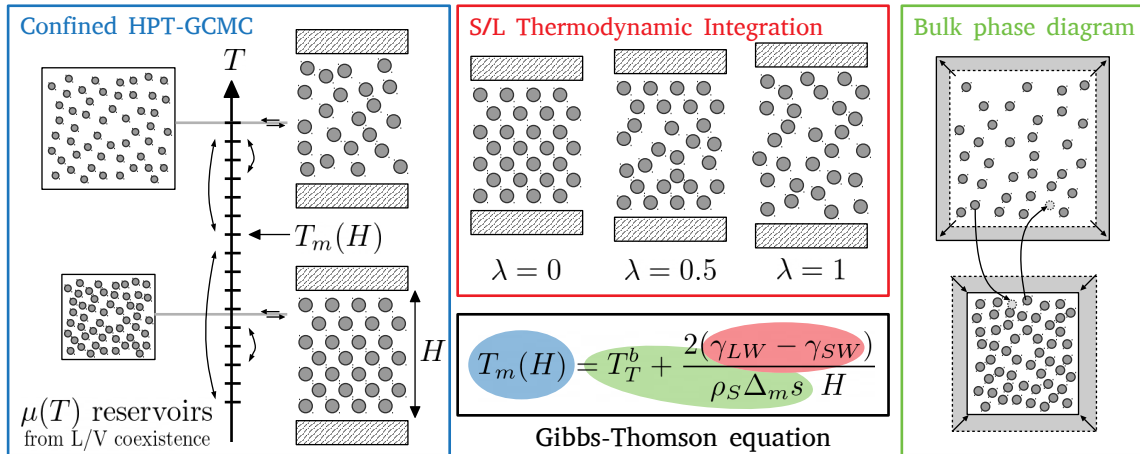


Figure 5.5: Illustration of the strategy of this work to study the GT equation Eq. 5.28. Bulk properties T_T^b , ρ_S and $\Delta_m s$ are computed using the bulk phase diagram (green area) and the surface tension term with a solid-liquid thermodynamic integration procedure (red area). Predictions are then compared to confined melting temperatures $T_m(H)$ as a function of the confinement height H , estimated using hyper-parallel tempering grand canonical Monte Carlo simulations (blue area). Reproduced from Ref. 278 with the permission of AIP Publishing.

To test the various assumptions made in section 5.2 and extract numerical values of the parameters appearing in Eq. 5.28, we perform molecular simulations of the simple Lennard-Jones (LJ) model system confined between unstructured Steele walls, corresponding to the confined system (S7) and its bulk equivalent (B7) in table 2.2. The interaction parameters are given in table 2.8 and it is important to highlight that we use a truncated shifted Lennard-Jones (TS-LJ – see section 2.1.3.2) with a cutoff radius $r_{\text{cut}}^* = 2.5$, which has a significant impact on the LJ phase diagram. In the following sections, we will use reduced LJ units introduced in section 2.1.2.2.

The strategy behind this work is illustrated in figure 5.5. In a first step, we estimate the terms involved in Eq. 5.28 by computing the bulk phase diagram as discussed in section 5.3.1 for the bulk properties and by using a thermodynamic integration procedure introduced in section 5.3.2 that yields the difference in surface tension $\gamma_{LW} - \gamma_{SW}$. In a second step, we compare the GT prediction with the melting temperature under confinement directly estimated using hyper-parallel tempering grand canonical Monte Carlo simulations of confined systems in equilibrium with an external reservoir in section 5.3.3.

5.3.1 Bulk properties

Before investigating the confined phase diagram and computing the bulk properties involved in Eq. 5.28, we study the phase diagram of the bulk LJ system. Its phase diagram was extensively studied^{179;280–285}, usually using long-range corrections (LRC-LJ), as mentioned in section 2.1.3.2. However, it has been shown^{286;287} that the treatment of the truncation of the potential has an important effect on the phase diagram which cannot be neglected. In this work, we set the cutoff radius to

$r_{\text{cut}}^* = 2.5$ for which data is available in the literature: Vrabec *et al.*²⁸⁸ computed the liquid-vapor coexistence line and determined the critical point $T_C^* = 1.0779$, whereas Ahmed and Sadus²⁸⁶ investigated the solid-liquid coexistence curve for high pressures. Their results are given in figure 5.6.

To accurately locate the triple point, additional points are needed at lower pressures on the solid-liquid line. We thus recomputed both the liquid-vapor (to have closer points) and the solid-liquid coexistence curves using the Gibbs-Duhem Integration (GDI) method explained in section 2.4.5.3. We used the cubic system (B7) in table 2.2 in the vapor, liquid and solid (face-centered cubic crystal) phases as shown in table 2.2. The starting point for the GDI method is crucial in order to obtain accurate results and was carefully chosen. For the liquid-vapor coexistence line, we determined, using Gibbs-Ensemble Monte Carlo (GEMC) simulations, as detailed in section 2.4.5.1, a point at high temperature (where the densities are lower and the GEMC is more efficient)

$$T_{\text{vap}}^* = 1.00 \quad P_{\text{vap}}^* = 0.0612 \pm 0.0005. \quad (5.33)$$

For the solid-liquid curve, GEMC does not yield accurate results because of the low probability of particle exchange in condensed phases. Therefore we use the fact that the difference in the phase behavior of the LRC-LJ and the TS-LJ vanishes at high pressure and temperature. We then use the results of Kofke *et al.*²⁸² at high pressure and temperature as starting point:

$$T_m^* = 2.74 \quad P_m^* = 36.9. \quad (5.34)$$

GEMC and GDI simulations were run using the implementation described in appendices D.1 and D.3, and furthermore tested for the LRC-LJ for which extensive numerical data are available^{196;282;283}.

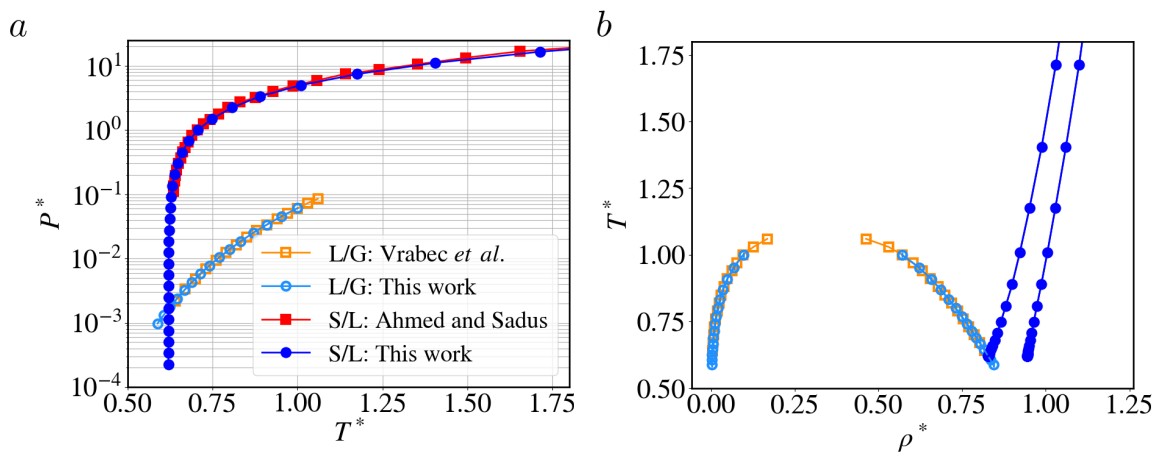


Figure 5.6: Bulk phase diagram of the truncated shifted Lennard-Jones system with a cutoff of $r_{\text{cut}}^* = 2.5$ in the (T^*, P^*) plane (a) and in the (ρ^*, T^*) plane (b). Results obtained by Gibbs-Duhem Integration, using the LJ model system (system (B7) in table 2.2), for the liquid-vapor (light blue open circles) and solid-liquid (dark blue full circles) coexistence curves are compared to the results of Vrabec *et al.*²⁸⁸ (orange open squares) and Ahmed and Sadus²⁸⁶ (red full squares), respectively. Adapted from Ref. 278 with the permission of AIP Publishing.

The resulting TS-LJ bulk phase diagram is shown in figure 5.6 and compared to the literature^{286;288}. The agreement with published data is good both for the coexistence pressure P^* as a function of temperature T^* (figure 5.6a) and for the coexistence densities ρ^* of the vapor, liquid and solid phases (figure 5.6b). The S/L and L/G coexistence lines are extended to temperatures and pressures lower than the triple point, following the metastable phase coexistence. From the crossing of the two coexistence lines, we extract the triple point as

$$T_T^* = 0.62 \quad P_T^* = 1.65 \cdot 10^{-3}, \quad (5.35)$$

which enters in the GT equation Eq. 5.28. Panel 5.6b allows to discuss a first approximation done in section 5.2, *i.e.* that the prefactor in Eq. 5.27, which includes the density of the solid phase at the

denominator, does not depend on temperature. On the solid-liquid coexistence, the evolution of the density with temperature is not negligible, up to 15 % over the range of temperature we are interested in ($\sim [T_T^*, T_C^*]$).

Additionally, the entropy of melting per particle at coexistence is directly obtained from the GDI simulations by using the relation with the enthalpy of melting at bulk coexistence $\Delta_m s = \Delta_m h / T_m$. The dependence with temperature of the factor $\rho_S \Delta_m s$ is shown in figure 5.7a. Taking the triple point (Eq. 5.35) as a reference, the error made on the denominator in the solid-liquid case is of only $\sim 5\%$ for $T^* = 0.65$ but already $\sim 13\%$ for $T^* = 0.75$. As a side note, figure 5.6b shows that the variation of the density of the liquid ρ_L at the liquid-vapor transition is about $\sim 30\%$ from the triple to the critical point and the $\rho_L \Delta_{\text{vap}} s$ contribution, shown in figure 5.7b, decreases approximately of 75 % between T_T and T_C , which is much more concerning for the derivation of Eq. 5.31. The surface tension term could balance or reduce the temperature dependence of the prefactor in the GT equation but we were not able to compute it as a function of temperature, as discussed below.

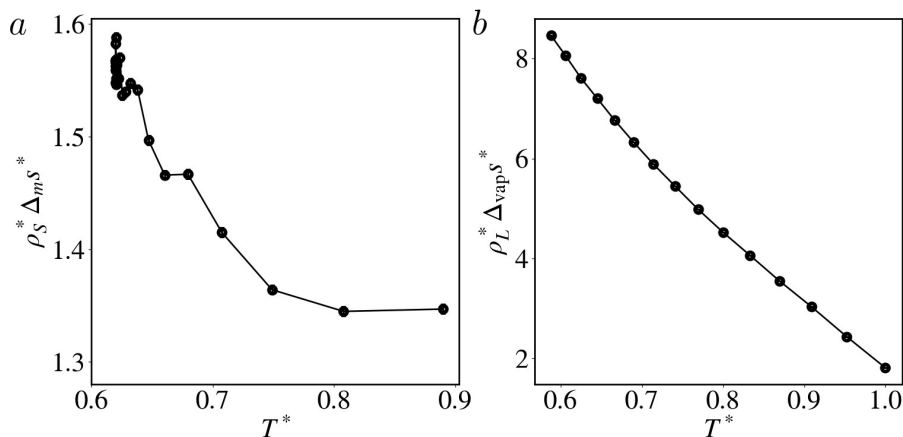


Figure 5.7: Evolution of the product of the bulk density ρ^* and the bulk transition entropy per particle Δs^* along the coexistence line, for the solid-liquid transition $\rho_S^* \Delta_m s^*$ (a) and the liquid-vapor transition $\rho_L^* \Delta_{\text{vap}} s^*$ (b), for the LJ model system (system (B7) in table 2.2). Panel (a) is adapted from Ref. 278 with the permission of AIP Publishing.

5.3.2 Surface tension calculation

There are two usual ways to compute surface tensions: using the definition of γ as a free energy per unit area, all the other parameters being fixed

$$\gamma = \left(\frac{\partial F}{\partial A_W} \right)_{NVT} = \left(\frac{\partial G}{\partial A_W} \right)_{NPT}, \quad (5.36)$$

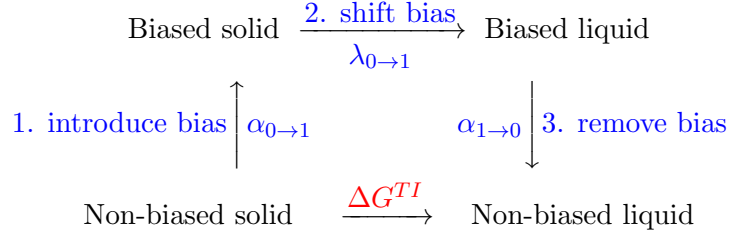
which can also be called surface energy, or using mechanical expressions involving the stress tensor^{289;290}. For fluid-fluid interfaces, these expressions are well known, widely used and provide a simple way of computing the surface tension related to such interface. However, interfaces involving solid phases or walls are conceptually more complex, because a solid surface can sustain stress so that the surface energy depends on the surface A_W . This can be shown by writing the free energy of formation of the interface $F^{\text{surf}} = \gamma A_W$ and its derivative with respect to A_W as

$$\sigma = \frac{\partial F^{\text{surf}}}{\partial A_W} = \gamma(A_W) + A_W \frac{\partial \gamma}{\partial A_W}, \quad (5.37)$$

given by Shuttleworth in Ref. 291. For a fluid, the term $\partial \gamma / \partial A_W = 0$ because it deforms and adapts to external shear but this is not true for solids, for which surface tension and surface energy are not equal in general. Moreover, because solid atoms do not diffuse, the mechanical route to compute the surface tension is even more complicated²⁹². To avoid this, we chose the unstructured Steele walls (for which $\partial \gamma / \partial A_W = 0$) and used a thermodynamic approach.

5.3.2.1 Thermodynamic Integration approach

We directly compute the difference $\gamma_{LW} - \gamma_{SW}$ from the difference in Gibbs free energy between a system with walls in contact with the liquid or the solid phase. This difference is obtained using the thermodynamic integration (TI) approach described in section 2.5.3 for which we reproduce here its three-step scheme:



The challenge of devising such method is to be able to drive the phase transition in a reversible way. To this end, we introduce a bias acting on the collective variable Q_6 , defined in section 2.4.5.4, which quantifies the local order on average over the whole system. We choose a quadratic bias

$$\mathcal{U}_{\text{bias}}(\lambda) = \frac{k}{2} [(1 - \lambda)(Q_6 - Q_6^S)^2 + \lambda(Q_6 - Q_6^L)^2], \quad (5.38)$$

where Q_6^S and Q_6^L are reference values for the collective value in the solid and liquid state determined for the specific thermodynamic conditions of the TI. By averaging the value or derivative of Eq. 5.38 along trajectories at fixed α and λ , we obtain the overall Gibbs free energy difference ΔG^{TI} using Eq. 2.92. Because the first and third steps introduce and remove a bias centered on the respective equilibrium values Q_6^S and Q_6^L , their contributions are small (around 1 kJ/mol) and cancel each other within the errorbars. The major contribution then arises entirely from the second step, which drives the phase transition and involves the derivative $\langle \partial \mathcal{U}_{\text{bias}} / \partial \lambda \rangle$.

This procedure is computationally expensive because of the calculation of the forces associated with the collective variable Q_6 , which involve all atoms in the system. This restricts the study to small system sizes and a few thermodynamic conditions only. We thus identify conditions for which both the liquid and the solid phases are sufficiently metastable to characterize the solid and liquid interfaces with the walls. This is done by fixing the pressure to $P^* = 0.2036$ (which corresponds to a bulk melting temperature $T_m^* = 0.638$) and performing temperature ramps in NPT , during which the LJ model system (S7) in table 2.2 is slowly heated or cooled (at a rate of $\pm 0.15 \text{ ns}^{-1}$ on 1-2 ns-long trajectories). The evolution of the pore size H^* with respect to temperature is given in figure 5.8 and shows two linear regimes corresponding to the solid (at low T) and liquid (at high T) phases (the slope being related to their thermal dilation coefficient), and an important hysteresis between the heating and cooling curves. Within the hysteresis loop, we select two temperatures $T^* = 0.659$ and 0.751 at which liquid and solid equilibrium NPT simulations are run for 20 ns to test their metastability. These are shown in green on figure 5.8 and indeed we do not observe any phase transition during such long simulations. These thermodynamic conditions are thus close enough to the coexistence line under confinement, which is not known *a priori*, to be able to run the thermodynamic procedure without observing spontaneous phase transitions when removing the bias. At the bulk coexistence on the contrary, the confined liquid spontaneously recrystallizes on the observed trajectory, which makes it an unsuitable thermodynamic condition. We also run 2 ns unbiased simulations, using the system (S7) in table 2.2, to determine the characteristic values for the collective variable in the solid and liquid phases: for $T_{TI}^* = 0.659$, we obtain $Q_6^S = 0.3632$ and $Q_6^L = 0.1425$, while for $T_{TI}^* = 0.751$, we find $Q_6^S = 0.3531$ and $Q_6^L = 0.0569$.

For both temperatures, we run 6 points in α from 0 to 1 (in steps of 0.2) and 11 points in λ from 0 to 1 (in steps of 0.1), using a spring constant $k = 10^5 \text{ kJ/mol}$. For each α or λ point, the simulation is first equilibrated for at least 20 ps, then run for at least 400 ps. These parameters allow to switch from the liquid to the solid configurations and vice-versa. We observe that increasing λ yielded the melting of the LJ crystal in the bulk region and the intermediate λ configurations are distinguished

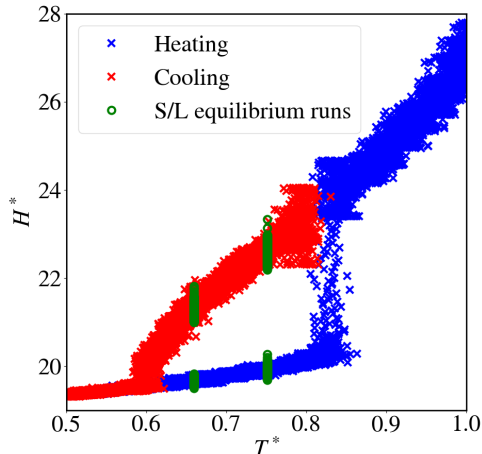


Figure 5.8: Evolution of pore width H^* as a function of temperature T^* for temperatures ramps from cold to hot (blue crosses) and vice-versa (red crosses), and for equilibrium NPT runs at three fixed temperatures in the liquid or solid phases (open green circles), for a LJ model system (system (S7) in table 2.2).

by different ratios of solid and liquid phases, as shown in the snapshots in figure 5.9. Short times (~ 10 ps) are sufficient to average correctly the collective variable but longer times can be necessary (up to $\sim 1 - 2$ ns) to sample the phase transition.

The average derivatives $\langle \partial U / \partial \lambda \rangle$ are shown as a function of λ in figure 5.9 for both selected temperatures. The equilibration is improved by starting the simulations at each λ value from a configuration obtained at a previous value. This in turn may lead to hysteresis, which is checked by following both the forward (solid to liquid) and reverse (liquid to solid) processes. The reversibility of the path is crucial to be able to write the TI equations and draw conclusions from such calculations. This is why usual methods^{36;284;293–296} avoid the explicit phase transition and instead relate each phase to known reference states such as the Einstein crystal or the ideal gas (as in the Frenkel-Ladd method²⁹⁷). The results of figure 5.9 show that we achieve a good reversibility of the transformation for $T_{TI}^* = 0.659$. Only for $\lambda = 0.3$, a small hysteresis was first observed, which was removed by simulated annealing (see section 2.5.1), *i.e.* heating the system at $T^* = 0.751$ for 100 ps and cooling it back to T_{TI}^* . For $T_{TI}^* = 0.751$ however, a large hysteresis between the forward and backward processes is observed. This can be explained by the fact that in the liquid to solid process, the system fails to recrystallize despite the bias. The difference in reversibility in that case is explained by the larger temperature difference with the confined transition temperature. Therefore, only the results at $T_{TI}^* = 0.659$ could be used to obtain the Gibbs free energy difference using Eq. 2.92 at $T_{TI}^* = 0.659$ and P^* . Taking into account the discretization error for the numerical integrations, we find $\Delta G^{TI*}(T_{TI}^*) = 50 \pm 28$. This large uncertainty arises mainly from the numerical estimate of the integral, due to the jump between $\lambda = 0.3$ and 0.4.

5.3.2.2 Surface tension

The Gibbs free energy difference ΔG^{TI} obtained from the above thermodynamic integration contains both a volume contribution $\Delta_m G^{\text{vol}}$ to the phase transition and a surface contribution ΔG^{surf} corresponding to the “bulk” and surface excess atoms

$$\begin{aligned} \Delta G^{TI} &= \Delta_m G^{\text{vol}} + \Delta G^{\text{surf}} \\ &= (\Delta_m H - T \Delta_m S) + 2A_W(\gamma_{LW} - \gamma_{SW}) \\ &= \Gamma_{\text{bulk}} A_W \left(1 - \frac{T}{T_m^b}\right) \Delta_m h^b + 2A_W(\gamma_{LW} - \gamma_{SW}), \end{aligned} \quad (5.39)$$

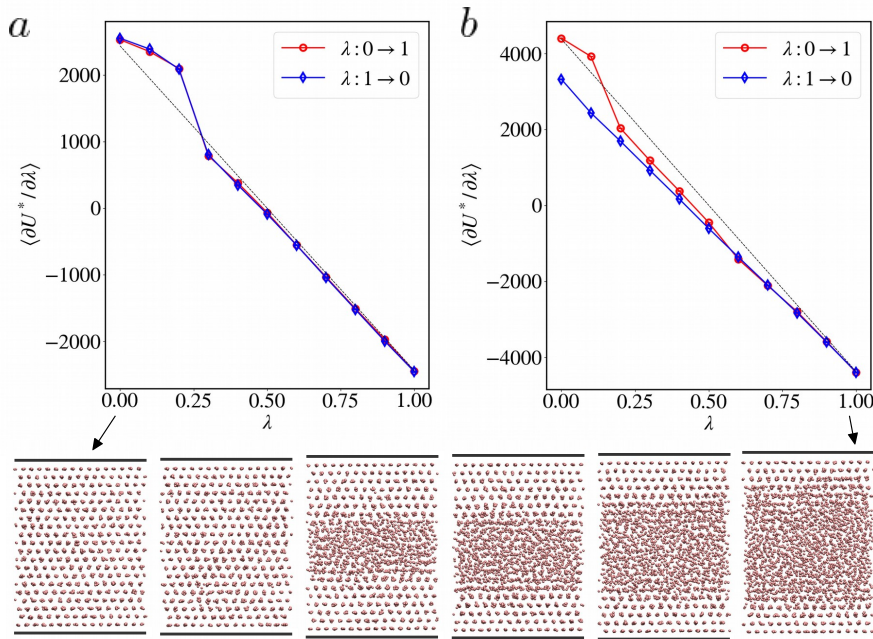


Figure 5.9: Energy derivative $\langle \partial U^* / \partial \lambda \rangle$ as a function of the biasing variable λ for the second step of the TI procedure, *i.e.* shifting the bias, for $T_{TI}^* = 0.659$ (a) and $T_{TI}^* = 0.751$ (b). Values are given for both the forward (solid-liquid, red open circles) and backward (liquid-solid, blue open diamonds) processes, for a LJ model system (system (S7) in table 2.2). The black dotted line is a guide to the eye, with vanishing integral. Typical snapshots for several λ values are shown, where LJ particles are in pink and the position of the Steele surfaces is indicated by the solid black lines. Panel (a) is adapted from Ref. 278 with the permission of AIP Publishing.

where $\Gamma_{\text{bulk}} = N_{\text{bulk}}/A_W$ is the number of “bulk” atoms per unit surface. We alternatively write $\Gamma_{\text{bulk}} = N/A_W - 2\Gamma$ using the excess number of atoms Γ at each interface and compute it from the density profiles $\rho(z)$ across the pore, shown for the liquid and solid phases in figure 5.10.

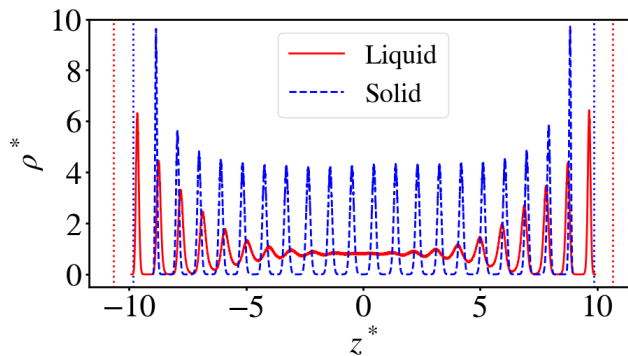


Figure 5.10: Density profiles across the pore, for system (S7) described in table 2.2, for the liquid (red solid line) and the solid (blue dashed line) phases, obtained from equilibrium NPT simulations of each phase at $T_{TI}^* = 0.659$. The average position of the walls is indicated by vertical dotted lines. Reproduced from Ref. 278 with the permission of AIP Publishing.

The thermodynamic definition of the surface excess is based on the position of the Gibbs dividing surface (GDS), z_{GDS} , introduced in Eq. 2.53, corresponding to a sharp interface between two homogeneous regions with densities $\rho_{\text{wall}} = 0$ and $\rho_{\text{bulk}} = \rho_L$ or ρ_S in the bulk region of the pore. Because we have two interfaces, we modify Eq. 2.53 as

$$\int_{z_{\text{wall}}}^{z_{\text{GDS}}} (\rho(z) - \rho_{\text{wall}}) dz = \int_{z_{\text{GDS}}}^{z_{\text{bulk}}} (\rho(z) - \rho_{\text{bulk}}) dz, \quad (5.40)$$

with z_{wall} the position of the wall and $z_{\text{bulk}} = 0$ the center of the pore. The bulk densities of the solid and liquid phases are $\rho_S^* = 0.94$ (averaged over a lattice spacing) and $\rho_L^* = 0.83$. As expected, we find that the GDS is located close to the maximum of the first density peak. The surface excess is then defined as

$$\Gamma = \int_{z_{\text{GDS}}}^{z_{\text{bulk}}} (\rho(z) - \rho_{\text{bulk}}) dz. \quad (5.41)$$

We obtain slightly different values of Γ^* from the liquid and solid density profiles, and take the average value and half difference as $\Gamma^* = 0.3 \pm 0.1$, giving $\Gamma_{\text{bulk}}^* = 17.0 \pm 0.2$. Eq. 5.39 then leads to the difference $\Delta\gamma^* = \gamma_{LW}^* - \gamma_{SW}^* = 0.40 \pm 0.05$.

5.3.2.3 Crystal structure under confinement

In the study of solids, and even more so of crystallization, the crystal structures and different crystal phases are of great importance as the interfacial energy depends strongly on the observed facet. The crystalline structure of the LJ fluid is face-centered cubic and for strong confinement, with $H^* \sim 3-4$, it has been shown that different crystal phases are stable with squared or triangular geometries^{36;37;39}. From the explorations using heating-cooling ramps, we find that the most stable face that crystallizes on the Steele wall is the (111) face, so that all solid configurations (systems (S7) and (S7b) in table 2.2) are initialized with perfect crystal configurations consistent with this observation.

We also observe from figure 5.10 that the strong attraction between the particles and the wall ($\epsilon_{WF}^* \approx 2.8$) results in a pronounced structuration in the vicinity of the surface in the liquid phase, with at least 4 solid-like layers at the wall. The main consequence is to reduce the effective size of the bulk liquid and solid regions, which we need to be sufficiently large for the GT equation to apply. Decreasing ϵ_{WF} would have decreased this layering effect, but we can hypothesize that reducing the interactions with the surface would also reduce the difference in surface tension $\Delta\gamma$, which we seek to be the largest in order to facilitate its accurate estimation.

5.3.3 Melting temperature under confinement

The numerical results from sections 5.3.1 and 5.3.2 provide a prediction of the melting temperature under confinement using the GT equation Eq. 5.28 (shown in figure 5.13). To assess its validity, we directly compute melting temperatures under confinement for different pore sizes H (see table 2.3). Several simulation methods are available that yield melting temperatures with different accuracies. The simplest method consists in increasing the temperature of a crystalline box until it melts or in decreasing the temperature of a liquid box until it freezes, which usually results in a large hysteresis because of the need to nucleate the new phase in the bulk crystal or liquid. Alternatively, the Direct Coexistence Method runs configurations half crystalline and half liquid at different temperatures in parallel and discriminates the configurations that are ultimately totally liquid from those totally crystalline. This method has the advantage to already have a solid-liquid interface present and is easy to implement. However, it also gives rise to significant hysteresis in some systems. To obtain more accurate estimates of the melting temperature, free energy methods are required that iteratively compute the equality of thermodynamic potential^{293;294;298;299}.

In this work, we use Hyper-Parallel Tempering Grand Canonical Monte Carlo (HPT-GCMC) simulations²¹¹, as described in section 2.5.1. These simulations were run by Prof. Benoît Coasne, from the Laboratoire Interdisciplinaire de Physique at Université Grenoble Alpes, using an in-house code. Building on the experiments schematized in figure 5.3, we set up the simulations using 16 replicas regularly spaced in $\beta = 1/k_B T$, where each replica is a GCMC simulation in contact with a chemical reservoir along the liquid-vapor coexistence line. The chemical potential along the coexistence is determined by Widom particle insertion method on system (B7) in table 2.2 (see section 2.4.5.2 and appendix D.2) and reported in figure 5.11 as a function of temperature.

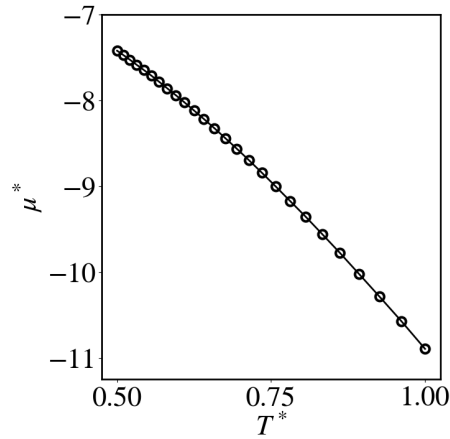


Figure 5.11: Chemical potential μ^* as a function of temperature, along the bulk liquid-vapor coexistence line (see figure 5.6), for the LJ model system (system (B7) in table 2.2). Adapted from Ref. 278 with the permission of AIP Publishing.

As highlighted in section 5.3.2.3, the crystal structure is crucial for these studies, and we initialize all crystal configurations using the (111) plane of the face centered cubic structure. To avoid polycrystalline configurations upon recrystallization, all liquid configurations are then obtained from melting of the crystalline ones. We also use a system with larger lateral dimension (system (S7b) in table 2.2, see also snapshots in figure 5.12) to avoid any commensurability issue.

Hyper-Parallel Tempering was chosen to improve the sampling of phase space thanks to the exchange of solid and liquid replicas, and provides an accurate estimate of the melting temperature provided the replicas are initialized with both crystal and liquid configurations^{300–302}. In these systems however, the swapping remains limited once the replicas have diverged in terms of number of particles and energy, which is a drawback for the determination of the phase transition. For most replicas, swapping occurs between solid and liquid configurations during the initial equilibration period, then only swapping between solid on one hand and liquid configurations on the other hand is observed, if any. To obtain a better measure of the melting temperature, we thus run two series of HPT-GCMC, one initialized only with liquid configurations and one with only crystal configurations, as to compute the freezing and the melting temperature.

Each replica is run in parallel until the convergence of the energy and number of particles and the melting temperature T_m is then determined for each pore size from the evolution of the average number of particles as a function of temperature, as illustrated for $H^* = 11.6$ in figure 5.12. Two linear regimes at low temperature and at high temperature correspond to the thermal expansion of the solid and liquid phases, and we identify the melting temperature at the crossover. An hysteresis is observed for the two sets of initial conditions (all crystal or all liquid), from which we determine a confidence interval for the melting temperature. In some occasions, visual inspection of the replicas is needed to determine whether a configuration is solid or liquid. For the larger pores, large error bars are due to non equilibrated replicas for which swapping did not accelerate the phase transition. Results are shown as a function of pore size in figure 5.13.

5.3.4 Discussion of the Gibbs-Thomson equation

We now compare the results obtained from HPT-GCMC simulations in section 5.3.3 to the prediction of the GT equation using the numerical results of section 5.3.1 for T_T^b and $\rho_S \Delta_m s^b(T_T^b)$ and section 5.3.2 for $\Delta\gamma(T_{TI})$. As in the previous chapter (*e.g.* in section 4.2.2), comparing atomistic simulations to continuum theories necessitates to locate a sharp interface between the region accessible to the particles and the walls. For a better comparison, we consider the effective width H_{eff}^* of the pore occupied by the particles, estimated from the position of the Gibbs dividing surfaces (see section 5.3.2) located

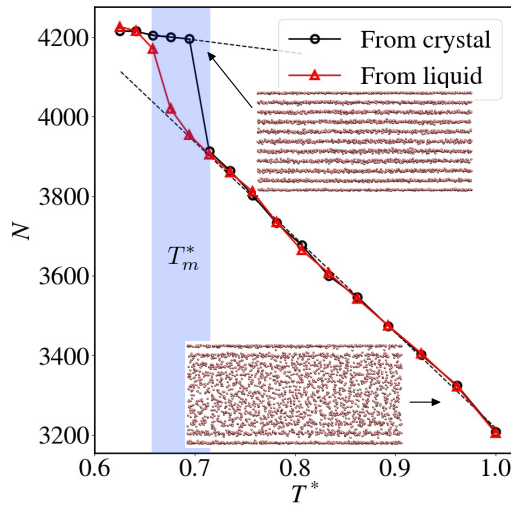


Figure 5.12: Average number of atoms N in each HPT-GCMC replica as a function of the replica's temperature T^* for a pore size $H^* = 11.6$. Evolution for both sets of initial configurations, starting either from crystal (black circles) or liquid (red triangles) configurations in all replicas, are shown. Black dashed lines are linear fits to the low and high temperature regions, used to locate the melting temperature T_m (blue shaded area indicating the confidence interval). The snapshots illustrate typical crystal (top right) and liquid (bottom) configurations. Reproduced from Ref. 278 with the permission of AIP Publishing.

at $\sim \sigma$ from the Steele walls. We thus define $H_{\text{eff}}^* = H^* - 2$, with H the distance between the positions of the walls. The difference between H_{eff}^* and H^* is important for smaller pores but does not influence the conclusions of the study. Figure 5.13 then shows the melting temperature T_m^* , computed in section 5.3.3, as a function of $1/H_{\text{eff}}^*$, along with the prediction of the GT equation. We first note that the error bars obtained for HPT-GCMC measurements are too large to be able to extract a trend, especially a linear trend for large pores (*i.e.* small $1/H_{\text{eff}}^*$). We nevertheless observe two regimes.

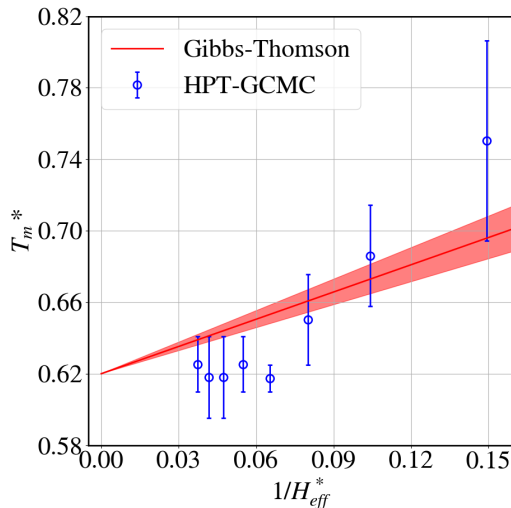


Figure 5.13: Melting temperature T_m^* as a function of the inverse effective pore size $1/H_{\text{eff}}^* = 1/(H^* - 2)$. The red line indicates the prediction of the GT equation 5.28 using the results of sections 5.3.1 and 5.3.2. The shaded red area illustrates the uncertainty on the prediction. The open blue circles correspond to the HPT-GCMC simulations. Reproduced from Ref. 278 with the permission of AIP Publishing.

For small pores, we notice an important effect of confinement on the melting temperature. This regime is dominated by disjoining pressure effects, *i.e.* the mutual effect of the two interfaces, through the medium in-between. As shown in figure 5.10 and discussed in section 5.3.2.3, the strong layering at

the interfaces and small bulk region suggests that these effects are present even for relatively large pores (up to $H^* \leq 17.3$). For even smaller pores (with only a few crystal layers between the walls), it has been shown that the melting temperature is extremely sensitive to the distance H^* between the walls and exhibits an oscillatory behavior, due to the commensurability of the pore width with the crystal structure. This phenomenon also leads to changes in crystalline structure at very large confinement³⁴⁻³⁹.

For large pores (up to $H^* = 28.8$), another regime is observed. The extrapolation to $H_{\text{eff}}^* \rightarrow \infty$ is consistent with the temperature of the triple point $T_T^{b*} = 0.62$, however the dependence on confinement length is rather disappointing as we cannot conclude due to the large error bars. Longer simulations, or repeated simulations, and closer replicas should improve these results. The GT prediction, with the approximations that the prefactor of Eq. 5.27 does not depend on the confinement width, obviously does not reproduce the two different regimes. The order of magnitude of the numerical prediction is correct down to very small pores, but does not reproduce the large pore regime, where the GT equation is expected to hold.

Ultimately, the comparison to HPT-GCMC measurements does not allow to conclude on the validity of the GT equation in the present case because of the several uncertainties on the different quantities. The strong attraction to the walls and subsequent layering at the interface makes it difficult to obtain a large portion of bulk atoms. This lead us to explore very large pores (up to $H^* = 28.8$, rarely studied in the literature) for which however the simulations are more difficult to converge, leading to large uncertainties. For such large pores, the replica exchange is also less favorable because of the larger difference in the number of atoms between solid and liquid configurations. This effect could be decreased by reducing ϵ_{WF} but this could also reduce the dependence on confinement length H .

Regarding the GT prediction, several uncertainties are taken into account in the calculation of the bulk properties and surface tensions that did not result in a large overall error bar. The somewhat disappointing comparison can then be attributed to different factors, such as the use of the value of $\Delta\gamma$ at $T_{TI} = 0.659$ and $P^* = 0.2036$, which is far from the triple point. Such large value of pressure was chosen from preliminary pressure calculations of GCMC confined simulations and to avoid crossing the liquid-vapor coexistence line when increasing the temperature. Because of the computational cost of the thermodynamic integration method, a systematic study of $\Delta\gamma$ exploring the phase diagram was not possible in this thesis, but would have helped validate the assumption that the prefactor $\rho_S^b \Delta_m s^b / \Delta\gamma$ does not depend on temperature T^* and confinement width H^* . The evolution with temperature shown in figure 5.7a suggests that the effect on $\rho_S^b \Delta_m s^b$ is limited to less than 10 %, but no information on the evolution of $\Delta\gamma$ is available.

Overall, this work highlights the difficulties related to the sampling of crystallization under confinement. In order to systematically study large pores, the methods used and developed in this work offer an interesting alternative to the straightforward calculation of melting temperatures. Provided a good knowledge of the bulk phase diagram, these methods can be applied to more complex fluids, such as water or ionic liquids. Using molecular simulations, one could go further and inject the temperature dependence of the density, melting entropy and difference in surface tensions in the integral along the thermodynamic path connecting the bulk and confined systems. Another interesting direction to explore would be to reproduce the comparison using different reservoir conditions, *i.e.* changing the chemical potential with respect to temperature for the HPT-GCMC replicas.

“Forget-me-not”: Phase transitions under confinement

- We revisited the derivation of the Gibbs-Thomson equation

$$T_m(H) = T_T^b + \frac{2(\gamma_{LW} - \gamma_{SW})}{H\rho_S^b\Delta_m s^b}$$

for the crystallization of a liquid confined in a slit pore, using a “confined-Clapeyron” approach, making it easily applicable to other geometries and external conditions.

- We numerically tested some of the assumptions, in particular the temperature dependence of several factors on a model system.
- We computed the bulk phase diagram of the model fluid and developed a thermodynamic integration procedure to directly obtain the surface tension difference $\gamma_{LW} - \gamma_{SW}$.
- We compared the predictions of the GT equation to melting temperatures computed using Hyper-Parallel Tempering Grand Canonical Monte Carlo and discussed the limitations of our methods.

Chapter 6

Effect of metallicity on interfacial free energies

6.1 The Thomas-Fermi Thermodynamic Integration

In chapter 5 on the crystallization under confinement, we learned that the phase coexistence was modified according to the difference in interfacial free energy, or surface tension, $\gamma_{LW} - \gamma_{SW}$ and we developed a thermodynamic integration procedure to obtain such difference by following a reversible path from the solid to the liquid phase under confinement. This procedure however turned out to be computationally expensive, especially because of the biasing force calculation due to the collective variable Q_6 , as detailed in section 5.3.2. With this in mind, we adopt a new strategy and, instead of repeating the solid-to-liquid calculation for different l_{TF} values, develop a framework based on thermodynamic integration to compute free energy differences as a function of l_{TF} to investigate the influence of metallicity on the phase behavior. We introduce this framework in section 6.1.1 then discuss different continuum expressions in section 6.1.2 and compare them to results from empty capacitors in section 6.1.3. In relation with the contact angle calculations in section 3.2.3, we then apply the Thomas-Fermi Thermodynamic Integration method to the liquid-vapor phase transition by simulating the vapor phase and the liquid phase separately, as discussed in section 6.2. We finally give preliminary results on the solid-liquid phase transition in section 6.3 using a molten salt.

6.1.1 Statistical mechanics framework

In electrochemical cells, free energy differences due to the charging of the capacitor is known and given by the reversible work exchanged with the generator (see Eq. 3.51). In the following however, we are interested in the free energy changes due to the screening length l_{TF} , with respect to the ideal metal case $l_{TF} = 0$. We thus consider, as in chapter 3, a system of N mobile atoms of electrolyte and M electrode atoms that carry a Gaussian charge distribution with fluctuating magnitudes $\mathbf{q} = (q_1, q_2 \dots q_M)$. To compute the free energy associated with a change in metallicity of the metal surface atoms, *i.e.* with a change in Thomas-Fermi screening length l_{TF} , we follow the steps of section 2.5.3, starting from the definition of free energy $F^{\Delta\psi} = -\beta^{-1} \ln(\mathcal{Z})$ at a given voltage $\Delta\psi$. The statistical mechanics framework derived in section 3.1 remains valid for the extended constant potential Thomas-Fermi simulations, since the associated Hamiltonian Eq. 4.25 is quadratic in the charges \mathbf{q} . Using the expression of the partition function in the constant potential ensemble Eq. 3.28 and its relation to the Born-Oppenheimer (BO) partition function Eq. 3.36, we write

$$\mathcal{Z}(l_{TF}) = \frac{1}{2\pi} \sqrt{\frac{(2\pi)^M}{\beta^M \det \mathbf{A}_{TF}}} \sqrt{\frac{2\pi}{\beta \mathbf{E}^T \mathbf{A}_{TF}^{-1} \mathbf{E}}} \mathcal{Z}^{BO}(l_{TF}), \quad (6.1)$$

where we used the modified matrix \mathbf{A}_{TF} defined in Eq. 4.28 and the vector \mathbf{E} defined in Eq. 3.7. We then introduce

$$\Delta F^{\Delta\psi}(l_{TF}) = F^{\Delta\psi}(l_{TF}) - F^{\Delta\psi}(l_{TF} = 0) = \Delta F^{\Delta\psi,BO}(l_{TF}) + \Delta F^{nBO}(l_{TF}), \quad (6.2)$$

where we separated the free energy difference between a metal characterized by finite l_{TF} and an ideal metal with $l_{TF} = 0$, $\Delta F^{\Delta\psi}(l_{TF})$, at fixed potential difference $\Delta\psi$, in two terms: a BO contribution that can be computed from simulations, and a contribution arising from the integrated fluctuations of charge discarded in the BO sampling.

6.1.1.1 Non-Born-Oppenheimer term

We first briefly give the non-BO contribution coming from the integrated charge fluctuations

$$\Delta F^{nBO}(l_{TF}) = F^{nBO}(l_{TF}) - F^{nBO}(l_{TF} = 0) = -\frac{\beta^{-1}}{2} \ln \left(\frac{\det \mathbf{A} \quad \mathbf{E}^T \mathbf{A}^{-1} \mathbf{E}}{\det \mathbf{A}_{TF} \quad \mathbf{E}^T \mathbf{A}_{TF}^{-1} \mathbf{E}} \right), \quad (6.3)$$

where \mathbf{A} is the original matrix appearing in Eq. 4.28, corresponding to $l_{TF} = 0$. This contribution depends only on the electrodes configuration, and not on the electrolyte positions \mathbf{r}^N nor the applied electric potential difference $\Delta\psi$.

The determinants of the matrices involved are numerically challenging to compute accurately. We can circumvent this numerical issue by using that the determinant of a matrix is the product of its eigenvalues. Taking the logarithm gives a well behaved number, allowing to carry out the calculation. Writing λ^i and $\lambda_{l_{TF}}^i$ for the eigenvalues of \mathbf{A} and \mathbf{A}_{TF} , respectively, we obtain

$$\Delta F^{nBO}(l_{TF}) = -\frac{\beta^{-1}}{2} \sum_i^M \ln \left(\frac{\lambda^i}{\lambda_{l_{TF}}^i} \right) - \frac{\beta^{-1}}{2} \ln \left(\frac{\mathbf{E}^T \mathbf{A}^{-1} \mathbf{E}}{\mathbf{E}^T \mathbf{A}_{TF}^{-1} \mathbf{E}} \right). \quad (6.4)$$

However, because the non-BO term cancels out in differences of free energy differences using the same electrode configurations, *e.g.* between the surface-liquid and surface-vapor free energy differences, this term is not investigated further.

6.1.1.2 Born-Oppenheimer term

To compute the Born-Oppenheimer contribution, we follow a thermodynamic integration approach, as in section 2.5.3, by rewriting

$$\Delta F^{\Delta\psi,BO}(l_{TF}) = F^{\Delta\psi,BO}(l_{TF}) - F^{\Delta\psi,BO}(l_{TF} = 0) = \int_0^{l_{TF}} dl \left(\frac{\partial F^{\Delta\psi,BO}}{\partial l} \right)_{NVT\Delta\psi}. \quad (6.5)$$

Using Eq. 3.36 and injecting the Thomas-Fermi Hamiltonian Eq. 4.25, we have

$$\begin{aligned} \left(\frac{\partial F^{\Delta\psi,BO}}{\partial l_{TF}} \right) &= -\beta^{-1} (\mathcal{Z}^{BO})^{-1} \int d\mathbf{r}^N e^{-\beta \mathcal{U}_0(\mathbf{r}^N)} \frac{\beta}{2} \left(\frac{\partial(\mathbf{q}^*)^T \mathbf{A}_{TF} \mathbf{q}^*}{\partial l_{TF}} \right) e^{\frac{\beta}{2} (\mathbf{q}^*)^T \mathbf{A}_{TF} \mathbf{q}^*} \\ &= -\frac{1}{2} \left\langle \left(\frac{\partial(\mathbf{q}^*)^T \mathbf{A}_{TF} \mathbf{q}^*}{\partial l_{TF}} \right) \right\rangle. \end{aligned} \quad (6.6)$$

Knowing that both \mathbf{A}_{TF} and \mathbf{q}^* depend on l_{TF} explicitly, but not $\mathbf{B}(\mathbf{r}^N)$ or Ψ , we then write

$$\begin{aligned}
 \frac{\partial}{\partial l_{TF}} [(\mathbf{q}^*)^T \mathbf{A}_{TF} \mathbf{q}^*] &= \frac{\partial}{\partial l_{TF}} [(\mathbf{q}^*)^T \mathbf{A}_{TF} \mathbf{A}_{TF}^{-1} \mathbf{A}_{TF} \mathbf{q}^*] = \frac{\partial}{\partial l_{TF}} [\mathbf{A}_{TF} \mathbf{q}^*]^T \mathbf{A}_{TF}^{-1} [\mathbf{A}_{TF} \mathbf{q}^*] \\
 &= \left[\frac{\partial(\mathbf{A}_{TF} \mathbf{q}^*)}{\partial l_{TF}} \right]^T \mathbf{A}_{TF}^{-1} [\mathbf{A}_{TF} \mathbf{q}^*] + [\mathbf{A}_{TF} \mathbf{q}^*]^T \left(\frac{\partial \mathbf{A}_{TF}^{-1}}{\partial l_{TF}} \right) [\mathbf{A}_{TF} \mathbf{q}^*] \\
 &\quad + [\mathbf{A}_{TF} \mathbf{q}^*]^T \mathbf{A}_{TF}^{-1} \left[\frac{\partial(\mathbf{A}_{TF} \mathbf{q}^*)}{\partial l_{TF}} \right] \\
 &= \left[-\frac{\partial \chi}{\partial l_{TF}} \mathbf{E} \right]^T \mathbf{q}^* + [(\mathbf{q}^*)^T \mathbf{A}_{TF}] \left(-\mathbf{A}_{TF}^{-1} \frac{\partial \mathbf{A}_{TF}}{\partial l_{TF}} \mathbf{A}_{TF}^{-1} \right) [\mathbf{A}_{TF} \mathbf{q}^*] + (\mathbf{q}^*)^T \left[-\frac{\partial \chi}{\partial l_{TF}} \mathbf{E} \right] \\
 &= 0 + (\mathbf{q}^*)^T \left(-\frac{2l_{TF}\rho}{\epsilon_0} \mathbf{I} \right) \mathbf{q}^* + 0 = -\frac{2l_{TF}\rho}{\epsilon_0} (\mathbf{q}^*)^T \mathbf{q}^*, \tag{6.7}
 \end{aligned}$$

where we used the relation between χ and \mathbf{q}^* in Eq. 3.26 and the electroneutrality condition Eq. 3.12, with \mathbf{I} the identity matrix and ρ the atomic density of the material. Using Eq. 6.5, we finally obtain that the free energy in the BO ensemble associated with the change in screening length l_{TF} of the surface with respect to the ideal metal case ($l_{TF} = 0$) is positive, increases with l_{TF} and is given by

$$\Delta F^{\Delta\psi, BO}(l_{TF}) = F^{\Delta\psi, BO}(l_{TF}) - F^{\Delta\psi, BO}(l_{TF} = 0) = \int_0^{l_{TF}} dl \frac{l\rho}{\epsilon_0} \langle (\mathbf{q}^*)^T \mathbf{q}^* \rangle_{NVT\Delta\psi, l}. \tag{6.8}$$

Notably, this quantity is readily calculated from molecular simulations, since $(\mathbf{q}^*)^T \mathbf{q}^* = \sum_{i=1}^M q_i^2$ is the sum of the individual squared charges, and Eq. 6.8 constitutes the practical expression of this thermodynamic integration method.

6.1.2 Continuum prediction from a thermodynamic cycle

We now consider the following thermodynamic cycle in the constant potential ensemble $NVT\Delta\psi$:

$$\begin{array}{ccc}
 \{l_{TF} = 0, \Delta\psi = 0\} & \xrightarrow{\Delta F^{l_{TF}=0}(\Delta\psi)} & \{l_{TF} = 0, \Delta\psi\} \\
 \uparrow -\Delta F^{\Delta\psi=0}(l_{TF}) & & \downarrow \Delta F^{\Delta\psi}(l_{TF}) \\
 \{l_{TF}, \Delta\psi = 0\} & \xleftarrow{-\Delta F^{l_{TF}}(\Delta\psi)} & \{l_{TF}, \Delta\psi\}
 \end{array}$$

where the free energy difference associated with the horizontal steps is given by taking into account the reversible work to charge the capacitor $-Q_{\text{tot}}\Delta\psi$, with Q_{tot} the total accumulated charge,

$$F(N, V, T, \Delta\psi) = U - TS - Q_{\text{tot}}\Delta\psi = F(N, V, T) - Q_{\text{tot}}\Delta\psi. \tag{6.9}$$

Noting that the energy stored upon charging is $\Delta U = \frac{Q_{\text{tot}}\Delta\psi}{2} = \frac{C\mathcal{A}\Delta\psi^2}{2}$, with C the capacitance per unit area, the free energy per unit area associated with the charge of a capacitor from 0 to $\Delta\psi$ at fixed l_{TF} is

$$\frac{\Delta F^{l_{TF}}(\Delta\psi)}{\mathcal{A}} = -\frac{Q_{\text{tot}}(l_{TF})\Delta\psi}{2\mathcal{A}} = -\frac{C(l_{TF})\Delta\psi^2}{2}. \tag{6.10}$$

We introduce this relation in the above thermodynamic cycle

$$\begin{aligned}
 -\frac{Q_{\text{tot}}(0)}{2} \Delta\psi + \Delta F^{\Delta\psi}(l_{TF}) + \frac{Q_{\text{tot}}(l_{TF})}{2} \Delta\psi - \Delta F^0(l_{TF}) &= 0 \\
 -\frac{Q_{\text{tot}}(0)}{2} \Delta\psi + \Delta F^{\Delta\psi, BO}(l_{TF}) + \frac{Q_{\text{tot}}(l_{TF})}{2} \Delta\psi - \Delta F^{0, BO}(l_{TF}) &= 0
 \end{aligned} \tag{6.11}$$

where to obtain the second line we used Eq 6.2 and the fact that ΔF^{nBO} is independent of the applied potential $\Delta\psi$. This finally yields

$$\Delta F^{\Delta\psi,BO}(l_{TF}) - \Delta F^{0,BO}(l_{TF}) = (Q_{\text{tot}}(0) - Q_{\text{tot}}(l_{TF})) \frac{\Delta\psi}{2} = (C(0) - C(l_{TF})) \frac{\Delta\psi^2 \mathcal{A}}{2}. \quad (6.12)$$

When $l_{TF} \rightarrow +\infty$ (insulating limit), the accumulated charge vanishes and we simply obtain the work to discharge the perfect metal capacitor

$$\Delta F^{\Delta\psi,BO}(+\infty) - \Delta F^{0,BO}(+\infty) = \frac{C(0)\Delta\psi^2 \mathcal{A}}{2}. \quad (6.13)$$

Eq. 6.12 shows that the free energy difference with metallicity $\Delta F^{\Delta\psi}(l_{TF})$ has an unknown zero-voltage component $\Delta F^0(l_{TF})$ and a term with a quadratic dependence on $\Delta\psi$, which we will verify in the following sections.

6.1.3 Empty capacitor

We first study the example of the empty planar capacitor for which several analytical expressions are available and were already verified in sections 3.2.1 and 4.2.2. The capacitor is composed of the electrodes facing in the z direction, with surface area \mathcal{A} and separated by L . Each electrode is composed of n atomic planes, indexed using $k \in \llbracket 1, \infty \llbracket$ (we take $n \rightarrow \infty$), each with m atoms per plane and separated by an interplane distance d . The atomic density ρ is thus related to the other parameters by $\rho = m/Ad$.

6.1.3.1 Analytical expressions

The results for the BO contribution are shown in figure 6.1 for a range of distances L between electrodes, but we first derive here an analytical prediction. Starting from the exponential decay of the total charge per plane Q_k in an empty capacitor, Eq. 4.34, and given that the charge is homogeneously distributed in each plane, we obtain the individual charge of an electrode atom i on plane k as

$$q_{i,k}^* = \pm \frac{Q_{\text{tot}}}{m} e^{-(k-1)d/l_{TF}} (1 - e^{-d/l_{TF}}), \quad (6.14)$$

where Q_{tot} is the total charge on the positive electrode. This results in

$$(\mathbf{q}^*)^T \mathbf{q}^* = \sum_{k=-\infty}'^{\infty} \sum_{i=1}^m q_{i,k}^{*2} = \frac{2Q_{\text{tot}}^2}{m} (1 - e^{-d/l_{TF}})^2 \sum_{k=1}^{\infty} e^{-2(k-1)d/l_{TF}} = \frac{2Q_{\text{tot}}^2}{m} \frac{(1 - e^{-d/l_{TF}})^2}{1 - e^{-2d/l_{TF}}}, \quad (6.15)$$

where the sum $\sum_{k=-\infty}'^{\infty}$ is over all the planes $k \in \llbracket 1, \infty \llbracket$ of both electrodes excluding the index 0.

Introducing the capacitance per unit charge and its expression Eq. 4.36 from continuum theory (see section 4.2.2.2 for a discussion of L_{eff}) gives

$$(\mathbf{q}^*)^T \mathbf{q}^* = \frac{2}{m} \left(\frac{\epsilon_0 \Delta\Psi \mathcal{A}}{L_{\text{eff}} + 2l_{TF}} \right)^2 \frac{(1 - e^{-d/l_{TF}})^2}{1 - e^{-2d/l_{TF}}}. \quad (6.16)$$

Injecting it in Eq. 6.8 and using $\rho = m/Ad$, we obtain an analytical expression for the empty capacitor

$$\Delta F_{SG}^{\Delta\psi,BO}(l_{TF}) = 2\epsilon_0 \Delta\Psi^2 \mathcal{A} \int_0^{l_{TF}} dl \frac{l(1 - e^{-d/l})^2}{d(L_{\text{eff}} + 2l)^2 (1 - e^{-2d/l})}, \quad (6.17)$$

where SG indicates the surface-vapor interface. This BO contribution thus vanishes at $\Delta\psi = 0$ V and has a quadratic dependence on $\Delta\psi$ as predicted in section 6.1.2. This expression takes into account

to some degree the discreteness of the atomic planes, introduced in the expression for the charge per plane. The continuum limit corresponds to $d \rightarrow 0$. Expanding the integrand in a Taylor series we get

$$\frac{l(1 - e^{-d/l})^2}{d(L_{\text{eff}} + 2l)^2(1 - e^{-2d/l})} \approx \frac{1}{2(L_{\text{eff}} + 2l)^2} + \mathcal{O}(d^2), \quad (6.18)$$

so that

$$\Delta F_{SG}^{\Delta\psi, BO}(l_{TF}) \xrightarrow{d \rightarrow 0} \epsilon_0 \Delta\psi^2 \mathcal{A} \int_0^{l_{TF}} \frac{dl}{(L_{\text{eff}} + 2l)^2} = \frac{\epsilon_0 \Delta\psi^2 \mathcal{A} l_{TF}}{L_{\text{eff}}(L_{\text{eff}} + 2l_{TF})}, \quad (6.19)$$

which is consistent with Eq. 6.12 derived using the thermodynamic cycle. We point out however that the Taylor expansion is accurate only for large l_{TF} values but very poor for small l_{TF} since the approximation $d \ll l_{TF}$ does not hold. The integral is therefore not expected to be a good approximation of the free energy difference with $l_{TF} = 0$. Nevertheless, while it is not straightforward to investigate the limit of $l_{TF} \rightarrow +\infty$ from Eq. 6.17, the approximation of Eq. 6.19 gives a limit for large l_{TF} , *i.e.* for the insulating surface,

$$\Delta F_{SG}^{\Delta\psi, BO}(l_{TF}) \xrightarrow{l_{TF} \rightarrow +\infty} \frac{\epsilon_0 \Delta\psi^2 \mathcal{A}}{2L_{\text{eff}}} \quad (6.20)$$

which is consistent with Eq. 6.13.

6.1.3.2 Simulation results

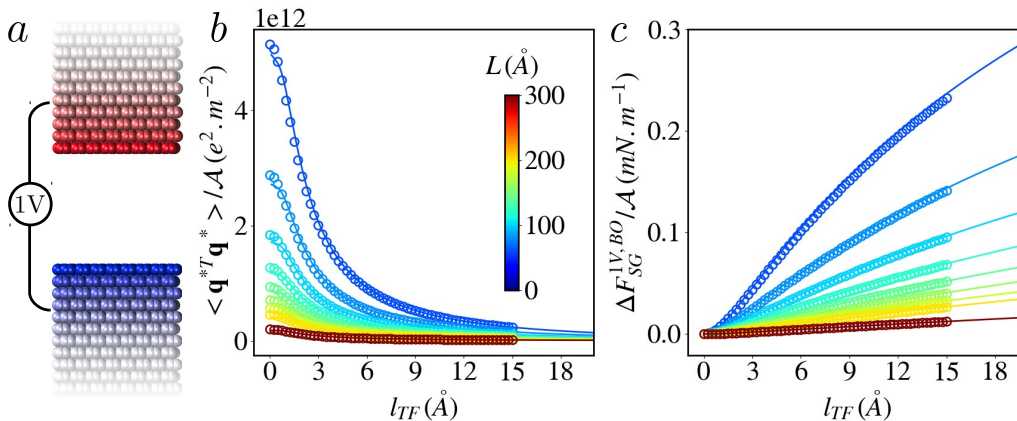


Figure 6.1: Thomas-Fermi Thermodynamic Integration for an empty graphite capacitor (system (G1) in table 2.1) with $n = 50$ planes and a range of distances L between the first atomic planes of electrodes, at $\Delta\psi = 1$ V, shown in the snapshot (a). Average squared charges per unit area as a function of l_{TF} (b) and BO contribution to the free energy difference as a function of l_{TF} (c). Values from simulations are shown as open circles while the solid lines are predictions of Eq. 6.16 in panel b and Eq. 6.17 in panel c.

Both graphite and gold capacitors were investigated at $\Delta\psi = 1$ and 2 V (systems (Au1) and (G1) in table 2.1) but only results for graphite electrodes are shown here. We used $n = 50$ planes and a range of distances $L \in [20, 300]$ Å. The BO contribution to the free energy difference Eq. 6.8 is computed using the value of $(\mathbf{q}^*)^T \mathbf{q}^*$ and compared to the prediction Eq. 6.17. Figure 6.1b shows the average squared charges per unit area as a function of l_{TF} while the integrated $\Delta F_{SG}^{1V, BO} / \mathcal{A}$ is plotted in figure 6.1c. The free energy difference ultimately should reach a plateau for large l_{TF} values, converging to the metallic-insulating free energy difference. The range of l_{TF} values that can be simulated is however limited by the depth of the electrode material nd , which needs to be large with respect to l_{TF} to ensure the last planes do not bear any charge.

The agreement with Eq. 6.17 is remarkable for $l_{TF} > d$, and holds equally for $\Delta\psi = 2$ V (not shown) and for gold electrodes. Two approximations made in this expression partly fail at small l_{TF} , explaining the discrepancies between the calculated values and the prediction: firstly the exponential decay of the charge within the electrode, shown in figure 4.2a-b and secondly the expression of the capacitance using $L_{\text{eff}} = L - d$, shown in figure 4.2c-e.

6.2 Influence of the metallicity on the surface tension: the impact of charge heterogeneity at the surface

We now move to the electrochemical systems investigated in section 4.2.3 to study the effect of metallicity on interfacial free energies in the presence of an electrolyte. We start by results at zero voltage in section 6.2.1, which we compare to the contact angle measurements of section 3.2.3, then test the influence of voltage in section 6.2.2. Lastly, we derive a simple model based on the lateral charge correlations on the surface to rationalize and propose a molecular understanding of the results in section 6.2.3.

6.2.1 Thomas-Fermi Thermodynamic Integration for electrochemical cells

Figure 6.2 shows the average squared charges per unit area and the associated BO free energy difference computed for a system of graphite electrodes with an 1M NaCl electrolyte (system (G4) in table 2.1) for an applied potential difference $\Delta\psi = 0$ V. Contrary to the empty capacitors, the BO contribution at 0 V does not vanish, although the total charge does on average. The shape is similar to the empty capacitor in figure 6.1, but the free energy values are one order of magnitude larger.

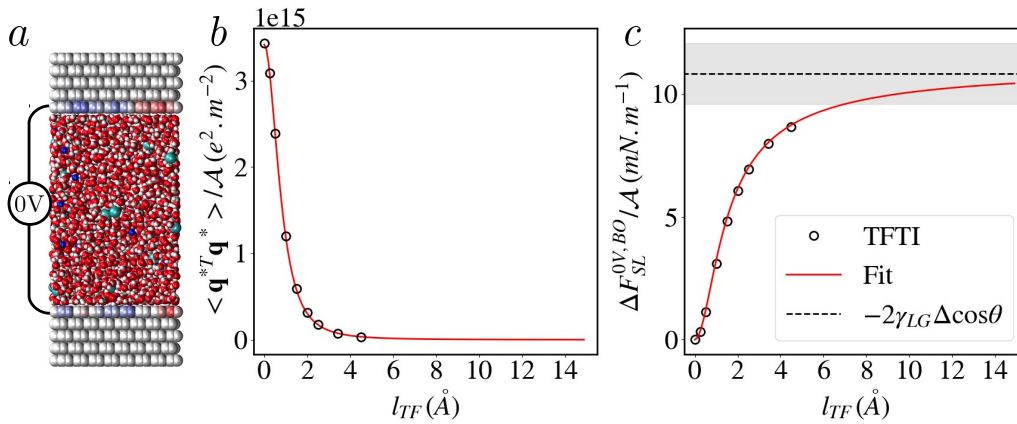


Figure 6.2: Thomas-Fermi Thermodynamic Integration for a graphite capacitor with a 1M NaCl electrolyte (system (G4) in table 2.1), at $\Delta\psi = 0$ V, shown in the snapshot (a). Average squared charges per unit area as a function of l_{TF} (b) and BO contribution to the free energy difference as a function of l_{TF} (c). Values from simulations are shown as open circles while the solid lines are fits using Eq. 6.21 in panel c and its analog in panel b.

We anticipate on section 6.2.3 and propose an empirical fitting function for the free energy per unit area of the form

$$\frac{\Delta F_{SL}^{0V, BO}}{\mathcal{A}}(l_{TF}) = 2k_B T \int_0^{l_{TF}} dl \frac{1}{\gamma_0 + \gamma_2 l^2} \frac{l(1 - e^{-d/l})^2}{d(1 - e^{-2d/l})}, \quad (6.21)$$

where γ_0 and γ_2 are two fitting parameters. The fit is shown in figure 6.2 and allows to extrapolate the asymptotic value at $l_{TF} \rightarrow \infty$, *i.e.* for the metallic-insulating difference, which is not reachable by direct computation because it would imply that the number of electrode planes $n \rightarrow \infty$. This value can be related to the surface tension difference Eq. 3.82 derived from the contact angle measurements

in section 3.2.3. Indeed, the free energy difference due to a change in metallicity corresponds to an interfacial effect and is therefore related to the difference in surface tension (considered as an interfacial free energy per unit area) as $\Delta F^{\Delta\psi} = (\Delta\gamma_L + \Delta\gamma_R)\mathcal{A}$. Here γ_L and γ_R are the surface tensions corresponding to the left L and right R interfaces, and the differences Δ are between a Thomas-Fermi metal at l_{TF} and an ideal metal. At $\Delta\psi = 0$ V, both interfaces are symmetric and the free energy difference reduces to $\Delta F_{SL}^{0V,BO} = \Delta F_{SL}^{0V} - \Delta F_{SG}^{0V} = 2\mathcal{A}\Delta\gamma_{SL} = -2\gamma_{LG}\Delta \cos\theta$, using also that $\Delta\gamma_{SG} = 0$ and that the non-BO contributions cancel. The corresponding value is reported on figure 6.2 and agrees very well with the extrapolated value at $l_{TF} \rightarrow \infty$, which validates the new thermodynamic integration approach.

6.2.2 Influence of voltage

In order to investigate the effect of voltage, we perform thermodynamic integrations of a gold capacitor with a 1M NaCl electrolyte (system (Au4) in table 2.1) at different voltages $\Delta\psi = 0, 1, 2$ V. Similar results were obtained for the previous graphite capacitors (system (G4) in table 2.1) for $\Delta\psi = 0, 2$ V but are not shown here. Figure 6.3 illustrates the free energy difference $\Delta F_{SL}^{\Delta\psi}(l_{TF})$ with respect to the ideal metal case, minus the zero voltage value $\Delta F_{SL}^0(l_{TF})$, as a function of voltage $\Delta\psi$. The behavior is quadratic as expected from Eq. 6.12 and agrees perfectly with this prediction using the capacitances per unit area $C_{SL}(0)$ and $C_{SL}(l_{TF})$ obtained from the average total charge of the electrodes (shown in figure 4.4c). This confirms that, for systems where linear response theory holds so that the integral capacitance C does not depend on voltage and is equal to the differential capacitance, it is sufficient to run simulations at zero voltage to obtain the zero voltage contribution $\Delta F^0(l_{TF})$ and to compute the voltage dependent contribution from the differential capacitance.

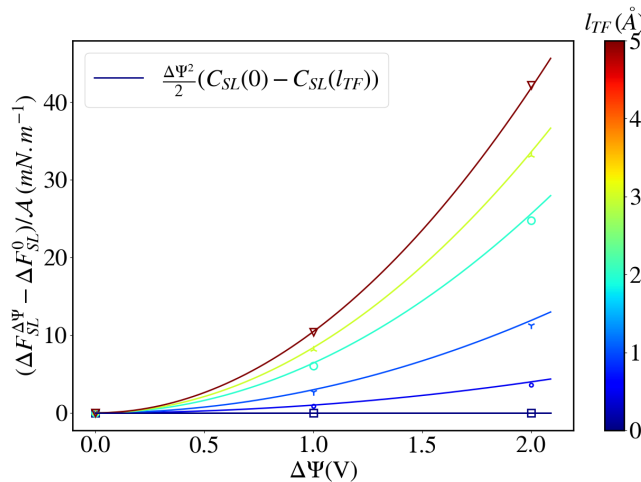


Figure 6.3: Free energy change $\Delta F_{SL}^{\Delta\psi}(l_{TF}) - \Delta F_{SL}^0(l_{TF})$ per unit area as a function of $\Delta\psi$ for a gold capacitor with a 1M NaCl aqueous electrolyte (system (Au4) in table 2.1). The simulation results (symbols) are shown for a range of Thomas-Fermi lengths l_{TF} and compared to the quadratic prediction Eq. 6.12 (lines) using the capacitances per unit area determined from the average total charge.

Contrary to section 6.2.1, these free energy differences cannot be easily converted into contact angle differences because the left and right electrodes are not symmetric in the presence of voltage, as shown *e.g.* in figure 4.5, and we thus expect γ_L and γ_R to be different. To circumvent this problem, we can hold the left electrode to a fixed l_{TF} value and only change the metallicity of the right electrode. We can show that the free energy is then computed using a modified Eq. 6.8 where the sum only takes into account the atoms of the right electrode. Preliminary simulations at $\Delta\psi = 2$ and -2 V yielded small differences between the negative and positive electrodes.

6.2.3 Analytical model: charge heterogeneity

Starting from the analytical prediction of section 6.1.3.1 for an empty capacitor and because of the similarities between figures 6.1 and 6.2, we develop a model based on Eq. 6.8. The three ingredients that yielded Eq. 6.17 are the exponential decay of the charge per planes within the electrodes, the homogeneous distribution of charge within a plane and the evolution of the capacitance with l_{TF} . We detail these elements for the case of a capacitor in the presence of an electrolyte in the following sections. Apart from the different value of capacitance, the main difference is the heterogeneous distribution of charge on the surface, as was already visible on figure 3.7b. In the following, the model is applied to the calculations of section 6.2.1 for a graphite-1M NaCl capacitor (system (G4) in table 2.1) at $\Delta\psi = 0$ V, if not stated otherwise.

6.2.3.1 Exponential decay of the charges

Even though the lateral symmetry of the system is broken in the presence of an electrolyte, considering the division of the electrodes into atomic planes is still useful. Indeed, the lateral heterogeneity does not change the decay of the charge with distance within the electrodes. Instantaneously, the decay is not exponential but in fact Eq. 4.34 still holds on average.

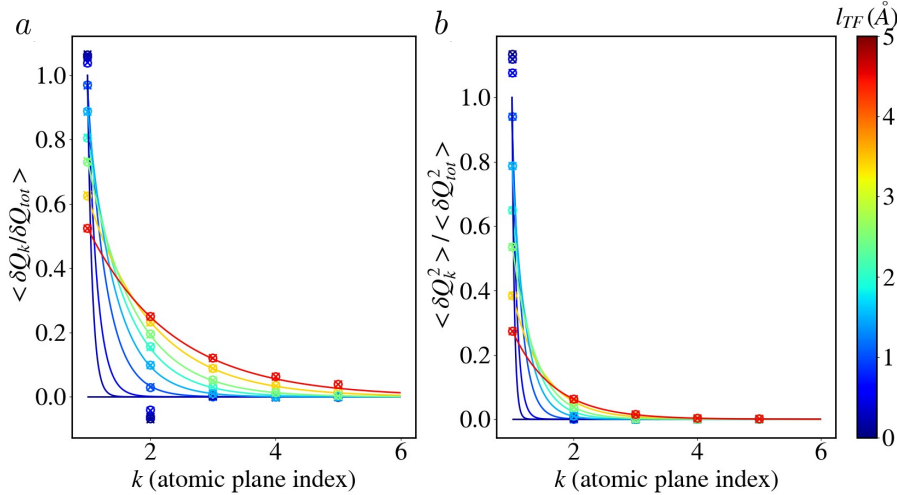


Figure 6.4: Average of the total charge per plane normalized by the total electrode charge $\langle \delta Q_k / \delta Q_{tot} \rangle$ (a) and average fluctuation of charge per plane normalized by the average fluctuation of the total electrode charge $\langle \delta Q_k^2 \rangle / \langle \delta Q_{tot}^2 \rangle$ (b), as a function of the atomic plane index k . The symbols are simulated values for different l_{TF} for both electrodes (circles and crosses) for a graphite capacitor with a 1M NaCl electrolyte (system (G4) in table 2.1) at $\Delta\psi = 0$ V, while the lines are the prediction of Eq. 6.23 in panel a) and Eq. 6.24 in panel b).

This was shown in figure 4.4a for a gold-1M NaCl capacitor at $\Delta\psi = 2$ V, which allows to write

$$\frac{\langle Q_k \rangle}{\langle Q_{tot} \rangle} = e^{-(k-1)d/l_{TF}} \left(1 - e^{-d/l_{TF}} \right). \quad (6.22)$$

For the graphitic capacitor at $\Delta\psi = 0$ V, the average value $\langle Q_k \rangle$ is equal to zero and the charge fluctuations become predominant. Figure 6.4a shows the dependence of the instantaneous fluctuations of charge around the mean, δQ_k , averaged over time and normalized by the total fluctuations, δQ_{tot} , with respect to the distance within the electrode for a range of l_{TF} . We observe it is exponentially decaying, as expected, so that

$$\left\langle \frac{\delta Q_k}{\delta Q_{tot}} \right\rangle = e^{-(k-1)d/l_{TF}} \left(1 - e^{-d/l_{TF}} \right). \quad (6.23)$$

This prediction is less accurate when l_{TF} becomes smaller than the intermolecular and interplanar distances, and we observe that for graphite electrodes it is worse than for gold electrodes (figure 4.4a), for which the distance between planes is smaller ($d_{\text{gold}} < d_{\text{graphite}}$). Finally figure 6.4b shows the decay for the fluctuations of charge $\langle \delta Q_k^2 \rangle / \langle \delta Q_{\text{tot}}^2 \rangle$ and allows to write the exponential decay

$$\frac{\langle \delta Q_k^2 \rangle}{\langle \delta Q_{\text{tot}}^2 \rangle} = e^{-2(k-1)d/l_{TF}} \left(1 - e^{-d/l_{TF}}\right)^2, \quad (6.24)$$

needed in the following derivation.

6.2.3.2 Average squared charges

With this knowledge, we then separate $\langle q_{i,k}^{*2} \rangle$ in its squared average value $\langle q_{i,k}^* \rangle^2 = \langle Q_k \rangle^2 / m^2$ and its fluctuations per plane $\langle \delta q_{i,k}^{*2} \rangle$, and write

$$\langle (\mathbf{q}^*)^T \mathbf{q}^* \rangle = \sum_{k=-\infty}^{\infty} \sum_{i=1}^m \langle q_{i,k}^{*2} \rangle = 2 \sum_{k=1}^{\infty} \sum_{i=1}^m \left(\langle q_{i,k}^* \rangle^2 + \langle \delta q_{i,k}^{*2} \rangle \right) = 2 \sum_{k=1}^{\infty} \sum_{i=1}^m \left(\frac{\langle Q_k \rangle^2}{m^2} + \frac{\alpha_k \langle \delta Q_k^2 \rangle}{m} \right), \quad (6.25)$$

where we introduced $\alpha_k = m \langle \delta q_{i,k}^{*2} \rangle / \langle \delta Q_k^2 \rangle$ to relate the individual charge fluctuations to those of the total charge of the k^{th} plane. We now sum over atoms in each plane and make the assumption, which we discuss in section 6.2.3.3, that α_k is equal in all planes, *i.e.* $\alpha_k = \alpha$. We then introduce the exponential decay of the charge, Eqs. 6.22 and 6.24, to obtain

$$\begin{aligned} \langle (\mathbf{q}^*)^T \mathbf{q}^* \rangle &= 2 \sum_{k=1}^{\infty} \left(\frac{\langle Q_k \rangle^2}{m} + \alpha \langle \delta Q_k^2 \rangle \right) = 2 \left(\frac{\langle Q_{\text{tot}} \rangle^2}{m} + \alpha \langle \delta Q_{\text{tot}}^2 \rangle \right) \sum_{k=1}^{\infty} e^{-2(k-1)d/l_{TF}} \left(1 - e^{-d/l_{TF}}\right)^2 \\ &= 2 \left(\frac{\langle Q_{\text{tot}} \rangle^2}{m} + \alpha \langle \delta Q_{\text{tot}}^2 \rangle \right) \frac{(1 - e^{-d/l_{TF}})^2}{1 - e^{-2d/l_{TF}}} = 2\mathcal{A} \left(\frac{C_{\text{int}}^2 \mathcal{A} \Delta \psi^2}{m} + \alpha k_B T C_{\text{diff}}^{BO} \right) \frac{(1 - e^{-d/l_{TF}})^2}{1 - e^{-2d/l_{TF}}}, \end{aligned} \quad (6.26)$$

where we used the definitions of the integral capacitance per unit area, C_{int} (Eq. 2.58), and the relationship between the BO contribution to the differential capacitance per unit area, C_{diff}^{BO} , and the total charge fluctuations (Eq. 3.55).

The BO free energy difference is then given by Eq. 6.8 as

$$\Delta F^{\Delta \psi, BO}(l_{TF}) = \frac{2\mathcal{A} \Delta \psi^2}{\epsilon_0} \int_0^{l_{TF}} dl C_{\text{int}}^2(l) \frac{l (1 - e^{-d/l_{TF}})^2}{d (1 - e^{-2d/l_{TF}})} + \Delta F^{0V, BO}(l_{TF}), \quad (6.27)$$

with a term that is quadratic in $\Delta \psi$, as predicted by Eq. 6.12, and

$$\Delta F^{0V, BO}(l_{TF}) = \frac{2mk_B T}{\epsilon_0} \int_0^{l_{TF}} dl \alpha(l) C_{\text{diff}}^{BO}(l) \frac{l (1 - e^{-d/l_{TF}})^2}{d (1 - e^{-2d/l_{TF}})}, \quad (6.28)$$

where we derived an expression for the term arising from charge fluctuations. This contribution becomes negligible for increasing voltages but is the only contribution to the free energy for $\Delta \psi = 0$ V.

Using the functional dependence of the capacitance with l_{TF} (Eq. 4.40), discussed in section 4.2.3.1, with an effective length L_{eff} (taken here as independent from l_{TF}),

$$C_{\text{int}}(l_{TF}) = \frac{\epsilon_0}{L_{\text{eff}} + 2l_{TF}}, \quad (6.29)$$

the first term has the same form as Eq. 6.17 for the empty capacitor with a different L_{eff} and can be further analyzed by taking the continuum limit $d \rightarrow 0$, as done in section 6.1.3.1, which gives

$$\Delta F^{\Delta\psi, BO}(l_{TF}) - \Delta F^{0, BO}(l_{TF}) \xrightarrow{d \rightarrow 0} \frac{\epsilon_0 \Delta\psi^2 \mathcal{A} l_{TF}}{L_{\text{eff}}(L_{\text{eff}} + 2l_{TF})}, \quad (6.30)$$

which is again consistent with Eq. 6.12.

6.2.3.3 Charge correlations term

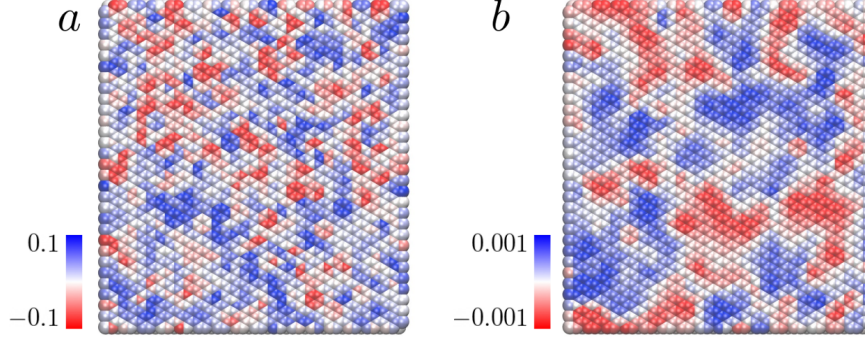


Figure 6.5: Instantaneous charge distribution (color bar in units of the elementary charge e) on the first electrode plane for $l_{TF} = 0.0 \text{ \AA}$ (a) and $l_{TF} = 4.5 \text{ \AA}$ (b), for a graphite capacitor with a 1M NaCl electrolyte (system (G4) in table 2.1 with a surface area four times larger $\mathcal{A}_2 = 68.202 \times 73.830 \text{ \AA}^2$) at $\Delta\psi = 0 \text{ V}$.

The term corresponding to charge fluctuations, $\Delta F^{0V, BO}(l_{TF})$ (Eq. 6.28), needs more discussion. The first aspect to discuss is the $\alpha_k = m \langle \delta q_{i,k}^{*2} \rangle / \langle \delta Q_k^2 \rangle$ factor introduced in Eq. 6.26. In the case of the empty capacitor, the surface is homogeneous so that there are no fluctuations with respect to the mean value and $\alpha_k = 0$. For the other limiting case, if the charge on each electrode atom is randomly distributed (without any correlations), we have

$$\langle \delta Q_k^2 \rangle = \left\langle \left(\sum_{i=1}^m \delta q_{i,k}^* \right)^2 \right\rangle = \left\langle \sum_{i=1}^m \delta q_{i,k}^{*2} \right\rangle + \left\langle \sum_{i=1}^m \sum_{j \neq i} \delta q_{i,k}^* \delta q_{j,k}^* \right\rangle = m \langle \delta q_{i,k}^{*2} \rangle, \quad (6.31)$$

so that $\alpha_k = 1$. Figure 6.5 shows that, at least for the first atomic plane in contact with the electrolyte, the charge distribution on the surface is heterogeneous with correlated regions, whose size depend on the screening length l_{TF} . To numerically characterize the charge correlation length, which visually seems to increase with the Thomas-Fermi length, we investigate the in-plane charge-charge radial distribution function, derived from Eq. 2.54 as

$$g_k^{qq}(r) = \frac{\langle \delta q_{i,k}^*(r) \delta q_{j,k}^*(0) \rangle}{\langle \delta q_{i,k}^{*2} \rangle} = \frac{\mathcal{A}}{2\pi r m \langle \delta q_{i,k}^{*2} \rangle} \left\langle \sum_{i=1}^m \sum_{j>i} \delta q_{i,k}^* \delta q_{j,k}^* \delta(r_{ij} - r) \right\rangle. \quad (6.32)$$

Results for a range of l_{TF} values in the first atomic plane $k = 1$ are shown in figure 6.6a. We observe a decay of the charge-charge correlations over a few angströms, faster for small l_{TF} than for larger ones. At long distances, the correlations become negative because of the electroneutrality constraint (see section 3.1.1.2).

In a first attempt, we used different fitting functions (*e.g.* Gaussian or exponential) to extract the characteristic decay length L_{corr} of g_1^{qq} , and obtained values for α_k . This approach suffered from the difficulty to fit the data and to determine the corresponding decay length. Instead, we note that we can consider the charge $Q_S = \frac{m}{\mathcal{A}} \iint_S dS \delta q(\mathbf{r})$ of a surface element S much larger than the correlation

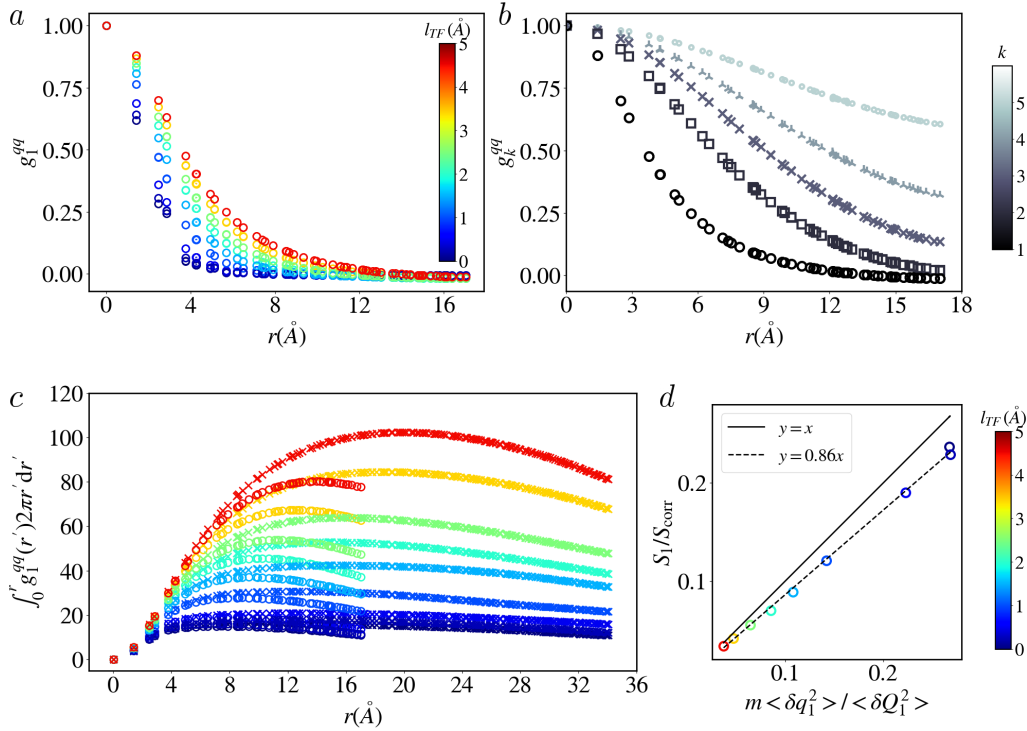


Figure 6.6: Charge correlations in a graphite capacitor with a 1M NaCl electrolyte (system (G4) in table 2.1) at $\Delta\psi = 0$ V. Charge-charge radial distribution function in the first atomic plane $g_1^{qq}(r)$ for a range of l_{TF} values (a) and $g_k^{qq}(r)$ at $l_{TF} = 4.5$ Å for different planes of the electrodes, with k the atomic plane index starting from 1, in contact with the electrolyte (black circles) to 5 (light grey small circles) (b). Integral $\int_0^r g_1^{qq}(r') 2\pi r' dr'$ for a range of l_{TF} values (c) and comparison of values for the main simulation box (open circles) and for one with double size in the x and y directions (crosses, corresponding to the snapshots of figure 6.5) for a selection of l_{TF} values. Ratio $S_1/S_{\text{corr},1}$ as a function of $m \langle \delta q_1^{*2} \rangle / \langle \delta Q_1^2 \rangle$ in the first atomic plane (d), for a range of l_{TF} . The solid black line corresponds to $y = x$ while the dashed line is a fit of the form $y = \gamma x$.

length and approximate¹⁶¹

$$\begin{aligned} \langle (\delta Q_S)^2 \rangle &= \left\langle \left(\frac{m}{\mathcal{A}} \iint_S dS \delta q^*(\mathbf{r}) \right)^2 \right\rangle = \left(\frac{m}{\mathcal{A}} \right)^2 \iint_S dS' \iint_S dS \langle \delta q^*(\mathbf{r}) \delta q^*(\mathbf{r}') \rangle \\ &\approx \left(\frac{m}{\mathcal{A}} \right)^2 S \langle \delta q^{*2} \rangle \int_0^\infty g^{qq}(r) 2\pi r dr, \end{aligned} \quad (6.33)$$

where we introduced polar coordinates, using the assumption that S is large, and extended the integral to $+\infty$. We then apply this relation to $S = \mathcal{A}$ the whole electrode surface area, to obtain

$$\frac{\langle \delta Q_k^2 \rangle}{m \langle \delta q_{i,k}^{*2} \rangle} \approx \frac{m}{\mathcal{A}} \int_0^\infty g^{qq}(r) 2\pi r dr. \quad (6.34)$$

We now introduce the surface area per atom $S_1 = \mathcal{A}/m$ and a correlation surface defined as

$$S_{\text{corr},k} = \int_0^\infty g_k^{qq}(r) 2\pi r dr, \quad (6.35)$$

so that we can express the factor α_k as

$$\alpha_k \approx \frac{S_1}{S_{\text{corr},k}}. \quad (6.36)$$

With Eq. 6.28 in mind, this formulation highlights the role of charge correlations and heterogeneity on the interfacial free energy. The assumption made in section 6.2.3.2 that α_k is the same in all planes is

clearly not verified, as shown by plotting g_k^{qq} for different planes in figure 6.6b for $l_{TF} = 4.5 \text{ \AA}$. Indeed, when going deeper into the electrode (larger k values), the molecular details of the electrolyte fade until the charge is homogeneously equal to zero within the bulk of the material. However, because of the exponential decay of the charge within the electrodes, the contribution of planes further from the surface decreases exponentially and we will show that the overall model is consistent with the data.

Lastly, the numerical evaluation of $S_{\text{corr},k}$ is conceptually challenging, because the measured g_k^{qq} values do not vanish for large distances, and the cumulative integral does not plateau. Therefore, taking the asymptotic value of the integral as $S_{\text{corr},k}$ is somewhat problematic. To further investigate this issue, we run shorter simulations for a larger system with cell dimensions twice as large in the x and y directions ($\mathcal{A}_2 = 68.202 \times 73.830 \text{ \AA}^2$). The cumulative integrals $\int_0^r g_1^{qq}(r') 2\pi r' dr'$ for both the main and larger system are compared in figure 6.6c. The short range behavior is similar for both system sizes, *i.e.* there is no finite size effect on the distribution of neighboring charges. At longer distances however, there is a clear discrepancy in the decrease in the integral, which reflects a negative correlation in the charge-charge radial distribution function g_1^{qq} . In larger boxes, the negative countercharge can be delocalized on a larger surface, leading to smaller individual charges at long distances. These observations are to connect to the calculations of induced charge profiles in section 3.2.1, where we also observed an influence of the finite box size with the electroneutrality constraint on the long-range induced charge, with larger charges at long distances in smaller boxes. It would seem that computing the correlation surface as the converged value of the integral is not possible, but we use the comforting observation that the total integral at half box size is comparable for both system sizes, which we thus take as the numerical value of $S_{\text{corr},k}$ (in the same way the integrated induced charge converged to 1e for both surface areas for an ion on top of a surface in section 3.2.1). This choice yields similar results to those obtained from the fitted correlation lengths and proves to be sufficiently accurate to describe the individual charge fluctuations. Figure 6.6d indeed compares the approximated value for α_1 from Eq. 6.36 using this correlation surface, with the value estimated directly from the charge fluctuations. The agreement is not perfect but there is a linear correlation, $\alpha_1 = 1.16 S_1/S_{\text{corr},1}$, with a coefficient close to 1.

6.2.3.4 Interfacial free energy and charge correlations

The previous developments yield the final analytical expression for the BO contribution to the free energy difference associated with a change in metallicity l_{TF} with respect to the ideal metal case for a zero applied voltage

$$\Delta F^{0,BO}(l_{TF}) = 2\mathcal{A} \frac{k_B T}{\epsilon_0} \int_0^{l_{TF}} dl \frac{C_{\text{diff}}^{BO}(l)}{S_{\text{corr}}(l)} \frac{l}{d} \frac{(1 - e^{-d/l_{TF}})^2}{1 - e^{-2d/l_{TF}}}, \quad (6.37)$$

which also inspired *a posteriori* the form of the fit of Eq. 6.21. This expression contains the contributions from the exponential decay of charge per plane, the magnitude of charge fluctuations, through the differential capacitance, and the lateral correlations of individual charges in a plane.

The evolution of the differential capacitance and of the correlation surface with the Thomas-Fermi length l_{TF} is shown in figure 6.7a-b. The capacitance decreases with l_{TF} as discussed in section 4.2.3.1 while the correlation surface increases with l_{TF} , consistently with a larger screening length and the visual observations made on figure 6.5. We also note that, even for the largest screening value $l_{TF} = 4.5 \text{ \AA}$ the correlation surface is much smaller than the surface area ($S_{\text{corr}} \ll \mathcal{A}$). Empirical fitting functions, shown on figure 6.7a-b, are used to extract the l_{TF} dependence for the capacitance

$$C_{\text{diff}}^{BO} = \epsilon_0 / (\gamma'_0 + 2l_{TF} + \gamma'_1 / (\gamma'_2 + l_{TF})), \quad (6.38)$$

and for the correlation surface

$$S_{\text{corr}} = \sqrt{\gamma''_0 + \gamma''_2 l_{TF}^2}, \quad (6.39)$$

where $\gamma'_0, \gamma'_1, \gamma'_2, \gamma''_0$ and γ''_2 are fitting parameters.

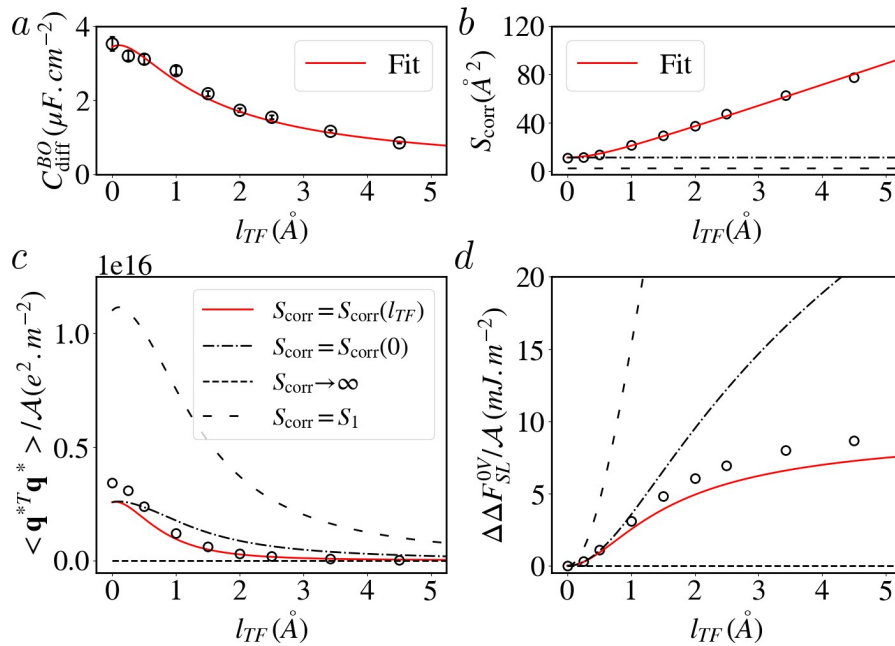


Figure 6.7: (a) Differential capacitance $C_{\text{diff}}^{\text{BO}}$ as a function of the Thomas-Fermi length l_{TF} computed from the electrode charge fluctuations at $\Delta\psi = 0.0$ V (open black circles); the line is a fit (see Eq. 6.38) used in panels (c) and (d). (b) Correlation surface S_{corr} obtained from the charge-charge correlation function (see Eq. 6.35); the solid red line is a fit (see Eq. 6.39) used in panels (c) and (d), while the dashed black line indicates the area per atom $S_1 = \mathcal{A}/m$ and the dash dotted line the value $S_{\text{corr}}(0)$. Average squared charges per unit area $\langle (\mathbf{q}^*)^T \mathbf{q}^* \rangle / \mathcal{A}$ (c) and interfacial free energy difference per unit area $\Delta \Delta F_{SL}^{0V}(l_{TF}) / \mathcal{A}$ (d): simulation results are compared to the predictions of Eqs. 6.26 and 6.37 (solid red line) using the fits of panels (a) and (b), as well as that for homogeneous ($S_{\text{corr}} \rightarrow \infty$, dotted line), uncorrelated ($S_{\text{corr}} = S_1$, dashed line) and l_{TF} -independent ($S_{\text{corr}} = S_{\text{corr}}(0)$, dash dotted line) charge distributions. Simulation results (open black circles) are given for a graphite capacitor with a 1M NaCl electrolyte (system (G4) in table 2.1) at $\Delta\psi = 0$ V.

Figure 6.7c compares the value of $\langle (\mathbf{q}^*)^T \mathbf{q}^* \rangle / \mathcal{A}$ per unit area from simulations to the approximation Eq. 6.26, estimated using the fits Eqs. 6.38 and 6.39. Some deviations are observed for small l_{TF} values but the overall shape is well reproduced. We also show that taking into account the heterogeneity of the surface is crucial by plotting the predictions corresponding at a homogeneous or random surface ($S_{\text{corr}} \rightarrow \infty$ or $S_{\text{corr}} = S_1$, *i.e.* $\alpha = 0$ or 1), which fail at estimating the order of magnitude. The l_{TF} dependence of the charge correlations $S_{\text{corr}}(l_{TF})$ is also shown to be important, since using the ideal metal value ($S_{\text{corr}} = S_{\text{corr}}(0)$) does not give the correct shape. The comparison for the free energy difference is given in figure 6.7d, now using Eq. 6.37. The deviations for large l_{TF} are due to the accumulation of errors upon integration, but we obtain a semi-quantitative agreement compared to the dramatic failure of the random, homogeneous and l_{TF} -independent distributions.

The simulations presented here allow to quantify the influence of metallicity on the interfacial free energies for a graphite-1M NaCl interface with good accuracy. The analytical model developed further supports the identification of the in-plane lateral charge-charge correlations as the microscopic explanation for the dependence on l_{TF} . During the course of this PhD, new studies have been published that also investigate the surface tension on metallic interfaces. In Ref. 303, Ntim and Sulpizi studied the [BMIM][BF₄] ionic liquid using the polarizable gold model¹⁰⁰ and computed the work of adhesion, *i.e.* the work to separate the liquid for the wall, which is related to the interfacial free energy, for both the polarizable and non-polarizable models. They found a value for the electrostatic contribution of 9.9 mN.m⁻¹, which compares well with the order of magnitude of our calculations (even though for a very different system). However, the same impact was found for solid configurations, which makes the authors conclude that the metallicity is not the dominant factor in the modification of the nanoscale freezing transition measured by Comtet *et al.*

On the contrary, Ref. 133 introduced a new simulation method using mobile charges restricted to the electrode region whose characteristics are carefully chosen to reproduce the behavior of a “virtual Thomas-Fermi fluid” of charged particles, by analogy with the Debye-Hückel equation. Note that in contrast with the Thomas-Fermi framework of this work, their reference was naturally chosen to be the insulator instead of the ideal metal. By simulating molten NaCl in contact with such electrode, they observe a crossover for small l_{TF} values from a non-wetting to a wetting of the surface, confirmed by surface tension calculations, which is consistent with our conclusion that metallic surfaces are more hydrophilic than insulating ones due to image charges.

6.3 Influence of metallicity on the crystallization

To investigate the crystallization phenomenon, we study a molten salt (NaCl) at different temperatures. We first analyze the lattice dilation of the NaCl face centered cubic crystal by heating up a bulk crystal at 350 K/ns, as shown in figure 6.8. We can roughly locate the melting temperature around $T_m \sim 1100$ K (considering that the melting during the temperature ramp occurs at a higher temperature due to liquid nucleation).

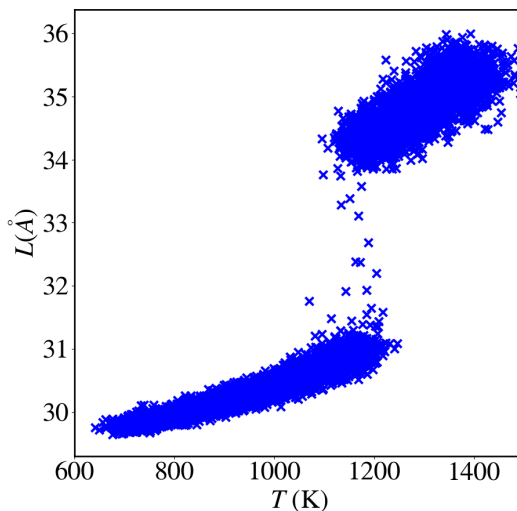


Figure 6.8: Evolution of the box size L as a function of temperature T during a heating ramp from $T = 700$ K to $T = 1400$ K, for a cubic box of crystalline NaCl containing 500 ion pairs.

From this, we choose to run simulations at 4 different temperatures: two in the solid phase (800 and 900 K) and two in the liquid phase (1200 and 1300 K). We thus build 4 graphite-molten salt capacitors (system (G5) in table 2.1) and equilibrate them using NP_zT simulations of 1 ns. The position of the graphite electrodes was fixed at the equilibrium distance (see table 2.3).

We then run simulations for a range of l_{TF} values for all systems, in order to perform the thermodynamic integration presented in section 6.1. The results are given for the different temperatures in figure 6.9. It appears that the metallicity has a larger impact on the liquid phase than the solid one for this system, contrary to the findings of Ref. 303. These are only preliminary results and a thorough analysis of the simulations is yet to be accomplished. As a first step in this direction, we plot in figure 6.10 the time autocorrelation function of the total charge both for $T = 800$ K and $T = 1300$ K. While the decay depends on the screening length l_{TF} for the liquid phase, as we found in section 4.2.3.3, the dependence of the BO contribution to the free energy on l_{TF} is much weaker in the solid phase, and a peculiar oscillating behavior appears. Further analyses will be carried out in the future. A particular attention will be focused on the evaluation of the non-BO term, which may play a role due to the difference of electrode separation for different temperatures. This will allow to

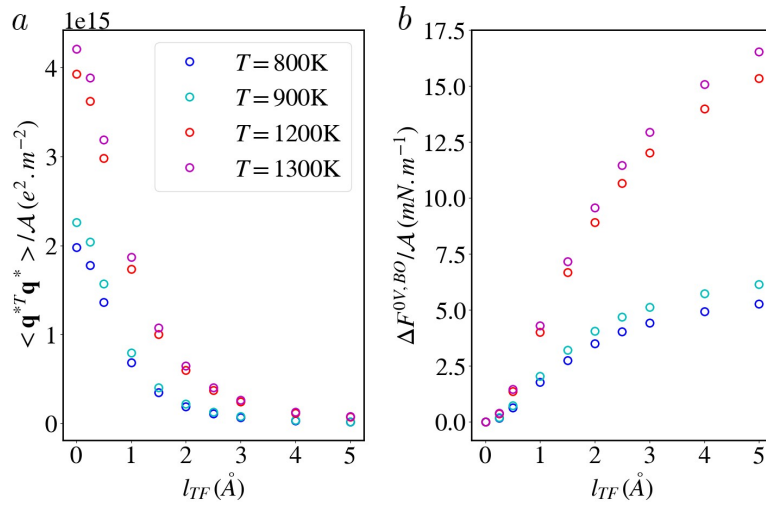


Figure 6.9: Thomas-Fermi thermodynamic integration for a graphite-molten salt capacitor (system (G5) in table 2.1) for different temperatures $T = 800, 900, 1200$ and 1300 K. Average squared charges per unit area as a function of l_{TF} (a) and BO contribution to the free energy difference as a function of l_{TF} (b).

investigate among others the influence of the difference in density between the solid and liquid phase, indicated by Comtet *et al.* as a major factor in the interfacial free energy differences.

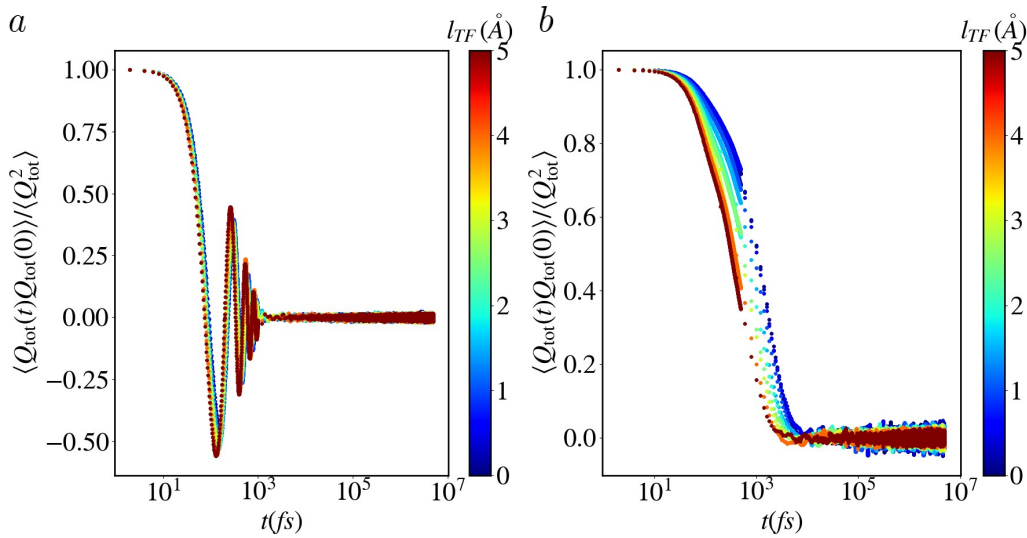


Figure 6.10: Time autocorrelation function of the total charge Q_{tot} as defined in Eq. 2.60 for a molten salt-graphite capacitor (system (G5) in table 2.1) at $\Delta\psi = 0\text{ V}$, at $T = 800\text{ K}$ (a) and $T = 1300\text{ K}$ (b), corresponding to solid and liquid phases, respectively.

“Forget-me-not”: Phase transitions under confinement

- We developed a new framework based on thermodynamic integration to compute the free energy difference associated with a change in the Thomas-Fermi length l_{TF} with respect to the ideal metal ($l_{TF} = 0$).
- We applied the method to an empty capacitor and compared it to analytical predictions. For an electrochemical cell, we validated the method by comparing the free energy results to previous contact angle measurements.
- In the presence of an electrolyte, we find that the free energy difference contains a term quadratic in the applied voltage $\Delta\psi$ and a term arising from the charge fluctuations on the electrode. We developed a model that reproduces the simulation results and that shows the crucial role of charge heterogeneity and lateral correlations on the interfacial free energy.
- We have finally presented preliminary results on molten salts in the liquid and solid phase.

Chapter 7

Conclusion and Perspectives

This PhD thesis aimed at investigating the influence of the metallicity of solids on the properties of interfacial electrolytes, in particular on the interfacial free energy, related to the shift of the phase diagram under confinement. This question arises from experiments of ionic liquids on a range of surfaces, that display surprisingly strong layering, or even solid-like layers on several tens of nanometers at the interface. In particular, the AFM measurements of Comtet *et al.*⁸⁴, highlighting a nanoscale freezing transition of ionic liquids under confinement, showed markedly different behavior on insulating surfaces of mica with respect to metallic platinum. Although these can seem exotic systems, such interfaces are *e.g.* common in electrochemical cells for electric double layer capacitors, and are investigated for applications in lubrication and heterogeneous catalysis.

Because of the time and length scales at play, molecular simulations are a useful tool to gain molecular insights into these complex interfaces, that further allow to investigate parameters such as the metallicity of the solid in a controlled fashion, and to extract free energy differences by using advanced enhanced sampling techniques. During this PhD, we followed the guideline of confined phase transitions and the effect of tuning the metallicity of the substrate. Along this path, we first made several theoretical developments.

- *The development of the statistical mechanical framework of the constant potential ensemble (see chapter 3).* We derived explicit analytical expressions for the partition function and showed that the Born-Oppenheimer sampling scheme, by suppressing some thermal charge fluctuations around the Born-Oppenheimer charge, does not exactly reproduce the probability distribution of the constant potential ensemble. This is without consequences for the computation of charge-independent observables, or even of observables that are a linear combination of the electrode charges. However, in general the ensemble average may lack a contribution, and this is the case for the differential capacitance. It can be obtained from the variance of the total charge distribution, containing fluctuations due to the electrolyte thermal motion, and an additional contribution corresponding to the capacitance of the empty capacitor.
- *The extension of the constant potential simulations to tune the metallicity of electrodes using the Thomas-Fermi model (see chapter 4).* In collaboration with Dr. Thomas Dufils and Prof. Mathieu Salanne, we added the kinetic energy of electrons in the Thomas-Fermi approximation, by using locally the free electron gas expression. This partially accounts for the quantum nature of electrons, and resulted in an additional quadratic term in the energy that depends on the Thomas-Fermi length l_{TF} . This screening length quantifies the electrostatic screening of an external perturbation by the electrons of the metal: the smaller the screening length, the better the metal. The ideal metal case corresponds to $l_{TF} = 0$, while the insulating case is for $l_{TF} \rightarrow \infty$. Analytical expressions for the exponential decay of the charge were verified in simulations of empty capacitors.
- *A look back at the Gibbs-Thomson equation for the melting temperature shift due to confinement (see chapter 5).* In collaboration with Prof. Benoît Coasne at Université Grenoble Alpes, we

revisited the derivation of the Gibbs-Thomson equation for a fluid confined in a slit pore. We took a “confined Clausius-Clapeyron” approach and integrated the resulting relation from a bulk to a confined system in equilibrium with an external reservoir, along the solid-liquid coexistence. This derivation allowed to identify the approximations of the equation, and to adapt it to other geometries or external reservoir conditions. We then studied a model Lennard-Jones system to test some of these approximations and the validity of the Gibbs-Thomson equation at the nanoscale. The results were somewhat disappointing, mainly because of the difficulties related to the solid-liquid phase transition (commensurability, barriers to nucleation, reversibility, phase space sampling, etc. . .). Nevertheless, we devised a new thermodynamic integration technique to extract the difference in surface tension by directly driving the system through the phase transition, from solid to liquid and vice-versa.

We then carried out a comparison of constant potential versus constant charge simulations and a systematic study of aqueous capacitors as a function of the Thomas-Fermi length l_{TF} , from that of an ideal metal to non-ideal metals with l_{TF} up to 5 Å. Note that previous studies (see section 1.2.3) found noticeable changes due to the polarization of the electrode only for ionic liquids at large voltages. In this work, we started by investigating aqueous systems to better assess the new Thomas-Fermi implementation – before turning to unusual phenomena with ionic liquids.

- For constant potential versus constant charge simulations, we looked for small effects at $\Delta\psi = 0$ V. As expected, we found no modification of the water structure and only little change on the free energy profile of an ion approaching a graphite surface in a solvent. However, small but quantitative changes, due to differences in the interfacial free energies, were measured in contact angles of 1M NaCl solution drops on insulating or metallic graphite.
- We showed by the systematic study of a model gold capacitor with a 1M NaCl solution that the electric potential indeed decreases exponentially within the electrode with a characteristic decay length equal to l_{TF} , and that increasing the screening length l_{TF} considerably reduces the capacity, *i.e.* the ability of the metal to accumulate charge at the surface. The results are comparable to analytical approximations including a “quantum capacitance” but the interplay between the electrolyte configurations and the electronic polarization on the electrode makes the measured capacitance values deviate ($\sim 20\%$) from such approximations, highlighting the importance of molecular simulations to obtain accurate results.
- The difference in accumulated charge at the interface with l_{TF} at finite voltage is only accompanied by a small reorientation of water molecules, but the overall water density remains unchanged. The ionic density profiles however show an evolution of the various peaks, which is consistent with a larger electrode charge for smaller l_{TF} values. Similar results were obtained for graphitic capacitors and more complex changes were observed for ionic liquids.
- The influence of the sole distribution of individual atomic charges (*i.e.* not the average charge of the electrode) as a function of l_{TF} was instead investigated on simulations at $\Delta\psi = 0$ V. We found that in this case, although no changes in the structure are visible, the charge dynamics are quantitatively affected, with faster relaxation times at larger l_{TF} values. We associated this with weaker interactions of the dangling hydrogen bonds with the surface.
- We further developed a thermodynamic integration method to study the interfacial free energy as a function of the screening length l_{TF} , taking the ideal metal as a reference. This confirmed that even at $\Delta\psi = 0$ V with a polar solvent there is a measurable change in surface tension, as confirmed by contact angle measurements, and that more metallic surfaces are more hydrophilic. By developing a semi-analytical model, we also showed that the microscopic origin of this change is related to increasing in-plane lateral charge correlations at the surface of the electrode with increasing l_{TF} .

This PhD thesis has thus developed the theoretical and numerical tools opening the door to the systematic investigation of the influence of the metallicity of a substrate, measured by its screening length l_{TF} , on the properties of electrochemical interfaces.

- Studies of molten salts using the new Thomas-Fermi free energy method, both in the liquid and the solid phase are ongoing and should help to shed some light on the dependence of the crystallization phenomenon on metallicity. In particular, the effect of crystal periodicity on the in-plane charge correlations should be interesting to study.
- Other properties could not be investigated during the length of this PhD. We could use the calculation of the force on the electrodes to study the phenomenon of electrostriction, *i.e.* swelling due to an applied voltage, and its dependence on the screening length. The effect of metallicity on transport properties and velocity profiles under flow could also be investigated.
- To better understand the experiments, it will also be necessary to go towards ionic liquid electrolytes. The Thomas-Fermi thermodynamic integration method can straightforwardly be adapted to such systems. However, care will be needed to determine the appropriate crystal structure under confinement of these complex liquids, which tend to have glassy transitions instead of proper crystallization.
- Finally, the implementation of the Thomas-Fermi model in classical molecular simulations allowed to systematically study the influence of metallicity, without changing any other parameter (such as crystal structure or non-electrostatic interactions). However, up to now it did not result in capacitance values closer to experimental ones, and there is therefore still significant room for improvement of the constant potential simulations. Evolutions of the model, *e.g.* adding a dependence of the Thomas-Fermi length l_{TF} on the applied voltage $\Delta\psi$ by parametrizing the material's density of states, were proposed. One aspect of constant potential simulations that has been put under the carpet by most studies is the determination of the Gaussian width of electrodes. It was fixed by Siepmann and Sprik¹⁰⁹ to match continuum electrostatics predictions but has not been reinvestigated since. A parametrization of this Gaussian width, similarly to the parametrization of the spring constant in Drude oscillators using the atom's polarizability¹⁰⁰, is a promising possibility. We could use common Gaussian basis sets developed for Density Functional Theory as input, or simply use the hardness as done in charge equilibration (QE) methods. Ongoing preliminary calculations seem to go in the right direction, with higher capacitance values arising from the appearance of "inner-sphere" complexes at the interface, but a detailed investigation remains necessary.

Appendix A

Publications from this work

Publications in peer-reviewed journals

- A. Serva, L. Scalfi, B. Rotenberg, M. Salanne, Effect of the metallicity on the capacitance of gold - aqueous sodium chloride interfaces, *J. Chem. Phys.*, 155 (2021).
- L. Scalfi, B. Coasne, B. Rotenberg, On the Gibbs-Thomson equation for the crystallization of confined fluids, *J. Chem. Phys.*, 154, 114711 (2021).
- L. Scalfi, M. Salanne, B. Rotenberg, Molecular Simulation of Electrode-Solution Interfaces, *Annu. Rev. Phys. Chem.*, 72 (2021).
- L. Scalfi, T. Dufils, K. Reeves, B. Rotenberg, M. Salanne, A semiclassical Thomas-Fermi model to tune the metallicity of electrodes in molecular simulations, *J. Chem. Phys.*, 153 (17), 174704 (2020).
- A. Marin-Lafleche, M. Haefele, L. Scalfi, A. Coretti, T. Dufils, G. Jeanmairret, S. Reed, A. Serva, R. Berthin, C. Bacon, S. Bonella, B. Rotenberg, P. A. Madden and M. Salanne, MetalWalls: A molecular dynamics software dedicated to the modelling of electrochemical systems, *J. Open Source Software*, 5 (53), 2373 (2020).
- A. Coretti, L. Scalfi, C. Bacon, B. Rotenberg, R. Vuilleumier, G. Ciccotti, M. Salanne and S. Bonella, Mass-zero constrained molecular dynamics for electrode charges in simulations of electrochemical systems, *J. Chem. Phys.*, 152, 194701 (2020).
- L. Scalfi, D. Limmer, A. Coretti, S. Bonella, P. Madden, M. Salanne, B. Rotenberg, Charge fluctuations from molecular simulations in the constant-potential ensemble, *Phys. Chem. Chem. Phys.*, 22, 10480-10489 (2020).

Publications submitted for review

- L. Scalfi and B. Rotenberg, Microscopic origin of the effect of substrate metallicity on interfacial free energies, arXiv:2105.06799 (2021).

Appendix B

A simulation code: *MetalWalls*

B.1 MetalWalls

MetalWalls is a molecular simulation software dedicated to the simulation of electrochemical cells. At the beginning of this PhD, the source code was mainly developed by Prof. Mathieu Salanne at laboratoire PHENIX, Matthieu Haeefele and Abel Marin-Laffèche, two research engineers who greatly improved the computational efficiency of the code. During this PhD work, several new functionalities were added to the code, with a lot of help from them. With Matthieu Haeefele, we were also able to participate in a workshop on “HPC (High Performance Computing) Performance Evaluation” in September 2019 and to profile the code using Scalasca and Paraver, *i.e.* to analyze what happens during the run in order to optimize the computation time. *MetalWalls* has been released open source in September 2020 at <https://gitlab.com/ampere2/metalwalls> and in Ref. 153.

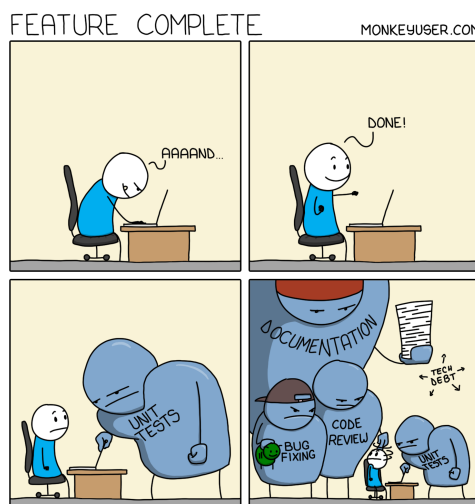


Figure B.1: A typical day of coding! Taken from the comics website <https://www.monkeyuser.com/2020/feature-complete/>.

MetalWalls is written in Fortran 90 and parallelized using MPI, and the compilation requires LAPACK for matrix inversions. A new GPU version is in development. It is hosted on a public Gitlab, as well as on a private Gitlab where the coding occurs, using the Git version control software. A Continuous Integration is set up, *i.e.* each new addition to the code is automatically run and tested on a panel of tests. An extensive documentation was also written (available in the Wiki section of the Gitlab) before the code was release.

MetalWalls has also been interfaced with PLUMED by Dr. Guillaume Jeanmairret, which allowed to run the Umbrella Sampling simulations of section 3.2.2 and the biased simulations of section 5.3.2.

B.2 Code improvements

B.2.1 Input/output

The first improvement to *MetalWalls* was the implementation of standard outputs for the trajectories, such as *XYZ*, *PDB*, *.lammprj* formats, to facilitate the visualization of trajectories using standard software such as VMD³⁰⁴. In particular, the *trajectories.lammprj* output file was designed to be able to easily visualize the fluctuating charges on the electrodes using a simple script provided with the source code.

B.2.2 Pistons and NP_zT simulations

Later, we modified the code to allow the rigid electrodes to translate on the z axis, subject to the forces from the electrolyte and an external constant pressure force, as detailed in section 2.3.2.3. This required the calculation of the force on the electrode, the addition of an integrator to translate the electrodes and a particular care to the Ewald summation and the calculation of electrode charges. This improvement allowed in particular to straightforwardly equilibrate the density in systems with two electrodes separated by an electrolyte.

B.2.3 Four-sites water models

The four-sites water models, such as the TIP4P water model³⁰⁵, are a class of water models that add a virtual atom away from the oxygen atom, along the bisector of the hydrogen-oxygen-hydrogen angle. This dummy atom bears the charge (and in some four-site models the dipole) of the oxygen atom, while the Lennard-Jones center stays on the oxygen atom. We implemented these models in *MetalWalls* to extend the possible force fields. Care must be taken to redistribute the forces and the stress tensor, according to Ref. 306, in order to maintain the constrained geometry of water.

B.2.4 Python interface to *MetalWalls*

A big addition to code was the creation of a Python interface to *MetalWalls*, in the same way LAMMPS is interfaced with Python (see appendix D). This allows a virtually illimited amount of possibilities using *MetalWalls* precompiled subroutines, *e.g.* accessing specific variables during the simulation, running complex thermodynamic integration procedures, use parts of it to run Monte Carlo simulations or even interface it with other codes. This interface allows to combine the simplicity of scripting with Python with the efficiency of Fortran subroutines, and to add new functionalities to *MetalWalls* without overly complicating the architecture of the source code.

The compilation of *MetalWalls* as an external library is done using the Python library *f2py* (Fortran to Python interface generator, part of the *numpy* package), as well as the wrapper *f90wrap*, which allows to interface Fortran derived types, largely used in *MetalWalls*.

This interface was intended to run the thermodynamic integrations of this thesis, but easier implementations using directly the PLUMED interface were used. Nevertheless, it allowed to examine the interaction matrix \mathbf{A} , and to easily script simple and repetitive calculations such as the energy profile of an ion as a function of the distance in figure 3.4.

Appendix C

Ewald summation

This appendix completes section 2.1.3.3 and gives the Ewald summation expressions for the electrostatic interactions for a system of N point charges q_i^{pc} and M Gaussian charges q_i with width η_i^{-1} , with 3D (see section C.1) and 2D (see section C.2) periodic boundary conditions. The total energy is separated into point charges interactions, Gaussian charges interactions and cross-terms interactions. We use here the same notations as in the main text, with α^{-1} the width of the Ewald gaussian and $\eta_{ij} \equiv \frac{\eta_i \eta_j}{\sqrt{\eta_i^2 + \eta_j^2}}$.

C.1 3D Ewald summation for Gaussian and point charges

C.1.1 Point charges

$$\begin{aligned} \mathcal{U}_{\text{el},3\text{D}}^{\text{pc-pc}} &= \frac{1}{2} \sum_{i=1}^N \sum_{j=1}^N \frac{q_i^{\text{pc}} q_j^{\text{pc}}}{4\pi\epsilon_0} \sum_{\mathbf{n}}' \frac{\text{erfc}(\alpha|\mathbf{r}_{ij} + \mathbf{n}|)}{|\mathbf{r}_{ij} + \mathbf{n}|} \\ &+ \frac{2\pi}{L_x L_y L_z} \sum_{i=1}^N \sum_{j=1}^N \frac{q_i^{\text{pc}} q_j^{\text{pc}}}{4\pi\epsilon_0} \sum_{\mathbf{k} \neq 0} e^{i\mathbf{k} \cdot \mathbf{r}_{ij}} \frac{1}{|\mathbf{k}|^2} e^{-\frac{|\mathbf{k}|^2}{4\alpha^2}} \\ &- \frac{\alpha}{\sqrt{\pi}} \sum_{i=1}^N \frac{(q_i^{\text{pc}})^2}{4\pi\epsilon_0} \end{aligned} \quad (\text{C.1})$$

C.1.2 Gaussian charges

$$\begin{aligned} \mathcal{U}_{\text{el},3\text{D}}^{\text{gc-gc}} &= \frac{1}{2} \sum_{i=1}^M \sum_{j=1}^M \frac{q_i q_j}{4\pi\epsilon_0} \sum_{\mathbf{n}}' |\mathbf{r}_{ij} + \mathbf{n}|^{-1} (\text{erfc}(\alpha|\mathbf{r}_{ij} + \mathbf{n}|) - \text{erfc}(\eta_{ij}|\mathbf{r}_{ij} + \mathbf{n}|)) \\ &+ \frac{2\pi}{L_x L_y L_z} \sum_{i=1}^M \sum_{j=1}^M \frac{q_i q_j}{4\pi\epsilon_0} \sum_{\mathbf{k} \neq 0} e^{i\mathbf{k} \cdot \mathbf{r}_{ij}} \frac{1}{|\mathbf{k}|^2} e^{-\frac{|\mathbf{k}|^2}{4\alpha^2}} \\ &+ \frac{1}{\sqrt{\pi}} \sum_{i=1}^M \frac{q_i^2}{4\pi\epsilon_0} \left(\frac{\eta_i}{\sqrt{2}} - \alpha \right) \end{aligned} \quad (\text{C.2})$$

C.1.3 Cross interactions

$$\begin{aligned} \mathcal{U}_{\text{el},3\text{D}}^{\text{pc-gc}} &= \sum_{i=1}^N \sum_{j=1}^M \frac{q_i^{\text{pc}} q_j}{4\pi\epsilon_0} \sum_{\mathbf{n}} |\mathbf{r}_{ij} + \mathbf{n}|^{-1} (\text{erfc}(\alpha|\mathbf{r}_{ij} + \mathbf{n}|) - \text{erfc}(\eta_j|\mathbf{r}_{ij} + \mathbf{n}|)) \\ &+ \frac{4\pi}{L_x L_y L_z} \sum_{i=1}^N \sum_{j=1}^M \frac{q_i^{\text{pc}} q_j}{4\pi\epsilon_0} \sum_{\mathbf{k} \neq 0} e^{i\mathbf{k} \cdot \mathbf{r}_{ij}} \frac{1}{|\mathbf{k}|^2} e^{-\frac{|\mathbf{k}|^2}{4\alpha^2}} \end{aligned} \quad (\text{C.3})$$

C.2 2D Ewald summation for Gaussian and point charges

In the following, we further use $\boldsymbol{\xi}_{ij} = (x_j - x_i)\mathbf{e}_x + (y_j - y_i)\mathbf{e}_y$ is the radial in-plane vector and $z_{ij} = z_j - z_i$, so that $\mathbf{r}_{ij} = \boldsymbol{\xi}_{ij} + z_{ij}\mathbf{e}_z$.

C.2.1 Point charges

$$\begin{aligned}
 \mathcal{U}_{\text{el},2\text{D}}^{\text{pc-pc}} &= \frac{1}{2} \sum_{i=1}^N \sum_{j=1}^N \frac{q_i^{\text{pc}} q_j^{\text{pc}}}{4\pi\epsilon_0} \sum_{\mathbf{n}}' \frac{\text{erfc}(\alpha|\mathbf{r}_{ij} + \mathbf{n}|)}{|\mathbf{r}_{ij} + \mathbf{n}|} \\
 &+ \frac{1}{L_x L_y} \sum_{i=1}^N \sum_{j=1}^N \frac{q_i^{\text{pc}} q_j^{\text{pc}}}{4\pi\epsilon_0} \sum_{\mathbf{k} \neq 0} \int_{-\infty}^{+\infty} du \frac{\cos(\mathbf{k} \cdot \boldsymbol{\xi}_{ij} + uz_{ij})}{|\mathbf{k}|^2 + u^2} e^{-\frac{|\mathbf{k}|^2 + u^2}{4\alpha^2}} \\
 &- \frac{\sqrt{\pi}}{L_x L_y} \sum_{i=1}^N \sum_{j=1}^N \frac{q_i^{\text{pc}} q_j^{\text{pc}}}{4\pi\epsilon_0} \left(\frac{e^{-z_{ij}^2 \alpha^2}}{\alpha} + \sqrt{\pi} |z_{ij}| \text{erf}(\alpha|z_{ij}|) \right) \\
 &- \frac{\alpha}{\sqrt{\pi}} \sum_{i=1}^N \frac{(q_i^{\text{pc}})^2}{4\pi\epsilon_0}
 \end{aligned} \tag{C.4}$$

C.2.2 Gaussian charges

$$\begin{aligned}
 \mathcal{U}_{\text{el},2\text{D}}^{\text{gc-gc}} &= \frac{1}{2} \sum_{i=1}^M \sum_{j=1}^M \frac{q_i q_j}{4\pi\epsilon_0} \sum_{\mathbf{n}}' |\mathbf{r}_{ij} + \mathbf{n}|^{-1} (\text{erfc}(\alpha|\mathbf{r}_{ij} + \mathbf{n}|) - \text{erfc}(\eta_j |\mathbf{r}_{ij} + \mathbf{n}|)) \\
 &+ \frac{1}{L_x L_y} \sum_{i=1}^M \sum_{j=1}^M \frac{q_i q_j}{4\pi\epsilon_0} \sum_{\mathbf{k} \neq 0} \int_{-\infty}^{\infty} du \frac{\cos(\mathbf{k} \cdot \boldsymbol{\xi}_{ij} + uz_{ij})}{|\mathbf{k}|^2 + u^2} e^{-\frac{|\mathbf{k}|^2 + u^2}{4\alpha^2}} \\
 &- \frac{\sqrt{\pi}}{L_x L_y} \sum_{i=1}^M \sum_{j=1}^M \frac{q_i q_j}{4\pi\epsilon_0} \left(\frac{e^{-z_{ij}^2 \alpha^2}}{\alpha} + \sqrt{\pi} |z_{ij}| \text{erf}(\alpha|z_{ij}|) \right) \\
 &+ \frac{1}{\sqrt{\pi}} \sum_{i=1}^M \frac{q_i^2}{4\pi\epsilon_0} \left(\frac{\eta_i}{\sqrt{2}} - \alpha \right)
 \end{aligned} \tag{C.5}$$

C.2.3 Cross interactions

$$\begin{aligned}
 \mathcal{U}_{\text{el},2\text{D}}^{\text{pc-gc}} &= \sum_{i=1}^N \sum_{j=1}^M \frac{q_i^{\text{pc}} q_j}{4\pi\epsilon_0} \sum_{\mathbf{n}}' |\mathbf{r}_{ij} + \mathbf{n}|^{-1} (\text{erfc}(\alpha|\mathbf{r}_{ij} + \mathbf{n}|) - \text{erfc}(\eta_j |\mathbf{r}_{ij} + \mathbf{n}|)) \\
 &+ \frac{2}{L_x L_y} \sum_{i=1}^N \sum_{j=1}^M \frac{q_i^{\text{pc}} q_j}{4\pi\epsilon_0} \sum_{\mathbf{k} \neq 0} \int_{-\infty}^{\infty} du \frac{\cos(\mathbf{k} \cdot \boldsymbol{\xi}_{ij} + uz_{ij})}{|\mathbf{k}|^2 + u^2} e^{-\frac{|\mathbf{k}|^2 + u^2}{4\alpha^2}} \\
 &- \frac{2\sqrt{\pi}}{L_x L_y} \sum_{i=1}^N \sum_{j=1}^M \frac{q_i^{\text{pc}} q_j}{4\pi\epsilon_0} \left(\frac{e^{-z_{ij}^2 \alpha^2}}{\alpha} + \sqrt{\pi} |z_{ij}| \text{erf}(\alpha|z_{ij}|) \right)
 \end{aligned} \tag{C.6}$$

Appendix D

Implementation of GEMC and GDI simulations

The Gibbs-Ensemble Monte Carlo simulation described in section 2.4.5.1 and the Widom insertion method described in section 2.4.5.2 and the Gibbs-Duhem Integration (GDI) method described in section 2.4.5.3, used in section 5.3.1, were implemented using the molecular dynamics code LAMMPS^{228;229} using its Python interface (see https://lammmps.sandia.gov/doc/Python_head.html). This consists in compiling LAMMPS as a shared library and use its functions within a Python script, to tailor its usage to a particular application. Indeed, both for the GEMC and the GDI simulations, we need to be able to run in parallel two simulation boxes (one in the liquid and one in the vapor phase for example), and to exchange information between them periodically. Using the MPI parallelization (Message Passing Interface, using the *mpi4py* library), the Python interface of LAMMPS allows to create two instances of LAMMPS on two different subcommunicators and easily run both boxes, using LAMMPS functions to initialize the simulation, store arrays of positions and box sizes, compute potential energy and the virial, etc. . .

D.1 Gibbs-Ensemble Monte Carlo

The GEMC simulations were implemented as described in Refs. 194, 195 and 184. We performed 4,005,000 Monte Carlo moves, chosen randomly between the displacement of an atom (in either box), the change of volume and the exchange of a particle between boxes, with a probability of 0.4994, 0.0012 and 0.4994, respectively. The displacement of an atom was between $[-0.5, 0.5]$ Å, while the volume dilation factor $d \ln[V_1/V_2]$ was in $[-0.01, 0.01]$.

D.2 Widom insertion method

Similarly, although only one box and one instance of LAMMPS is needed in this case, we used the Python interface to LAMMPS to compute the chemical potential at a given point in the phase diagram and followed the implementation given in Ref. 184. we performed 6,400,000 Monte Carlo moves, chosen randomly between the displacement of an atom between $[-0.5, 0.5]$ Å, and a Widom insertion move, *i.e.* the temporary insertion of an atom to compute the average in Eq. 2.72, with a probability of 1/3 and 2/3, respectively.

D.3 Gibbs-Duhem Integration

The GDI method also needs the coupling of two instances of LAMMPS. The integration of the Clausius-Clapeyron equation Eq. 2.73 was done using the predictor-corrector procedure as described by Kofke *et al.* in Ref. 196 using steps in reciprocal temperature $d\beta^* = 0.01$ for the liquid-vapor curve and steps in pressure $d\ln P^* = -0.4$ for the vertical part of the solid-liquid one to minimize integration errors. Each iteration of the predictor-corrector procedure was 20 ps long (with a timestep of 2 fs) and after convergence equilibrated data for Δh and Δv were collected for 200 ps.

Bibliography

- [1] M. Salanne, B. Rotenberg, K. Naoi, K. Kaneko, P.-L. Taberna, C. P. Grey, B. Dunn, and P. Simon. Efficient Storage Mechanisms for Building Better Supercapacitors. *Nat. Energy*, 1:16070, 2016.
- [2] Zhi Wei Seh, Jakob Kibsgaard, Colin F. Dickens, Ib Chorkendorff, Jens K. Nørskov, and Thomas F. Jaramillo. Combining theory and experiment in electrocatalysis: Insights into materials design. *Science*, 355(6321), January 2017.
- [3] P. Lannelongue, R. Bouchal, E. Mourad, C. Bodin, M. Olarte, S. Le Vot, F. Favier, and O. Fontaine. “water-in-salt” for supercapacitors: A compromise between voltage, power density, energy density and stability. *J. Electrochem. Soc.*, 165:A657–A663, 2018.
- [4] J. Vatamanu and O. Borodin. Ramifications of water-in-salt interfacial structure at charged electrodes for electrolyte electrochemical stability. *J. Phys. Chem. Lett.*, 8:4362–4367, 2017.
- [5] Dong Zhou, Devaraj Shanmukaraj, Anastasia Tkacheva, Michel Armand, and Guoxiu Wang. Polymer Electrolytes for Lithium-Based Batteries: Advances and Prospects. *Chem*, 5(9):2326–2352, September 2019.
- [6] R. Parsons. The electrical double layer: recent experimental and theoretical developments. *Chem. Rev.*, 90:813–826, 1990.
- [7] H. Helmholtz. Studien über elektrische Grenzsichten. *Annalen der Physik*, 243(7):337–382, 1879.
- [8] G. Gouy. Sur la constitution de la charge électrique à la surface d’un électrolyte. *J. Phys. Theor. Appl*, 9:457, 1910.
- [9] D. Chapman. LI. A contribution to the theory of electrocapillarity. *Phil. Mag.*, 25:475, 1913.
- [10] O. Stern. Zur Theorie Der Elektrolytischen Doppelschicht. *Z. Elektrochem.*, 30:508, 1924.
- [11] Alexei A. Kornyshev. Double-Layer in Ionic Liquids: Paradigm Change? *The Journal of Physical Chemistry B*, 111(20):5545–5557, May 2007.
- [12] M. Z. Bazant, B. D. Storey, and A. A. Kornyshev. Double layer in ionic liquids: Overscreening versus crowding. *Phys. Rev. Lett.*, 106:046102, 2011.
- [13] Z. A. H. Goodwin, G. Feng, and A. A. Kornyshev. Mean-field theory of electrical double layer in ionic liquids with account of short-range correlations. *Electrochim. Acta*, 225:190–197, 2017.
- [14] Michael McEldrew, Zachary A. H. Goodwin, Alexei A. Kornyshev, and Martin Z. Bazant. Theory of the Double Layer in Water-in-Salt Electrolytes. *J. Phys. Chem. Lett.*, 9(19):5840–5846, 2018.
- [15] Martin Z. Bazant, Katsuyo Thornton, and Armand Ajdari. Diffuse-charge dynamics in electrochemical systems. *Phys. Rev. E*, 70(2):021506, August 2004.
- [16] Mathijs Janssen and Markus Bier. Transient dynamics of electric double layer capacitors: Exact expressions within the Debye-Falkenhagen approximation. *Physical Review E*, 97:052616, February 2018.

- [17] J. Vatamanu, Z. Hu, D. Bedrov, C. Perez, and Y. Gogotsi. Increasing energy storage in electrochemical capacitors with ionic liquid electrolytes and nanostructured carbon electrodes. *J. Phys. Chem. Lett.*, 4:2829, 2013.
- [18] Frieder Mugele and Jean-Christophe Baret. Electrowetting: from basics to applications. *Journal of Physics: Condensed Matter*, 17(28):R705–R774, July 2005.
- [19] Christopher D. Daub, Dusan Bratko, Kevin Leung, and Alenka Luzar. Electrowetting at the Nanoscale. *J. Phys. Chem. C*, 111(2):505–509, January 2007.
- [20] Jyoti Roy Choudhuri, Davide Vanzo, Paul Anthony Madden, Mathieu Salanne, Dusan Bratko, and Alenka Luzar. Dynamic Response in Nanoelectrowetting on a Dielectric. *ACS Nano*, 10(9):8536–8544, September 2016.
- [21] James Sweeney, Florian Hausen, Robert Hayes, Grant B. Webber, Frank Endres, Mark W. Rutland, Roland Bennewitz, and Rob Atkin. Control of Nanoscale Friction on Gold in an Ionic Liquid by a Potential-Dependent Ionic Lubricant Layer. *Physical Review Letters*, 109(15):155502, October 2012.
- [22] Hua Li, Ross J. Wood, Mark W. Rutland, and Rob Atkin. An ionic liquid lubricant enables superlubricity to be “switched on” in situ using an electrical potential. *Chemical Communications*, 50(33):4368–4370, March 2014.
- [23] Xiaoyong Yang, Yonggang Meng, and Yu Tian. Effect of Imidazolium Ionic Liquid Additives on Lubrication Performance of Propylene Carbonate under Different Electrical Potentials. *Tribology Letters*, 56(1):161–169, October 2014.
- [24] Xiaoyong Yang, Yonggang Meng, and Yu Tian. Controllable friction and wear of nitrided steel under the lubrication of [DMIm]PF₆/PC solution via electrochemical potential. *Wear*, 360-361:104–113, August 2016.
- [25] Christian Dold, Tobias Amann, and Andreas Kailer. Influence of electric potentials on friction of sliding contacts lubricated by an ionic liquid. *Physical Chemistry Chemical Physics*, 17(16):10339–10342, April 2015.
- [26] O. Y. Fajardo, F. Bresme, A. A. Kornyshev, and M. Urbakh. Electrotunable lubricity with ionic liquid nanoscale films. *Sci. Rep.*, 5:7698, 2015.
- [27] O. Y. Fajardo, F. Bresme, A. A. Kornyshev, and M. Urbakh. Electrotunable friction with ionic liquid lubricants: How important is the molecular structure of the ions? *J. Phys. Chem. Lett.*, asap, 2015.
- [28] Karina Pivnic, Fernando Bresme, Alexei A. Kornyshev, and Michael Urbakh. Electrotunable Friction in Diluted Room Temperature Ionic Liquids: Implications for Nanotribology. *ACS Applied Nano Materials*, October 2020.
- [29] Céline Merlet, Benjamin Rotenberg, Paul A. Madden, Pierre-Louis Taberna, Patrice Simon, Yury Gogotsi, and Mathieu Salanne. On the molecular origin of supercapacitance in nanoporous carbon electrodes. *Nature Materials*, 11(4):306–310, March 2012.
- [30] C. Merlet, C. Péan, B. Rotenberg, P. A. Madden, B. Daffos, P. L. Taberna, P. Simon, and M. Salanne. Highly confined ions store charge more efficiently in supercapacitors. *Nature Communications*, 4, October 2013.
- [31] Doriano Brogioli. Extracting Renewable Energy from a Salinity Difference Using a Capacitor. *Physical Review Letters*, 103(5), July 2009.
- [32] Michele Simoncelli, Nidhal Ganfoud, Assane Sene, Matthieu Haefele, Barbara Daffos, Pierre-Louis Taberna, Mathieu Salanne, Patrice Simon, and Benjamin Rotenberg. Blue Energy and Desalination with Nanoporous Carbon Electrodes: Capacitance from Molecular Simulations to Continuous Models. *Physical Review X*, 8(2):021024, April 2018.

- [33] Nidhal Ganfoud, Assane Sene, Matthieu Haefele, Abel Marin-Laffèche, Barbara Daffos, Pierre-Louis Taberna, Mathieu Salanne, Patrice Simon, and Benjamin Rotenberg. Effect of the carbon microporous structure on the capacitance of aqueous supercapacitors. *Energy Storage Materials*, 21:190–195, September 2019.
- [34] Luis G. Cámara and Fernando Bresme. Molecular dynamics simulations of crystallization under confinement at triple point conditions. *The Journal of Chemical Physics*, 119(5):2792–2800, August 2003.
- [35] Li Wan, Christopher R. Iacovella, Trung D. Nguyen, Hugh Docherty, and Peter T. Cummings. Confined fluid and the fluid-solid transition: Evidence from absolute free energy calculations. *Physical Review B*, 86(21), December 2012.
- [36] Chandan K. Das and Jayant K. Singh. Effect of confinement on the solid-liquid coexistence of Lennard-Jones Fluid. *The Journal of Chemical Physics*, 139(17):174706, November 2013.
- [37] Toshihiro Kaneko, Toshiki Mima, and Kenji Yasuoka. Phase diagram of Lennard-Jones fluid confined in slit pores. *Chemical Physics Letters*, 490(4-6):165–171, April 2010.
- [38] Yun Long, Jeremy C. Palmer, Benoit Coasne, Malgorzata Śliwinska-Bartkowiak, George Jackson, Erich A. Müller, and Keith E. Gubbins. On the molecular origin of high-pressure effects in nanoconfinement: The role of surface chemistry and roughness. *The Journal of Chemical Physics*, 139(14):144701, October 2013.
- [39] Toshihiro Kaneko. Elevation/depression mechanism of freezing points of liquid confined in slit nanopores. *Molecular Simulation*, 43(13-16):1364–1369, November 2017.
- [40] Hugo K Christenson. Confinement effects on freezing and melting. *Journal of Physics: Condensed Matter*, 13(11):R95–R133, March 2001.
- [41] R Evans. Fluids adsorbed in narrow pores: phase equilibria and structure. *Journal of Physics: Condensed Matter*, 2(46):8989–9007, November 1990.
- [42] Lev D. Gelb, K. E. Gubbins, R. Radhakrishnan, and M. Sliwinska-Bartkowiak. Phase separation in confined systems. *Reports on Progress in Physics*, 62(12):1573–1659, December 1999.
- [43] L. R. Fisher and J. N. Israelachvili. Direct experimental verification of the Kelvin equation for capillary condensation. *Nature*, 277(5697):548–549, February 1979.
- [44] M. Binggeli and C. M. Mate. Influence of capillary condensation of water on nanotribology studied by force microscopy. *Applied Physics Letters*, 65(4):415–417, July 1994.
- [45] L. Bocquet, E. Charlaix, S. Ciliberto, and J. Crassous. Moisture-induced ageing in granular media and the kinetics of capillary condensation. *Nature*, 396(6713):735–737, December 1998.
- [46] Elisa Riedo, Francis Lévy, and Harald Brune. Kinetics of Capillary Condensation in Nanoscopic Sliding Friction. *Physical Review Letters*, 88(18), April 2002.
- [47] C Alba-Simionesco, B Coasne, G Dosseh, G Dudziak, K E Gubbins, R Radhakrishnan, and M Sliwinska-Bartkowiak. Effects of confinement on freezing and melting. *Journal of Physics: Condensed Matter*, 18(6):R15–R68, February 2006.
- [48] Mataz Alcoutlabi and Gregory B. McKenna. Effects of confinement on material behaviour at the nanometre size scale. *Journal of Physics: Condensed Matter*, 17(15):R461–R524, April 2005.
- [49] F. G. Alabarse, J. Haines, O. Cambon, C. Levelut, D. Bourgogne, A. Haidoux, D. Granier, and B. Coasne. Freezing of Water Confined at the Nanoscale. *Physical Review Letters*, 109(3):035701, July 2012.
- [50] David V. Wiltschko and John W. Morse. Crystallization pressure versus “crack seal” as the mechanism for banded veins. *Geology*, 29(1):79–82, January 2001.

- [51] Francesca Borghi and Alessandro Podestà. Ionic liquids under nanoscale confinement. *Advances in Physics: X*, 5(1):1736949, January 2020.
- [52] Carla Sofia Perez-Martinez and Susan Perkin. Surface forces generated by the action of electric fields across liquid films. *Soft Matter*, 15(21):4255–4265, May 2019.
- [53] Kenneth R. Seddon. Ionic Liquids for Clean Technology. *Journal of Chemical Technology & Biotechnology*, 68(4):351–356, 1997.
- [54] R. Hayes, G. G. Warr, and R. Atkin. Structure and nanostructure in ionic liquids. *Chem. Rev.*, 115:6357–6426, 2015.
- [55] Céline Merlet, Benjamin Rotenberg, Paul A. Madden, and Mathieu Salanne. Computer simulations of ionic liquids at electrochemical interfaces. *Physical Chemistry Chemical Physics*, 15(38):15781, 2013.
- [56] R. Wen, B. Rahn, and O. M. Magnussen. Potential-dependent adlayer structure and dynamics at the ionic liquid/au(111) interface: A molecular-scale in situ video-stm study. *Angew. Chem., Int. Ed.*, 54:6062–6026, 2015.
- [57] Susan Perkin, Tim Albrecht, and Jacob Klein. Layering and shear properties of an ionic liquid, 1-ethyl-3-methylimidazolium ethylsulfate, confined to nano-films between mica surfaces. *Physical Chemistry Chemical Physics*, 12(6):1243–1247, 2010.
- [58] Susan Perkin, Lorna Crowhurst, Heiko Niedermeyer, Tom Welton, Alexander M. Smith, and Nitya Nand Gosvami. Self-assembly in the electrical double layer of ionic liquids. *Chemical Communications*, 47(23):6572–6574, 2011.
- [59] Céline Merlet, Mathieu Salanne, Benjamin Rotenberg, and Paul A. Madden. Imidazolium Ionic Liquid Interfaces with Vapor and Graphite: Interfacial Tension and Capacitance from Coarse-Grained Molecular Simulations. *The Journal of Physical Chemistry C*, 115(33):16613–16618, August 2011.
- [60] R. Atkin and G. G. Warr. Structure in confined room-temperature ionic liquids. *J. Phys. Chem. C*, 111:5162–5168, 2007.
- [61] E. Hayes, G. G. Warr, and R. Atkin. At the interface: solvation and designing ionic liquids. *Phys. Chem. Chem. Phys.*, 12:1709–1723, 2010.
- [62] R. M. Espinosa-Marzal, A. Arcifa, A. Rossi, and N. D. Spencer. Microslips to “Avalanches” in Confined, Molecular Layers of Ionic Liquids. *The Journal of Physical Chemistry Letters*, 5(1):179–184, January 2014.
- [63] Sami Tazi, Mathieu Salanne, Christian Simon, Pierre Turq, Michael Pounds, and Paul A. Madden. Potential-Induced Ordering Transition of the Adsorbed Layer at the Ionic Liquid/Electrified Metal Interface. *The Journal of Physical Chemistry B*, 114(25):8453–8459, July 2010.
- [64] K. Kirchner, T. Kirchner, V. Ivanistsev, and M. V. Fedorov. Electrical double layer in ionic liquids: structural transitions from multilayer to monolayer structure at the interface. *Electrochim. Acta*, 110:762–771, 2013.
- [65] C. Merlet, D. T. Limmer, M. Salanne, R. van Roij, P. A. Madden, D. Chandler, and B. Rotenberg. The electric double layer has a life of its own. *J. Phys. Chem. C*, 118:18291–18298, 2014.
- [66] Benjamin Rotenberg and Mathieu Salanne. Structural Transitions at Ionic Liquid Interfaces. *The Journal of Physical Chemistry Letters*, 6(24):4978–4985, December 2015.
- [67] David T. Limmer. Interfacial Ordering and Accompanying Divergent Capacitance at Ionic Liquid-Metal Interfaces. *Physical Review Letters*, 115(25), December 2015.

- [68] A. A. Lee and S. Perkin. Ion-image interactions and phase transition at electrolyte-metal interfaces. *J. Phys. Chem. Lett.*, 7:2753, 2016.
- [69] N. N. Rajput, J. D. Monk, and F. R. Hung. Structure and dynamics of an ionic liquid confined inside a charged slit graphitic nanopore. *J. Phys. Chem. C*, asap, 2012.
- [70] R. Singh, N. N. Rajput, X. He, J. Monk, and F. R. Hung. Molecular dynamics simulations of the ionic liquid [emim+][tfmsi-] confined inside rutile (110) slit nanopores. *Phys. Chem. Chem. Phys.*, asap, 2013.
- [71] L. Andres Jurado, Hojun Kim, Andrea Arcifa, Antonella Rossi, Cecilia Leal, Nicholas D. Spencer, and Rosa M. Espinosa-Marzal. Irreversible structural change of a dry ionic liquid under nanoconfinement. *Physical Chemistry Chemical Physics*, 17(20):13613–13624, May 2015.
- [72] M. Mezger, H. Schröder, H. Reichert, S. Schramm, J. S. Okasinski, S. Schröder, V. Honkimäki, M. Deutsch, B. M. Ocko, J. Ralston, M. Rohwerder, M. Stratmann, and H. Dosch. Molecular layering of fluorinated ionic liquids at a charged sapphire (0001) surface. *Science*, 322:424–428, 2008.
- [73] Simone Bovio, Alessandro Podestà, Cristina Lenardi, and Paolo Milani. Evidence of Extended Solidlike Layering in [Bmim][NTf₂] Ionic Liquid Thin Films at Room-Temperature. *The Journal of Physical Chemistry B*, 113(19):6600–6603, May 2009.
- [74] R. S. Anareddy and S. K. Shaw. Long-range ordering of ionic liquid fluid films. *Langmuir*, asap, 2016.
- [75] Francesca Borghi, Matteo Mirigliano, Cristina Lenardi, Paolo Milani, and Alessandro Podestà. Nanostructure Determines the Wettability of Gold Surfaces by Ionic Liquid Ultrathin Films. *Frontiers in Chemistry*, 9, 2021.
- [76] Francesca Borghi, Claudio Piazzoni, Matteo Ghidelli, Paolo Milani, and Alessandro Podestà. Nanoconfinement of Ionic Liquid into Porous Carbon Electrodes. *The Journal of Physical Chemistry C*, 125(2):1292–1303, January 2021.
- [77] Massimiliano Galluzzi, Simone Bovio, Paolo Milani, and Alessandro Podestà. Surface Confinement Induces the Formation of Solid-Like Insulating Ionic Liquid Nanostructures. *The Journal of Physical Chemistry C*, 122(14):7934–7944, April 2018.
- [78] P. Ballone, M. G. Del Pópolo, S. Bovio, A. Podestà, P. Milani, and N. Manini. Nano-indentation of a room-temperature ionic liquid film on silica: a computational experiment. *Physical Chemistry Chemical Physics*, 14(7):2475–2482, January 2012.
- [79] Mitsuhiro Kanakubo, Yusuke Hiejima, Kimitaka Minami, Takafumi Aizawa, and Hiroshi Nanjo. Melting point depression of ionic liquids confined in nanospaces. *Chemical Communications*, 0(17):1828–1830, 2006.
- [80] Marie-Alexandra Neouze and Marco Litschauer. Confinement of 1-Butyl-3-methylimidazolium Nitrate in Metallic Silver. *The Journal of Physical Chemistry B*, 112(51):16721–16725, December 2008.
- [81] Kazuyuki Fujie, Teppei Yamada, Ryuichi Ikeda, and Hiroshi Kitagawa. Introduction of an Ionic Liquid into the Micropores of a Metal–Organic Framework and Its Anomalous Phase Behavior. *Angewandte Chemie*, 126(42):11484–11487, 2014.
- [82] Sanjin Marion, Sebastian J. Davis, Zeng-Qiang Wu, and Aleksandra Radenovic. Nanocapillary confinement of imidazolium based ionic liquids. *Nanoscale*, 12(16):8867–8874, April 2020.
- [83] Shimou Chen, Guozhong Wu, Maolin Sha, and Shirong Huang. Transition of Ionic Liquid [bmim][PF₆] from Liquid to High-Melting-Point Crystal When Confined in Multiwalled Carbon Nanotubes. *Journal of the American Chemical Society*, 129(9):2416–2417, March 2007.

- [84] J. Comtet, A. Niguès, V. Kaiser, B. Coasne, L. Bocquet, and A. Siria. Nanoscale capillary freezing of ionic liquids confined between metallic interfaces and the role of electronic screening. *Nat. Mater.*, 16:634–639, 2017.
- [85] Alok Kumar Tripathi and Rajendra Kumar Singh. Immobilization induced molecular compression of ionic liquid in ordered mesoporous matrix. *Journal of Physics D: Applied Physics*, 51(7):075301, February 2018.
- [86] Antoine Lainé, Antoine Niguès, Lydéric Bocquet, and Alessandro Siria. Nanotribology of Ionic Liquids: Transition to Yielding Response in Nanometric Confinement with Metallic Surfaces. *Physical Review X*, 10(1):011068, March 2020.
- [87] L. Canale, A. Laborieux, A. Aroul Mogane, L. Jubin, J. Comtet, A. Lainé, L. Bocquet, A. Siria, and A. Niguès. MicroMegascop. *Nanotechnology*, 29(35):355501, June 2018.
- [88] Antoine Lainé, Laetitia Jubin, Luca Canale, Lydéric Bocquet, Alessandro Siria, Stephen H. Donaldson, and Antoine Niguès. MicroMegascop based dynamic surface force apparatus. *Nanotechnology*, 30(19):195502, February 2019.
- [89] Léo Garcia, Léa Jacquot, Elisabeth Charlaix, and Benjamin Cross. Nano-mechanics of ionic liquids at dielectric and metallic interfaces. *Faraday Discussions*, 206(0):443–457, December 2017.
- [90] Ibrahim Bou-Malham and Lionel Bureau. Nanoconfined ionic liquids: effect of surface charges on flow and molecular layering. *Soft Matter*, 6(17):4062–4065, 2010.
- [91] V. Kaiser, J. Comtet, A. Niguès, A. Siria, B. Coasne, and L. Bocquet. Electrostatic interactions between ions near thomas-fermi substrates and the surface energy of ionic crystal at imperfect metals. *Faraday Discuss.*, 199:129–158, 2017.
- [92] G. M. Torrie and J. P. Valleau. Electrical double layers. I. Monte Carlo study of a uniformly charged surface. *J. Chem. Phys.*, 73(11):5807–5816, December 1980.
- [93] James N. Glosli and Michael R. Philpott. Molecular dynamics simulation of adsorption of ions from aqueous media onto charged electrodes. *J. Chem. Phys.*, 96(9):6962–6969, May 1992.
- [94] Kenji Kiyohara and Kinji Asaka. Monte Carlo simulation of electrolytes in the constant voltage ensemble. *J. Chem. Phys.*, 126(21):214704, June 2007.
- [95] Kenji Kiyohara and Kinji Asaka. Monte Carlo Simulation of Porous Electrodes in the Constant Voltage Ensemble. *J. Phys. Chem. C*, 111(43):15903–15909, November 2007.
- [96] Wolfgang Schmickler and Douglas Henderson. The interphase between jellium and a hard sphere electrolyte. A model for the electric double layer. *J. Chem. Phys.*, 80(7):3381–3386, April 1984.
- [97] Giovanni Aloisi, Maria Luisa Foresti, Rolando Guidelli, and Paul Barnes. A Monte Carlo simulation of water molecules near a charged wall. *J. Chem. Phys.*, 91(9):5592–5596, November 1989.
- [98] William van Megen and Ian Snook. The grand canonical ensemble Monte Carlo method applied to the electrical double layer. *J. Chem. Phys.*, 73(9):4656–4662, November 1980.
- [99] Paul S. Crozier, Richard L. Rowley, and Douglas Henderson. Molecular-dynamics simulations of ion size effects on the fluid structure of aqueous electrolyte systems between charged model electrodes. *J. Chem. Phys.*, 114(17):7513–7517, May 2001.
- [100] Isidro Lorenzo Geadá, Hadi Ramezani-Dakhel, Tariq Jamil, Marialore Sulpizi, and Hendrik Heinz. Insight into induced charges at metal surfaces and biointerfaces using a polarizable Lennard–Jones potential. *Nat. Commun.*, 9(1):716, December 2018.
- [101] Song Hi Lee, Jayendran C. Rasaiah, and J. B. Hubbard. Molecular dynamics study of a dipolar fluid between charged plates. *J. Chem. Phys.*, 85(9):5232–5237, November 1986.

- [102] G. Nagy and K. Heinzinger. A Molecular Dynamics simulation of electrified platinum/water interfaces. *Journal of Electroanalytical Chemistry and Interfacial Electrochemistry*, 296(2):549–558, December 1990.
- [103] J. Hautman, J. W. Halley, and Y.-J. Rhee. Molecular dynamics simulation of water between two ideal classical metal walls. *J. Chem. Phys.*, 91(1):467–472, July 1989.
- [104] Masakatsu Watanabe, Anatol M. Brodsky, and William P. Reinhardt. Dielectric properties and phase transitions of water between conducting plates. *J. Phys. Chem.*, 95(12):4593–4596, June 1991.
- [105] Daniel A. Rose and Ilan Benjamin. Adsorption of Na^+ and Cl^- at the charged water–platinum interface. *J. Chem. Phys.*, 98(3):2283–2290, February 1993.
- [106] B. B. Smith and J. W. Halley. Simulation study of the ferrous ferric electron transfer at a metal–aqueous electrolyte interface. *J. Chem. Phys.*, 101(12):10915–10924, December 1994.
- [107] S.-B. Zhu and G. W. Robinson. Structure and dynamics of liquid water between plates. *J. Chem. Phys.*, 94(2):1403–1410, January 1991.
- [108] J. Ilja Siepmann and Michiel Sprik. Ordering of fractional monolayers of H_2O on Ni(110). *Surface Science Letters*, 279(1):L185–L190, December 1992.
- [109] J. I. Siepmann and M. Sprik. Influence of Surface-Topology and Electrostatic Potential on Water Electrode Systems. *J. Chem. Phys.*, 102:511–524, 1995.
- [110] Guymon, Rowley, Harb, and Wheeler. Simulating an electrochemical interface using charge dynamics. *Condensed Matter Physics*, 8(2):335, 2005.
- [111] S. K. Reed, O. J. Lanning, and P. A. Madden. Electrochemical Interface Between an Ionic Liquid and a Model Metallic Electrode. *J. Chem. Phys.*, 126:084704, 2007.
- [112] M. Pounds, S. Tazi, M. Salanne, and P. A. Madden. Ion adsorption at a metallic electrode: an *ab initio* based simulation study. *J. Phys.: Condens. Matter*, 21:424109, 2009.
- [113] Jenel Vatamanu, Oleg Borodin, and Grant D. Smith. Molecular dynamics simulations of atomically flat and nanoporous electrodes with a molten salt electrolyte. *Phys. Chem. Chem. Phys.*, 12(1):170–182, December 2009.
- [114] M. K. Petersen, R. Kumar, H. S. White, and G. A. Voth. A computationally efficient treatment of polarizable electrochemical cells held at a constant potential. *J. Phys. Chem. C*, 116:4903–4912, 2012.
- [115] Sandeep Tyagi, Mehmet Süzen, Marcello Sega, Marcia Barbosa, Sofia S. Kantorovich, and Christian Holm. An iterative, fast, linear-scaling method for computing induced charges on arbitrary dielectric boundaries. *J. Chem. Phys.*, 132(15):154112, April 2010.
- [116] J. C. Shelley, G. N. Patey, D. R. Bérard, and G. M. Torrie. Modeling and structure of mercury–water interfaces. *J. Chem. Phys.*, 107(6):2122–2141, August 1997.
- [117] G. M. Torrie, J. P. Valleau, and G. N. Patey. Electrical double layers. II. Monte Carlo and HNC studies of image effects. *J. Chem. Phys.*, 76(9):4615–4622, May 1982.
- [118] Neville G. Parsonage and David Nicholson. Computer simulation of water between metal walls. *J. Chem. Soc., Faraday Trans. 2*, 82(9):1521–1535, January 1986.
- [119] Anne A. Gardner and John P. Valleau. Water–like particles at surfaces. II. In a double layer and at a metallic surface. *J. Chem. Phys.*, 86(7):4171–4176, April 1987.
- [120] Sabine H. L. Klapp. Monte-Carlo simulations of strongly interacting dipolar fluids between two conducting walls. *Molecular Simulation*, 32(8):609–621, July 2006.

- [121] Kyohei Takae and Akira Onuki. Fluctuations of local electric field and dipole moments in water between metal walls. *J. Chem. Phys.*, 143(15):154503, October 2015.
- [122] Matheus Giroto, Alexandre P. dos Santos, and Yan Levin. Simulations of ionic liquids confined by metal electrodes using periodic Green functions. *J. Chem. Phys.*, 147(7):074109, 2017.
- [123] Sandeep Tyagi, Axel Arnold, and Christian Holm. ICMMM2D: An accurate method to include planar dielectric interfaces via image charge summation. *J. Chem. Phys.*, 127(15):154723, October 2007.
- [124] A. Arnold, K. Breitsprecher, F. Fahrenberger, S. Kesselheim, O. Lenz, and C. Holm. Efficient algorithms for electrostatic interactions including dielectric contrasts. *Entropy*, 15:4569–4588, 2013.
- [125] Daniel A. Rose and Ilan Benjamin. Solvation of Na^+ and Cl^- at the water–platinum (100) interface. *J. Chem. Phys.*, 95(9):6856–6865, November 1991.
- [126] Rosalind Allen, Jean-Pierre Hansen, and Simone Melchionna. Electrostatic potential inside ionic solutions confined by dielectrics: a variational approach. *Phys. Chem. Chem. Phys.*, 3(19):4177–4186, January 2001.
- [127] Dezső Boda, Dirk Gillespie, Wolfgang Nonner, Douglas Henderson, and Bob Eisenberg. Computing induced charges in inhomogeneous dielectric media: Application in a Monte Carlo simulation of complex ionic systems. *Phys. Rev. E*, 69(4):046702, April 2004.
- [128] K. Breitsprecher, K. Szuttor, and C. Holm. Electrode models for ionic liquid-based capacitors. *J. Phys. Chem. C*, 119:22445–22451, 2015.
- [129] E. Spohr. Computer simulation of the water/platinum interface. *J. Phys. Chem.*, 93(16):6171–6180, August 1989.
- [130] F. Iori and S. Corni. Including image charge effects in the molecular dynamics simulations of molecules on metal surfaces. *J. Comput. Chem.*, 29(10):1656–1666, July 2008.
- [131] F. Iori, R. Di Felice, E. Molinari, and S. Corni. GolP: An atomistic force-field to describe the interaction of proteins with Au(111) surfaces in water. *J. Comput. Chem.*, 30(9):1465–1476, 2009.
- [132] A. S. Pensado and A. A. H. Pádua. Solvation and stabilization of metallic nanoparticles in ionic liquids. *Angew. Chem., Int. Ed.*, 50:8683–8687, 2011.
- [133] Alexander Schlaich, Dongliang Jin, Lydéric Bocquet, and Benoit Coasne. Wetting transition of ionic liquids at metal surfaces: A computational approach to electronic screening using a virtual Thomas–Fermi fluid, 2020. <https://arxiv.org/abs/2002.11526>.
- [134] M. W. Finnis. The interaction of a point charge with an aluminium (111) surface. *Surface Science*, 241(1):61–72, January 1991.
- [135] M. W. Finnis, R. Kaschner, C. Kruse, J. Furthmuller, and M. Scheffler. The interaction of a point charge with a metal surface: theory and calculations for (111), (100) and (110) aluminium surfaces. *Journal of Physics: Condensed Matter*, 7(10):2001–2019, March 1995.
- [136] R. F. Nalewajski. Electrostatic effects in interactions between hard (soft) acids and bases. *J. Am. Chem. Soc.*, 106:944–945, 1984.
- [137] Wilfried J. Mortier, Swapan K. Ghosh, and S. Shankar. Electronegativity-equalization method for the calculation of atomic charges in molecules. *J. Am. Chem. Soc.*, 108(15):4315–4320, July 1986.
- [138] A. K. Rappe and W. A. Goddard III. Charge equilibration for molecular dynamics simulations. *J. Phys. Chem.*, 95:3358–3363, 1991.

- [139] F. H. Streitz and J. W. Mintmire. Electrostatic potentials for metal-oxide surfaces and interfaces. *Phys. Rev. B*, 50(16):11996–12003, October 1994.
- [140] N. Onofrio and A. Strachan. Voltage equilibration for reactive atomistic simulations of electrochemical processes. *J. Chem. Phys.*, 143:054109, 2015.
- [141] N. Onofrio, D. Guzman, and A. Strachan. Atomic origin of ultrafast resistance switching in nanoscale electrometallization cells. *Nat. Mater.*, 14:440–446, 2015.
- [142] Tao Liang, Andrew C. Antony, Sneha A. Akhade, Michael J. Janik, and Susan B. Sinnott. Applied Potentials in Variable-Charge Reactive Force Fields for Electrochemical Systems. *J. Phys. Chem. A*, 122(2):631–638, January 2018.
- [143] Hiroshi Nakano and Hirofumi Sato. A chemical potential equalization approach to constant potential polarizable electrodes for electrochemical-cell simulations. *J. Chem. Phys.*, 151(16):164123, October 2019.
- [144] M. Buraschi, S. Sansotta, and D. Zahn. Polarization effects in dynamic interfaces of platinum electrodes and ionic liquid phases: A molecular dynamics study. *J. Phys. Chem. C*, 124:2002–2007, 2020.
- [145] Razvan A. Nistor and Martin H. Müser. Dielectric properties of solids in the regular and split-charge equilibration formalisms. *Phys. Rev. B*, 79(10):104303, March 2009.
- [146] Lars Pastewka, Tommi T. Järvi, Leonhard Mayrhofer, and Michael Moseler. Charge-transfer model for carbonaceous electrodes in polar environments. *Physical Review B*, 83(16):165418, April 2011.
- [147] David L. Price and J. W. Halley. Molecular dynamics, density functional theory of the metal–electrolyte interface. *J. Chem. Phys.*, 102(16):6603–6612, April 1995.
- [148] S. Walbran, A. Mazzolo, J.W. Halley, and D.L. Price. Model for the electrostatic response of the copper – water interface. *J. Chem. Phys.*, 109(18):8076–8080, 1998.
- [149] A. A. Kornyshev, A. I. Rubinshtein, and M. A. Vorotyntsev. Image potential near a dielectric–plasma-like medium interface. *physica status solidi (b)*, 84(1):125–132, 1977.
- [150] A. A. Kornyshev and M. A. Vorotyntsev. Analytic expression for the potential energy of a test charge bounded by solid state plasma. *J. Phys. C: Solid State Phys.*, 11:L691–L694, 1978.
- [151] N. B. Luque and W. Schmickler. The electric double layer on graphite. *Electrochimica Acta*, 71:82–85, June 2012.
- [152] A. A. Kornyshev, N. B. Luque, and W. Schmickler. Differential capacitance of ionic liquid interface with graphite: the story of two double layers. *J. Solid State Electrochem.*, 18:1345–1349, 2014.
- [153] Abel Marin-Lafèche, Matthieu Haefele, Laura Scalfi, Alessandro Coretti, Thomas Dufils, Guillaume Jeanmairet, Stewart K. Reed, Alessandra Serva, Roxanne Berthin, Camille Bacon, Sara Bonella, Benjamin Rotenberg, Paul A. Madden, and Mathieu Salanne. MetalWalls: A classical molecular dynamics software dedicated to the simulation of electrochemical systems. *Journal of Open Source Software*, 5(53):2373, September 2020.
- [154] Guang Feng and Peter T. Cummings. Supercapacitor Capacitance Exhibits Oscillatory Behavior as a Function of Nanopore Size. *The Journal of Physical Chemistry Letters*, 2(22):2859–2864, November 2011.
- [155] Justin B. Haskins and John W. Lawson. Evaluation of molecular dynamics simulation methods for ionic liquid electric double layers. *J. Chem. Phys.*, 144(18):184707, May 2016.
- [156] S. Kondrat and A. Kornyshev. Superionic state in double-layer capacitors with nanoporous electrodes. *Journal of Physics: Condensed Matter*, 23(2):022201, December 2010.

- [157] S. Kondrat, N. Georgi, M. V. Fedorov, and A. A. Kornyshev. A superionic state in nano-porous double-layer capacitors: insights from Monte Carlo simulations. *Physical Chemistry Chemical Physics*, 13(23):11359, 2011.
- [158] Zhenxing Wang, Yang Yang, David L. Olmsted, Mark Asta, and Brian B. Laird. Evaluation of the constant potential method in simulating electric double-layer capacitors. *J. Chem. Phys.*, 141(18):184102, November 2014.
- [159] Céline Merlet, Clarisse Péan, Benjamin Rotenberg, Paul A. Madden, Patrice Simon, and Mathieu Salanne. Simulating Supercapacitors: Can We Model Electrodes As Constant Charge Surfaces? *The Journal of Physical Chemistry Letters*, 4(2):264–268, January 2013.
- [160] J. Vatamanu, O. Borodin, and G. D. Smith. Molecular simulations of the electric double layer structure, differential capacitance, and charging kinetics for n-methyl-n-propylpyrrolidinium bis(fluorosulfonyl)imide at graphite electrodes. *J. Phys. Chem. B*, 115(12):3073–3084, 2011.
- [161] David T. Limmer, Céline Merlet, Mathieu Salanne, David Chandler, Paul A. Madden, René van Roij, and Benjamin Rotenberg. Charge Fluctuations in Nanoscale Capacitors. *Phys. Rev. Lett.*, 111(10), September 2013.
- [162] P. Hohenberg and W. Kohn. Inhomogeneous Electron Gas. *Physical Review*, 136(3B):B864–B871, November 1964.
- [163] H. J. C. Berendsen, J. R. Grigera, and T. P. Straatsma. The missing term in effective pair potentials. *The Journal of Physical Chemistry*, 91(24):6269–6271, November 1987.
- [164] Durba Roy and Mark Maroncelli. An Improved Four-Site Ionic Liquid Model. *The Journal of Physical Chemistry B*, 114(39):12629–12631, October 2010.
- [165] Attila Szabo and Neil S. Ostlund. *Modern Quantum Chemistry: Introduction to Advanced Electronic Structure Theory*. Courier Corporation, July 1996.
- [166] Bingqing Cheng, Edgar A. Engel, Jörg Behler, Christoph Dellago, and Michele Ceriotti. Ab initio thermodynamics of liquid and solid water. *Proceedings of the National Academy of Sciences*, 116(4):1110–1115, January 2019. Publisher: National Academy of Sciences Section: Physical Sciences.
- [167] Jörg Behler. Perspective: Machine learning potentials for atomistic simulations. *The Journal of Chemical Physics*, 145(17):170901, November 2016.
- [168] Todd R. Gingrich and Mark Wilson. On the ewald summation of gaussian charges for the simulation of metallic surfaces. *Chem. Phys. Letters*, 500(1-3):178–183, 2010.
- [169] Liem X. Dang. Mechanism and Thermodynamics of Ion Selectivity in Aqueous Solutions of 18-Crown-6 Ether: A Molecular Dynamics Study. *Journal of the American Chemical Society*, 117(26):6954–6960, July 1995.
- [170] Samantha Weerasinghe and Paul E. Smith. A Kirkwood–Buff derived force field for sodium chloride in water. *The Journal of Chemical Physics*, 119(21):11342–11349, November 2003.
- [171] T. Werder, J. H. Walther, R. L. Jaffe, T. Halicioglu, and P. Koumoutsakos. On the Water Carbon Interaction for Use in Molecular Dynamics Simulations of Graphite and Carbon Nanotubes. *The Journal of Physical Chemistry B*, 107(6):1345–1352, February 2003.
- [172] Nathan Schmid, Andreas P. Eichenberger, Alexandra Choutko, Sereina Riniker, Moritz Winger, Alan E. Mark, and Wilfred F. van Gunsteren. Definition and testing of the GROMOS force-field versions 54A7 and 54B7. *European Biophysics Journal*, 40(7):843, April 2011.
- [173] Milton W. Cole and James R. Klein. The interaction between noble gases and the basal plane surface of graphite. *Surface Science*, 124(2):547–554, January 1983.

- [174] Andrej Berg, Christine Peter, and Karen Johnston. Evaluation and Optimization of Interface Force Fields for Water on Gold Surfaces. *Journal of Chemical Theory and Computation*, 13(11):5610–5623, November 2017.
- [175] Fumi and Tosi. Ionic sizes and born repulsive parameters in the NaCl-type alkali halides—I: The Huggins-Mayer and Pauling forms. *Journal of Physics and Chemistry of Solids*, 25(1):31–43, January 1964.
- [176] C. Valeriani, E. Sanz, and D. Frenkel. Rate of homogeneous crystal nucleation in molten NaCl. *The Journal of Chemical Physics*, 122(19):194501, May 2005.
- [177] William A. Steele. The physical interaction of gases with crystalline solids: I. Gas-solid energies and properties of isolated adsorbed atoms. *Surface Science*, 36(1):317–352, April 1973.
- [178] William A. Steele. The interaction of rare gas atoms with graphitized carbon black. *The Journal of Physical Chemistry*, 82(7):817–821, April 1978.
- [179] Jean-Pierre Hansen and Loup Verlet. Phase Transitions of the Lennard-Jones System. *Physical Review*, 184(1):151–161, August 1969.
- [180] S. T. Cui, P. T. Cummings, and H. D. Cochran. Molecular simulation of the transition from liquidlike to solidlike behavior in complex fluids confined to nanoscale gaps. *The Journal of Chemical Physics*, 114(16):7189–7195, April 2001.
- [181] In-Chul Yeh and Max L. Berkowitz. Ewald summation for systems with slab geometry. *J. Chem. Phys.*, 111(7):3155–3162, August 1999.
- [182] R. W. Hockney and J. W. Eastwood. *Computer Simulation Using Particles*. Taylor & Francis, January 1988.
- [183] Tom Darden, Darrin York, and Lee Pedersen. Particle mesh Ewald: An Nlog(N) method for Ewald sums in large systems. *The Journal of Chemical Physics*, 98(12):10089–10092, June 1993.
- [184] Daan Frenkel and Berend Smit. *Understanding molecular simulation: from algorithms to applications*. Number 1 in Computational science series. Academic Press, San Diego, 2nd ed edition, 2002.
- [185] David Chandler. *Introduction to Modern Statistical Mechanics*. Oxford University Press, 1987.
- [186] Loup Verlet. Computer "Experiments" on Classical Fluids. I. Thermodynamical Properties of Lennard-Jones Molecules. *Physical Review*, 159(1):98–103, July 1967.
- [187] William C. Swope, Hans C. Andersen, Peter H. Berens, and Kent R. Wilson. A computer simulation method for the calculation of equilibrium constants for the formation of physical clusters of molecules: Application to small water clusters. *The Journal of Chemical Physics*, 76(1):637–649, January 1982.
- [188] Hans C Andersen. Rattle: A "velocity" version of the shake algorithm for molecular dynamics calculations. *Journal of Computational Physics*, 52(1):24–34, October 1983.
- [189] Jean-Paul Ryckaert, Giovanni Ciccotti, and H. J. C. Berendsen. Numerical integration of the cartesian equations of motion of a system with constraints: molecular dynamics of n-alkanes. *Journal of Computational Physics*, 23(3):327–341, March 1977. Publisher: Academic Press.
- [190] Shuichi Nosé. A unified formulation of the constant temperature molecular dynamics methods. *The Journal of Chemical Physics*, 81(1):511–519, July 1984.
- [191] William G. Hoover. Canonical dynamics: Equilibrium phase-space distributions. *Physical Review A*, 31(3):1695–1697, March 1985.
- [192] Glenn J. Martyna, Michael L. Klein, and Mark Tuckerman. Nosé–Hoover chains: The canonical

- ensemble via continuous dynamics. *The Journal of Chemical Physics*, 97(4):2635–2643, August 1992.
- [193] Robert Zwanzig and Narinder K. Ailawadi. Statistical Error Due to Finite Time Averaging in Computer Experiments. *Physical Review*, 182(1):280–283, June 1969.
- [194] Athanassios Z. Panagiotopoulos. Direct determination of phase coexistence properties of fluids by Monte Carlo simulation in a new ensemble. *Molecular Physics*, 61(4):813–826, July 1987.
- [195] A.Z. Panagiotopoulos, N. Quirke, M. Stapleton, and D.J. Tildesley. Phase equilibria by simulation in the Gibbs ensemble: Alternative derivation, generalization and application to mixture and membrane equilibria. *Molecular Physics*, 63(4):527–545, March 1988.
- [196] David A. Kofke. Direct evaluation of phase coexistence by molecular simulation via integration along the saturation line. *The Journal of Chemical Physics*, 98(5):4149–4162, March 1993.
- [197] Paul J. Steinhardt, David R. Nelson, and Marco Ronchetti. Bond-orientational order in liquids and glasses. *Physical Review B*, 28(2):784–805, July 1983.
- [198] Stefan Auer and Daan Frenkel. Numerical Simulation of Crystal Nucleation in Colloids. In Christian Dr. Holm and Kurt Prof. Dr. Kremer, editors, *Advanced Computer Simulation: Approaches for Soft Matter Sciences I*, Advances in Polymer Science, pages 149–208. Springer, Berlin, Heidelberg, 2005.
- [199] Wolfgang Lechner and Christoph Dellago. Accurate determination of crystal structures based on averaged local bond order parameters. *The Journal of Chemical Physics*, 129(11):114707, September 2008.
- [200] Aleks Reinhardt, Jonathan P. K. Doye, Eva G. Noya, and Carlos Vega. Local order parameters for use in driving homogeneous ice nucleation with all-atom models of water. *The Journal of Chemical Physics*, 137(19):194504, November 2012.
- [201] Pieter Rein ten Wolde, Maria J. Ruiz-Montero, and Daan Frenkel. Numerical calculation of the rate of crystal nucleation in a Lennard-Jones system at moderate undercooling. *The Journal of Chemical Physics*, 104(24):9932–9947, June 1996.
- [202] Takeshi Kawasaki and Akira Onuki. Construction of a disorder variable from Steinhardt order parameters in binary mixtures at high densities in three dimensions. *The Journal of Chemical Physics*, 135(17):174109, November 2011.
- [203] E. Sanz, C. Vega, J. R. Espinosa, R. Caballero-Bernal, J. L. F. Abascal, and C. Valeriani. Homogeneous Ice Nucleation at Moderate Supercooling from Molecular Simulation. *Journal of the American Chemical Society*, 135(40):15008–15017, October 2013.
- [204] Massimiliano Bonomi, Giovanni Bussi, Carlo Camilloni, Gareth A. Tribello, Pavel Banáš, Alessandro Barducci, Mattia Bernetti, Peter G. Bolhuis, Sandro Bottaro, Davide Branduardi, Riccardo Capelli, Paolo Carloni, Michele Ceriotti, Andrea Cesari, Haochuan Chen, Wei Chen, Francesco Colizzi, Sandip De, Marco De La Pierre, Davide Donadio, Viktor Drobot, Bernd Ensing, Andrew L. Ferguson, Marta Filizola, James S. Fraser, Haohao Fu, Piero Gasparotto, Francesco Luigi Gervasio, Federico Giberti, Alejandro Gil-Ley, Toni Giorgino, Gabriella T. Heller, Glen M. Hocky, Marcella Iannuzzi, Michele Invernizzi, Kim E. Jelfs, Alexander Jussupow, Evgeny Kirilin, Alessandro Laio, Vittorio Limongelli, Kresten Lindorff-Larsen, Thomas Löhr, Fabrizio Marinelli, Layla Martin-Samos, Matteo Masetti, Ralf Meyer, Angelos Michaelides, Carla Molteni, Tetsuya Morishita, Marco Nava, Cristina Paissoni, Elena Papaleo, Michele Parrinello, Jim Pfaendtner, Pablo Piaggi, GiovanniMaria Piccini, Adriana Pietropaolo, Fabio Pietrucci, Silvio Pipolo, Davide Provasi, David Quigley, Paolo Raiteri, Stefano Raniolo, Jakub Rydzewski, Matteo Salvalaglio, Gabriele Cesare Sosso, Vojtěch Spiwok, Jiří Šponer, David W. H. Swenson, Pratyush Tiwary, Omar Valsson, Michele Vendruscolo, Gregory A. Voth, Andrew White, and

- The PLUMED consortium. Promoting transparency and reproducibility in enhanced molecular simulations. *Nature Methods*, 16(8):670–673, August 2019.
- [205] Gareth A. Tribello, Massimiliano Bonomi, Davide Branduardi, Carlo Camilloni, and Giovanni Bussi. PLUMED 2: New feathers for an old bird. *Computer Physics Communications*, 185(2):604–613, February 2014.
- [206] Sergei Izrailev, Sergey Stepaniants, Barry Isralewitz, Dorina Kosztin, Hui Lu, Ferenc Molnar, Willy Wriggers, and Klaus Schulten. Steered Molecular Dynamics. In Peter Deuffhard, Jan Hermans, Benedict Leimkuhler, Alan E. Mark, Sebastian Reich, and Robert D. Skeel, editors, *Computational Molecular Dynamics: Challenges, Methods, Ideas*, Lecture Notes in Computational Science and Engineering, pages 39–65, Berlin, Heidelberg, 1999. Springer.
- [207] S. Kirkpatrick, C. D. Gelatt, and M. P. Vecchi. Optimization by Simulated Annealing. *Science*, 220(4598):671–680, May 1983.
- [208] A. P. Lyubartsev, A. A. Martsinovski, S. V. Shevkunov, and P. N. Vorontsov-Velyaminov. New approach to Monte Carlo calculation of the free energy: Method of expanded ensembles. *The Journal of Chemical Physics*, 96(3):1776–1783, February 1992.
- [209] E. Marinari and G. Parisi. Simulated Tempering: A New Monte Carlo Scheme. *Europhysics Letters (EPL)*, 19(6):451–458, July 1992.
- [210] Charles J. Geyer and Elizabeth A. Thompson. Annealing Markov Chain Monte Carlo with Applications to Ancestral Inference. *Journal of the American Statistical Association*, 90(431):909–920, September 1995.
- [211] Qiliang Yan and Juan J. de Pablo. Hyperparallel tempering Monte Carlo simulation of polymeric systems. *The Journal of Chemical Physics*, 113(3):1276–1282, July 2000.
- [212] G.M. Torrie and J.P. Valleau. Nonphysical sampling distributions in Monte Carlo free-energy estimation: Umbrella sampling. *Journal of Computational Physics*, 23(2):187–199, February 1977.
- [213] Johannes Kästner. Umbrella sampling. *Wiley Interdisciplinary Reviews: Computational Molecular Science*, 1(6):932–942, November 2011.
- [214] Shankar Kumar, John M. Rosenberg, Djamel Bouzida, Robert H. Swendsen, and Peter A. Kollman. The weighted histogram analysis method for free-energy calculations on biomolecules. I. The method. *Journal of Computational Chemistry*, 13(8):1011–1021, October 1992.
- [215] Marc Souaille and Benoit Roux. Extension to the weighted histogram analysis method: combining umbrella sampling with free energy calculations. *Computer Physics Communications*, 135(1):40–57, March 2001.
- [216] Benjamin Rotenberg, Jean-Pierre Morel, Virginie Marry, Pierre Turq, and Nicole Morel-Desrosiers. On the driving force of cation exchange in clays: Insights from combined microcalorimetry experiments and molecular simulation. *Geochimica et Cosmochimica Acta*, 73(14):4034–4044, July 2009.
- [217] Laura Scalfi, Mathieu Salanne, and Benjamin Rotenberg. Molecular Simulation of Electrode-Solution Interfaces. *Annual Review of Physical Chemistry*, 72(1):annurev-physchem-090519-024042, April 2021.
- [218] Laura Scalfi, David T. Limmer, Alessandro Coretti, Sara Bonella, Paul A. Madden, Mathieu Salanne, and Benjamin Rotenberg. Charge fluctuations from molecular simulations in the constant-potential ensemble. *Physical Chemistry Chemical Physics*, 2020.
- [219] S. K. Reed, P. A. Madden, and A. Papadopoulos. Electrochemical charge transfer at a metallic electrode: a simulation study. *J. Chem. Phys.*, 128(12):124701, 2008.

- [220] A. P. Willard, S. K. Reed, P. A. Madden, and D. Chandler. Water at an electrochemical interface - a simulation study. *Faraday Discuss.*, 141:423–441, 2009.
- [221] A. P. Willard, D. T. Limmer, P. A. Madden, and D. Chandler. Characterizing heterogeneous dynamics at hydrated electrode surfaces. *J. Chem. Phys.*, 138:184702, 2013.
- [222] David T. Limmer, Adam P. Willard, Paul Madden, and David Chandler. Hydration of metal surfaces can be dynamically heterogeneous and hydrophobic. *Proc. Nat. Acad. Sci. USA*, 110(11):4200–4205, 2013.
- [223] R. Burt, K. Breitsprecher, B. Daffos, P.-L. Taberna, P. Simon, G. Birkett, X. S. Zhao, C. Holm, and M. Salanne. Capacitance of nanoporous carbon-based supercapacitors is a trade-off between the concentration and the separability of the ions. *J. Phys. Chem. Lett.*, 7:4015–4021, 2016.
- [224] Zhujie Li, Guillaume Jeanmairet, Trinidad Mendez-Morales, Benjamin Rotenberg, and Mathieu Salanne. Capacitive Performance of Water-in-Salt Electrolytes in Supercapacitors: A Simulation Study. *The Journal of Physical Chemistry C*, 122(42):23917–23924, 2018.
- [225] Sudeep N. Punnathanam. A Gibbs-ensemble based technique for Monte Carlo simulation of electric double layer capacitors (EDLC) at constant voltage. *J. Chem. Phys.*, 140(17):174110, May 2014.
- [226] Samuel Stenberg, Bjern Stenqvist, Cliff Woodward, and Jan Forsman. Grand canonical simulations of ions between charged conducting surfaces using exact 3D Ewald summations. *Phys. Chem. Chem. Phys.*, 22(24):13659–13665, 2020.
- [227] Todd Gingrich. Simulating Surface Charge Effects in Carbon Nanotube Templated Ionic Crystal Growth. 2010.
- [228] Steve Plimpton. Fast Parallel Algorithms for Short-Range Molecular Dynamics. *Journal of Computational Physics*, 117(1):1–19, March 1995.
- [229] Large-scale Atomic/Molecular Massively Parallel Simulator. <https://lammps.sandia.gov>. Accessed: 2020-08-20.
- [230] LAMMPS fix for constant potential simulations. <https://github.com/zhenxingwang/lammps-conp>. Accessed: 2020-08-20.
- [231] Peter Eastman, Jason Swails, John D. Chodera, Robert T. McGibbon, Yutong Zhao, Kyle A. Beauchamp, Lee-Ping Wang, Andrew C. Simmonett, Matthew P. Harrigan, Chaya D. Stern, Rafal P. Wiewiora, Bernard R. Brooks, and Vijay S. Pande. OpenMM 7: Rapid development of high performance algorithms for molecular dynamics. *PLOS Computational Biology*, 13(7):e1005659, July 2017.
- [232] OpenMM. <http://openmm.org>. Accessed: 2020-08-20.
- [233] Openmm plugin for constant potential simulations. https://github.com/scychon/openmm_constV. Accessed: 2020-08-20.
- [234] Florian Weik, Rudolf Weeber, Kai Szuttor, Konrad Breitsprecher, Joost de Graaf, Michael Kuron, Jonas Landsgesell, Henri Menke, David Sean, and Christian Holm. ESPResSo 4.0, an extensible software package for simulating soft matter systems. *The European Physical Journal Special Topics*, 227(14):1789–1816, March 2019.
- [235] Extensible Simulation Package for Research on Soft Matter. espressomd.org. Accessed: 2020-08-20.
- [236] M. H. B. M. Shariff. A constrained conjugate gradient method and the solution of linear equations. *Computers & Mathematics with Applications*, 30(11):25–37, December 1995.

- [237] A. Coretti, L. Scalfi, C. Bacon, B. Rotenberg, R. Vuilleumier, G. Ciccotti, M. Salanne, and S. Bonella. Mass-zero constrained molecular dynamics for electrode charges in simulations of electrochemical systems. *The Journal of Chemical Physics*, 152(19):194701, May 2020.
- [238] J. Johnson. Thermal agitation of electricity in conductors. *Phys. Rev.*, 32:97–109, 1928.
- [239] H. Nyquist. Thermal agitation of electric charge in conductors. *Phys. Rev.*, 32:110, 1928.
- [240] Nicéphore Bonnet, Tetsuya Morishita, Osamu Sugino, and Minoru Otani. First-principles molecular dynamics at a constant electrode potential. *Phys. Rev. Lett.*, 109:266101, 2012.
- [241] Orion Ciftja. Electrostatic interaction energy between two coaxial parallel uniformly charged disks. *Results in Physics*, 15:102684, December 2019.
- [242] M. N. Tamashiro and M. A. Constantino. Ions at the Water Vapor Interface. *The Journal of Physical Chemistry B*, 114(10):3583–3591, March 2010.
- [243] C. Merlet, M. Salanne, B. Rotenberg, and P. A. Madden. Influence of solvation on the structural and capacitive properties of electrical double layer capacitors. *Electrochim. Acta*, 101:262–271, 2013.
- [244] J. Vatamanu, D. Bedrov, and O. Borodin. On the application of constant electrode potential simulation techniques in atomistic modelling of electric double layers. *Mol. Simulat.*, asap, 2017.
- [245] Philip Loche, Cihan Ayaz, Alexander Schlaich, Douwe Jan Bonthuis, and Roland R. Netz. Breakdown of Linear Dielectric Theory for the Interaction between Hydrated Ions and Graphene. *The Journal of Physical Chemistry Letters*, 9(22):6463–6468, November 2018.
- [246] Grossfield, Alan. WHAM: the weighted histogram analysis method, version 2.0.10.2. http://membrane.urmc.rochester.edu/?page_id=126.
- [247] Bradley Efron and R.J. Tibshirani. *An Introduction to the Bootstrap*. Chapman and Hall/CRC, 0 edition, May 1994.
- [248] M. Rami Reddy and M. Berkowitz. The dielectric constant of SPC/E water. *Chemical Physics Letters*, 155(2):173–176, February 1989.
- [249] Douwe Jan Bonthuis, Stephan Gekle, and Roland R. Netz. Profile of the Static Permittivity Tensor of Water at Interfaces: Consequences for Capacitance, Hydration Interaction and Ion Adsorption. *Langmuir*, 28(20):7679–7694, 2012.
- [250] Douwe Jan Bonthuis and Roland R. Netz. Beyond the Continuum: How Molecular Solvent Structure Affects Electrostatics and Hydrodynamics at Solid–Electrolyte Interfaces. *The Journal of Physical Chemistry B*, 117(39):11397–11413, October 2013.
- [251] Neil W Ashcroft and N. David Mermin. *Solid State Physics*. Thomson Learning, 1976.
- [252] Robert G. Parr and Weitao Yang. *Density-Functional Theory of Atoms and Molecules*. Oxford University Press, USA, May 1994.
- [253] Gerald D. Mahan. *Many-Particle Physics*. Physics of Solids and Liquids. Springer US, 3 edition, 2000.
- [254] L.H. Thomas. The calculation of atomic fields. *Proc. Cambridge Phil. Roy. Soc.*, 23:542–548, 1927.
- [255] E. Fermi. Un metodo statistico per la determinazione di alcune proprieta dell’atomo. *Rend. Accad. Naz. Lincei*, 6:602–607, 1927.
- [256] Laura Scalfi, Thomas Dufils, Kyle G. Reeves, Benjamin Rotenberg, and Mathieu Salanne. A semiclassical Thomas–Fermi model to tune the metallicity of electrodes in molecular simulations. *The Journal of Chemical Physics*, 153(17):174704, November 2020.

- [257] H. Gerischer. An interpretation of the double layer capacity of graphite electrodes in relation to the density of states at the Fermi level. *J. Phys. Chem.*, 89:4249–4251, 1985.
- [258] A. J. Pak, E. Paek, and G. S. Hwang. Relative contributions of quantum and double layer capacitance toward the supercapacitor performance of carbon nanotubes in an ionic liquid. *Phys. Chem. Chem. Phys.*, 15:19741–19747, 2013.
- [259] N. V. Smith, C. T. Chen, and M. Weinert. Distance of the image plane from metal surfaces. *Phys. Rev. B*, 40:7565–7573, 1989.
- [260] N. D. Lang and W. Kohn. Theory of metal surfaces: induced surface charge and image potential. *Phys. Rev. B*, 7:3541–3550, 1973.
- [261] J. Warnock, D. D. Awschalom, and M. W. Shafer. Geometrical Supercooling of Liquids in Porous Glass. *Physical Review Letters*, 57(14):1753–1756, October 1986.
- [262] D. D. Awschalom and J. Warnock. Supercooled liquids and solids in porous glass. *Physical Review B*, 35(13):6779–6785, May 1987.
- [263] Fernando Bresme and Luis G. Cámara. Computer simulation studies of Crystallization under confinement conditions. *Chemical Geology*, 230(3-4):197–206, June 2006.
- [264] Kenichiro Koga and Hideki Tanaka. Phase diagram of water between hydrophobic surfaces. *The Journal of Chemical Physics*, 122(10):104711, March 2005.
- [265] Catheryn L. Jackson and Gregory B. McKenna. The melting behavior of organic materials confined in porous solids. *The Journal of Chemical Physics*, 93(12):9002–9011, December 1990.
- [266] Oleg Petrov and István Furó. Curvature-dependent metastability of the solid phase and the freezing-melting hysteresis in pores. *Physical Review E*, 73(1), January 2006.
- [267] George W Scherer. Crystallization in pores. *Cement and Concrete Research*, 29(8):1347–1358, August 1999.
- [268] M. B. Ritter, D. D. Awschalom, and M. W. Shafer. Collective Behavior of Supercooled Liquids in Porous Media. *Physical Review Letters*, 61(8):966–969, August 1988.
- [269] Somendra Nath Chakraborty and Lev D. Gelb. A Monte Carlo Simulation Study of Methane Clathrate Hydrates Confined in Slit-Shaped Pores. *The Journal of Physical Chemistry B*, 116(7):2183–2197, February 2012.
- [270] J. S. Rowlinson and B. Widom. *Molecular Theory of Capillarity*. Courier Corporation, April 2013.
- [271] Ph. Buffat and J-P. Borel. Size effect on the melting temperature of gold particles. *Physical Review A*, 13(6):2287–2298, June 1976.
- [272] George Kaptay. The Gibbs Equation versus the Kelvin and the Gibbs-Thomson Equations to Describe Nucleation and Equilibrium of Nano-Materials. *Journal of Nanoscience and Nanotechnology*, 12(3):2625–2633, March 2012.
- [273] Rodolfo G. Pereyra, Igal Szleifer, and Marcelo A. Carignano. Temperature dependence of ice critical nucleus size. *The Journal of Chemical Physics*, 135(3):034508, July 2011.
- [274] R. Evans and U. Marini Bettolo Marconi. Phase equilibria and solvation forces for fluids confined between parallel walls. *The Journal of Chemical Physics*, 86(12):7138–7148, June 1987.
- [275] R. Evans, U. Marini Bettolo Marconi, and P. Tarazona. Fluids in narrow pores: Adsorption, capillary condensation, and critical points. *The Journal of Chemical Physics*, 84(4):2376–2399, February 1986.

- [276] Robert Evans, Umberto Marini Bettolo Marconi, and Pedro Tarazona. Capillary condensation and adsorption in cylindrical and slit-like pores. *Journal of the Chemical Society, Faraday Transactions 2: Molecular and Chemical Physics*, 82(10):1763–1787, 1986.
- [277] H. Dominguez, M. P. Allen, and R. Evans. Monte Carlo studies of the freezing and condensation transitions of confined fluids. *Molecular Physics*, 96(2):209–229, January 1999.
- [278] Laura Scalfi, Benoît Coasne, and Benjamin Rotenberg. On the Gibbs–Thomson equation for the crystallization of confined fluids. *The Journal of Chemical Physics*, 154(11):114711, March 2021.
- [279] David C. Johnston. *Advances in Thermodynamics of the van der Waals Fluid*.
- [280] A. J. C. Ladd and L. V. Woodcock. Triple-point coexistence properties of the lennard-jones system. *Chemical Physics Letters*, 51(1):155–159, October 1977.
- [281] Rupal Agrawal and David A. Kofke. Solid-Fluid Coexistence for Inverse-Power Potentials. *Physical Review Letters*, 74(1):122–125, January 1995.
- [282] Rupal Agrawal and David A. Kofke. Thermodynamic and structural properties of model systems at solid-fluid coexistence. *Molecular Physics*, 85(1):23–42, May 1995.
- [283] Rupal Agrawal and David A. Kofke. Thermodynamic and structural properties of model systems at solid-fluid coexistence: II. Melting and sublimation of the Lennard-Jones system. *Molecular Physics*, 85(1):43–59, May 1995.
- [284] Ethan A. Mastny and Juan J. de Pablo. Melting line of the Lennard-Jones system, infinite size, and full potential. *The Journal of Chemical Physics*, 127(10):104504, September 2007.
- [285] Xipeng Wang, Simón Ramírez-Hinestrosa, Jure Dobnikar, and Daan Frenkel. The Lennard-Jones potential: when (not) to use it. *Physical Chemistry Chemical Physics*, 2020.
- [286] Alauddin Ahmed and Richard J. Sadus. Effect of potential truncations and shifts on the solid-liquid phase coexistence of Lennard-Jones fluids. *The Journal of Chemical Physics*, 133(12):124515, September 2010.
- [287] Aziz Ghoufi, Patrice Malfreyt, and Dominic J. Tildesley. Computer modelling of the surface tension of the gas–liquid and liquid–liquid interface. *Chemical Society Reviews*, 45(5):1387–1409, 2016.
- [288] Jadran Vrabec, Gaurav Kumar Kedia, Guido Fuchs, and Hans Hasse. Comprehensive study of the vapour–liquid coexistence of the truncated and shifted Lennard–Jones fluid including planar and spherical interface properties. *Molecular Physics*, 104(9):1509–1527, May 2006.
- [289] J. H. Irving and John G. Kirkwood. The Statistical Mechanical Theory of Transport Processes. IV. The Equations of Hydrodynamics. *The Journal of Chemical Physics*, 18(6):817–829, June 1950.
- [290] John G. Kirkwood and Frank P. Buff. The Statistical Mechanical Theory of Surface Tension. *The Journal of Chemical Physics*, 17(3):338–343, March 1949.
- [291] R. Shuttleworth. The Surface Tension of Solids. *Proceedings of the Physical Society. Section A*, 63(5):444, 1950.
- [292] M. J. P. Nijmeijer, van, and J. M. J. Leeuwen. Microscopic expressions for the surface and line tension. *Journal of Physics A: Mathematical and General*, 23(19):4211, 1990.
- [293] Gregory Grochola. Constrained fluid λ -integration: Constructing a reversible thermodynamic path between the solid and liquid state. *The Journal of Chemical Physics*, 120(5):2122–2126, January 2004.

- [294] David M. Eike, Joan F. Brennecke, and Edward J. Maginn. Toward a robust and general molecular simulation method for computing solid-liquid coexistence. *The Journal of Chemical Physics*, 122(1):014115, December 2004.
- [295] N. B. Wilding and A. D. Bruce. Freezing by Monte Carlo Phase Switch. *Physical Review Letters*, 85(24):5138–5141, December 2000.
- [296] Graham C. McNeil-Watson and Nigel B. Wilding. Freezing line of the Lennard-Jones fluid: A phase switch Monte Carlo study. *The Journal of Chemical Physics*, 124(6):064504, February 2006.
- [297] Daan Frenkel and Anthony J. C. Ladd. New Monte Carlo method to compute the free energy of arbitrary solids. Application to the fcc and hcp phases of hard spheres. *The Journal of Chemical Physics*, 81(7):3188–3193, October 1984.
- [298] Ulf R. Pedersen, Felix Hummel, Georg Kresse, Gerhard Kahl, and Christoph Dellago. Computing Gibbs free energy differences by interface pinning. *Physical Review B*, 88(9), September 2013.
- [299] Ulf R. Pedersen. Direct calculation of the solid-liquid Gibbs free energy difference in a single equilibrium simulation. *The Journal of Chemical Physics*, 139(10):104102, September 2013.
- [300] Benoit Coasne, Surendra K. Jain, Linda Naamar, and Keith E. Gubbins. Freezing of argon in ordered and disordered porous carbon. *Physical Review B*, 76(8):085416, August 2007.
- [301] Benoit Coasne, J. Czwartos, M. Sliwinska-Bartkowiak, and Keith E. Gubbins. Effect of Pressure on the Freezing of Pure Fluids and Mixtures Confined in Nanopores. *The Journal of Physical Chemistry B*, 113(42):13874–13881, October 2009.
- [302] Dongliang Jin and Benoit Coasne. Molecular Simulation of the Phase Diagram of Methane Hydrate: Free Energy Calculations, Direct Coexistence Method, and Hyperparallel Tempering. *Langmuir*, 33(42):11217–11230, October 2017.
- [303] Samuel Ntim and Marialore Sulpizi. Role of image charges in ionic liquid confined between metallic interfaces. *Phys. Chem. Chem. Phys.*, 22(19):10786–10791, 2020.
- [304] William Humphrey, Andrew Dalke, and Klaus Schulten. VMD: Visual molecular dynamics. *Journal of Molecular Graphics*, 14(1):33–38, February 1996.
- [305] William L. Jorgensen, Jayaraman Chandrasekhar, Jeffrey D. Madura, Roger W. Impey, and Michael L. Klein. Comparison of simple potential functions for simulating liquid water. *The Journal of Chemical Physics*, 79(2):926–935, July 1983.
- [306] K. Anton Feenstra, Berk Hess, and Herman J. C. Berendsen. Improving efficiency of large time-scale molecular dynamics simulations of hydrogen-rich systems. *Journal of Computational Chemistry*, 20(8):786–798, 1999.

Abstract

A variety of electrochemical processes involved in energy applications rely on the electric double layer that forms between a metallic electrode and an electrolyte. Modeling such interfaces provides a molecular understanding of the mechanisms involved but remains a challenge where statistical physics meets quantum chemistry. In constant potential simulations, we apply a voltage between two electrodes allowing their charges to fluctuate, but usual implementations do not account for the electrodes metallicity that reflects how external electric fields are screened by the charge distribution.

This work provides an extension of this framework using a semi-classical Thomas-Fermi model, that introduces a characteristic screening length l_{TF} in the material. We study its impact for a range of l_{TF} on the charge distribution within the electrode, the capacitance, the structure of the electrolyte and the charging dynamics of the capacitor. This framework allows to tackle recent experiments of freezing under confinement suggesting a strong influence of the metallicity on surface tension. We first revisit the Gibbs-Thomson equation to study its limitations. Then, building on the formalization of the statistical mechanics of the constant potential ensemble, which reveals the impact of Born Oppenheimer sampling on measured properties, we develop a thermodynamic integration method that yields the interfacial free energy as a function of l_{TF} . This shows the crucial role of lateral charge correlations on surface tension and opens the way to the study of solid-liquid transitions.

Keywords: interfaces; molecular dynamics; surface tension; metallicity; confinement; capacitors

Résumé

Influence de la métallicité des surfaces solides sur les propriétés des fluides confinés ou aux interfaces

De nombreux processus électrochimiques sont basés sur la double couche électrique qui se forme entre une électrode métallique et un électrolyte. Modéliser ces interfaces permet une vision moléculaire des mécanismes impliqués mais reste un défi où la physique statistique rencontre la chimie quantique. Les simulations à potentiel constant permettent d'imposer une différence de potentiel (ddp) entre deux électrodes en laissant leurs charges fluctuer, mais n'incluent pas leur métallicité qui reflète la façon dont les champs électriques externes sont écartés par la distribution de charge.

Ce travail étend ces simulations en utilisant un modèle semi-classique de Thomas-Fermi, qui introduit une longueur d'écrantage l_{TF} dans le matériau. Nous étudions son impact pour une gamme de l_{TF} sur la distribution de charge dans l'électrode, la capacité, la structure de l'électrolyte et la dynamique de charge du condensateur. Ce modèle permet d'aborder des expériences récentes de solidification sous confinement suggérant une forte influence de la métallicité sur la tension de surface. Nous revisitons d'abord l'équation de Gibbs-Thomson pour étudier ses limites. Puis, en nous appuyant sur la formalisation de l'ensemble thermodynamique à potentiel constant, qui révèle l'impact de l'échantillonnage de Born Oppenheimer sur les propriétés, nous développons une méthode d'intégration thermodynamique donnant l'énergie libre interfaciale en fonction de l_{TF} . Ceci montre le rôle crucial des corrélations de charge latérales sur la tension de surface et ouvre la voie à l'étude des transitions solide-liquide.

Mots-clé : interfaces ; dynamique moléculaire ; tension de surface ; métallicité ; confinement ; condensateurs